Structural and magnetic properties of low dimensional Heusler alloys

A thesis submitted in partial fulfillment of the requirement for the award of the degree of

Doctor of Philosophy in Physics

By

Manisha Srivastava

Under the supervision of

Prof. A. Srinivasan

Department of Physics

Indian Institute of Technology Guwahati

Guwahati – 781039, India

April 2024

Dedicated to

my grandparents

Declaration statement

I, Manisha Srivastava, hereby declare that the research work presented in the thesis, entitled "**Structural and magnetic properties of low dimensional Heusler alloys**" has been carried out by me under the supervision of Prof. A. Srinivasan, at the Department of Physics, Indian Institute of Technology Guwahati. I further confirm that no part of this work has been submitted elsewhere for the award of any other degree/diploma or any other academic award.

April 1st 2024

Manisha Srivastava

Roll No.: 176121011

Department of Physics

Indian Institute of Technology Guwahati

Guwahati – 781039, India

Certificate

It is certified that the work contained in the thesis entitled "**Structural and magnetic properties of low dimensional Heusler alloys**" submitted by Manisha Srivastava (Roll No. 176121011), a Ph. D. student of the Department of Physics, Indian Institute of Technology Guwahati for the award of the degree of Doctor of Philosophy has been carried out under the supervision of Prof. A. Srinivasan. This work has not been submitted elsewhere for the award of any degree.

April 1st 2024

Prof. A. Srinivasan

Professor

Department of Physics

Indian Institute of Technology Guwahati

Guwahati – 781039, India

Acknowledgments

Looking back, I am overwhelmed with profound gratitude to the individuals who have played a vital role in assisting me to achieve this significant milestone.

With immense gratitude, I acknowledge the debt I owe to my supervisor, Prof. A. Srinivasan, whose mentorship not only nurtured my intellectual curiosity but his encouragement for discussions and debates on various topics also laid the essential foundation for cultivating a scientific mindset. His insightful advice, innovative ideas, and broad envisage helped me a lot to expand my understanding. He gave me the freedom to express my opinions and ideas and believed in my abilities. It's the result of his vision and guidance that gave me unconditional liberty to work and turned a Ph.D. scholar into an independent researcher. Other than research, I have been tremendously amazed by his energetic spirit and relentless dedication to his work, which has left an unforgettable imprint on my scholastic career.

I am greatly indebted to the chairperson of my doctoral committee, Prof. A. Perumal, for his valuable time and suggestions whenever required. I can't forget to acknowledge the weekend group meetings with Prof. Srinivasan and Prof. Perumal, which enhanced my comprehension of various concepts and principles of Physics. I was astonished by the immeasurable depth of their knowledge and phenomenal expertise in this field, which has created a firm backbone for my research career.

My gratitude extends to my doctoral community members, Prof. A. Perumal, Prof. Subhradip Ghosh, and Prof. P. S. Robi, for their continuous academic guidance and monitoring of my research progress during my thesis work. Their instructive comments and feedback improved the quality of my thesis work and pointed me in the right direction by illuminating the road toward my research objectives.

I am grateful to the current and former Heads of the Department of Physics for substantial administrative cooperation and for giving me the opportunity to utilize all the departmental resources with full freedom. I am also thankful to all the faculty members of the Department of Physics during my Ph.D. journey at IIT Guwahati.

I express my sincere thanks to the Council of Scientific and Industrial Research, Government of India, for the funding through the project (project no: 03(1431)/18/EMR-II), and the Ministry of Education, Government of India, for providing the fellowship to pursue a Ph.D. without any financial constraints. I extend my heartfelt appreciation to the Department of Physics (including the facility acquired under the Department of Science and Technology, Government of India for project no: SR/FST/PSII-037/2016), Central Instrument Facility (CIF), North East Centre for Biological Sciences and Healthcare Engineering (NECBH for the FESEM/EDX facilities acquired under the Department of Biotechnology, Government of India for project no: BT/COE/34/SP28408/2018), Computer Centre (for supercomputing resources), and other departments of the Indian Institute of Technology Guwahati for providing me with the sample preparation, characterization, and computational facilities to carry on my research.

I convey my gratitude to my collaborators Dr. Munima B. Sahariah, Gajendra S. Bisht, and Payal Saha, for assisting me in the theoretical calculations through their expertise, which helped me strengthen the calibre of my work.

I remain indebted to my M. Tech. Lab (Novel Materials and Interface Physics Laboratory) mates in the Department of Physics, IIT Delhi, headed by Dr. Rajendra S. Dhaka. Dr. Dhaka sowed the seeds of research in me and introduced me to this world of research and innovations. I have learned many things from him, starting from research to many life values including hard work and enthusiasm.

I would like to convey my heartfelt gratitude to Dr. Sidananda Sarma for his consistent support at various stages of my Ph.D. journey. His presence in the department and on campus was like an elder brother who is always available to resolve any hurdle in the Ph.D. work. I am highly thankful to Dr. Sidananda Sarma, Mr. Aditya Kalita, Dr. Arnab Kumar Das, Dr. Aakansha, and Dr. Rajkumar Modak for upskilling me in operating arc melting, X-ray diffractometer, electrospinning, vibrating sample magnetometer, and other equipment. Furthermore, I extend my sincere appreciation to Dr. Sidananda Sarma, Mr. Aditya Kalita, Mr. Chandan Borgohain, Dr. Kula Kamal Senapati, Dr. Kh. Kesho Singh, Mr. Sujit Kumar Deb, and Dr. Dolly Gogoi for allowing me to use the XRD, VSM, SEM, TEM, ESR and other instruments whenever required even at odd hours. I was fascinated to see the enthusiastic demonstrations of physics experiments for school children by Lokesh da, Sida da, and Aditya da at IITG, which inspired me a lot by awakening me to the need for the intellectual growth of students through their genuine concern. I am grateful to the non-teaching staff of the Department of Physics and the IIT campus for their kind help and assistance in various ways. I appreciate the technical support from Mr. Bhaskar, Mr. Kishor, Mr. Milan, Mr. Rupak, and other operators of the various instruments in their efforts to perform measurements at the desired conditions. I thank Dinesh and Alok for their efforts in EDS and TEM measurements, even at odd hours. I am thankful to my seniors, Dr. Arnab Kumar Das, Dr. Rajkumar Modak, Dr. Aneeta Manjari Padhan, and Dr. Dolly Taparia, who enriched me with their valuable inputs in the research field even in a short span of time on campus. I had a lot of amazing instructors during school, especially Yadav sir, Happy sir, Ishan sir, and Jyoti ma'am, whose fascinating teaching directed me toward where I am today.

I am extremely fortunate to have a wonderful lab group that gave me a comfortable and stress-free working environment. I will take this opportunity to thank Amritava Bhaiya, Sunil Bhaiya, Nitu, Subrata, Pushpesh, Alok, Madhav, Dev, Didwmsha, Debraj, Dinesh, Aritra,

Harekrushna, Sourav, Tandrima, Nidhi, Praduman, Pratibha, Abul, Abhinath and Franky. Their homely care, and selfless assistance in research as well as in personal matters are priceless. They are companions in my joys and sorrows. With them all, I felt like a family here. We had a marvellous time together, which always kept me calm and cheerful and made this journey easy-going. I started this amazing Ph.D. journey here with Nitu with a promise that we will handle any difficult situation together and now it's exciting to reach the finishing point of this beautiful journey together with a more powerful friendship. On hectic working days, Sunil Bhaiya, Pushpesh, Debraj, Alok, Dinesh, Harekrushna, and Sourav were always there, whether it was about requesting them to close the furnace/stirrer/gas flow late at night or about sitting together to complete the regular working tasks. I am deeply grateful to Debraj for upskilling me with the *ab initio* calculations, which will definitely help me throughout my research career. The worthwhile discussions with Debraj and Madhav reinforced my proficiency in research.

The entire poets' corner and literary society group, especially Abhishek, Avikshit, Sujeet, Upendra bhaiya, Manoshi mam, Abrar, Shreeram, Rishabh, and Anmol, deserve a special mention for bringing a refreshing change to a monotonous research life. In this long journey, full of challenges and numerous ups and downs, the company of people like them not only provided me with a delightful and enjoyable surrounding but also helped me refine myself through discussions on various topics. Furthermore, while working as the literary secretary, I learned many skills, including leadership, management, *etc.*, which polished my overall personality. I express my deep sense of gratitude to my friends Pooja and Monu for all their moral support and motivation. I cannot forget to acknowledge my fellow scholars Madhurima, Ipsita, Pragya, Prajna, Neda, Pronoy, Shilpi, Suresh, Suchit, Akanshu, and other members of the Physics department who provided a healthy and stimulating research environment.

I consider myself eternally fortunate to be surrounded by a caring family. I owe a lot to my parents for all their sacrifices and unconditional love, which shaped me into the person I

am today. I owe a significant debt to my father-in-law and my mother-in-law for their wholehearted blessing, care, and trust in me, which made me strong. I am really blessed to have a loving and understanding family, which made things easier for me so that I could make a balance between research and personal life. I am eternally grateful to the whole of my family ch$\bar{a}$ch$\bar{a}$, ch$\bar{a}$chi, mausi, mausa, m$\bar{a}$m$\bar{a}$, m$\bar{a}$mi, bua, fufa, and all my brothers and sisters who were always the constant source of happiness. Special thanks to Piyush, whose unwavering belief in me carried me forward. He always stood by my side and backed me in every possible way, which sustained me through the challenges and obstacles along the way. He always encouraged and inspired me to follow my dreams. Words are not enough to express my profound emotions for his togetherness. I would like to express my deepest gratitude toward my d$\bar{a}$d$\bar{a}$ Late Madan Kishor Srivastava, d$\bar{a}$di Late Smt. Chandramukhi Srivastava, n$\bar{a}$n$\bar{a}$ Late Shree Daya Shankar Laal Srivastava and n$\bar{a}$ni Late Smt. Shakuntala Devi for their values and lessons instilled in me, which left an indelible mark on my life. I extend my sincere appreciation to my d$\bar{a}$di (in law's) Smt. Shiromani Devi and n$\bar{a}$n$\bar{a}$ (in law's) Shree Bal Krishna Sahay for being a constant source of inspiration and endless love.

Finally, I would like to express my heartfelt gratitude to everyone who has assisted me directly or indirectly in any way and helped me get to where I am now. Some of whom I may have inadvertently skipped to include in this appreciation, I thank you all for enabling me to reach this milestone.

Sincerely

Manisha Srivastava

Preface

Magnetic nanoparticles are currently experiencing significant demand across a wide range of applications, extending from cutting-edge technologies to breakthroughs in healthcare. Magnetic particles ranging in size from 50 to 500 nm exhibiting high saturation magnetization ($M_s \approx 70 – 170$ emu/g), significant effective anisotropy constant ($K_{eff} \approx 10^4 – 10^6$ erg/cc), high density ($\rho \approx 4.8 – 6$ g/cc) and low coercive field ($H_c \approx 251 – 2011$ Oe) serve as pivotal components in perpendicular magnetic recording media employed in high-density magnetic recording systems. Moreover, magnetic nanoparticles with high M_s of ~ 60 emu/g with a low H_c of ~ 175 Oe have found application in magnetic field sensing. Heusler alloy nanoparticles primarily composed of Cobalt (Co) and Iron (Fe) have emerged as compelling options that satisfy various criteria, including substantial M_s, elevated Curie temperature (T_C), high ρ, increased K_{eff}, and minimal H_c, *etc*. Consequently, Heusler alloy nanoparticles are getting recognition in diverse applications, including the detection of SARS-Covid-2 virus, catalysts, biosensing, and hyperthermia treatment of cancer. Moreover, the versatility of Heusler alloys is apparent as they can be tailored to exhibit ferromagnetic, nonmagnetic, antiferromagnetic, or ferrimagnetic properties based on the choice of constituent elements with their elemental compositions. The revelation of half-metallicity in Heusler alloys has unlocked the possibility of the development of spintronic devices. The conjunction of half-metallicity together with quantum confinement can be anticipated in Heusler alloy nanoparticles, heralding several novel and new possibilities.

However, these nanoparticles can only be utilized at their full potential if one can obtain them in their fully ordered ($L2_1$ or X type), impurity free, and phase pure form as the appearance of various atomic disorders ($B2$ or $A2$ type) are quite prevalent, which may degrade their qualities. Unfortunately, there exist a lot of gaps in the existing literature on these Heusler alloy nanoparticles. Most of the previous reports on these nanoparticles reveal the coexistence of

impurity phases and/or the lack of ordered crystal structure in them, which immensely impact their structural and magnetic properties. Further, the customary utilization of diamagnetic silica templates in their synthesis process has imposed another challenge in obtaining them in impurity free form. Additionally, many of the earlier studies suffered from the inability to obtain the desired nominal composition in the final product, which have led to deviations in the expected properties. Moreover, the existing crystallite size or composition dependent research on Heusler alloy nanoparticles are limited and unsystematic. Thus, a facile methodology for the synthesis of Heusler alloy nanoparticles with stable and highly ordered phase pure crystal structure providing good control on crystallite size and chemical composition is missing in the literature. Such a refined methodology could result in enhanced structural and magnetic properties, thereby opening up a plethora of nanomagnetic device applications. This thesis work attempts to address these challenges.

First, a simple template-less chemical route was developed to synthesize ternary Heusler alloy nanoparticles. *viz.*, Co_2FeGa, Fe_2CoGa, and Fe_2CoAl. After establishing a procedure to obtain phase pure and highly ordered near-stoichiometric Heusler alloy compounds in nanoparticle form, the variation of magnetic properties of these nanoparticles as a function of crystallite size was explored. Having mastered the procedure to obtain the nominal stoichiometry in the Heusler alloy compounds, $Fe_{2-x}Co_{1+x}Ga$ ($0 \leq x \leq 1$) nanoparticles were synthesized, and their composition dependent properties were determined. Finally, the synthesis of a quaternary Heusler alloy nanoparticle was demonstrated for the first time by preparing $Fe_2CoGa_{0.5}Al_{0.5}$ nanoparticles. This showcased the prowess of the developed methodology to synthesize other intermediate off-stoichiometric quaternary Heusler alloy compositions. The experimental research carried out has been supported by theoretical studies. These include the prediction of magnetic properties, electronic density of states, and half

metallic properties of these Heusler alloys and interpretation and validation of the experimental results with standard theoretical models.

The results not only showcase the spirit of the methodology to obtain such a highly ordered, impurity free, single phase, single domain, soft ferromagnetic Heusler alloy nanoparticles with enhanced structural and magnetic properties but also bring out insights and new information about these nanoparticle alloys not known so far. These studies also help us in understanding the behavior of these systems so that they can be effectively utilized in practical applications because of their enhanced magnetization, Curie temperature, and magnetic anisotropy coupled with low coercivity.

Table of Contents

1. Introduction

1.1 Heusler alloys 2

1.1.1 Structure 3

1.1.2 Properties and phenomena 6

1.1.3 Developments in X_2YZ Heusler alloys 16

1.2 Low dimensional materials 17

1.2.1 Magnetic nanoparticles 18

1.3 Advancements in low dimensional Heusler alloys 24

1.4 Motivation behind this thesis work 25

2. Experimental and Theoretical Details 27

2.1 Sample preparation 27

2.1.1 Synthesis of Heusler alloy nanoparticles 27

2.1.2 Synthesis of bulk Heusler alloys using arc melting method 31

2.2 Characterization techniques 33

2.2.1 Powder X-ray Diffractometer 33

2.2.2 Electron microscopes 44

2.2.3 Vibrating Sample Magnetometer (VSM) 55

2.2.4 Electron Spin Resonance (ESR) spectrometer 59

2.3 Details of theoretical calculations 62

2.3.1 Input files in VASP 63

2.3.2 Steps involved in DOS calculations performed through VASP 69

3. Crystallite size dependent properties of Co_2FeGa nanoparticles 72

3.1 Sample preparation 73

3.2 Structural analysis 74

3.3 Elemental composition and morphology 78

3.4 DOS calculations 80

3.5 Magnetic properties 83

3.6 Summary and Highlights 90

4. Crystallite size dependent properties of Fe_2CoGa nanoparticles 92

4.1 Sample preparation 93

4.2 Structural analysis 93

4.3 Elemental composition and morphology 98

4.4 DOS calculations 100

4.5 Magnetic properties 101

4.6 Summary and Highlights 107

5. Crystallite size dependent properties of Fe_2CoAl nanoparticles 109
5.1 Sample preparation 110
5.2 Structural analysis 110
5.3 Elemental composition and morphology 115
5.4 DOS calculations 116
5.5 Magnetic properties 118
5.6 Summary and Highlights 124
6. Composition dependent properties of $Fe_{2-x}Co_{1+x}Ga$ ($0 \leq x \leq 1$) nanoparticles 126
6.1 Sample preparation 127
6.2 Structural analysis 127
6.3 Elemental composition and morphology 135
6.4 DOS calculations 136
6.5 Magnetic properties 138
6.6 Summary and highlights 143
7. Investigations on $Fe_2CoGa_{0.5}Al_{0.5}$ nanoparticles 145
7.1 Sample preparation 145
7.2 Structural analysis 146
7.3 Elemental composition and morphology 148
7.4 DOS calculations 149
7.5 Magnetic properties 151
7.6 Summary and highlights 153
8. Summary and scope for future work 155
8.1 Summary of the current study 155
8.2 Scope for future work 157
References 159
Publications/Presentations 184

Chapter 1

Introduction

In order to fulfill new technological demands, there is the necessity for the development of new materials. The utility of magnetic nanoparticles in various sectors opens up the door of opportunities for materials scientists. Small magnetic particles with sizes ranging from 50 to 500 nm, having high mass density (ρ = 4.8 to 6 × 10^3 kg/m^3), high saturation magnetization (M_s = 70 to 170 Am^2/kg), high effective anisotropy constant (K_{eff} ~10^4 – 10^6 erg/cc), and low coercivity (H_c ~ 20 to 160 kA/m), are sought after for their application in perpendicular magnetic recording media in the high density magnetic recording systems [1]. Similarly, ferrite nanoparticles having high M_s (60 emu/g) with low H_c (175 Oe) have found utilizations in magnetic field sensing [2]. Fe and Co based Heusler alloy nanoparticles meet the majority of these criteria owing to their sufficiently high ρ, M_s, K_{eff}, Curie temperature (T_C) and low H_c. As a result, Heusler alloy nanoparticles are progressively being utilized in a variety of fields ranging from emerging technologies to medical sectors. Several recent publications suggest numerous promising applications for Co and Fe based Heusler alloy nanoparticles [3–6]. For example, Dahiya *et al.* [4] utilized Co_2FeAl nanoparticles in the detection of SARS Cov-2 virus. Karim *et al.* [3] employed Co_2FeSn nanoparticles in magnetothermal applications such as in hyperthermia treatment of cancer. Kappe *et al.* [6] demonstrated the suitability of Co_2MnSi nanoparticles in biosensing applications. Kojima *et al.* [5] applied Co_2FeGe nanoparticles in catalysis. These reports showcase that these Heusler alloy nanoparticles with their superior properties, have the potential to replace many traditional magnetic nanoparticles in diverse sectors. Also, these researches demonstrate the necessity for further exploration of the field of Heusler alloy nanoparticles to unfold many hidden opportunities.

1.1 Heusler alloys

Heusler alloys are prototype ternary intermetallic compounds having the chemical formula X_2YZ [7]. Here, X and Y are typically transition metals, whereas Z is a Group III – V element, as depicted in Figure 1.01. These Heusler alloys are named after the German chemist Friedrich Heusler [8], who first investigated the Cu_2MnAl compound in the year 1903. He discovered that this material is soft ferromagnetic in nature despite containing no ferromagnetic element. At that time, the crystal structure of this compound was not known. Later, in 1934, the crystal structure of Heusler alloys was determined by Otto Heusler [9], the son of Friedrich Heusler, and Bradley *et al.* [10]. This triggered the investigations on many such compounds having similar structures.

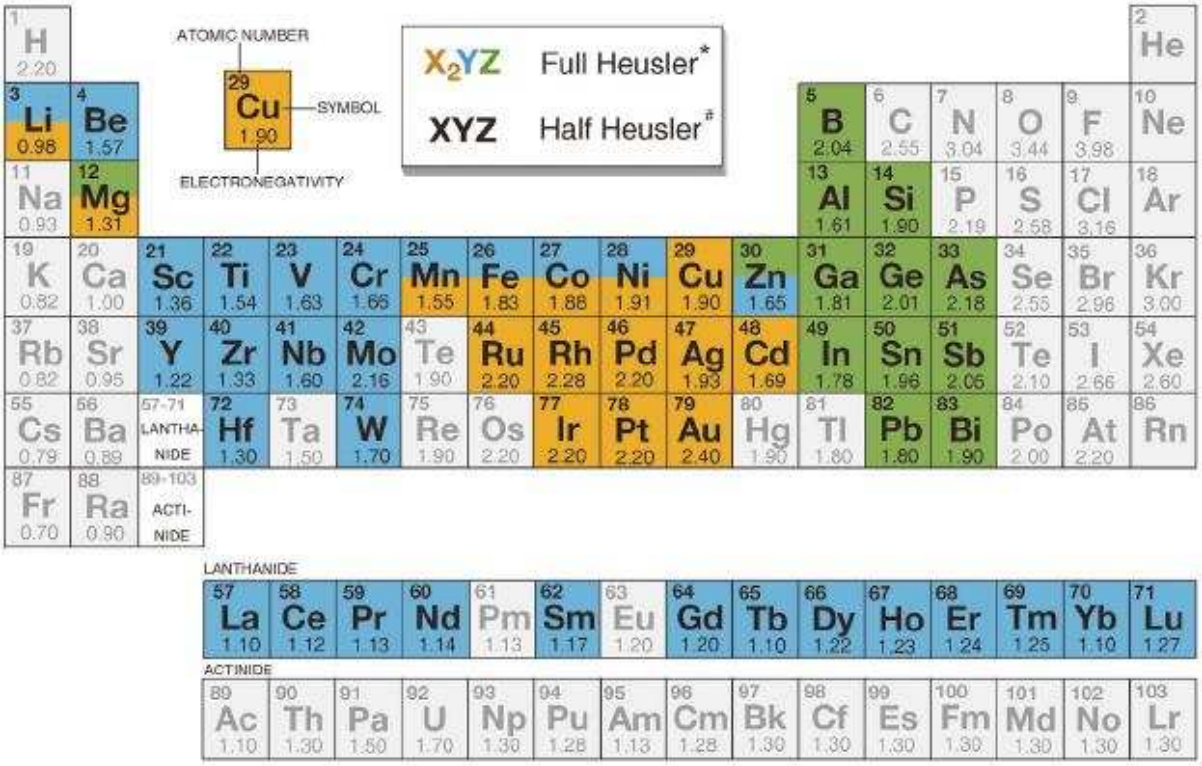

Figure 1.01. Periodic table showing various choice of elements as X, Y, and Z in Heusler alloys [11].

1.1.1 Structure

The novel properties and phenomena of Heusler alloys, which lead to various applications, are attributed to their unique crystal structure. The unit cell of a full Heusler alloy comprises of four interpenetrating face cantered cubic (fcc) sublattices positioned at (0, 0, 0), (¼, ¼, ¼), (½, ½, ½), and (¾, ¾, ¾) [12]. The distribution of X, Y, and Z elements at these positions determines the ordered/disordered crystal structures for these compounds.

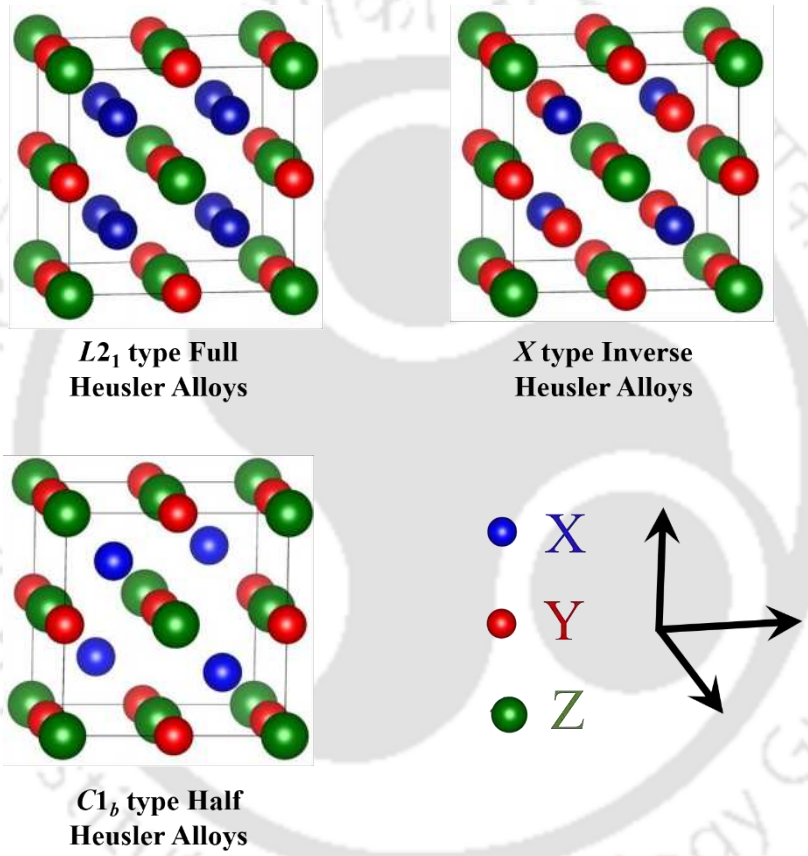

Figure 1.02. Unit cells of $L2_1$ type, *X* type and $C1_b$ type Heusler alloys.

Depending upon the choice of the X and Y elements, the fully ordered Heusler alloys can be classified in two categories. If the atomic number of the X atom is higher than that of the Y atom, then it is known as $L2_1$ type full Heusler alloy. On the other hand, if the atomic number of the Y atom is higher than that of the X atom, then it is called *X* type inverse Heusler alloy [12]. In $L2_1$ type full Heusler alloy (prototype being Cu_2MnAl) with the space group

$Fm\bar{3}m$ (space group number 225), the X atom occupies the equivalent positions (¼, ¼, ¼), and (¾, ¾, ¾), the Y atom occupies (½, ½, ½), and the Z atom stays at (0, 0, 0), as displayed in Figure 1.02 [12]. On the other hand, in *X* type inverse Heusler alloy (prototype being $CuHg_2Ti$), with the space group $F\bar{4}3m$ (space group number 216), both the X atoms occupy the non-equivalent positions (½, ½, ½), and (¾, ¾, ¾), the Y atom occupies (¼, ¼, ¼), and the Z atom stays at (0, 0, 0) [12]. In other words, in *X* type structure, half of the X atoms exchange their position with the Y atoms as illustrated in Figure 1.02. Both these structures can be identified by the presence of superlattice reflections (111) and (200) in their X-ray or electron diffraction patterns.

Subsequently, it was realized that if one of the four sublattices remains unoccupied, the unit cell reduces to $C1_b$ type structure with the space group $F\bar{4}3m$ (space group number 216) [12]. Such structures are called half Heusler alloy with the chemical formula XYZ.

The crystal structure has a significant influence on the properties of these alloys. Hence, it is imperative to synthesize them with the stable, fully ordered $L2_1$ or *X* type structure characterized by superlattice reflections (111) and (200) in their diffraction patterns. However, the crystal structure of these Heusler alloys often exhibits various atomic disorders due to the intermixing of constituent elements at ambient temperatures. This tends to deteriorate the special properties inherited due to their unique crystal structure. There are several types of disordered structures possible in Heusler alloys, as depicted in Figure 1.03. The *B*2 type partially disordered structure arises from the intermixing of Y and Z atoms in the $L2_1$ type structure [12]. This structure can be visualized on the basis of CsCl prototype, resulting in the reduced symmetric space group $Pm\bar{3}m$ (space group number 221) [12]. This structure can be identified by the exclusive presence of the (200) superlattice reflection along with the absence of the (111) superlattice reflection. The DO_3 type structure is another type of disordered

structure, which arises from the intermixing of X with Y atom or X with Z atoms in $L2_1$ type structure [12]. Its prototype structure is of BiF_3 [12] with a space group $Fm\bar{3}m$ (space group number 225). Further, an *A*2 type fully disordered structure results from the total intermixing of all three X, Y, and Z elements, having a further reduced symmetric space group $Im\bar{3}m$ (space group number 229) [12]. It follows the prototype structure of the tungsten (W), resulting in a body cantered cubic (bcc) lattice [12]. This structure can be identified by the absence of both the (111) and (200) superlattice reflections in the X-ray or electron diffraction patterns. Other than the aforementioned cubic structures, some of the Heusler alloys (Co-Ni-Z, Ni-Mn-Z, *etc.*) transform into tetragonal structures (*I*4/mmm (space group number - 139), $I\bar{4}2m$ (space group number - 121), *P*4/*mmm* (space group number - 123), *etc.*) at low temperatures during first order, diffusion-less phase transition called martensitic transformation (will be discussed later) [12].

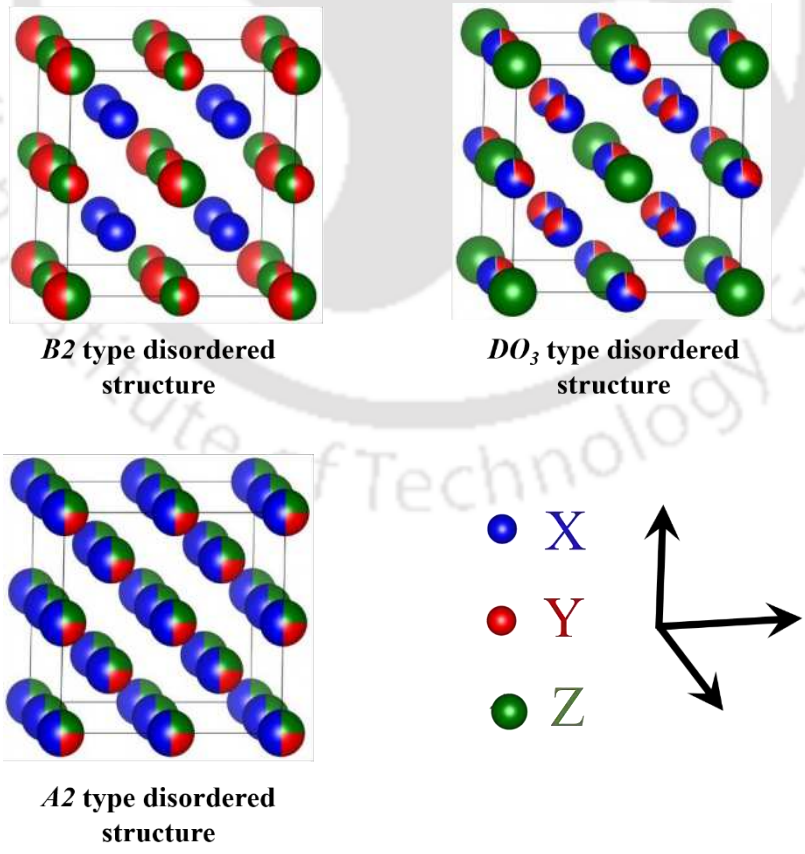

Figure 1.03. *B*2, *A*2 and DO_3 type disordered Heusler alloy structures.

Since the crystal structure plays a crucial role in deciding the properties of these alloys, a thorough examination of the crystal structure is required to comprehend the structure-property correlation in these Heusler alloys. Several disorders can be assessed by examining the XRD patterns of these alloys. The typical XRD pattern of Heusler alloys comprises first three reflections, *viz.*, (111), (200), and (220) as the characteristic reflections, which can be utilized to analyse the degree of ordering or presence of disorders in these alloys.

The degree of *B*2 and $L2_1$ (or *X*) ordering for the Heusler alloy structures can be identified using the theoretically estimated and experimentally observed intensity ratios of the (200) and (111) superlattice reflections with highly intense (220) reflection, using the relations [13],

$$\left(\frac{I_{200}}{I_{220}}\right)_{exp} = S_{B2}^2 \left(\frac{I_{200}}{I_{220}}\right)_{th} \quad \text{------} \quad 1.01$$

$$\left(\frac{I_{111}}{I_{220}}\right)_{exp} = \left[S_{L2_1}(or\ S_X)\left(\frac{3-S_{B2}}{2}\right)\right]^2 \left(\frac{I_{111}}{I_{220}}\right)_{th} \quad \text{------} \quad 1.02$$

Here, S_{B2} and S_{L2_1} (or S_X) indicate the degree of *B2* and $L2_1$ (or *X*) order in the alloy, respectively. For a fully ordered $L2_1$ system, S_{B2} and S_{L2_1} should have the ideal value of unity. But in practice, S_{B2} and S_{L2_1} values can be lower than the ideal value. The amount of deviation in $S_{L2_1}(or\ S_X)$ from the ideal value indicates the deviation from the $L2_1$ (or *X*) structure. Similarly, the amount of deviation from the S_{B2} indicates the deviation from the *B*2 type structure towards *A*2 type fully disordered structure. Here, it is important to mention that several disorders, *viz.* DO_3 type cannot be detected through XRD measurements.

1.1.2 Properties and phenomena

Heusler compounds exhibit a wide range of physical properties and phenomena, including thermoelectricity (*e.g.* Fe_2TiAl [14]), superconductivity (*e.g.* Ni_2ZrAl [15]), topological

insulator properties (*e.g.* GdPtBi [16]), heavy fermion behaviour (*e.g.* $Fe_{3-x}V_xGa$ [17]), martensite transformations and shape memory effect (*e.g.* Ni-Mn-Ga [18]), metamagnetic transitions (*e.g.* NiCoMnIn [19]), high spin polarization (*e.g.* Co_2MnSi [20]), high magnetic moment (*e.g.* Co_2FeSi [21]), high anisotropy (*e.g.* Rh_2CoSb [22]), high Curie temperature (*e.g.* Fe_2CoGa [23]), *etc.* The origin and description of some of the properties are detailed below:

Heusler alloys exhibit diverse magnetic phenomena due to the wide range of elements constituting the X, Y, and Z components. The empirical Slater-Pauling (S-P) rule [24] for half metallic Heusler alloys provides the flexibility to select a wide range of magnetic behaviors, spanning from ferrimagnetic/antiferromagnetic to non-magnetic to ferromagnetic. This can be achieved by choosing the appropriate elemental composition to attain the desired property and magnetic moment of the compound. Thus, in this manner, the S-P rule provides a strong relationship between the electronic property, *i.e.* total number of valance electrons (Z_t) with the magnetic property *i.e.* total spin magnetic moment (M_t). By definition, Z_t represents the sum of spin up ($N_\uparrow$) and spin down ($N_\downarrow$) valance electrons, *i.e.*

$$Z_t = N_\uparrow + N_\downarrow \qquad \text{------} \quad 1.03$$

whereas M_t arises due to the excess number of uncompensated valance electrons, which can be represented as,

$$M_t = N_\uparrow - N_\downarrow \qquad \text{------} \quad 1.04$$

Combining both the above equations,

$$M_t = Z_t - 2\,N_\downarrow \qquad \text{------} \quad 1.05$$

In the case of half metallic full Heusler compounds, M_t can be estimated using the formula,

$$M_t = Z_t - 24 \qquad \text{------} \quad 1.06$$

The half Heusler (XYZ) compounds exhibit a similar relationship (due to reduced number of uncompensated electrons),

$$M_t = Z_t - 18 \qquad \text{------} \quad 1.07$$

and the inverse Heusler alloys follow three distinct rules, *viz.*,

$$\left.\begin{aligned} M_t &= Z_t - 18 \\ M_t &= Z_t - 24 \\ M_t &= Z_t - 28 \end{aligned}\right\} \quad \text{------} \quad 1.08$$

These rules are called as the generalized Slater-Pauling (S-P) rules for the half metallic Heusler alloys. Thus, in the case of full Heusler alloys, compounds having Z_t lower than 24 are usually ferrimagnetic, compounds with $Z_t = 24$ have zero moment and so non-magnetic, and compounds having Z_t greater than 24 are usually ferromagnetic in nature. Fe and Co based Heusler alloys usually possess $Z_t > 24$, resulting in ferromagnetic behavior. Being ferromagnetic, they demonstrate magnetic hysteresis (*M-H*) loops when subjected to a reversible magnetic field at particular temperatures, as illustrated in Figure 1.04.

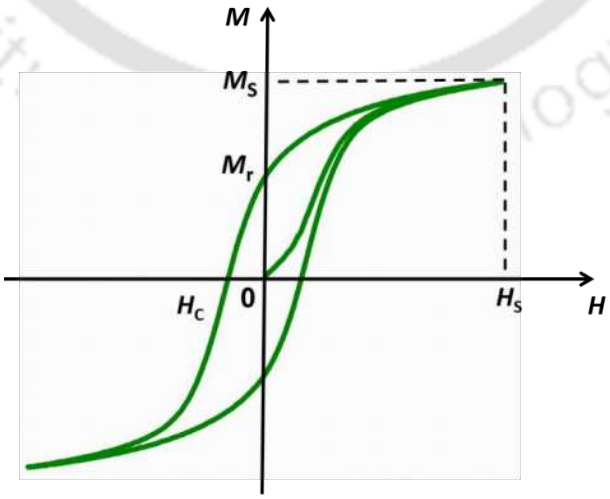

Figure 1.04. Typical *M-H* loop for a ferromagnetic material.

This *M-H* loop provides valuable insights about the ferromagnetic nature of the compounds. The most essential components extracted from *M-H* loops are saturation magnetization (M_s), coercive field (H_c), and magnetic remanence (M_r). Determination of these parameters is critical to recognize the suitability of a magnetic material for different applications. Numerous applications require materials with high M_s with low H_c. In addition to the aforementioned parameters, the 1st quadrant of the *M-H* loop (initial or virgin curve) can be utilized in calculating the effective anisotropy constant (K_{eff}) of the compound. The law of approach to saturation (LAS) relates the magnetization (M) to the applied magnetic field (H) with the relationship [25],

$$M(H) = M_s\left(1 - \frac{m}{\sqrt{H}} - \frac{n}{H} - \frac{o}{H^2} - \cdots\right) + \chi_{hf} + p\sqrt{H} \qquad \text{------} \quad 1.09$$

where the constants m and n indicate contributions from different types of defects, o is associated with magneto-crystalline anisotropy, p is related to thermally excited spin waves, and χ_{hf} is the high field susceptibility. At high values of magnetic fields, only the term o/H^2 dominates, resulting in the simplified version of equation 1.09 [25], *viz.*,

$$M(H) = M_s\left(1 - \frac{o}{H^2}\right) \qquad \text{------} \quad 1.10$$

The above equation can now be used to model the saturation region of the initial (virgin) *M-H* curve and in the estimation of the value of the coefficient o and M_s. These values can be substituted in the following equation [25],

$$K_{eff} = \mu_0 M_s \left(\frac{105\, o}{8}\right)^{1/2} \qquad \text{------} \quad 1.11$$

to estimate the value of K_{eff} of cubic samples (μ_0 indicates the permeability of the free space in equation 1.11).

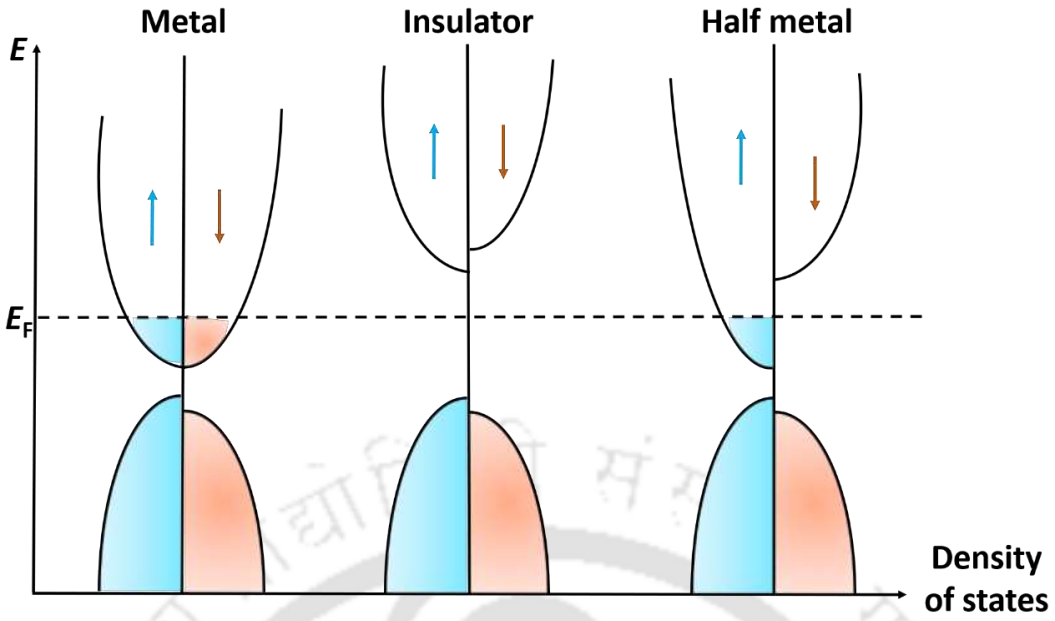

Figure 1.05. Typical representation of DOS of metallic, insulating, and half metallic compounds. Upward and downward pointing arrows represent the spin-up and spin-down electrons.

Half metallicity is a novel property of a material resulting from its unique density of states (DOS). The DOS of a half metal exhibits metallic characteristics in one (majority) spin channel and insulating/semiconducting characteristics in the other (minority) spin channel at the Fermi energy level (E_F), as displayed in Figure 1.05. In other words, the majority (spin up) spin channel of the material demonstrates continuum states, while the minority (spin down) spin channel of the material displays an energy band gap at E_F. Hence, the material is 100% spin polarized. Therefore, only one type of spin enables the spin transport at E_F, which is the key factor for developing spin electronic or spintronic devices. Compared to charge based electronic devices, spintronic devices suffer less Joule heating and hence are efficient in terms of increased data processing speed, reduced electric power consumption, enhanced integration densities, reduced size of the devices, non-volatile character, and many more features. Thus, the development of new half metallic materials is an essential part in the field of spintronics.

In the year 1983, de Groot *et al.* [26] demonstrated half metallicity in half Heusler compound NiMnSb through first principle calculations. Since then, these Heusler alloys have emerged as the forefront candidates for spintronic applications. The physical quantity, which is used to quantify the half metallicity in these alloys, is the value of spin polarization P at the E_F, which can be calculated using the formula,

$$P = \frac{D_\uparrow - D_\downarrow}{D_\uparrow + D_\downarrow} \qquad \text{------} \quad 1.12$$

where $D_\uparrow$ and $D_\downarrow$ are the DOS for up and down spin channels, respectively, at the E_F. For half metallic materials, one of the spin channels (say up) is occupied, whereas the other spin channel (down) is empty, which results in 100 % spin polarization P at E_F, which maximizes the efficiency of the spintronic devices.

A major characteristic of these half metallic compounds is the inclusion of at least one transition metal element, whose *d* state plays a crucial role in the appearance of half metallicity. The interaction of these *d* states with the states of other elements, such as with *d* state of other transition metal elements or *p* state of other Group III – V elements, contributes to various distinctive properties, including the half metallicity. Thus, the emergence of half metallic behaviour and S-P behaviour in Heusler alloys stems from the *d-d* or *d-p* hybridizations between the constituent elements in their unit cell. Let us take an example of full Heusler compound Co_2MnGe [27] with the band structure shown in Figure 1.06. Here, the *d* orbitals of the transition metals X (Co in this case) and Y (Mn in this case) undergo splitting into doubly and triply degenerate multiplets, namely, *d*1, *d*2, *d*3, *d*4, and *d*5, which correspond to the orbitals d_{xy}, d_{yz}, d_{zx}, d_{3z2-r2}, and d_{x2-y2}, respectively. Now, due to symmetry, the e_g (*d*4, *d*5) orbitals of one transition metal can only couple with e_g orbitals of the other transition metals. Similarly, the t_{2g} (*d*1, *d*2, *d*3) orbitals of one transition metal can only couple with t_{2g} orbitals of another transition metal. In the case of full Heusler alloys, the two X atoms (Co in this case)

situated at octahedral sites first hybridize with each other. Later, the hybridized *d* states of the X atoms (Co atoms in this case) interact with the Y atom (Mn in this case) or the Z atom (Ge in this case). Therefore, as represented in the first part of Figure 1.06, after the hybridization of two Co atoms, their *d*4 and *d*5 orbitals combine to create doubly degenerate bonding states e_g and doubly degenerate antibonding states e_u. Similarly, the orbitals *d*1, *d*2, and *d*3 of the two Co atoms also undergo hybridization, resulting in triply degenerate bonding states t_{2g} and triply degenerate antibonding states t_{1u}. The second part of Figure 1.06 shows the second step of hybridization, where the hybridized *d* states of two Co atoms now hybridize with *d* states of Mn atom. Here, the hybridized doubly degenerate e_g states of the Co atoms will combine with *d*4, and *d*5 orbitals of Mn atom to result in doubly degenerate bonding states e_g at lower energy and doubly degenerate antibonding states e_g at higher energy. Similarly, the hybridized triply degenerate t_{2g} states of Co atoms will combine with *d*1, *d*2, and *d*3 orbitals of Mn atom to give rise to triply degenerate bonding states t_{2g} at lower energy and triply degenerate antibonding states t_{2g} at higher energy. Here, it should also be noted that doubly degenerate e_u and triply degenerate t_{1u} states of hybridized Co atoms cannot couple with any of the *d* orbitals of Mn atom as there is no *u* states available for Mn atom. Now, as indicated in Figure 1.06, the t_{1u} states are occupied and situated below the E_F, whereas the e_u states are positioned immediately above the E_F. Consequently, a total of eight minority *d* bands are occupied, leaving seven *d* bands vacant. Additionally, the Z (or non-transition metal) atom will create one *s* and three *p* bands, which will be situated below these levels in low energy regions. Thus, in total, one *s* band, three *p* bands, and eight *d* bands will collectively make 12 occupied spin down states, which can accommodate a total of 24 valance electrons. Therefore, the excess number of valance electrons beyond this value will only contribute to the total spin magnetic moment due to these uncompensated spins. Thus, the generalized rule of $M_t = Z_t - 24$ has emerged for full

Heusler alloys, where the numeral indicates the presence of 12 occupied spin down states. Figure 1.07 represents the dependence of M_t on Z_t for various full Heusler alloys.

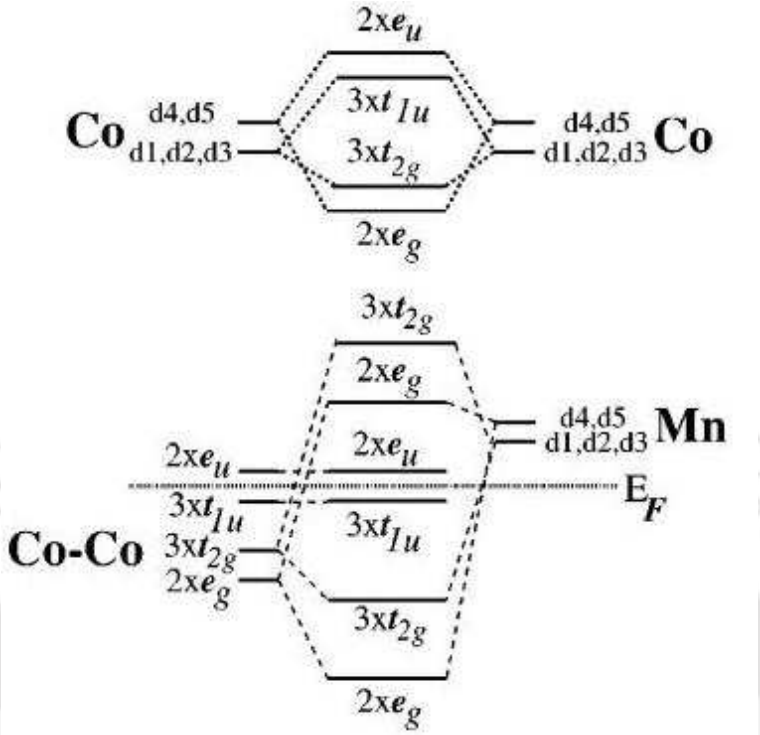

Figure 1.06. Hybridization in spin down channel in full Heusler alloy Co_2MnGe [27].

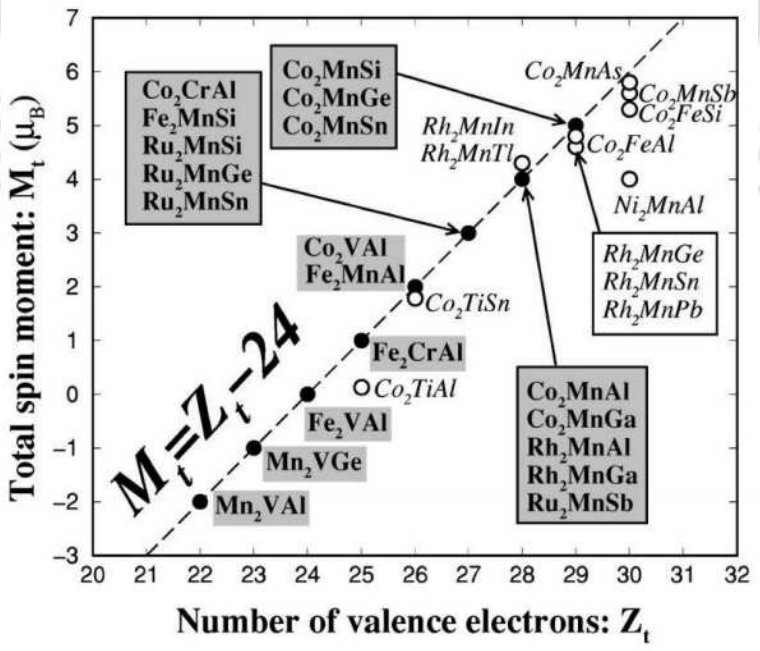

Figure 1.07. M_t-Z_t dependency according to S-P rule for full Heusler alloys [27].

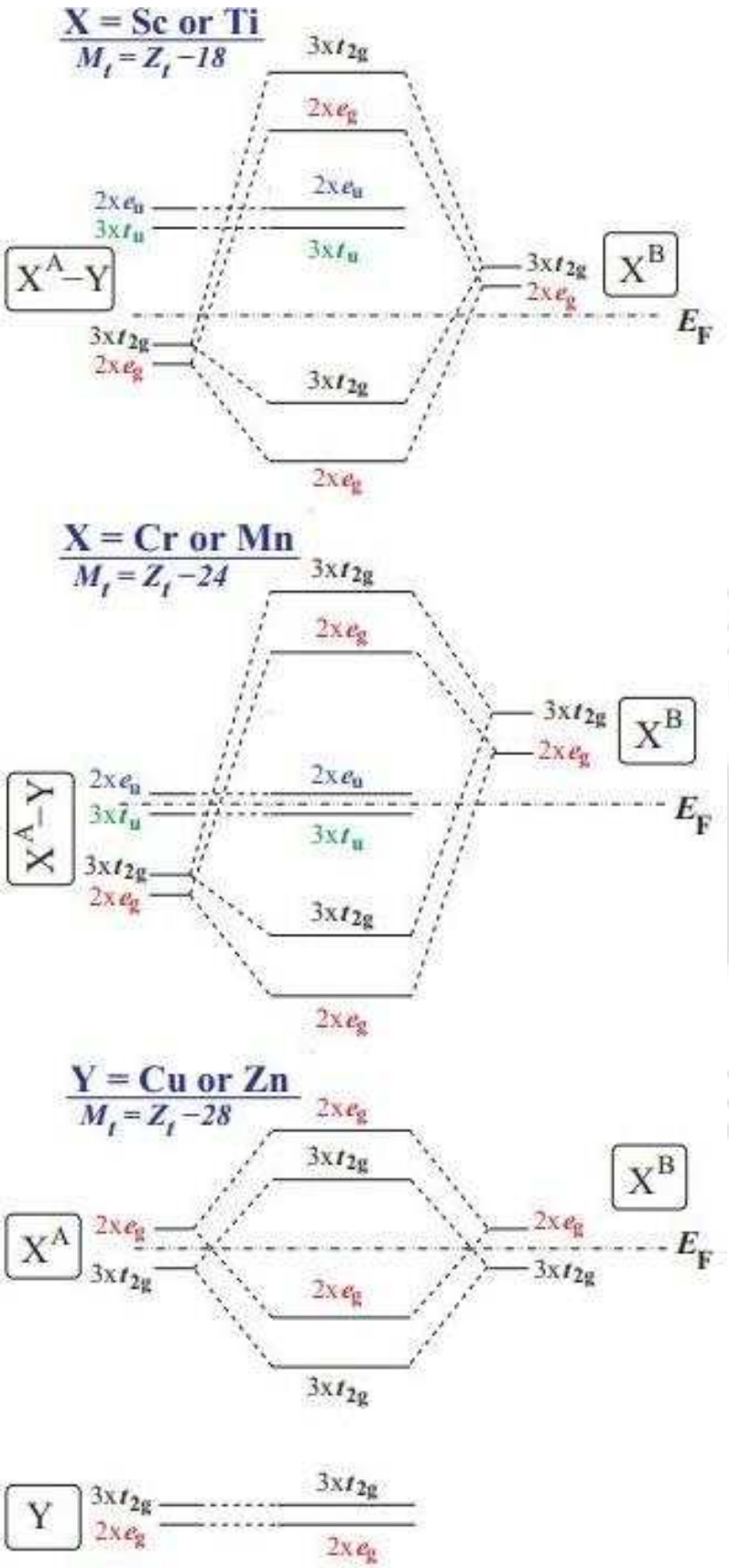

Figure 1.08. Hybridization in spin down channel in inverse Heusler alloys X_2YZ [28].

In the case of inverse Heusler alloys, the situation is different due to the exchange of position of half of the X type atoms with Y type atoms. So, half of the X type atoms (say X^A), which are situated at the octahedral site of Y atoms first hybridize with the Y atoms [28]. Then, the hybridized *d* states of X^A and Y will further hybridize with the other half of the X type atoms (say X^B), as depicted in Figure 1.08. Now, the difference in the splitting of these states after hybridization leads to different numbers of occupied spin down states, leading to three different rules, *viz.*, $M_t = Z_t - 18$, $M_t = Z_t - 24$, and $M_t = Z_t - 28$ rules. Figure 1.09 represents the three dependencies of M_t on Z_t for various inverse Heusler alloys.

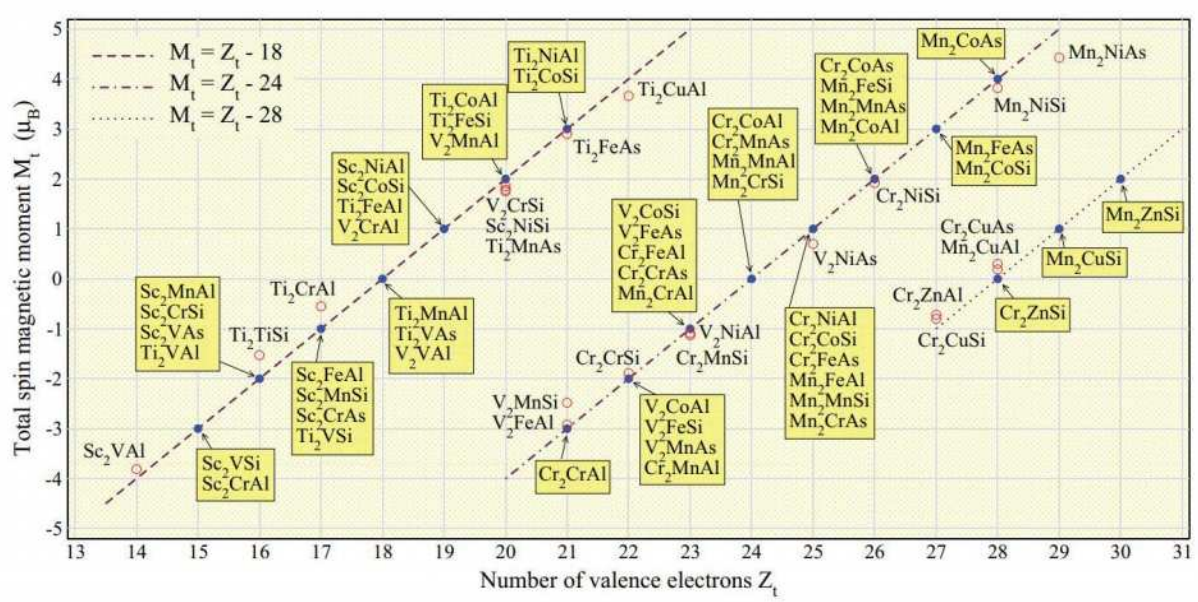

Figure 1.09. M_t-Z_t dependency according to S-P rule for inverse Heusler alloys [28].

Several compounds in this Heusler alloy family show temperature dependent phase transition from highly symmetric austenite (cubic) to low symmetric martensite (tetragonal/hexagonal/*etc.*) phase on lowering the temperature. This first order, diffusion-less, reversible phase transition is called martensitic transition, which enables the shape memory effect (SME) in these compounds. SME is nothing but the property of transformation of the shape of the material, which is in the martensite phase, on the application of external stimuli and regain of its original shape after heat treatment up to the temperature required to acquire

the austenite phase, as depicted in Figure 1.10. Such materials, which show this SME are called as shape memory alloys (SMA). The process gets faster when magnetic fields acts as the stimulus for some of the ferromagnetic materials. These materials are called as ferromagnetic shape memory alloys (FSMA). Usually, Heusler alloys containing Ni and/or Mn fall in this category, *viz.* Ni-Mn-Z (Z = Ga, Al, Sn, In), Co-Ni-Z (Z = Ga, Al), Ni-Fe-Z (Z = Ga, Al) *etc.*

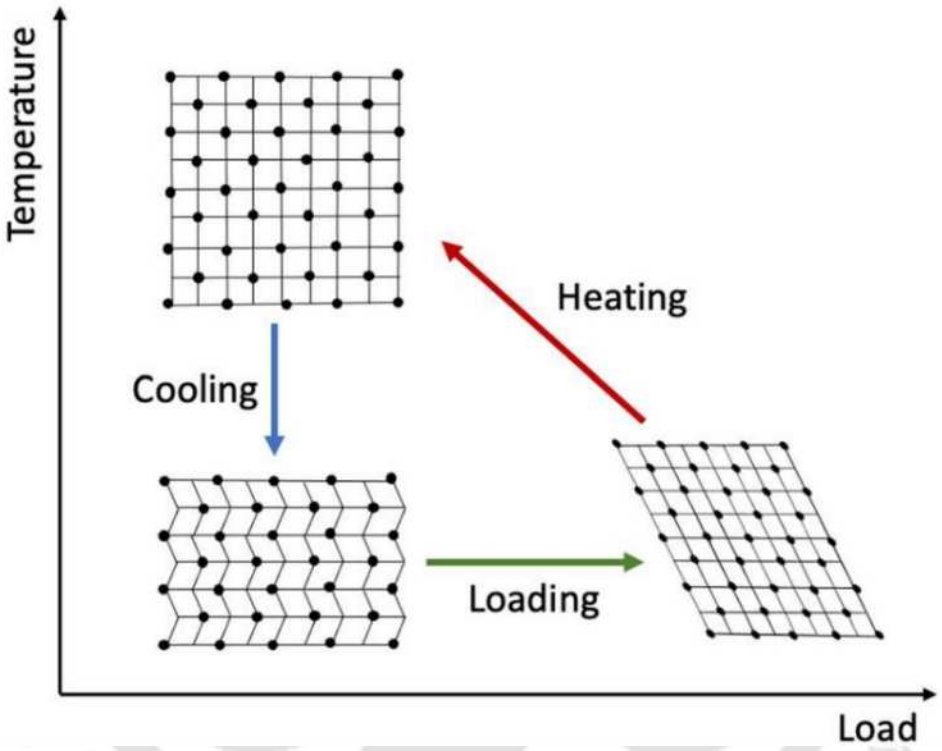

Figure 1.10. Schematic showing martensitic transformation enabling shape memory effect by temperature and pressure variations [29].

1.1.3 Developments in X_2YZ Heusler alloys

As discussed earlier, Heusler alloys find numerous applications. The choice of their constituent elements decides the type of targeted applications. An extensive category of Heusler alloys containing Ni and/or Mn, named as FSMA, *viz.*, Ni-Mn-Z (Z = Ga, Al, Sn, In), Co-Ni-Z (Z = Ga, Al), Ni-Fe-Z (Z = Ga, Al), *etc.* show incredible applicabilities as actuators in biomedical fields, thermostats, sensors, *etc.* A relatively new category of Heusler alloys known as fully compensated ferrimagnetic compounds also known as spin gapless semiconductors, possessing

zero magnetic moment, *viz.*, Cr_2CoGa [30], Cr_2FeGe [30], Cr_2MnAs [30], Cr_2CoAl [31], Cr_2FeSi [31], Mn_2CrSi [32], Mn_2CrGe [32], V_2CoSb [33], *etc.* show exciting applications in spintronics [34].

Apart from these categories, Co and Fe based Heusler alloys retain an exclusive space since long ago. These Co and Fe based Heusler alloys have proved to be one of the most studied, most appreciated, and most demanding categories in Heusler alloys due to their exceptional properties, including high M_s, high T_C, and high P. The initial investigations on Fe and Co based Heusler alloys were executed by Jaggi *et al.* [23] in the year 1978, on induction melted Co_2FeGa and Fe_2CoGa compounds. The authors explored the local environment and site preferences of elements in these compounds. In the year 1980, Grover *et al.* [35] synthesized Co_2FeAl and Fe_2CoAl compounds using the similar methodology and analysed their local environment and site preferences. Later, Buschow *et al.*, in the years 1981 [36] and 1983 [37], synthesized a series of Fe_2YZ and Co_2YZ alloys by arc melting and investigated the magneto-optical and other properties of numerous newly developed Fe and Co based Heusler compounds. In the same year, Whittle *et al.* [38] synthesized $Co_2Fe_xGa_{2-x}$ ($0.01 \leq x \leq 1.00$) compounds by melting and investigated magnetic ordering in them. In 1985, Yoshimura *et al.* [39] synthesized Co_2YZ compounds using arc melting and analysed magnetic characteristics of several new compounds. From 1990 onwards, abundant studies have been published on these compounds, revealing their remarkable properties and potential for numerous applications.

1.2 Low dimensional materials

The regular materials having the expansion in all three dimensions are referred as bulk or 3 dimensional (3-d) materials. Reducing one of the three dimensions up to the nano scale gives rise to 2 dimensional (2-d) materials which are termed as thin films. Similarly, lowering the sizes of the materials up to nano regime in two dimensions results in 1 dimensional (1-d) materials, also named as nano wires or nano rods. The size confinement in all three dimensions

to the nano scale leads to 0 dimensional (0-d) materials which are also known as nanoparticles. Lowering the dimensions results in quantum confinement, which is responsible for the change in various physical properties of the materials. Thus, lowering the dimensions enables the possibility to control and manipulate the properties of the materials.

1.2.1 Magnetic nanoparticles

Various physical properties exhibit a size dependence in the nano regime. The variation in these parameters with their size is essential to understand the behaviour of the nanoparticles in order to utilize them in practical applications.

According to the core shell model of nanoparticles, the surface of the nanoparticles is expected to be enclosed with a magnetically dead layer. The appearance of this dead layer is attributed to the loss of crystal symmetry at the surface of the nanoparticles due to the surface effects involving dangling bonds, atom vacancies, surface disorders, *etc.* [40]. This loss of symmetry at the surface results in the breaking of the exchange bond/interaction between the magnetic atoms present at the surface. The presence of this dead layer on top of the surface leads to a decrement in M_s. Thus, with a decrease in the size of the nanoparticles, due to the increased surface to volume (S/V) ratio, a thicker dead layer appears at the surface, resulting in decreased M_s [40]. If a magnetic dead layer of thickness t emerges on the surface of a nanoparticle of size d, it decreases the M_s of the nanoparticle $M_s(d)$ from the bulk magnetization value $M_s(b)$ by an amount represented by the formula [40],

$$M_s(d) = M_s(b)\left(1 - \frac{6t}{d}\right) \qquad \text{------} \quad 1.13$$

Now, if the observed M_s of the nanoparticles and the expected M_s of its bulk counterpart are known, then it is straightforward to calculate t using equation 1.13. Thus, in this manner,

the core-shell model is helpful in understanding the magnetic behaviour of the magnetic nanoparticles.

The coercivity (H_c) of the nanoparticle exhibits a remarkable size dependent effect. As the particle size decreases, H_c usually increases, reaches a peak, and again falls down to zero, as depicted in Figure 1.11. This behaviour can be understood by splitting the size range into three distinct regions. The particle size range, where the H_c increases with decreasing size, represents the multidomain regime. The experimentally observed variation in H_c with size in this regime approximately follows the relation [41],

$$H_c = a + \frac{b}{d} \qquad \text{------} \quad 1.14$$

where *a* and *b* are constants. The above equation is an empirical formula without any theoretical basis. On further decreasing the particle size, H_c starts to drop after reaching the peak value and reaches to zero. Below the size where the highest H_c appears, the nanoparticles belong to single domain regime. The critical value of the size, where the maximum H_c appears, is termed as single domain to multi domain critical size D_{cr}. The decrease in H_c value in single domain regime follows the relation [41],

$$H_c = g - \frac{h}{d^{3/2}} \qquad \text{------} \quad 1.15$$

where *g* and *h* are constants. This decrease in H_c with size in the single domain regime can be understood using the Stoner-Wohlfarth model. This model relates the anisotropy energy E_{aniso} of single domain nanoparticles with magneto crystalline anisotropy constant *K* and volume of the nanoparticle *V* by the relation [40],

$$E_{aniso} = KV\sin^2\theta \qquad \text{------} \quad 1.16$$

where θ is the angle between the easy axis and the direction of magnetization. As the size of the nanoparticle decreases, E_{aniso} also decreases due to its proportional dependence on V. Further, K too decreases with a decrease in size due to size effects. Since H_c signifies the strength of the magnetic field needed to overcome this anisotropy energy required for the spin-flip, decrease in E_{aniso} with the decrease in size of the nanoparticles will in turn result in decreasing H_c in the single domain regime [40].

At a particular value of particle size, the H_c becomes zero. This size is referred as superparamagnetic critical size D_{sp}, below which the particles are called as superparamagnetic nanoparticles. In this region, the influence of the thermal effect is powerful enough to spontaneously demagnetize the highly saturated nanoparticle assemblies [41].

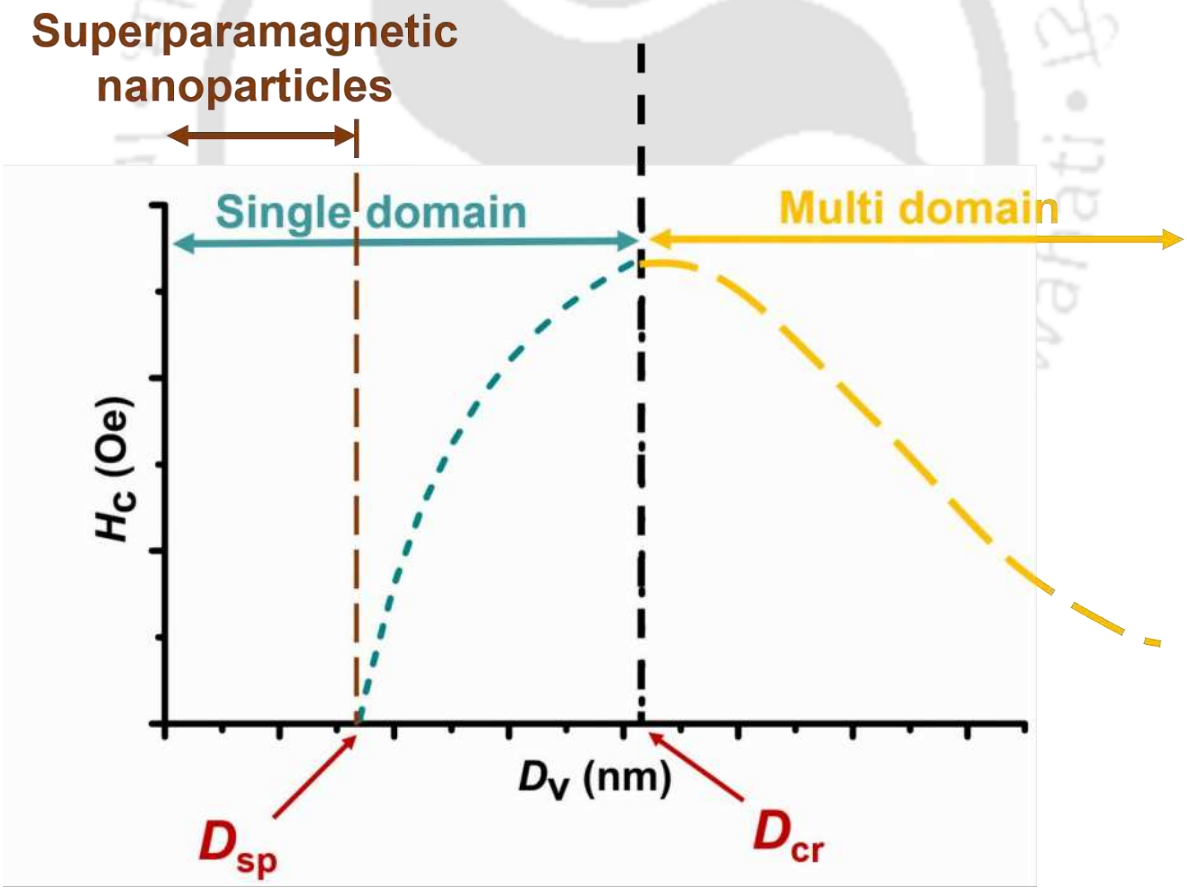

Figure 1.11. Schematic diagram showing H_c variation with crystallite size D_v.

The Néel-Brown thermally activated model [42] describes the activation of the relaxation of the single domain nanoparticles, which obeys the Arrhenius law. According to this law, the temperature *T* dependent relaxation time τ of magnetization can be defined as,

$$\tau = \tau_0 \exp\left(\frac{\Delta E}{k_B T}\right) \qquad \text{------} \quad 1.17$$

where τ_0, ΔE, and k_B are characteristic attempt time, average energy barrier and Boltzmann constant, respectively. The value of ΔE can now be defined as,

$$\Delta E = K_{eff} V \qquad \text{------} \quad 1.18$$

where *V* denotes the average volume of the nanoparticles. Therefore, if ΔE depicts a linear dependence with *V*, then the nanoparticles are known to possess mainly bulk anisotropy with negligible contribution from surface anisotropy. In this case, all the contributions to the effective anisotropy emanate from its volume, and hence, $K_{eff} \approx K_v$. On the other hand, if the ΔE *versus V* does not show a linear dependence, the additional contribution from the surface of the nanoparticles adds up to equation 1.18. To specify this contribution, Mørup *et al.* introduced an additional term related to the surface anisotropy K_s along with the volume anisotropy K_v as [42],

$$K_{eff}\, V = \Delta E = K_v V + K_s\, S \qquad \text{------} \quad 1.19$$

where *S* is the average surface area of the nanoparticles. Equation 1.19 can also be modified as [42],

$$K_{eff} = \frac{\Delta E}{V} = K_v + K_s \frac{S}{V} \qquad \text{------} \quad 1.20$$

$$K_{eff} = \frac{\Delta E}{V} = K_v + 6 \frac{K_s}{d} \qquad \text{------} \quad 1.21$$

where *d* is the average diameter of the nanoparticles. Now, a linear fit to $\Delta E/V$ *versus* $1/d$ can provide the values of K_s and K_v as the slope and the intercept of the fitted line, respectively.The

value of the K_v can be utilized in estimating the quality factor Q [43], which classifies the material into high or low anisotropic materials using the relation [42],

$$Q = \frac{K_v}{0.5 \times 4\pi \times M_S^2} \quad \text{------} \quad 1.22$$

Materials having $Q < 0.1$ correspond to low anisotropic materials, while the materials possessing $Q > 0.1$ are defined as high anisotropic materials. High anisotropic materials can be utilized in many applications such as high density magnetic recording, *etc.* There could be various reasons for the high values of K_{eff} in magnetic nanoparticles, such as (i) escalated interparticle interactions ascribed to agglomerations in magnetic nanoparticles [44], (ii) high *S/V* ratio, which results into breaking of surface symmetry, which in turn breaks the exchange bonds on the particle surface [40,45,46], and (iii) dipolar interactions between the single domain magnetic nanoparticles [40].

In order to categorize the high anisotropic magnetic nanoparticles into single domain or multi domain regimes, D_{cr} is calculated using the formula [42,47],

$$D_{cr} = \frac{72\sqrt{A\,K_v}}{4\pi\,M_S^2} \quad \text{------} \quad 1.23$$

where A refers to the exchange stiffness constant for the magnetic material, indicating the strength of the exchange interaction between adjacent spins. The determination of A can be done by the following equation [48],

$$A(T) = \frac{M_S(T)D(T)}{2g\mu_B} \quad \text{------} \quad 1.24$$

where g, μ_B, and $D(T)$ are values of Lande's g factor, Bohr magnetron, and spin wave stiffness constant, respectively. Further, the value of $D(T)$ can be calculated using the slope B estimated using Bloch's $T^{3/2}$ law for temperature dependent M_s in low temperature regime [49], using the equations [50,51],

$$B = 2.612 \frac{g\,\mu_B}{M_S(0)} \left(\frac{k_B}{4\pi D}\right)^{3/2} \quad \text{------} \quad 1.25$$

$$\frac{M_S(T)}{M_S(0)} = 1 - T^{3/2} \quad \text{------} \quad 1.26$$

In this manner, the D_{cr} calculation can help us to assess whether the magnetic nanoparticles are in single domain or multi domain regime.

The loss of symmetry at the surface, which is responsible for the breaking of magnetic bonds, also results in the decrement in the T_C on decreasing the particle size [52]. Chhabra *et al.* [53] proposed an energy and bond based theoretical model to explain the size dependent T_C variation in 2-d, 1-d, and 0-d magnetic materials. The authors found a decreasing trend in T_C values on decreasing the size of the spherical nanoparticles following the relation [53],

$$\frac{T_c\,(d)}{T_c\,(b)} = \left(1 - \frac{3h}{d}\right)^k \quad \text{------} \quad 1.27$$

where $T_c(b)$ and $T_c(d)$ are T_c values for the bulk and nanoparticle of size *d*, respectively, *h* is the atomic diameter, and *k* is a dimensionless parameter, which can take different values. For example, $k = 0$ represents a bulk system depicting no size effect, negative values of *k* are associated with nanoparticles embedded in other host materials, and positive *k* values denote routine low dimensional magnetic materials. The *k* value varies from material to material. Usually, *k* values between 1 to 3 yielded good results for the mentioned materials in the work by Chhabra *et al.* [53]. In order to validate their experimental finding, the authors also compared the theoretical results with the experimental findings. Figure 1.12 represents the T_C variation with particle size for Fe_3O_4 specimen of various shapes and sizes. The mentioned behaviour was verified for various magnetic materials by the authors, which made them suggest that this behaviour can be generalized to other materials too.

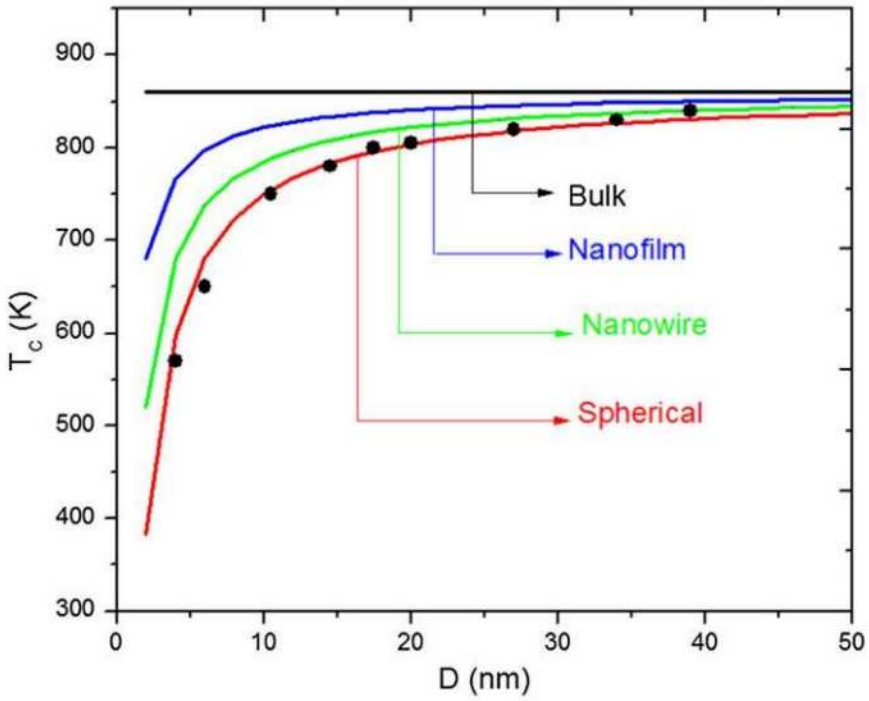

Figure 1.12. Variation of T_C with particle size for Fe_3O_4 specimen of various shapes and sizes. (●) correspond to experimental data [53].

1.3 Advancements in low dimensional Heusler alloys

The incredible properties of the Heusler alloy family make it inevitable to synthesize them in nano dimensional forms. Though abundant studies have been performed on the synthesis of these compounds in thin film (2-d) forms, the most confined form of materials *i.e.*, nanoparticle (0-d) form of these Heusler alloys was developed less than two decades ago. Ni_2MnGa nanoparticles were the first Heusler alloy to be produced in nanoparticle form in the year 2007 *via* mechanical alloying method which built a pathway to an immense opportunity in this discipline [54]. In the same year, Dai *et al.* [55] also synthesized Co_2NiGa nanoparticles using the same methodology, which showed enhanced properties compared to the bulk sample. In the year 2008, pioneering *ab initio* calculations [56,57] established exceptional magnetic properties of Co-Mn-Ga and Ni-Mn-Ga Heusler alloys in nanocrystal form compared to their bulk component. In the subsequent year 2009, Basit *et al.* [58] employed silica template

assisted chemical route to synthesize Co_2FeGa nanoparticles. Afterwards, some other Heusler alloy nanoparticles such as Fe_2CoGa [59], Co_2FeAl [60], Co_2FeSn [61], Fe_2CrGa [62], Fe_2CoAl [63], Co-Ni-Ga [64], Fe-Co-Sn [65], Ni_2FeGa [45], and Co_2FeGe [66] have been synthesized using various methods. Being less than two decade old field, a large part of these studies were concentrated on the successful synthesis of a single composition nanoparticles with particular particle/crystallite size [58,59,67] or synthesis parameter dependent property variation studies [61,68,77,78,69–76]. Still, several attempts have been made to execute particle/crystallite size dependent [79–83] or composition dependent [65,84–87] studies on a few Heusler alloy nanoparticles.

1.4 Motivation behind this thesis work

The available literature highlights several gaps in the literature that need to be explored to utilize these materials with their full potential in various applications. Some of the limitations are,

(i) Most researchers could not obtain single phase fully ordered $L2_1$ or *X* type structure in their synthesized nanoparticles but rather obtained either impurity phases or *B*2/*A*2 type disordered structure in their work [59,63,81,82,84].

(ii) The conventional utilization of templates in the chemical method further posed a limitation in the applicabilities of these nanoparticles by degrading their properties [58,59,79–82,84].

(iii) The available crystallite size or composition dependent studies are limited and not performed in a systematic manner [79–81,84].

(iv) The composition plays a crucial role in deciding the properties of these compounds. In many of the reports, a deviation in the obtained composition compared to the stoichiometric composition has been observed [79–81,84].

(v) There is a scarcity of literature on the synthesis of any quaternary Heusler alloy nanoparticles.

Thus, this thesis will aim to address the following gaps in the existing literature in Heusler alloy nanoparticles:

- Fabrication of impurity free, highly ordered, single phase Co and Fe based Heusler alloy nanoparticles using a template-less chemical process.
- Comprehensive examination of the structural and magnetic characteristics of these Co and Fe based Heusler alloy nanoparticles as a function of their crystallite size.
- Regulation of the structural and magnetic characteristics of these Heusler alloy nanoparticles by altering the alloy compositions.
- Investigations of the half metallic behavior of mentioned Heusler alloys through *ab initio* calculations.
- Development of quaternary Heusler alloy nanoparticles and evaluation of their potential for applications.

We have adopted a template-less chemical methodology [83] to successfully fabricate stoichiometric Co_2FeGa, Fe_2CoGa, and Fe_2CoAl nanoparticles of different crystallite sizes and analyzed their properties. We have also explored the properties of $Fe_{2-x}Co_{1+x}Ga$ ($0 \leq x \leq 1$) nanoparticles as a function of composition. Further, this thesis also showcases the first report on the successful synthesis of quaternary Heusler alloy nanoparticles $Fe_2CoGa_{0.5}Al_{0.5}$.

Chapter 2

Experimental and Theoretical Details

The synthesis process is crucial for obtaining high quality materials. Every synthesis technique has some advantages and some drawbacks. Therefore, the selection of a synthesis technique that provides the highest quality material with minimal compromises in their properties has to be chosen. This chapter will briefly outline the problems associated with various techniques for synthesizing Heusler alloy nanoparticles along with complete details of the procedure adopted in this thesis work to produce the required nanoparticles. This chapter also includes the methodology to synthesize bulk Heusler alloys. Details of all the characterization techniques utilized to analyze the properties of these Heusler alloys are also provided in the current chapter. Theoretical calculations used to predict, support, and validate the experimental data have also been described in this chapter.

2.1 Sample preparation

2.1.1 Synthesis of Heusler alloy nanoparticles

There are multiple ways to synthesize Heusler alloy nanoparticles, such as mechanical alloying [63], co-precipitation, and chemical routes [58,59,79–82,84]. The unavoidable inclusion of mechanical strain and the need for a sophisticated ball milling setup with very hard grinding vials and balls limits the utility of the mechanical alloying process. On the other side, the chemical route is an economical and easy way to produce these nanoparticles. The only drawback in the traditional template assisted chemical route is the utilization of silica (fumed silica, SBA-15 silica, *etc.*) templates in order to suspend these nanoparticles in their pores [58,59,79–82,84]. The silica template provides a narrow size distribution to the nanoparticles

[59,79,80,82,84] and prevents their agglomeration by physically separating them [88,89]. It also helps in varying the crystallite/particle size of these nanoparticles by altering the amount of silica templates with respect to the metal precursors [79–82]. However, the finally obtained nanoparticles contain diamagnetic silica template residues as impurity, which degrade the structural and magnetic properties of the magnetic nanoparticles [88–90]. Removal of this silica contamination from the resulting nanoparticles using hydrofluoric acid (HF) treatment presents its own challenges. These limitations forced researchers to search for template free synthesis techniques. However, in template-less approaches, the only way to control or alter the crystallite/particle size is by controlling heat treatment conditions of the nucleating nanoparticles. In this regard, a few attempts have been made to modify the crystallite/particle sizes of chemically synthesized Co_2FeAl nanoparticles without using templates by varying heat treatment time or temperature [76,78,83]. In this thesis work, a modified template-less chemical approach has been developed to synthesize various Heusler alloy nanoparticles with distinct crystallite sizes.

2.1.1.1 A template-less chemical route to synthesize Heusler alloy nanoparticles

Let us take the synthesis of Fe_2CoGa nanoparticles as an example in describing the methodology adopted in this thesis work. Initially, the constituent metal precursors of Fe_2CoGa, namely, $Fe(NO_3)_3.9H_2O$ (*Molecular Weight (MW)* = 404.00, purity 98 %, Loba Chemie Pvt. Ltd. India), $CoCl_2.6H_2O$ (*MW* = 237.93, purity 98 %, Loba Chemie Pvt. Ltd. India), $Ga(NO_3)_3.xH_2O$ (x = 8 [59,80,84], *MW* = 399.86, purity 99.9 %, Alfa Aesar, Thermo Fisher Scientific) are taken in appropriate amounts as described below:

$$P1_{Fe} = \frac{2\times MW_{P1}}{MW_{comp}} = \frac{2\times 404.00}{240.35} = 3.3618 \quad \text{------} \quad 2.01$$

$$P1_{Co} = \frac{MW_{P2}}{MW_{comp}} = \frac{237.93}{240.35} = 0.9899 \quad \text{------} \quad 2.02$$

$$P1_{Ga} = \frac{MW_{P3}}{MW_{comp}} = \frac{399.86}{240.35} = 1.6637 \qquad \text{------} \quad 2.03$$

where $P1_{Fe}$, $P1_{Co}$, and $P1_{Ga}$ are the initially estimated precursor amounts (in g) and MW_{P1}, MW_{P2}, MW_{P3} are the molecular weights of the metal precursors, $Fe(NO_3)_3.9H_2O$, $CoCl_2.6H_2O$, and $Ga(NO_3)_3.8H_2O$, respectively, and MW_{comp} is the molecular weight of Fe_2CoGa compound.

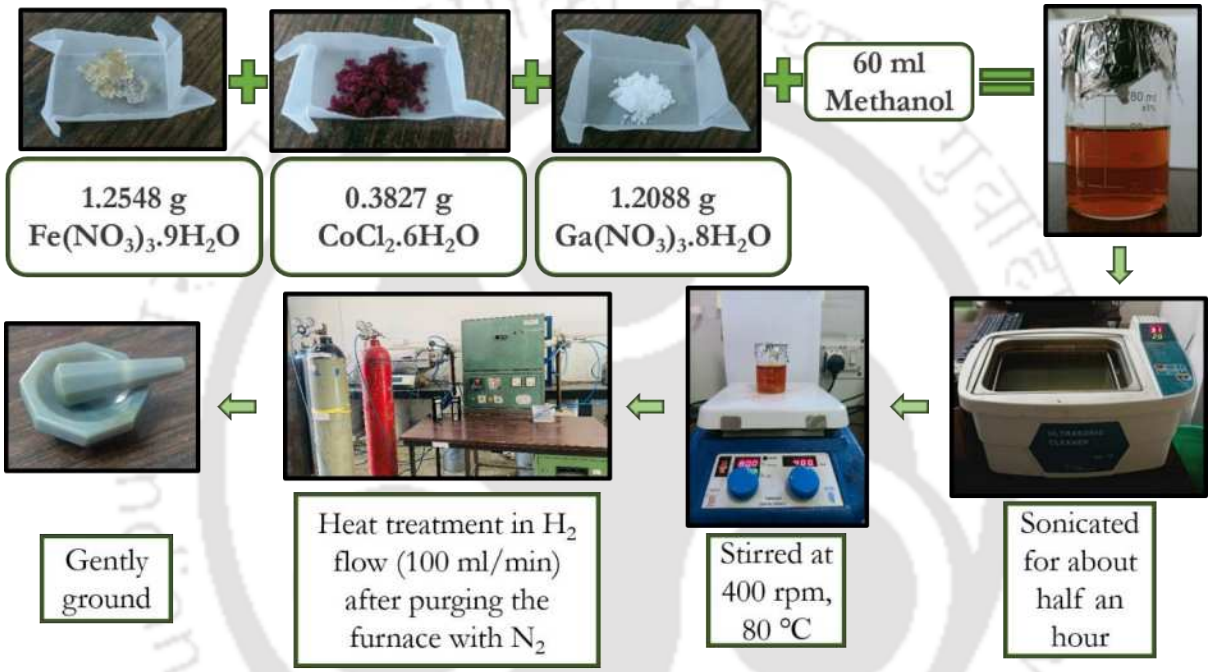

Figure 2.01. Flow chart representing the process for the formation of Fe_2CoGa Heusler alloy nanoparticles by template-less method.

The total precursor amount was normalized to 3 g. The corresponding amounts of $Fe(NO_3)_3.9H_2O$, $CoCl_2.6H_2O$, and $Ga(NO_3)_3.8H_2O$ are 1.6766 g, 0.4937 g, and 0.8297 g, respectively. These weighed quantities of the metal precursors are then dispersed in 60 ml of methanol (purity 99.8 %, Merck Life Science Pvt. Ltd.) to make up a well-dispersed solute to solvent ratio of ~0.05 g/ml. The precursor mixture is sonicated in an ultrasonic bath for about thirty minutes. The adequately mixed solution is then stirred continuously at a temperature of 80 ℃ till the solvent is completely evaporated. The dried mixture is kept in an alumina boat

and heat treated in a tubular furnace at various temperatures and times as required, under a continuous flow (@ 100 mL/min) of high purity H_2 gas. The heat treated samples are gently ground into a fine powder form and stored in a vacuum desiccator for further experimental analyses. Composition analysis of the synthesized nanoparticles indicated a variation in actual composition from the desired stoichiometric composition due to the variation in amount of water of hydration present in the precursors. Therefore, the aforementioned process was repeated by adjusting the precursor amounts in an iterative manner until the desired stoichiometry is achieved in the final product. The final precursor amounts after a few iterations were 1.2548 g of $Fe(NO_3)_3.9H_2O$, 0.3827 g of $CoCl_2.6H_2O$, and 1.2088 g of $Ga(NO_3)_3.8H_2O$ in a total amount of 2.8463 g, which yielded a near stoichiometric Fe_2CoGa nanoparticles. The flow chart depicting the synthesis process adopted for obtaining stoichiometric Fe_2CoGa nanoparticles is shown in Figure 2.01. All nanoparticle compositions described in this thesis work have been prepared by the above template free process.

2.1.1.2 Heat treatment of as-synthesized nanoparticles

Heat treatment is an important step in this procedure since an appropriate atmosphere has to be provided for the decomposition of chlorides/nitrates and nucleation and controlled growth of the intermetallic compound with desired crystallite/particle size, composition, and properties. In commercial tubular furnaces, the thermocouple is attached at the outer side of the tube and it cannot detect the actual sample temperature under the flow of a gas. So, a calibration of the tubular furnace was performed by placing a K-type thermocouple close to the alumina boat inside the tube of the furnace under a constant flow of nitrogen gas. During the heating process, the temperature readings from the furnace temperature controller (displaying the outer thermocouple reading) and inner thermocouple were noted in steps of 5 °C. A ready reckoner table displaying the temperature of the sample boat and the one displayed in temperature controller is then prepared and used to set the required temperature for the heat treatment of

the nanoparticles. The tubular furnace along with the gas manifold used in the processing of the nanoparticles is shown in Figure 2.02.

Figure 2.02. Tubular furnace along with the gas manifold used for processing the nanoparticles.

2.1.2 Synthesis of bulk Heusler alloys using arc melting method

In order to compare the properties of the nanoparticles with the bulk counterpart, bulk Fe_2CoGa was synthesized by arc melting method. The arc melting unit comprises of a melting chamber, a high vacuum pump, a power supply, and an argon gas manifold is shown in Figure 2.03.

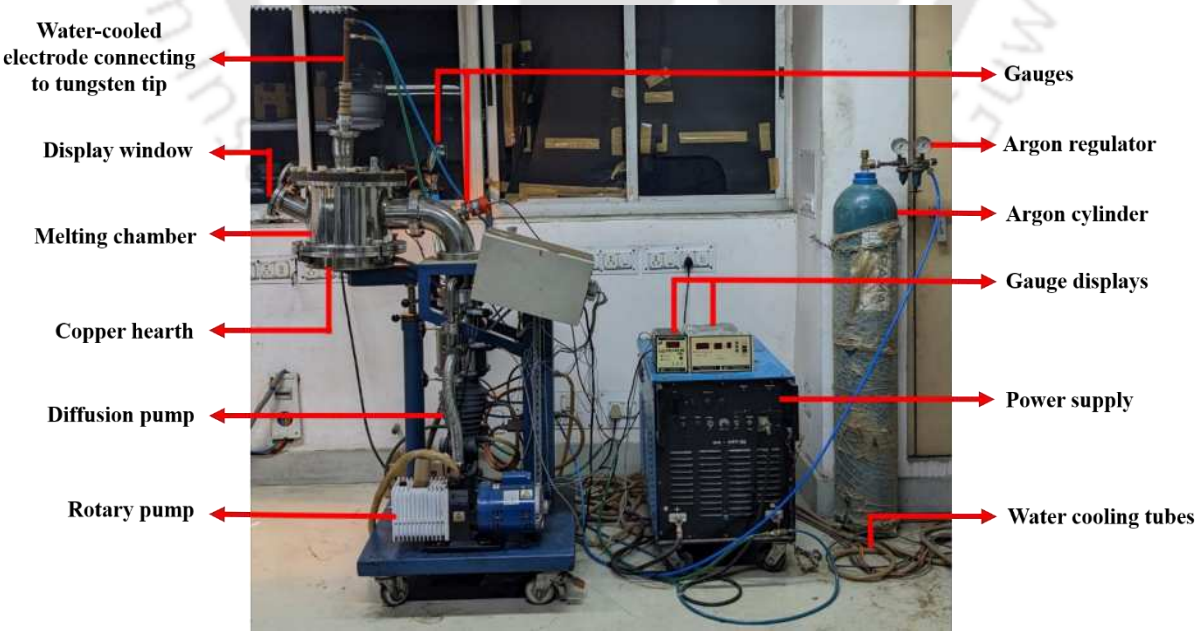

Figure 2.03. Arc melting unit utilized to synthesize bulk Heusler alloys.

Appropriately weighed quantities of the constituent metal pieces of the targeted alloy composition are kept in the copper hearth of the melting chamber. The pre-cleaned melting chamber is repeatedly purged with argon gas and evacuated to $<10^{-3}$ Pa several times prior to melting the metal pieces in the presence of Ti as getter. The metal pieces are then melted together by the high temperature created by the well-directed electric arc generated between a sharp tungsten electrode (anode) and metal pieces placed on the copper hearth (cathode). A high current (180 - 230 A) power supply such as the one used in welding process is used to generate the electric arc between the tungsten electrode and the copper hearth. The electric arc generates a very high local temperature (~3000 ℃), which melts the elements to form the alloy ingot. The alloy ingot is flipped and re-melted several times to enhance its compositional homogeneity. The homogenized alloy ingot is then sealed in a fused silica ampoule under a low pressure of 10^{-3} Pa. The flame sealed ampoule is then subjected to an appropriate heat treatment in a raising hearth furnace and finally quenched in ice water.

Figure 2.04. Ampoule vacuum sealing setup (left) and the raising hearth furnace (right) used for processing as-melted bulk Heusler alloy ingot.

The arc melting, vacuum sealing, and heat treatment set-ups are represented in Figures 2.03 and 2.04. In the synthesis of Fe_2CoGa alloy ingot, appropriately weighted amounts of high purity (99.99 % pure, Alfa Aesar) elements Fe (1.4136 g), Co (0.7459 g) and Ga (0.9177 g) were used. The homogenized alloy ingot in vacuum sealed fused silica ampoule was heat treated for 24 h at 1000 °C and then quenched in ice water. The processed ingot was gently ground and stored in a vacuum desiccator for further studies.

2.2 Characterization techniques

Characterization of materials involves many probes such as X-rays, photons, electrons, atoms, ions, *etc.* The quantification of a property of a material after the interaction of these probes provides valuable insights about the nature of the material. Thus, depending upon the probe and the property analysed, a vast range of techniques are available as a tool to investigate and understand these materials. The characterization tools and methodologies utilized in the current investigations are described below:

2.2.1 Powder X-ray Diffractometer

Identification of the atomic structure is the first step in characterizing any material. X-ray diffraction (XRD) technique allows us to identify various crystalline phases present in any material and the atomic arrangement in them. It also enables one to infer structural information about the material, such as the lattice constants (a, b, c), average crystallite size (D_v), strain (ε), *etc.* The Bragg's law is the fundamental principle behind XRD [91]. It is commonly known that a crystal has a periodic arrangement of atoms. When incoming X-rays interact with an array of parallel atomic planes in the crystal at certain angles, diffraction of X-rays takes place, and the constructive interference of the scattered X-rays gives rise to the appearance of atomic planes, as depicted in Figure 2.05. The condition for constructive interference can be written as,

$$\text{path difference} = n\,\lambda \qquad \text{------} \quad 2.04$$

where n is an integer, and λ is the wavelength of the X-rays. From Figure 2.05, the path difference between the X-ray waves 1 and 2 is,

$$CB + BD = n\,\lambda \qquad \text{------} \quad 2.05$$

If d is the interplanar distance and θ is the diffraction angle (*a.k.a.* Bragg's angle) at which the diffraction takes place.

$$d\sin\theta + d\sin\theta = n\,\lambda \qquad \text{------} \quad 2.06$$

or

$$2\,d\sin\theta = n\,\lambda \qquad \text{------} \quad 2.07$$

The above equation is commonly known as the Bragg's law [91].

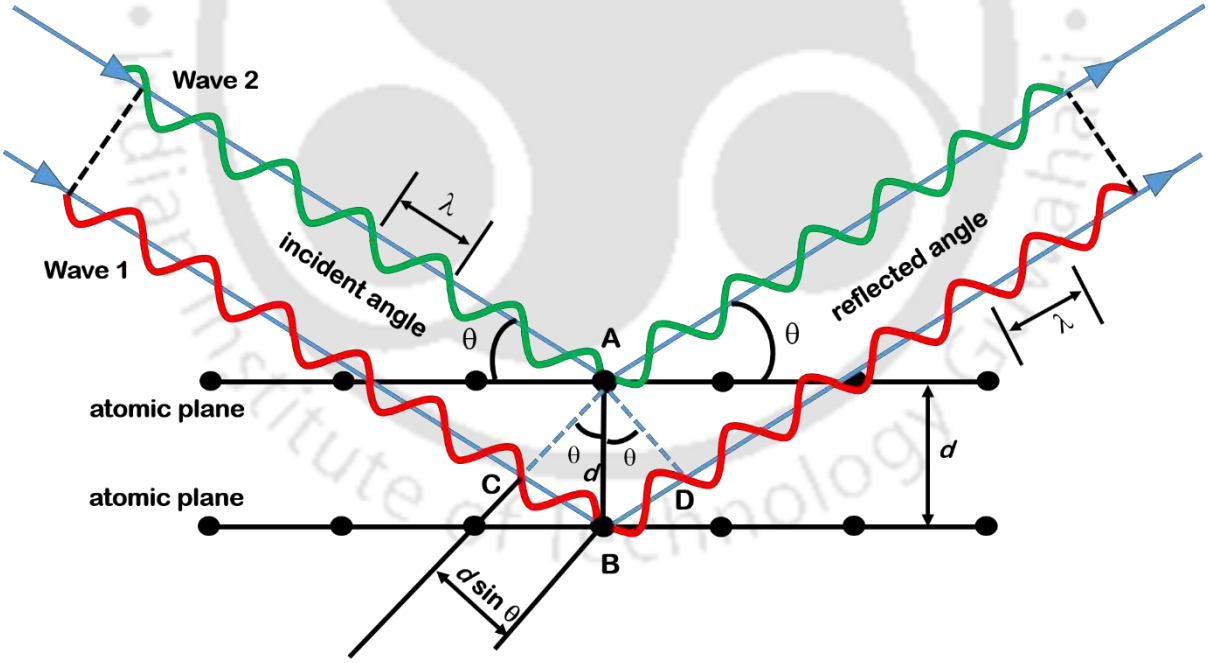

Figure 2.05. Schematic diagram of Bragg's law.

In the typical X-Ray diffractometer, a source of X-rays (Coolidge tube) and the X-ray detector move with identical angular displacement at each step. This configuration is referred to as θ-2θ geometry. This arrangement ensures the collection of diffracted beams from a

particular set of parallel planes into the detector. A powder X-ray diffractometer (Rigaku TTRAX III) set in θ-2θ geometry and operating at 5 kW power with Cu-K_α (wavelength λ = 1.5406 Å) radiation was utilized in the present investigations. The instrument is equipped with a Ni-Cu-K_β filter, pyrolytic graphite, and a scintillation counter as the filter, monochromator, and detector, respectively. A photograph of the instrument is depicted in Figure 2.06.

Figure 2.06. Schematic diagram of the goniometer in θ-2θ geometry (left) and photograph (right) of the rotating anode based Rigaku TTRAX III X-ray diffractometer.

The lattice constants (*a, b, c*) of a crystal unit cell are related to the interplanar distance d_{hkl} for any plane defined by the Miller's indices (*h k l*) by the relation [91],

$$\frac{1}{d_{hkl}^2} = \frac{h^2}{a^2} + \frac{k^2}{b^2} + \frac{l^2}{c^2} \qquad \text{------} \quad 2.08$$

Since the Heusler alloys have cubic structure, their unit cell is defined by the lattice constant *a* (= *b* = *c*). So the above relation reduces to [91],

$$\frac{1}{d_{hkl}^2} = \frac{h^2+ k^2+ l^2}{a^2} \qquad \text{------} \quad 2.09$$

The intensity of the X-rays reflected from each plane depends on the structure factor *F* [91],

$$F = \sum_{i=1}^{N_{eff}} f_n \, e^{2\pi i \, (hx_i+ ky_i+ lz_i)} \qquad \text{------} \quad 2.10$$

where f_n is the atomic scattering factor of n^{th} atom, and N_{eff} is the number of atoms in the unit cell having fractional co-ordinates (x_i, y_i, z_i). *i.e.*, [91],

$$N_{eff} = \frac{1}{8}N_c + \frac{1}{2}N_f + 1\, N_i \qquad \text{------} \quad 2.11$$

where N_c, N_f and N_i are the number of atoms at corner, face, and interstitial positions, respectively. For a face centred cubic (fcc) unit cell, N_c = 8, N_f = 6 and N_i = 0. So, N_{eff} = 4. These four atoms of the same kind are located at positions 0 0 0, ½ ½ 0, ½ 0 ½, 0 ½ ½. Therefore, equation 2.10 can be written as [91],

$$F = f\,[1 + e^{\pi i(h+k)} + e^{\pi i(k+l)} + e^{\pi i(l+h)}] \qquad \text{------} \quad 2.12$$

The above equation gives a non-zero value only when the Miller indices (*h k l*) are unmixed, *i.e.* either all even or all odd. This results in the presence of (111), (200), (220), (311), (222), (400), (331), (420), (333), (511), … planes in the XRD pattern of Heusler alloys. The identification of these planes can be done by combining equations 2.07 and 2.09 for *n* = 1 as,

$$\frac{sin^2\theta}{h^2+ k^2+l^2} = \frac{\lambda^2}{4\, a^2} \qquad \text{------} \quad 2.13$$

The right hand side (RHS) of the above relation is a constant for a particular structure with a particular source of X-rays. This implies that different planes with specific (*h k l*) values will satisfy particular angles (or θs) for which the left hand side (LHS) will be equal to the RHS. In this manner, all the peaks (or reflections) which appear in the XRD pattern of a Heusler alloy can be indexed, enabling the estimate of the lattice constant.

Theoretically simulated XRD pattern for a crystal with a unit cell with a specific arrangement of atoms can be compared with experimentally obtained XRD pattern. Such a comparison can help in assigning an appropriate unit cell to the experimental sample. Several software packages, such as CaRIne and Vesta, enable the simulation of theoretical XRD patterns for ideal bulk crystals from their unit cells. Several information about the crystal including the space group, lattice constants, atomic positions and occupancies, wavelength of X-ray, *etc.*, have to be fed into these programs for them to simulate the ideal XRD pattern for the specific crystal. Apart from these, there are other software packages (*e.g.* FullProf Suite [92]) for performing the Rietveld refinement of the experimental XRD patterns. These software packages require inputs such as expected phase(s), space group(s), atomic positions and occupancies in the unit cell, and X-ray wavelength to model the unit cell. The software creates a simulated XRD pattern on the basis of the model unit cell. Then, the software matches the simulated pattern with the experimentally observed pattern by least squares fitting process. If the matching is not good, as pointed out by the refinement quality parameters, the program manipulates the unit cell parameters and again compares the modified simulation with the experimental XRD pattern. This iterative process is continued until the best possible match is obtained with the experimental XRD pattern. If the match is good, as inferred from the refinement quality factors, then the unit cell with which the XRD pattern was simulated is the best possible unit cell model for the experimental sample. Once the unit cell of the sample is found, it is a trivial exercise to extract the until cell information such as refined lattice constant,

atomic positions, bond length, and bond angles of various atoms, *etc*. The refinement quality can be inferred using several parameters. These include the profile residual factor (R_p), weighted profile residual factor (R_{wp}), expected profile residual factor (R_{exp}), reduced goodness of fit parameter (χ^2), which are defined as [93],

$$R_p = \sum_{i=1}^{n} \frac{\left|Y_i^{obs} - Y_i^{cal}\right|}{\sum_i^n Y_i^{obs}} \times 100 \qquad \text{------} \quad 2.14$$

$$R_{wp} = \left(\sum_i^n \frac{w_i(Y_i^{obs} - Y_i^{cal})^2}{\sum_i^n w_i (Y_i^{obs})^2}\right)^{\frac{1}{2}} \times 100 \qquad \text{------} \quad 2.15$$

$$R_{exp} = \left(\frac{n-p}{\sum_i^n w_i (Y_i^{obs})^2}\right)^{\frac{1}{2}} \times 100 \qquad \text{------} \quad 2.16$$

$$\chi^2 = \left(\frac{R_{wp}}{R_{exp}}\right)^2 \qquad \text{------} \quad 2.17$$

where n, Y_i^{obs}, Y_i^{cal}, w_i, p, and $n - p$ are the number of data points, observed data points, calculated data points, statistical weights for each data point, number of refined parameters, degree of freedom, respectively. The *R*-factors (R_p, R_{wp}, and R_{exp}) and χ^2 obtained after the final refinement are used to verify the refinement quality. *R*-factors close to 10 and χ^2 below 5 are usually considered as acceptable values for a good refinement. 1 is the ideal value of χ^2 where the simulated and the experimental patterns match perfectly. Figures 2.07 and 2.08 show input parameters corresponding to approximate information of the unit cell bearing information about the atomic positions, occupancies, lattice parameters, bond angles, *etc.*, for Co_2FeGa (named as CFG-3). Figure 2.09 shows the refined XRD pattern along with various parameters such as R-factors and χ^2 values. Figure 2.10 shows the refinement result with final lattice parameter values for Co_2FeGa (CFG-3) nanoparticles obtained from the SUM file. Figure 2.11 shows final R-factors and χ^2 values after refinement of XRD pattern of Co_2FeGa (CFG-3) nanoparticles, which are well within the acceptable range, as mentioned previously.

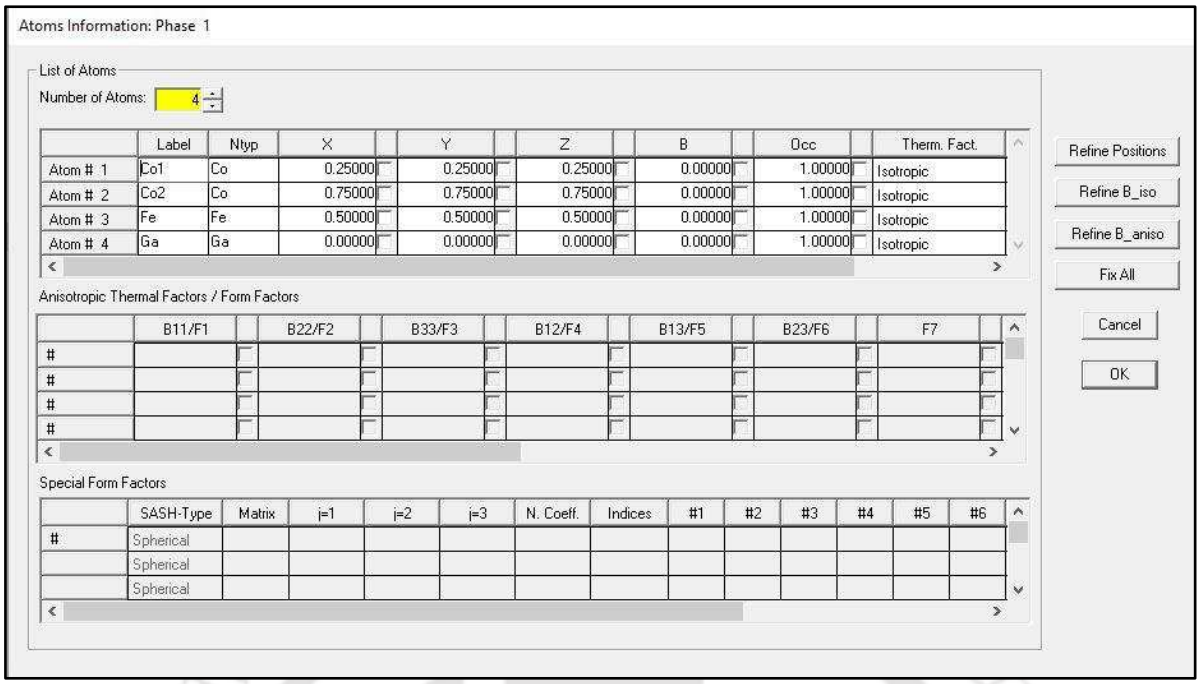

Figure 2.07. Wyckoff positions, along with atomic occupancies in the unit cell provided for refinement of XRD pattern of Co_2FeGa (CFG-3) nanoparticles.

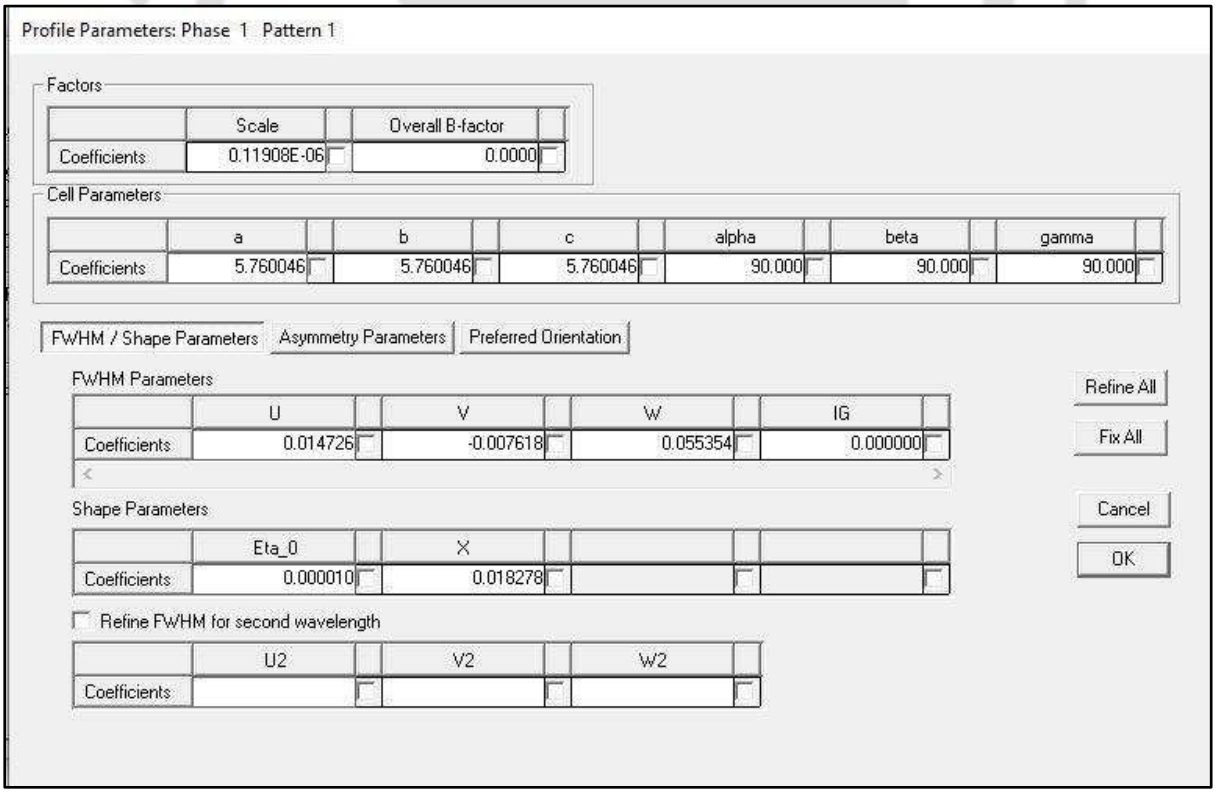

Figure 2.08. Unit cell information (profile parameters) provide for refinement of XRD pattern of Co_2FeGa (CFG-3) nanoparticles.

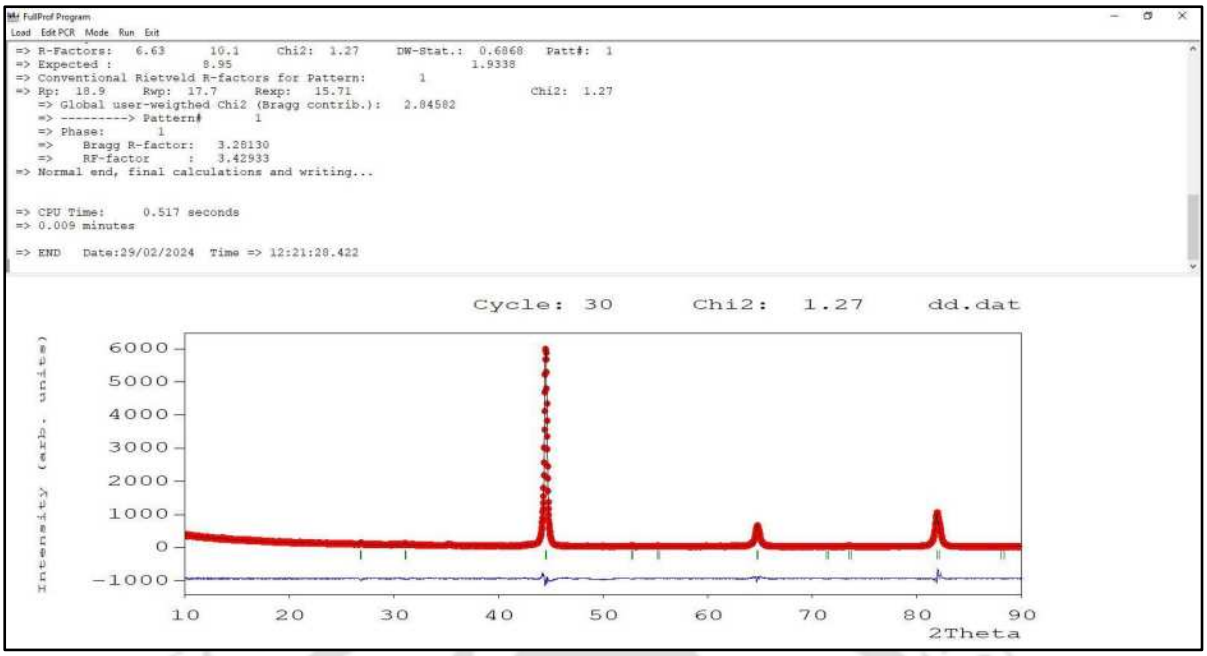

Figure 2.09. Output file and the Rietveld refined XRD pattern of Co_2FeGa nanoparticles.

```
==> RESULTS OF REFINEMENT:

=> No. of fitted parameters:   63

------------------------------------------------------------------------------
=> Phase No.  1 FCC                                        225
------------------------------------------------------------------------------

=>  No. of reflections for pattern#:   1:    22/2

==> ATOM PARAMETERS:

 Name      x      sx       y      sy       z      sz      B    sB   occ.  socc.  Mult
Co1     0.25000(   0)  0.25000(   0)  0.25000(   0)  0.000(  0)  1.000(  0)    8
Co2     0.75000(   0)  0.75000(   0)  0.75000(   0)  0.000(  0)  1.000(  0)    8
Fe      0.50000(   0)  0.50000(   0)  0.50000(   0)  0.000(  0)  1.000(  0)    4
Ga      0.00000(   0)  0.00000(   0)  0.00000(   0)  0.000(  0)  1.000(  0)    4

==> PROFILE PARAMETERS FOR PATTERN#  1

=> Cell parameters      :
                          5.76005   0.00000
                          5.76005   0.00000
                          5.76005   0.00000
                         90.00000   0.00000
                         90.00000   0.00000
                         90.00000   0.00000
```

Figure 2.10. Refinement result (SUM file) for Co_2FeGa (CFG-3) nanoparticles.

```
==> RELIABILITY FACTORS WITH ALL NON-EXCLUDED POINTS FOR PATTERN:  1

 => Cycle:  1 => MaxCycle: 30
=> N-P+C:  3938
=>  R-factors (not corrected for background) for Pattern:  1
=> Rp:  6.63     Rwp:  10.1     Rexp:    8.95 Chi2:  1.27      L.S. refinement
```

Figure 2.11. Final R-factors and χ^2 values after refinement for Co_2FeGa (CFG-3) nanoparticles.

In addition to enabling the identification of the appropriate crystal phase and refining the lattice constants, other useful information, such as the bond length and bond angle between component atoms can also be extracted from Rietveld fitting. In this thesis work, the refinement goals were limited to the identification of the crystal phase and obtaining the refined lattice parameters. Figure 2.12 displays the refined XRD pattern of Co_2FeGa nanoparticles (CFG-3) with a satisfactorily low χ^2 value. In the plot, open circles (red) indicate the experimental data I_{obs}, whereas solid line (black) represents the simulated XRD data I_{cal}. The minimal deviations (nearly straight line with minimum noise) in the difference data *i.e.*, $I_{obs} - I_{cal}$ (in blue), along with the low χ^2 value indicate the good quality of refinement.

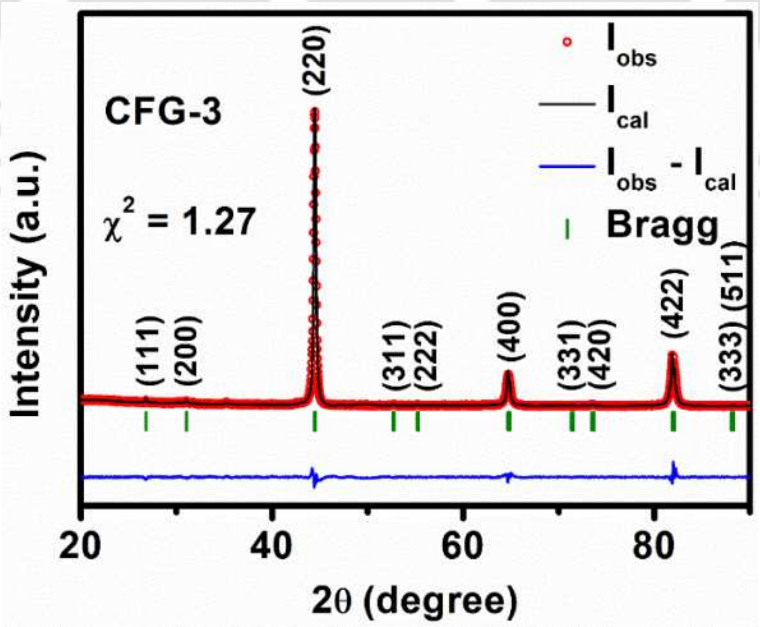

Figure 2.12. Rietveld refined XRD pattern for Co_2FeGa (CFG-3) nanoparticles.

The peaks in the XRD patterns should ideally be Dirac delta functions. But, practically, we observe broadening in the XRD peaks of nanocrystalline materials due to several factors like nanocrystallite size, internal strain, and instrumental contributions. The peak width (full width at half maximum, FWHM) increases upon lowering the size of the crystallites to nanometer scale due to reduced number of crystalline planes. Schërrer's equation [94] provides a means to estimate the average crystallite size (D_v) of sub-micrometer crystallites using this FWHM. The modification in the Schërrer's equation (*a.k.a.* Williamson-Hall or W-H plot) can provide an estimate of the contributions from nanometer size and internal stress to this peak broadening. In chemically synthesized nanoparticles, the major contributions to the broadening of XRD peaks come from the reduced crystallite size and instrumental broadening. Apart from being very small, one requires XRD patterns with a large (five or more) number peaks to obtain a reasonably good estimate of the strain from the W-H plots. Therefore, the Schërrer's equation has been used throughout this thesis work for the estimation of D_v from the peak profile of the synthesized nanoparticles using the relation [91],

$$D_v = \frac{k\lambda}{\beta \cos\theta} \qquad \text{------} \quad 2.18$$

where k is a constant with a value of 0.9 for nearly spherical nanoparticles with cubic symmetry, λ is the wavelength of X-rays (= 1.5406 Å), and β is the FWHM of the Bragg peak expressed in radians. The most intense peak in the XRD pattern is chosen for this analysis. Figure 2.13(a) shows a typical example of the process in which the (220) peak in the XRD pattern of Co_2FeGa (CFG-3) Heusler alloy nanoparticles (at ≈ 44.48°) is fitted using the pseudo-Voigt function. The FWHM extracted from the fitting is β_{obs} = 0.29512° = 0.005153 rad. β_{obs} includes contribution from the instrumental broadening (β_{ins}) arising from non-monochromaticity of X-ray beams, finite X-ray beam size, limitations in collimator to yield a perfectly parallel beam of X-rays, resolution (pixel size) of the detector, *etc.* It is important to subtract β_{ins} from β_{obs} to

obtain the actual FWHM (β_{act}) due to size effect. To get an estimate of β_{ins}, the XRD pattern standard Si crystal substrate was recorded using the same conditions (input power, scan rate, scan step, *etc.*) as utilized for recording the XRD pattern of the sample. The FWHM (β_{Si} = 0.10808° = 0.001887 rad.) of the Si (220) peak appearing at ≈ 47.3° (see Figure 2.13(b)), which is at the nearest position to the most intense Heusler alloy peak position (≈ 44.5°) was taken as β_{ins}. Then, the actual FWHM of the (220) peak of CFG-3 nanoparticles is,

$$\beta_{act} = \beta_{obs} - \beta_{ins} \quad = 0.003266 \text{ rad.} \quad \text{------} \quad 2.19$$

Using this β_{act} in equation 2.18, a coarse estimate of D_v (= 39 nm) was made. The error in the D_v estimate has been evaluated from the derivative of D_v, *i.e.*,

$$dD_v = D_v \left[\frac{d\beta}{\beta} + \tan\theta \, d\theta\right] \quad \text{------} \quad 2.20$$

to be D_v = 39 ± 1 nm for the aforementioned CFG-3 nanoparticles.

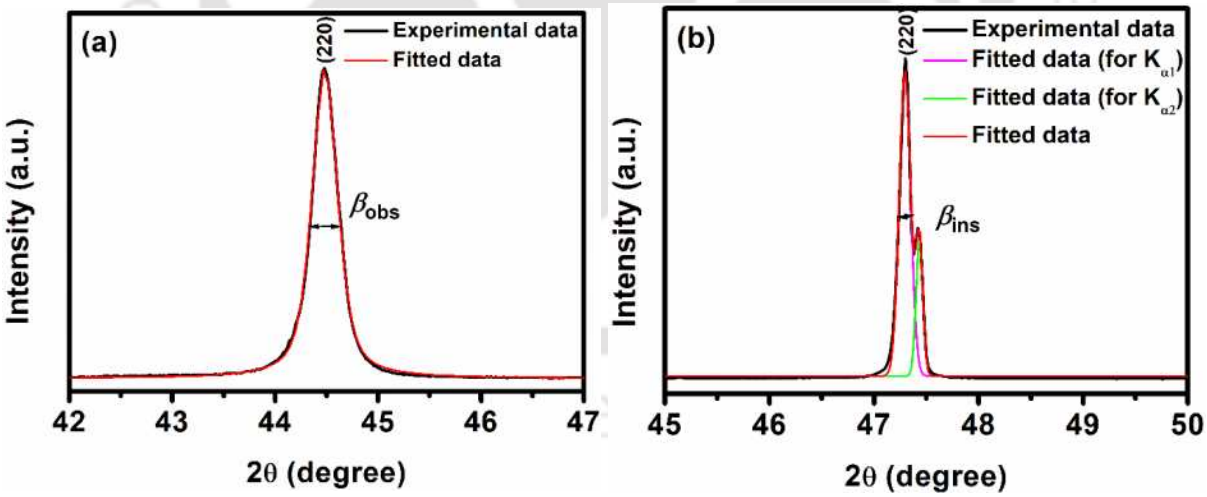

Figure 2.13. (a) Highly intense (220) peak for Co_2FeGa (CFG-3) nanoparticles and (b) (220) peak of standard Si fitted using pseudo-Voigt distribution function.

2.2.2 Electron microscopes

In order to validate the formation of nanoparticles and to investigate other morphological properties of the nanoparticles, electron microscopes have been employed. Electron microscopes exploit the wave nature of electrons to capture images of sub-micron structures. The de Broglie wave equation relates the wavelength (λ) and velocity (v) of electron [95] as,

$$\lambda = \frac{h}{mv} \quad \text{------} \quad 2.21$$

where h is Planck's constant and m is the rest mass of the electron. Under an applied potential V (in volt), an electron acquires a kinetic energy of ½ mv^2 [95]. So,

$$v = \sqrt{\frac{2eV}{m}} \quad \text{------} \quad 2.22$$

where e is the charge of the electron. From equations 2.21 and 2.22, one can obtain [95],

$$\lambda = \frac{h}{\sqrt{2meV}} \quad \text{------} \quad 2.23$$

Substituting $h = 6.625 \times 10^{-34}$ J/s, $m = 9.11 \times 10^{-31}$ kg and $e = 1.6 \times 10^{-19}$ C in equation 2.23, one can obtain the following relation for λ of electrons (in nm) in terms of V (in volt) [95],

$$\lambda = \frac{1.226}{\sqrt{V}} \quad \text{------} \quad 2.24$$

The working potential (usually V~1-20 kV for scanning mode and ~200 kV for transmission mode) results in λ values of ~0.039 - 0.0087 nm for scanning mode and ~0.0027 nm for transmission mode. Since the electrons have considerably lower wavelengths than visible light (λ = 400 – 700 nm), electron waves provide better resolution of the image of sub-micron structures as compared to optical microscopes. Electron beams are used in both reflection and transmission geometries and in elastic and inelastic scattering geometries to explore various features of nanostructures.

2.2.2.1 Scanning Electron Microscopy (SEM)

When an incident electron beam interacts with the specimen, some of the electrons may get scattered, some may get absorbed, and some may get transmitted after interacting with the material, as depicted in Figure 2.14. The typical scanning electron microscopy (SEM) is designed to utilize the scattered electrons after interaction with the specimen.

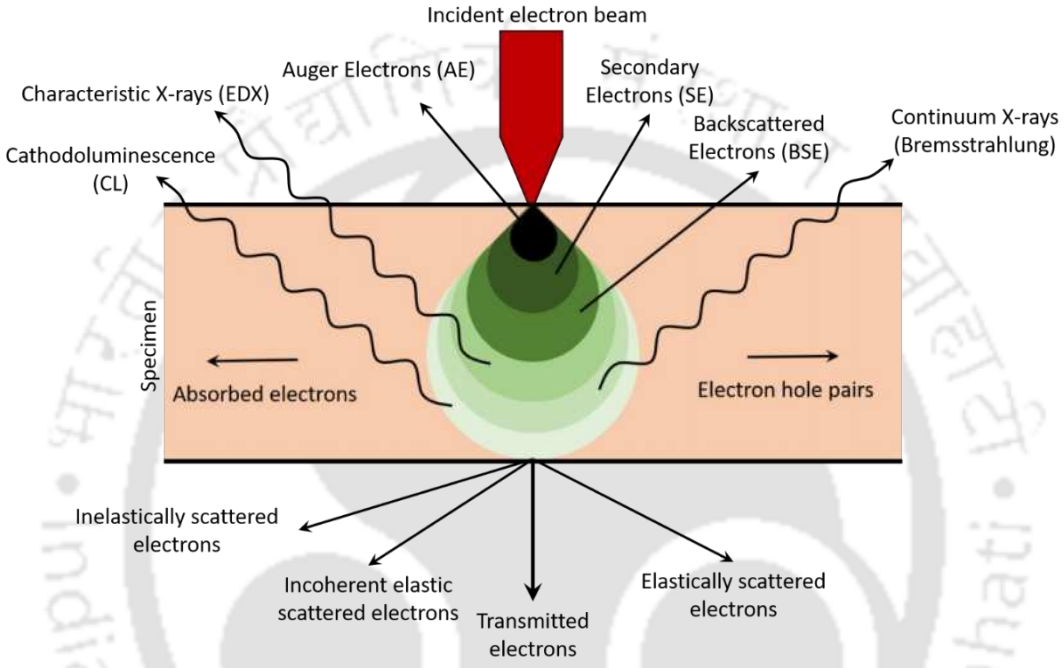

Figure 2.14. Schematic diagram showing the interaction of electrons with the specimen, resulting in various possible scattering processes.

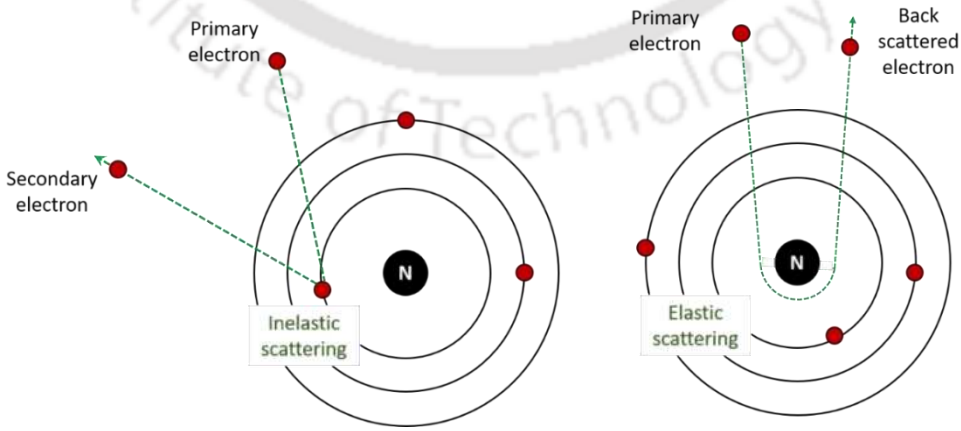

Figure 2.15 Secondary (left) and back scattered (right) electrons scattered after interaction with a specimen.

When the incoming electrons interact with a loosely bound outer electron of the specimen, low energy secondary electrons are generated, as depicted in Figure 2.15(left). These secondary electrons are generally produced close to the surface of the specimen and utilized to construct the topographic image of the specimen. On the other hand, the elastic scattering of the incoming electrons with the specimen is called as back scattered (or reflected) electron, as depicted in Figure 2.15 (right). These are high energy electrons that can travel through more depth as compared to the secondary electron and can provide contrast depending upon the atomic number of the scattering atom. In addition to outcoming electrons, the interaction of energetic incoming electrons with the specimen also results into photon emission, which can be utilized for composition analysis, which will be described later.

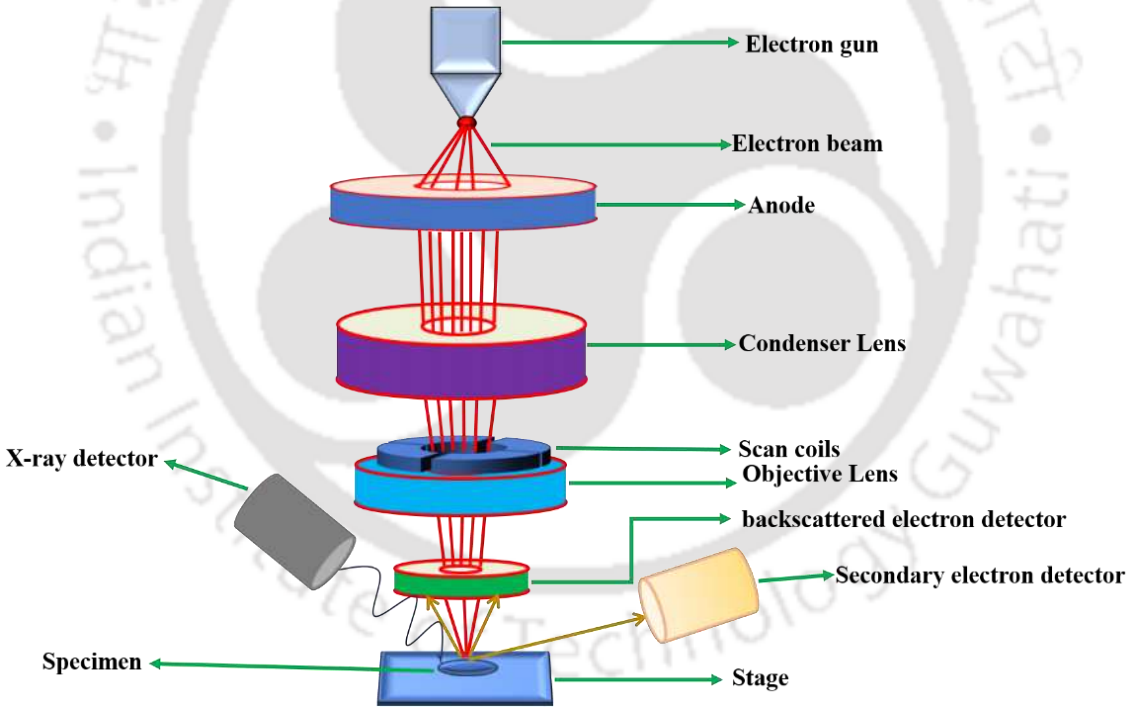

Figure 2.16. Schematic diagram of a typical SEM setup.

An SEM consists of an electron source (electron gun), condenser lenses, objective lenses, scan coils, and detectors. The schematic of a typical SEM is shown in Figure 2.16. The electron gun is usually a thermionic or field emitter. The thermionic emitter is the traditional source of electrons, which works on the principle of thermionic emission. Field emitter is

another advanced source of electron beam, which provides better resolution to the micrographs due to its reduced beam diameter. In our case, we have utilized a field emitter as a source of electron beam thus, the instrument is named as Field Emission Scanning Electron Microscope (FESEM). Electron microscopes have electromagnetic lenses whose focal length can be varied by altering the current in the coil of a solenoid [95]. The electron microscope is equipped with two types of lenses. The condenser lens with a large focal length is used to focus the beam on the sample [95]. The objective lens with a small focal length is utilized for magnification and projection of the image on the image plane [95]. The scan coils have the function of moving the electron beam across the specimen as needed. In order to detect the scattered electrons and photons, various detectors are used. A field emission scanning electron microscope (FESEM, Zeiss Gemni 300) was used in this work. The image of the instrument is shown in Figure 2.17.

Figure 2.17. Photograph of Zeiss Gemni 300 FESEM.

ImageJ software was used in analysing the particle size distribution. For this, the length scale was determined upon importing the image. Then, the diameters of the individual non-agglomerated particles were used using the tool option provided in the software. After measuring diameters of more than about 400 particles, the histogram was plotted. A Gaussian function was fitted to the histogram data to extract the mean particle size (d) and the standard

deviation (σ). Figure 2.18(a) is a typical FESEM micrograph of Co_2FeGa nanoparticles (CFG-3), revealing the particle morphology. Figure 2.18(b) shows the particle size histogram plotted using the data in Figure 2.18(a) and the Gaussian fit to the data.

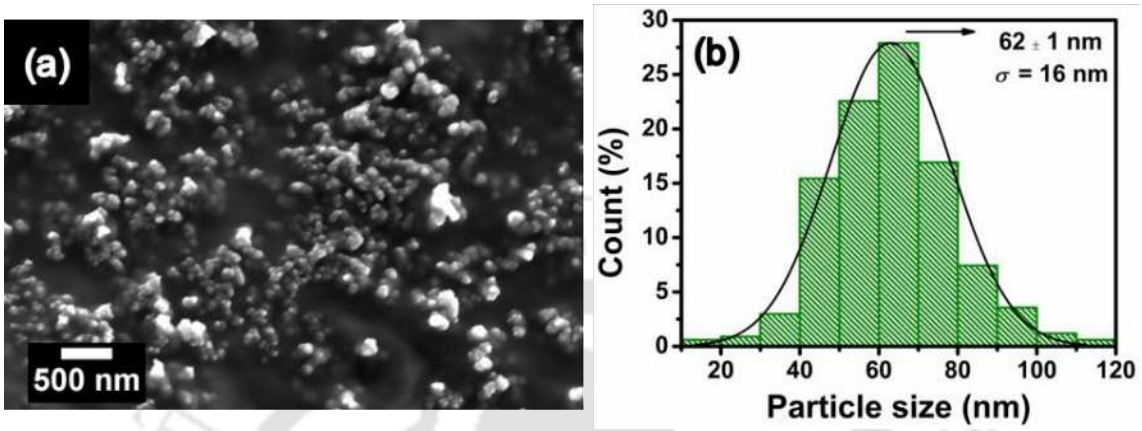

Figure 2.18. (a) FESEM image and (b) particle histogram of Co_2FeGa nanoparticles (CFG-3).

2.2.2.2 Energy Dispersive X-ray Spectroscopy (EDX)

After the structural identification, the subsequent essential step is to determine the elemental composition of the alloy nanoparticles. In the SEM, after the interaction of the incoming electrons with the specimen, various processes can occur as depicted in Figure 2.14.

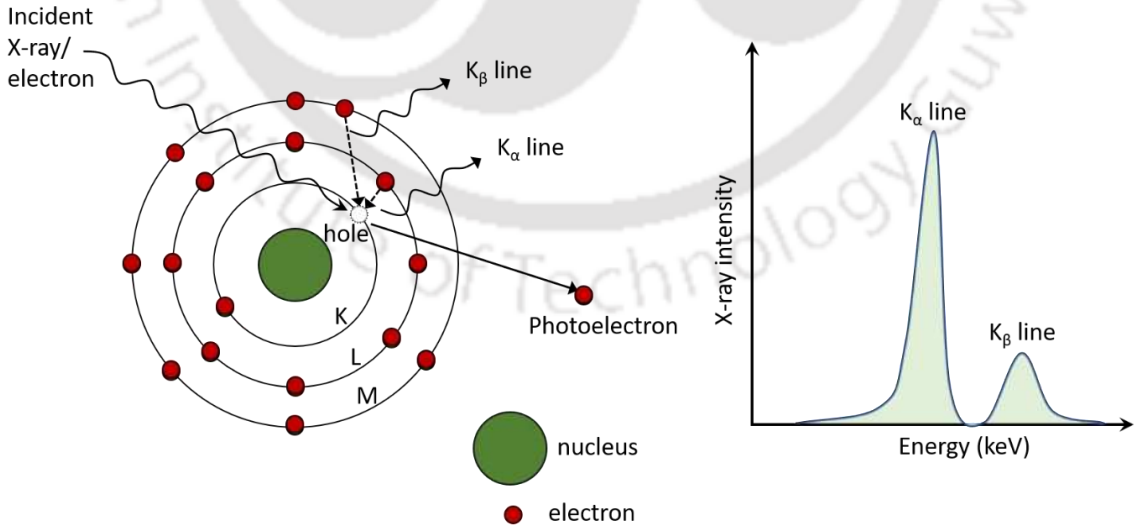

Figure 2.19. Schematic of characteristic X-ray generation process by the incident electrons (left) and the typical EDS spectrum (right).

These interactions include core electron excitations, which ultimately result in the emission of X-rays, as depicted in Figure 2.19 (left). Since these are characteristic X-rays, their energies are unique to each element. So, these can be used to identify the elements present in the specimen and their relative concentrations. In a SEM with an energy dispersive spectrometer (EDS) or Energy dispersive X-ray spectroscope (EDX) attachment, an X-ray detector collects these X-rays as a function of their energies. Figure 2.20 is a photograph of the EDS (Zeiss Σigma) operated under an acceleration voltage of 20 kV used for compositional analysis of the samples.

Figure 2.20. Image of Zeiss Σigma EDX utilized in this work.

The EDS spectrum, which is simply a plot of the amount of X-rays received at each energy level, as shown in Figure 2.19 (right). Each peak in this spectrum is a unique characteristic of an element. Figure 2.21 shows a raw EDS spectrum of Co_2FeGa (CFG-1) nanoparticles. Analysis of the spectrum reveals the at.% of each element present in the specimen. The ≈ 5% oxygen shown in this metallic alloy is the adsorbed oxygen on the surface of the sample. The carbon is from the carbon tape used to connect it to the electrode, and the gold is from the conducting gold coating provided at the top of nanoparticles to avoid charging issues. Once the O, C, and Au are eliminated from the raw data, the actual constituents of the

specimen, along with their relative concentrations can be obtained, as shown in Figure 2.22. From the figure, it is clear that Co, Fe, and Ga are the only constituents, and their at.% are Co:Fe:Ga::49.7:26.0:24.3. The elemental compositions have been evaluated in this work by taking the average of 10-15 individual spectral scans for each sample.

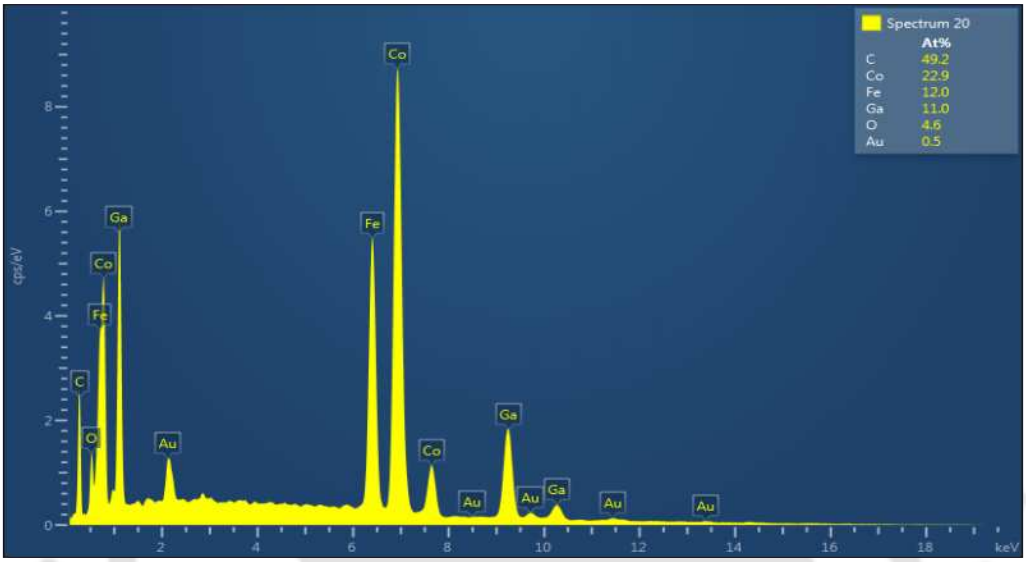

Figure 2.21. Raw EDS micrograph of Co_2FeGa nanoparticles (CFG-1).

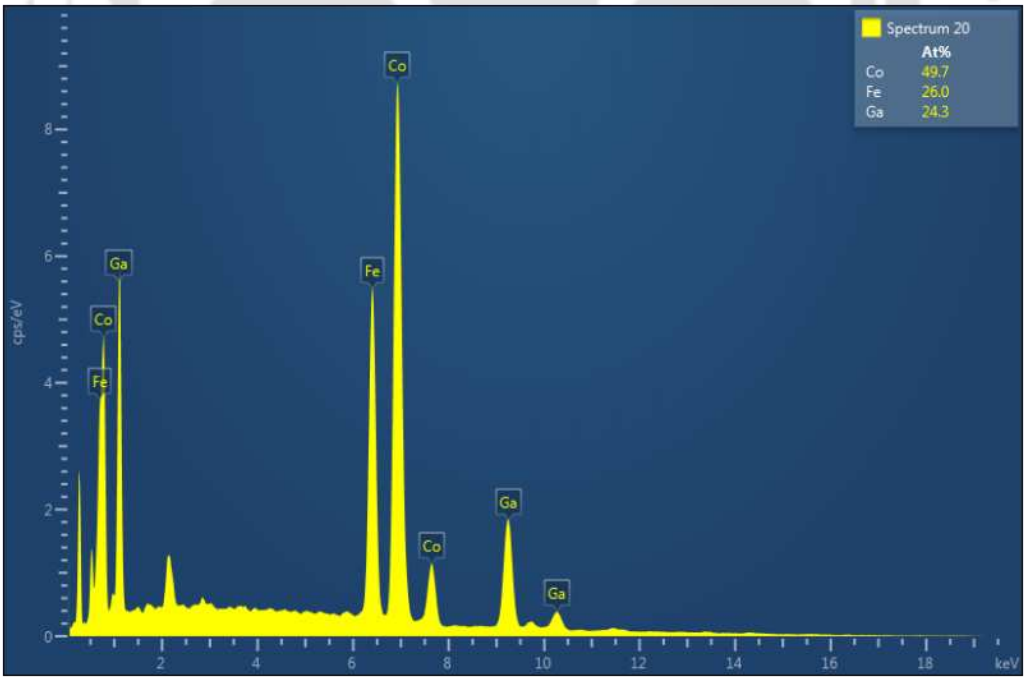

Figure 2.22. Actual EDS micrographs of Co_2FeGa nanoparticles (CFG-1) after elimination of adsorbed oxygen and elements used for bottom (C) and top (Au) contacts.

2.2.2.3 Transmission Electron Microscopy (TEM)

As mentioned earlier, the incoming electrons can interact with the specimen in various ways, as depicted in Figure 2.14. A portion of the incoming energetic electron beam may pass through (transmit) a thin specimen after interacting with it. In transmission electron microscope (TEM), these transmitted electrons are imaged to understand the atomic structure. In a TEM, electrons emitted from the electron gun are accelerated and projected toward the thin specimen using electromagnetic condenser lenses. While transmitting through the specimen, the electrons (a) go through unobstructed, (b) are elastically scattered with no energy loss due to the interaction of the electrons with the potential field of the atom/ion cores, leading to the construction of electron diffraction patterns, and (c) are inelastically scattered by the electron matrix, defects, dislocations, grain boundaries, *etc.* resulting in variation in their intensities. A set of intermediate as well as projector lenses are utilised to further magnify the transmitted beams, which are then displayed on a fluorescent screen. The transmitted electrons are detected to extract various information about the specimen. The TEM is operated in imaging mode or diffraction mode. Figure 2.23 gives schematic diagrams of both imaging and diffraction modes of a TEM. Just as to SEM, in this work, a field emission transmission electron microscope (FETEM, JEOL-2100F) shown in Figure 2.24 has been used.

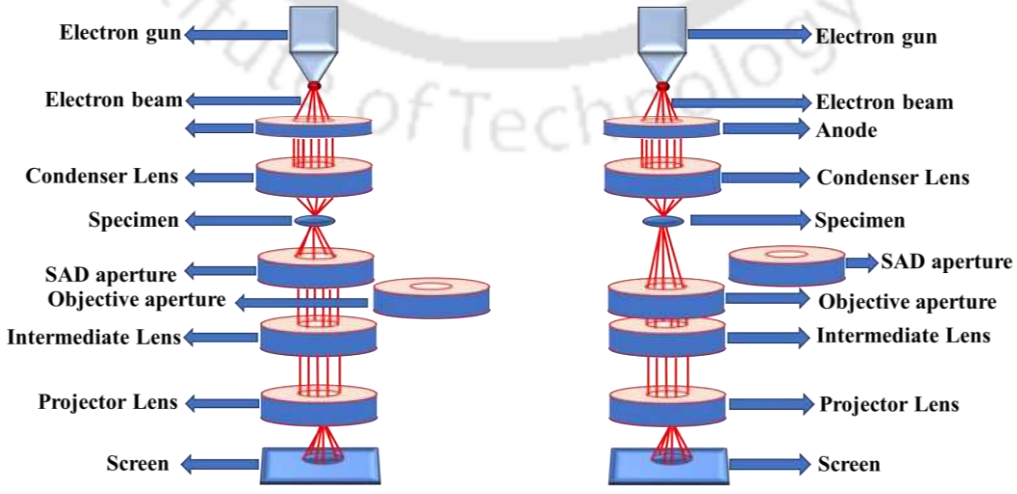

Figure 2.23. Schematic diagram of TEM in diffraction (left) and imaging (right) modes.

Figure 2.24. Photograph of JEOL-2100F TEM utilized in this work.

Bright field images are generated by deliberately removing all the diffracted beams and permitting only the central beam to traverse the material. This is achieved with apertures of suitable dimensions in the rear focal plane of the objective lens. On the other side, dark field images can be generated using an aperture that obstructs the central beam and all diffracted beams except a selected diffracted beam. The third way of imaging involves the recombination of the main transmitted and one or more diffracted beams after taking care to preserve both their phases and amplitudes. This approach is used to obtain high-resolution transmission electron micrographs (HRTEM) images to identify lattice planes as well as arrays of atoms. Thus, HRTEM images can be utilized to evaluate the crystallographic structures and lattice parameters of the specimen. In contrast, selected area electron diffraction (SAED) is obtained by completely eliminating the central beam with the help of a beam blocker and aggregating all the diffracted beams to generate the diffraction pattern. For single crystals, the SAED patterns consist of distinct spots, whereas for polycrystalline specimens, concentric rings of

distinct spots are obtained. In Bragg's law (equation 2.07), for very small θ, sinθ ≈ θ and if n = 1, then,

$$2\theta d_{hkl} = \lambda \qquad \text{------} \quad 2.25$$

Figure 2.25 shows the geometry of a SAED pattern. Here, L is the distance between the sample and the screen (camera length), and r is the radius of the circle connecting the diffraction spots from a plane (distance between transmitted and diffracted beam from a plane).

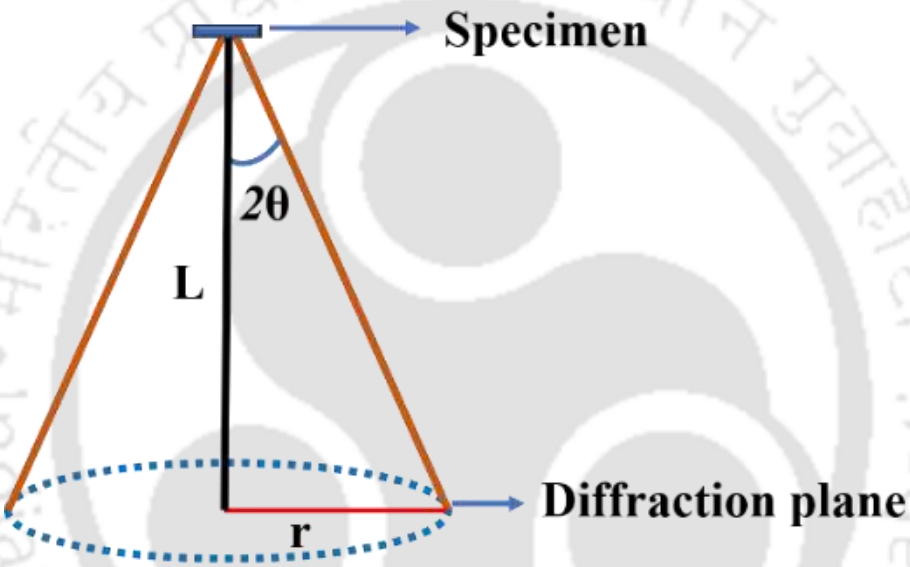

Figure 2.25. Schematic diagram of the geometry of an SAED pattern.

From the above figure, for small θ,

$$2\theta = r/L \qquad \text{------} \quad 2.26$$

Combining equations 2.25 and 2.26,

$$rd_{hkl} = L\lambda \qquad \text{------} \quad 2.27$$

$$d_{hkl} = \frac{L\lambda}{r} \qquad \text{------} \quad 2.28$$

If the TEM is operated at 200 kV, $\lambda \approx 0.0027$ nm (using equation 2.24), which is a constant value. Now, L and r depend upon each other, which shows that the camera length L can modify the radius of the ring pattern for a particular plane. Adjusting the camera length allows us to control the magnification of the diffraction pattern to optimize the visibility of a specific diffraction spot or ring. Rewriting equation 2.28, we get,

$$d_{hkl} = \frac{1}{\left(\frac{r}{L\lambda}\right)} \qquad \text{------} \quad 2.29$$

Now, the length scale given in the SAED image is a measure of $\frac{r}{L\lambda}$ in nm^{-1}. Therefore, we need not calculate the individual values of r, L, and λ. By merely measuring the radius of the ring in nm^{-1} scale, one can determine d_{hkl}. Figure 2.26(a) displays the indexed SAED pattern of Fe_2CoAl nanoparticle. $L \approx 25$ cm in this case. For performing FETEM measurements, a small amount of the nanoparticles is dispersed in a suitable solvent (ethanol/methanol/acetone), and a few drops of mixture were placed on a carbon-coated copper TEM grid. After permitting for the solvent to dry, the TEM grid with the dry particles was mounted in the TEM for analysis. ImageJ was used to analyse the TEM images. The radius of the 1st and 2nd rings in the SAED pattern shown in Figure 2.26(a) were found to be ≈3.2 nm^{-1} and ≈3.45 nm^{-1}, respectively, which yielded $d_{111} \approx 3.1$ Å and $d_{200} \approx 2.9$ Å using relation 2.29. To analyse the HRTEM images (see Figure 2.26(b and c)), the first step is to select the area of the HRTEM image using the crop or duplicate tool. After this, the fast Fourier transform (FFT) of the selected HRTEM image is taken. In the FFT image, different sets of bright spots indicate the different planes. A particular spot was selected to process the inverse fast Fourier transformed (iFFT) images (see insets of Figure 2.26(b and c)), which show fringes corresponding to the selected plane. Then, using the line tool, the interplanar spacing d_{hkl} between the planes is calculated.

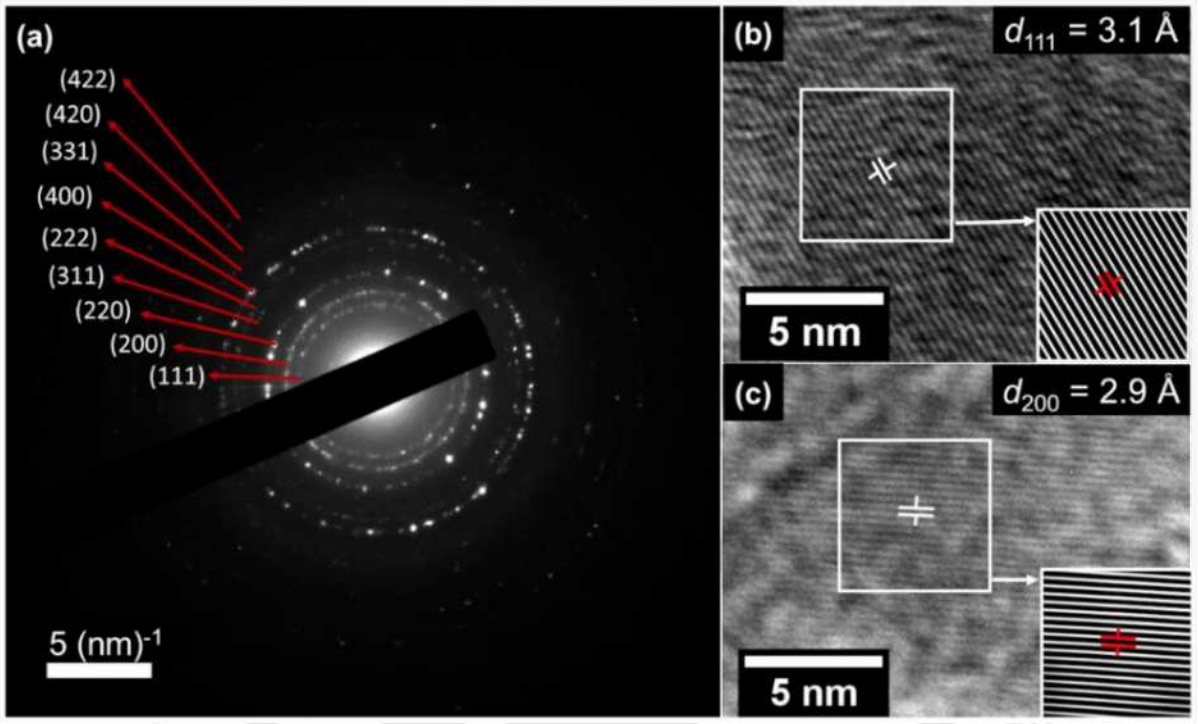

Figure 2.26. (a) SAED pattern and (b and c) HRTEM and iFFT images of Fe_2CoAl particles.

2.2.3 Vibrating Sample Magnetometer (VSM)

The magnetic properties of the samples are measured using a vibrating sample magnetometer (VSM) which is based on the Faraday's law for electromagnetic induction, schematically depicted in Figure 2.27. It states that the induced electromagnetic induction (ε) is proportional to the rate of change of magnetic flux through the coil.

$$\varepsilon \propto -\frac{d\varphi}{dt} \qquad \text{------} \quad 2.30$$

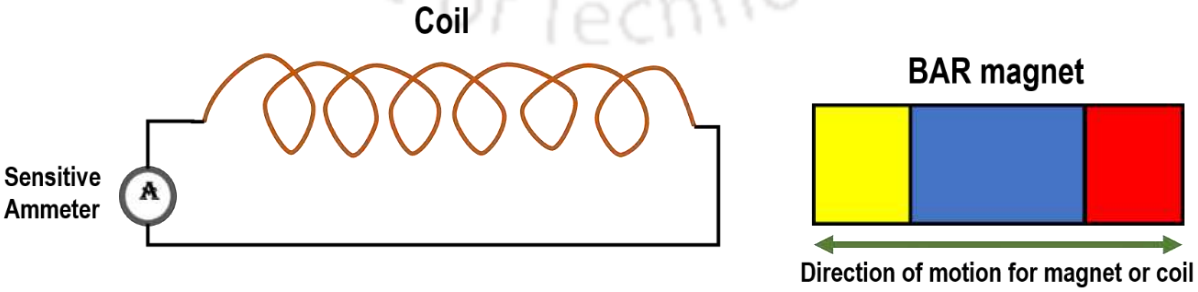

Figure 2.27. Schematic diagram representing electromagnetic induction (Faraday's law).

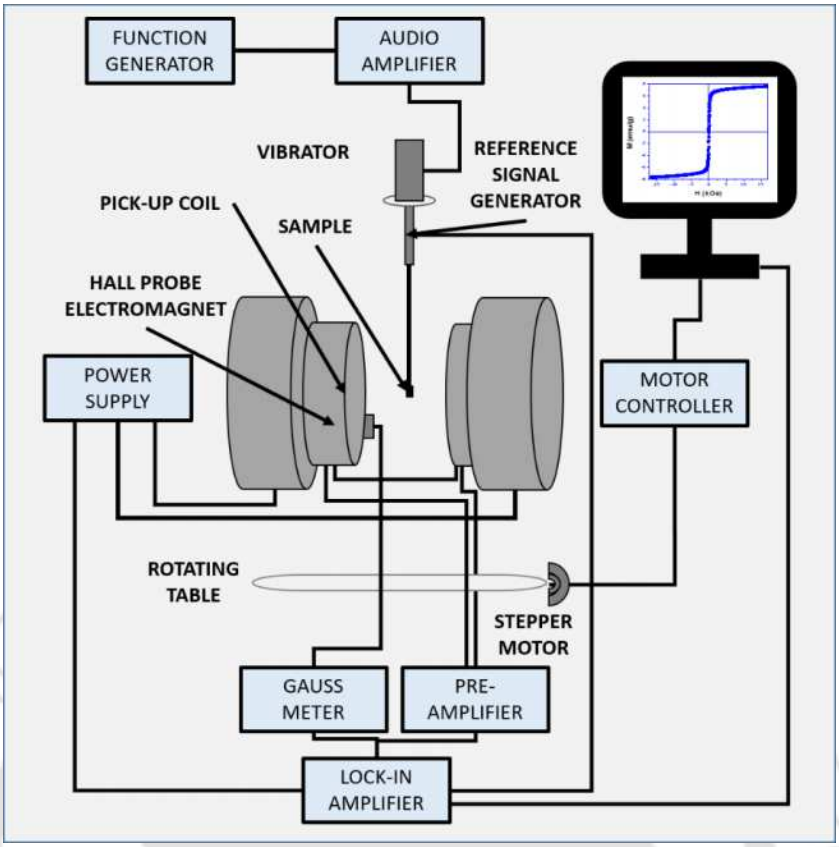

Figure 2.28. Schematic diagram of a VSM.

A schematic representation of a contemporary VSM is illustrated in Figure 2.28. The VSM comprises of the following components *viz.*, (i) sample vibrator unit, (ii) sample holding rod, (iii) electromagnet and power supply, (iv) Hall probe, (v) pick up coil pairs, (vi) lock-in amplifier, (vii) control panel and (viii) computer interface. The specimen undergoing analysis is positioned in a homogeneous magnetic field and vibrated at a fixed frequency using the sample vibration exciter unit. The variation of the flux within the pickup coils, caused by the vibration of a magnetic specimen, generates an induced electromotive force owing to electromagnetic induction. A lock-in amplifier measures this induced voltage using the reference voltage as a piezoelectric vibration frequency signal. The amplitude of the induced voltage signal is directly proportional to the magnetic moment of the specimen and amplitude and frequency of the vibration. Using lock-in amplifier and feedback methods, only the

component of the signal emanating from the magnetic moment is extracted, transformed into the unit of magnetization (*e.g.* emu), and displayed on a digital panel metre.

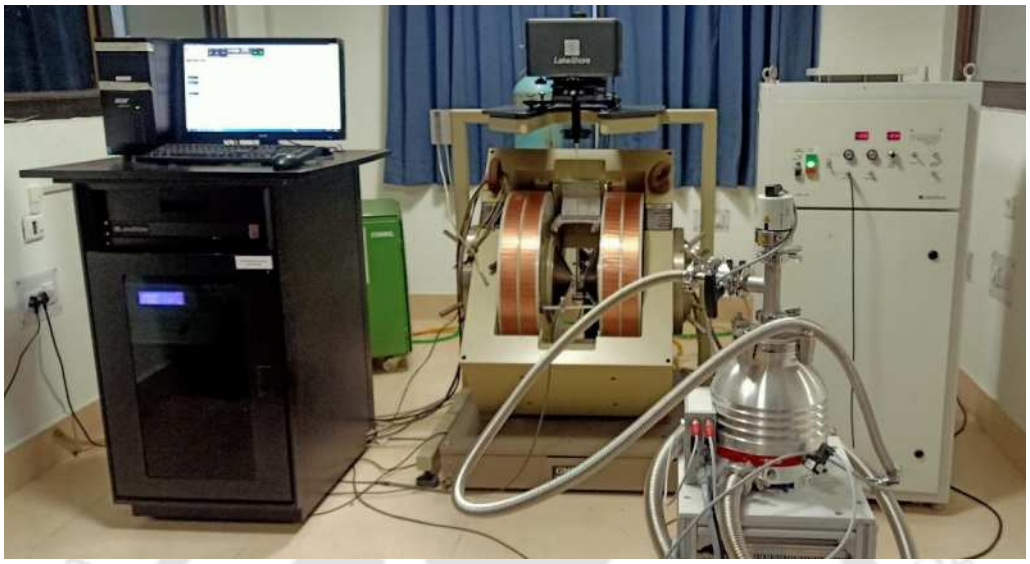

Figure 2.29. Photograph of the electromagnet based Lakeshore 7410 VSM.

Figure 2.30. Photograph of the 9T PPMS (Quantum Design, DynaCool) with a VSM insert.

The calibration of the system is usually done using a standard nickel sphere specimen with known magnetic moment (M = 6.92 emu at H = 5000 Oe) prior to measurements on the samples. A program sequence is defined by the user as per the requirement in the software packaged with the instrument. The sequence is customized with optimum steps of magnetic

fields (H) or temperatures (T) to gather the optimum number of data points to minimize the errors in the derived magnetic parameters (M_S, M_r, H_C, T_C, *etc.*). Many improvements have been made in the VSM instrumentation to enhance its sensitivity, utilizing the same basic concept. An electromagnet based VSM (Lakeshore, 7410) and a 9 Tesla physical property measurement system (PPMS, Quantum Design, DynaCool) based VSM were utilized in the current work for high (300 – 1273 K) and low temperature (5 – 300 K) magnetic measurements, respectively. A high temperature oven assembly and a closed cycle refrigerator based low temperature assembly were utilized for the alteration in the temperatures in VSM and PPMS, respectively. The VSM and PPMS utilized are displayed in Figures 2.29 and 2.30, respectively. Sample holders made of polychloro-trifluoro-ethylene (Kel-F) and polypropylene capsules inserted in a brass holder case were utilized in VSM and PPMS, respectively. For high temperature measurements, a sustainable quartz rod was utilized to hold the sample. A high temperature ceramic putty was employed to stick the sample to the high temperature quartz rod. Argon gas was continuously purged in the oven to prevent the sample from oxidising at high temperatures.

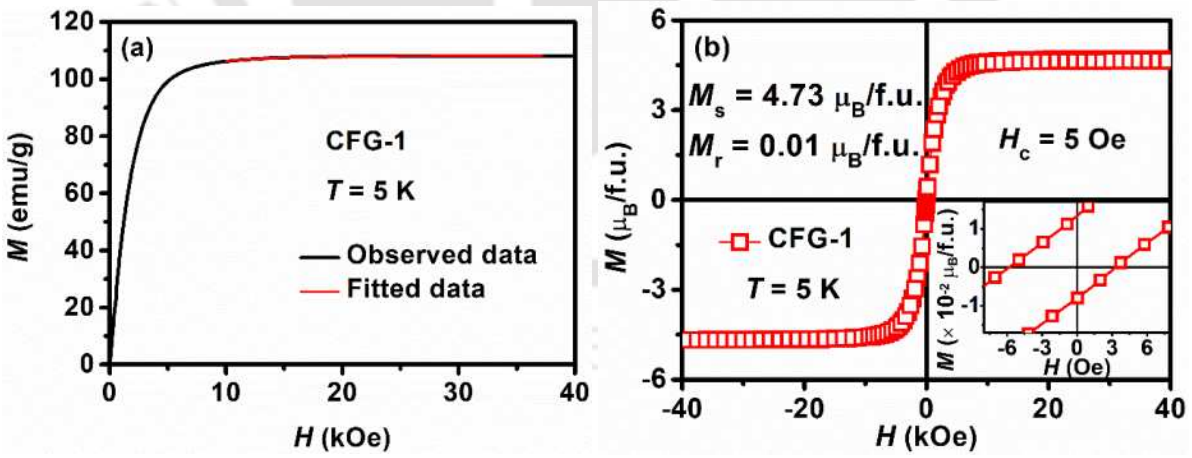

Figure 2.31. (a) Virgin curve fitted to LAS and (b) *M-H* loop recorded Co_2FeGa nanoparticles (CFG-1) at 5 K.

The initial (1st quadrant) virgin curve and *M-H* loops recorded for Co_2FeGa nanoparticles (CFG-1) at 5 K are depicted in Figures 2.31(a and b), respectively. The virgin

curve was fitted to LAS using equation 1.10. M_s (= 108.47 emu/g) was obtained from the fitting. The M_s is then converted into the unit emu/cc (= 923 emu/cc) by multiplying the M_s (= 108.47 emu/g) with the mass density (8.51 gm/cc). Equation 1.11 is then utilized to obtain the value of K_{eff} (= 4.87 × 10^6 erg/cc). The value of M_s is then converted to the unit of μ_B/f.u. following the procedure explained below for the composition X_2YZ,

$$1 \text{ emu} = 10^{-3} \text{ J/T} \quad \text{------} \quad 2.31$$

$$1\ \mu_B = 9.27402 \times 10^{-24} \text{ J/T} \quad \text{------} \quad 2.32$$

Combining the above two equations,

$$1\ emu = \frac{10^{-3}}{9.27402 \times 10^{-24}}\ \mu_B \quad \text{------} \quad 2.33$$

Therefore, M_s in μ_B/f.u. for X_2YZ can be estimated as,

$$M_s\ (\mu_B/f.u.) = M_s\ (emu/g) \times \frac{(2 \times u_X + 1 \times u_Y + 1 \times u_Z)}{N_A} \times \frac{10^{-3}}{9.27402 \times 10^{-24}} \quad \text{------} \quad 2.34$$

where u_X, u_Y, and u_Z are atomic masses of X, Y, and Z atoms, respectively, and N_A is Avagadro's number (N_A = 6.022 × 10^{23} atoms/mole). For Co_2FeGa nanoparticles (CFG-1), equation 2.34 yields M_s = 4.73 μ_B/f.u.

2.2.4 Electron Spin Resonance (ESR) spectrometer

Electron spin resonance (ESR), also known as electron paramagnetic resonance (EPR), is a technique for studying systems with more than one unpaired electron. The approach utilizes the angular momentum of the electrons to provide the information. Electrons, in general, undergo two distinct types of motion, *viz.*, orbital and spin motions. In general, an electron's magnetic moment is predominantly attributed to its spin motion, with the orbital motion making no significant contribution to the overall magnetic moment. When placed in an external magnetic field (H), the specimen will interact with the magnetic field. Now, the interaction

energy is influenced by the magnetic field strength and the spin quantum number. This will result in the splitting of the energy levels. The relationship between applied magnetic field *H* and the frequency ν of this ESR transition between the split energy levels can be expressed as,

$$h\nu = g\,\mu_B\,H \qquad \text{------} \quad 2.35$$

The above equation is called the resonance condition, which is the basic principle behind the ESR spectrometer. There are two different ways to fulfill this resonance condition. The first technique involves varying the magnetic field while maintaining a constant frequency, and the second method involves varying the frequency while maintaining a constant magnetic field. In most circumstances, it is simpler to create a variable magnetic field by altering the current in a coil. Therefore, the variable magnetic field approach is popular.

The instrumentation of the ESR spectrometer requires (a) an electromagnet to generate a stable, homogeneous, and strong magnetic field, (b) a sample container to retain the sample, (c) a variable current source (modulator) to adjust the magnetic field, (d) a frequency source also known as oscillator (Klystron oscillator) of the desired frequency range (microwave), (e) a transmittance coil to couple the microwave power from the oscillator to the sample cell, (f) a receiving coil to receive the microwave signal from the specimen and couple to the detector, (g) a semiconductor crystal detector to detect the signal, (h) a preamplifier to amplify the signal, (i) a recording device with the signal processing unit, *i.e.*, a computer with an appropriate software. The microwave power from the Klystron oscillator is coupled with a rectangular microwave cavity, whose second arm is attached to a sample holder. The sample holder is placed in between the pole pieces of the electromagnet. The third arm of the cavity is attached to a dummy load, while the fourth arm is coupled with the crystal detector. The schematic diagram of the ESR spectrometer is given in Figure 2.32. When the magnetic field applied to the specimen is gradually increased, resonance occurs at a particular frequency, and a

deflection (signal) appears in the fourth arm. The signal that arrives at the 4th arm is detected by the semiconducting crystal detector and amplified using a preamplifier. The amplified signal is then fed to the recorder which shows results either in the absorption mode or in the derivative mode. The derivative mode of the signal gives the accurate value of the field at which resonance occurs. An ESR spectrometer (JEOL-JES-FA200) shown in Figure 2.33, was used to determine the value of Lande's g factor of the nanoparticles required for critical size calculations.

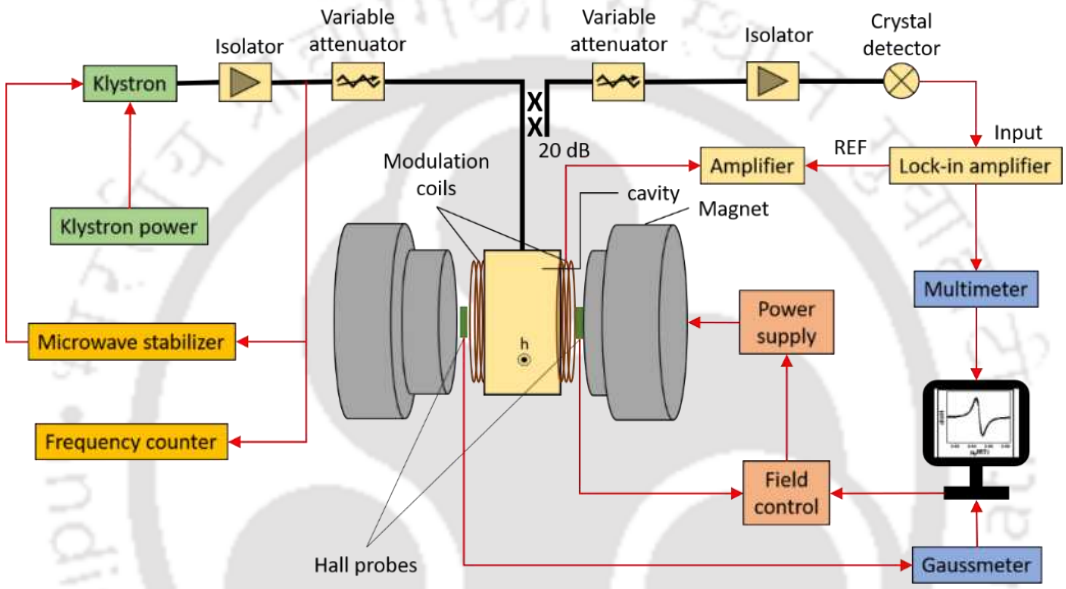

Figure 2.32. Schematic diagram of an ESR spectrometer.

Figure 2.33. Photograph of JEOL-JES-FA200 ESR spectrometer.

2.3 Details of theoretical calculations

Theoretical studies have been performed to ensure that the experimental findings are consistent with the theory. Density functional theory (DFT) [96,97] has proved to be a valuable tool for understanding various properties in these systems. DFT calculations can predict properties, including the lattice structures, band structures, density of states, half metallicity, magnetic moments, and many more properties related to the systems. DFT has its foundation in the Hohenberg-Kohn theorem, which states that the properties of a system depend upon its ground state electron density. DFT calculations yield accurate solutions using the Born-Oppenheimer approximation [98], Kohn-Sham formalism [97], and exchange correlation potential approximation. The exchange-correlation potential refers to the effects of the Coulomb potential. The most basic approximation is the Local Density Approximation (LDA), which replaces an inhomogeneous system's exchange-correlation energy density with that of a homogeneous electron gas assessed at the local density. The inclusion of gradient corrections can improve the performance of LDA, which can be referred to as Generalized Gradient Approximation (GGA) [99]. Vienna *ab initio* simulation package (VASP) [100,101] was utilised for performing the *ab initio* calculations incorporating the DFT along with projected augmented wave (PAW) [102,103] pseudopotentials. VASP having spin polarized version combined with the Perdew-Burke-Ernzerhof (PBE) parametrization of the GGA was utilized for the exchange correlation potential.

The standard DOS calculation involves three steps, *viz.*, relaxation (1st step), self-consistent field (SCF) (2nd step), and density of states (DOS) calculations (3rd step). VASP requires four input files, *viz.*, INCAR, POSCAR, POTCAR, and KPONTS. After the completion of each step (relaxation/SCF/DOS), several output files are generated, such as, CHGCAR, DOSCAR, OSZICAR, OUTCAR, WAVECAR, *etc.* The detailed process, including the input/output files format and details of input parameters, are available in the

VASP manual provided on the webpage of VASP wiki [104]. A brief description of these files and parameters utilized in the current work are presented below.

2.3.1 Input files in VASP

2.3.1.1 INCAR

The INCAR file delineates the input parameters that dictate the execution and methodology of a given operation. Additionally, it also contains the pivotal parameters required for the computations, including the smearing parameters, plane wave cut-off energy, convergence criteria for ionic and electronic iterations *etc.* One can tune these parameters to obtain the optimized output. VASP also provides default values for these input parameters, which are effective for most of the routine calculations. Specific computations, including the density of states, band structure, spin-orbit coupling, *etc.*, require adjustments in certain parameters. A brief description of the INCAR file parameters is given below:

ISTART

This parameter defines whether to read WAVECAR file (of the previous step) or not. The WAVECAR file contains information about the initial cut-off energy, initial basis vectors defining the supercell, initial wavefunctions, *etc.* There are different possible values for ISTART, such as 0 | 1 | 2 | 3. Generally, in the relaxation and SCF steps, "ISTART = 0" is used to start the calculation from scratch. In DOS calculations, "ISTART = 1" is used to restart the calculation with constant cut-off energy and to read the output CHARGCAR file from SCF step.

ISMEAR

This parameter determines how the partial occupancies are set for each orbital, and this process is referred to as smearing. There are various possible values, *viz.*, 0 | -1 | -2 | -3 | -4 | -5. In the relaxation and SCF calculations, Gaussian smearing (ISMEAR = 0) is used, which is changed

to tetrahedron method with Blöchl corrections (ISMEAR = -5) for DOS calculation requiring higher accuracy in total energy calculations.

SIGMA

This parameter specifies the width of the smearing in eV. A maximum width of (SIGMA = 0.05) has been used in the calculations.

EDIFF

This parameter is employed to define the termination criterion for electronic iterations in eV. Iterative computations were performed till the energy convergence criterion $\leq 10^{-5}$ eV (EDIFF = 1E-5) was achieved to ensure the required precision in energy calculations.

NSW

This parameter sets the maximum number of ionic steps. "NSW = 500" has been used in the relaxation step as it has been found to be appropriate.

ENCUT

This parameter specifies the energy cut-off for the plane-wave basis set in eV. A minimum value of "ENCUT = 450" has been used for the calculations.

ISPIN

This parameter specifies the requirement of spin polarization. Two possible values, *viz.*, "ISPIN = 1" and "ISPIN = 2" are available. The former shows that non spin polarized calculations are performed, whereas the latter shows that spin polarized calculations are performed. Therefore, "ISPIN = 2" has been used throughout the calculations.

ISIF

This parameter is used in the relaxation step to specify ionic degrees of freedom (position, cell shape, cell volume) and the requirements to calculate the stress tensor. ISIF can take values

like 0 | 1 | 2 | 3 | 4 | 5 | 6 | 7 | 8. "ISIF = 2" is used when only atomic positions are to be varied without optimizing the cell shape and volume. On the other hand, "ISIF = 3" is used when all the degrees of freedom, including position, cell shape, and cell volume, should be varied.

PREC

This parameter defines the precision level of input values such as Low | Medium | High | Normal | Single | SingleN | Accurate. "PREC = Accurate" has been utilized throughout the calculations to yield the best precision.

LORBIT

This parameter defines the projection method related to quantum number *l* & *m*. Among various possible values, *viz.*, 0 | 1 | 2 | 5 | 10 | 11 | 12 | 13 | 14, "LORBIT = 10" provides only element-resolved DOS without specifying contributions from s/p/d/… orbitals. On the other hand, "LORBIT = 11" provides orbital resolved DOS for each element.

LWAVE

This parameter specifies whether the wavefunction is to be given in the output WAVECAR file. "LWAVE = .FALSE." in the relaxation step, and "LWAVE = .TRUE." in the SCF step has been utilized in the calculations.

LCHARG

This parameter defines whether to write the output CHGCAR file or not. "LCHARG = .FALSE." is used at the time of relaxation. Further, "LCHARG = .TRUE." is employed in SCF calculations to write the output CHGCAR file, which is then utilized in the DOS calculations.

ICHARG

This parameter provides information about initial charge density. Among the available values, "ICHARG = 2" is used in the relaxation and SCF calculations. "ICHARG = 11" is used at the time of DOS calculations to utilize the CHGCAR file obtained from the SCF calculations.

IBRION

This parameter defines how the ions are updated and moved. Among different possible values, such as 1 | 0 | 1 | 2 | 3 | 5 | 6 | 7 | 8 | 40 | 44, "IBRION = 2" is employed to use conjugate gradient algorithm for the relaxation calculations.

POTIM

This parameter defines the step width in ionic relaxation. Among the various possibilities, such as none | 0.5 | 0.015, "POTIM = 0.5" is used for "IBRION = 2" in relaxation calculations.

MAGMOM

Through this parameter, the initial magnetic moment of each element is provided in the form of number of atoms times the approximate magnetic moment of that element. For example, "MAGMOM = 8*4.0 4*2.0 4*1.0" for 8 Fe, 4 Co, and 4 Ga atoms.

LDAU

This enables the use of Hubbard parameter (U), which accounts for onsite coulomb repulsion among 3*d* electrons. U was applied using "LDAU = .TRUE." in the DOS for Co_2FeGa.

LDAUJ

This sets the effective on-site exchange interaction (J) in eV for each element. J was set to 0.0 eV while performing calculations for Co_2FeGa as "LDAUJ = 0 0 0" for Co, Fe, and Ga.

LDAUL

This parameter specifies the quantum number *l* for each element. For Co_2FeGa, "LDAUL = 2 2 0" was utilized for Co, Fe, and Ga elements.

LDAUU

This sets the value of U (in eV) for each element. The introduction of large U often results in unexpectedly large electron correlations, leading to exaggerated magnetic moment values

[105]. Therefore, U values are generally limited to 2.0 eV, as followed in several reports on Co and Fe based Heusler alloys (*e.g.*, U_{Fe} = 1.80 eV and U_{Co} = 1.92 eV for Co_2YZ (Y = Fe, Ti, V, Cr, Mn; Z = Ga, Al, Si, Ge, Sn), $Fe_2Y'Z'$ (Y' = Ti, V, Mn; Z' = Z = Ga, Al, Si, Ge, Sn), *etc.* [106], U_{Co} = 1.92 eV for Co_2VZn [107], U_{Fe} = 2.1 eV and U_{Co} = 2.2 eV for Co_2FeAl [108–110]). U values were utilized in the range of 0.0 eV to 2.0 eV in steps of 0.5 eV in the present work. For example, "LDAUU = 2.0 2.0 0.0" has been used for Co, Fe and Ga elements, respectively.

LDAUTYPE

This parameter specifies the DFT+U variant to be used. Among various possible values, *viz.*, 1 | 2 | 3 | 4, "LDAUTYPE = 2" is used for simplified approach introduced by Dudarev *et al.* [111] while performing calculations for Co_2FeGa.

LDAUPRINT

This parameter decides whether to write the onsite occupancy matrix to the OUTCAR file or not. Among possible values, *viz.*, 0 | 1, "LDAUPRINT = 1" was utilized to write the abovementioned information to OUTCAR file while performing calculations for Co_2FeGa.

The above parameters can be varied from system to system at different stages according to requirements. The INCAR file used in SCF calculations of Fe_2CoGa is given in Figure 2.34.

```
SYSTEM = Fe2CoGa
 ISTART = 0
 ISMEAR = 0
 ICHARG = 2
 SIGMA = 0.05
 EDIFF = 1E-5
 ENCUT = 450
 PREC = Accurate
 ISPIN = 2
 MAGMOM = 8*4.0 4*2.0 4*1.0
 LORBIT = 11
 LWAVE = .TRUE.
 LCHARG = .TRUE.
```

Figure 2.34. A typical INCAR file utilized for SCF calculations on Fe_2CoGa compound.

2.3.1.2 POSCAR

This input file contains information about the position of each atom in the lattice, along with the approximate starting values of lattice parameters. A unit cell of a minimum 16 atoms (4 inter-penetrating fcc lattices containing 4 atoms each) has been utilized for the calculations. The typical structure of POSCAR file for Fe_2CoGa containing 16 atoms (8 Fe, 4 Co, 4 Ga) is given in Figure 2.35. Here, the 1st line is the comment line, where one can write the name of the system or any other comment. The 2nd line represents the scaling factor for the lattice. The next three (3rd to 5th) lines contain unit cell information related to lattice constant in the form of a matrix followed by element name (6th line) and the corresponding number of atoms (7th line). The 8th line represents the co-ordinate system (cartesian or fractional/direct) utilized to define the positions of the atoms. The last 16 lines represent the position of each atom. It is important to mention here that the positions should be given in a series in accordance with the elements specified in the 6th and 7th lines.

```
FeCoFeGa
1.0
        5.730064          0.0000000000        0.0000000000
        0.0000000000      5.730064            0.0000000000
        0.0000000000      0.0000000000        5.730064
   Fe   Co   Ga
    8    4    4
Direct
     0.750000000       0.750000000       0.750000000
     0.250000000       0.250000000       0.750000000
     0.250000000       0.750000000       0.250000000
     0.750000000       0.250000000       0.250000000
     0.500000000       0.500000000       0.500000000
     0.500000000       0.000000000       0.000000000
     0.000000000       0.500000000       0.000000000
     0.000000000       0.000000000       0.500000000
     0.250000000       0.250000000       0.250000000
     0.750000000       0.750000000       0.250000000
     0.750000000       0.250000000       0.750000000
     0.250000000       0.750000000       0.750000000
     0.000000000       0.000000000       0.000000000
     0.000000000       0.500000000       0.500000000
     0.500000000       0.000000000       0.500000000
     0.500000000       0.500000000       0.000000000
```

Figure 2.35. A typical POSCAR file utilized for the relaxation of Fe_2CoGa compound.

2.3.1.3 POTCAR

It comprises of the pseudopotentials used in the calculations for each element of the compound. This file contains details of the elements, including mass, valency, electronic configuration, *etc.*

2.3.1.4 KPONTS

This input file contains information about the Bloch vectors (*k*-points) utilized in the calculations. A Γ-centered Monkhorst pack up to 10 × 10 × 10 *k*-point mesh was used in the Brillouin zone integration required for the electronic part. However, DOS calculations were performed using a denser *k*-mesh up to 24 × 24 × 24 where better accuracy is required for determining states close to the E_F. A typical KPOINT file is given in Figure 2.36.

```
Automatic mesh
0
Gamma
10 10 10
 0  0  0
```

Figure 2.36. A typical KPOINTS file utilized in relaxation and SCF calculations of Fe_2CoGa.

2.3.2 Steps involved in DOS calculations performed through VASP

The process of computation through VASP includes three steps of calculations given below:

2.3.2.1 Relaxation

In the relaxation step, all the aforementioned four input files, along with the vasp-script file have to be placed in a folder and run. The process of relaxation is then to be repeated by varying the lattice parameter values and calculating the total energy of the compound. A plot is drawn between lattice volume and corresponding total energy in order to converge on the lattice constant value for which the total energy of the compound is minimum. If the compound can have two or more possible structures, this process can help in identifying the stable structure amongst these by determining the one with the lowest energy configuration. The energy *versus*

volume curve for Fe_2CoGa compound plotted using $L2_1$ and *X* type unit cells are shown in Figure 2.37. The appearance of lower energies for *X* type unit cell compared to $L2_1$ type unit cell confirms that the *X* type structure is the stable structure for this compound.

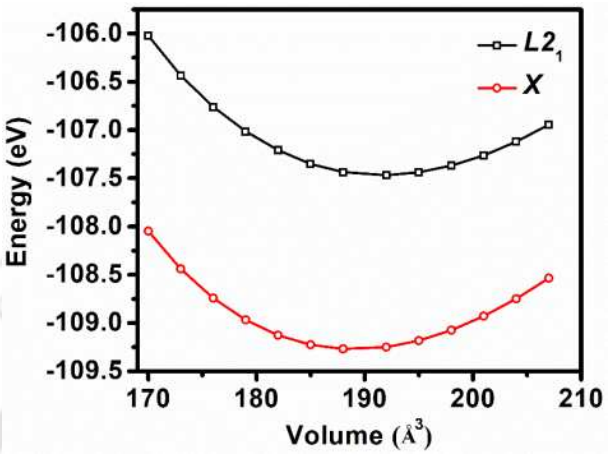

Figure 2.37. Energy *versus* volume plots for Fe_2CoGa obtained using $L2_1$ and *X* type unit cells.

2.3.2.2 SCF calculations

In this step, the output file CONTCAR of the relaxation step should be placed in another folder by renaming it as POSCAR file. Other input files (INCAR, POTCAR, KPOINTS) should be modified accordingly (see description for INCAR parameters) and placed in the same folder to be run again along with the vasp-script file.

2.3.2.3 DOS calculations

In this step, the CONTCAR file obtained from the SCF calculations is used as POSCAR file. Additionally, CHGCAR file obtained from the SCF calculations is also taken as an input file for the DOS calculations. Other modifications are made in other input files (INCAR, POTCAR, KPOINTS) wherever needed (see the description for INCAR parameters), and they are run with the vasp-script file. The required output can be now extracted for further analysis after the completion of the run. Figure 2.38 represents the total density of states (TDOS) and element-resolved partial density of states (PDOS) plots obtained for Fe_2CoGa compound with stable *X* type unit cell.

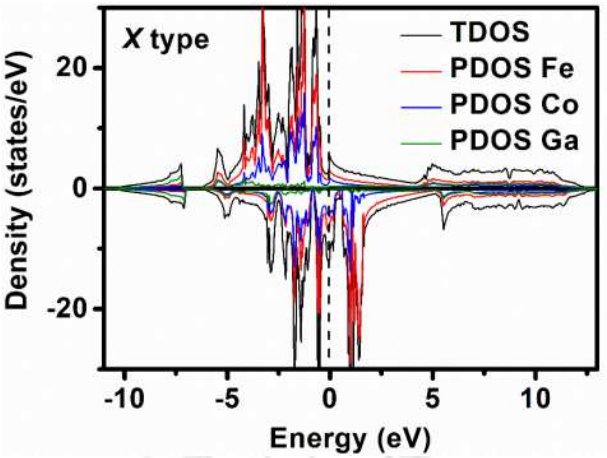

Figure 2.38. DOS near E_F of Fe_2CoGa obtained using *X* type unit cell.

Chapter 3

Crystallite size dependent properties of Co_2FeGa nanoparticles

As highlighted in the introduction chapter, Co based Heusler alloys are identified as promising materials having applications in diverse fields. Among Co based Heusler alloys, Co_2FeGa is a well investigated alloy even before the discovery of half metallicity in Heusler alloys by de Groot *et al.* [26]. However, the initial experimental studies [23,37,112] on Co_2FeGa alloys provided limited information about its crystal structure, atomic site preference, and magnetic and magneto-optical properties. Ishida *et al.* [113] were the first to explore its functionality as a half metallic ferromagnet. Following this pioneering work, abundant theoretical [106,114,123–132,115,133–138,116–122] and experimental [50,114,144–146,115–117,139–143] work has been published on bulk Co_2FeGa alloys describing its half metallic or other novel properties such as high M_s, high T_C, high P, soft ferromagnetic behavior, *etc.*, which established it as a futuristic material. Considering the advantages of Co_2FeGa Heusler alloy, some attempts have been made to synthesize this alloy in two-dimensional (thin film) [147–150] and one-dimensional (nanowire) [81,151] forms so that the advantages of the low dimensional, quantum confined alloy could be exploited. However, the preparation of these Heuser alloy nanoparticles with fully ordered phase-pure $L2_1$ type structure and stoichiometric composition by a simple and cost-effective template-less method has remained a challenge. The first successful attempt to prepare Co_2FeGa in nanoparticle form was made by Basit *et al.* [58] in 2009 by silica template-assisted chemical route. Though the authors succeeded in

preparing Co_2FeGa nanoparticles, the synthesized nanoparticles contained silica template impurity. This study motivated researchers to further investigate the crystallite/particle size dependent properties of Co_2FeGa nanoparticles. Wang *et al.* [79,80,84] utilized the same methodology to synthesize Ga deficient non-stoichiometric Co_2FeGa nanoparticles with different particle sizes by varying the amount of silica template. However, the authors found Fe and Co impurity phases along with silica template impurities in all their samples. Gellesch *et al.* [152,153] utilized carbon nanotubes (CNT) as a template in the place of silica template to prepare Co_2FeGa nanoparticles. Though this method avoided silica template, presence of CNT influenced the magnetic properties of the final product. Xu *et al.* [81] utilized SBA-15 silica as a template in a chemical assisted method which again left silica residues along with the nanoparticles. Later, Nehla *et al.* [82] followed the silica template-assisted approach proposed by Basit *et al.* [58] and varied the size of the nanoparticles by varying amount of silica template. Additionally, Nehla *et al.* [82] attempted to prepare these nanoparticles without using any template by co-precipitation method, but the absence of (111) and (200) reflections in the XRD pattern indicated the lack of stable $L2_1$ type ordering in their nanoparticles. Thus, it is evident that the template-assisted methods enabled synthesis of Co_2FeGa nanoparticles with controlled crystallite/particle size by varying amount of silica, [79,80,82] these methods could not yield impurity-free and highly ordered Co_2FeGa nanoparticles. In this chapter, crystallite size dependent structural and magnetic properties of single domain Co_2FeGa nanoparticles with $L2_1$ type ordered crystal structure synthesized using a template-less chemical route is presented. Theoretical calculations have also been performed to obtain the DOS near the E_F to assess the potential of Co_2FeGa for various applications.

3.1 Sample preparation

A modified template-less chemical route described in chapter 2 has been employed to prepare three sets of Co_2FeGa nanoparticles designated as CFG-1, CFG-2 and CFG-3. Optimized

amounts of chemicals, *viz*., $Fe(NO_3)_3.9H_2O$ (0.5785 g), $CoCl_2.6H_2O$ (0.6256 g) and $Ga(NO_3)_3.8H_2O$ (1.6790 g) were used as the precursors. The synthesis procedure followed is represented in Figure 2.01. Table 3.01 lists the three sets of Co_2FeGa nanoparticles (designated as CFG-1, CFG-2 and CFG-3) obtained by three different heat treatment conditions.

Ab initio computations employed a supercell of Co_2FeGa with a total of 16 atoms (8 Co, 4 Fe, and 4 Ga). The unit cell comprising of atoms occupying the Wyckoff position of a $L2_1$ type (space group no. 225 ($Fm\bar{3}m$)) full Heusler alloy structure as Co1 (¼, ¼, ¼) 4c, Co2 (¾, ¾, ¾) 4d, Fe (½, ½, ½) 4b and Ga (0, 0, 0) 4a, respectively [114,119] was utilized in Rietveld refinement as well as *ab initio* calculations. The lattice parameter obtained from Rietveld refined XRD data was used in the calculations. The detailed methodology followed in the *ab initio* calculations are mentioned in chapter 2.

3.2 Structural analysis

Figure 3.01 shows room temperature XRD patterns along with their Rietveld refined patterns of three sets of Co_2FeGa nanoparticles. The presence of reflections from the planes (111), (200), (220), (311), (222), (400), (331), (420) and (422) confirms the formation of the stable $L2_1$ phase Heusler alloy with high crystalline order and phase purity. The normalized intensities of the experimental XRD reflections for the three sets of nanoparticles match with the normalized intensity of the simulated XRD pattern as listed in Table 3.02. The simulated pattern was generated using the Vesta software using the CIF file created using the Rietveld refined crystallographic data. It is to be noted that the three elements (*i.e*., Co, Fe and Ga) in the alloy belong to a single horizontal row of the periodic table due to which they possess almost similar X-ray scattering factors, resulting in very weak super-lattice reflections (111) and (200) [154]. The intensities of these super-lattice reflections are ≤1% of the most intense (220) reflection as mentioned in Table 3.02, which makes it difficult to identify them in the powder XRD patterns.

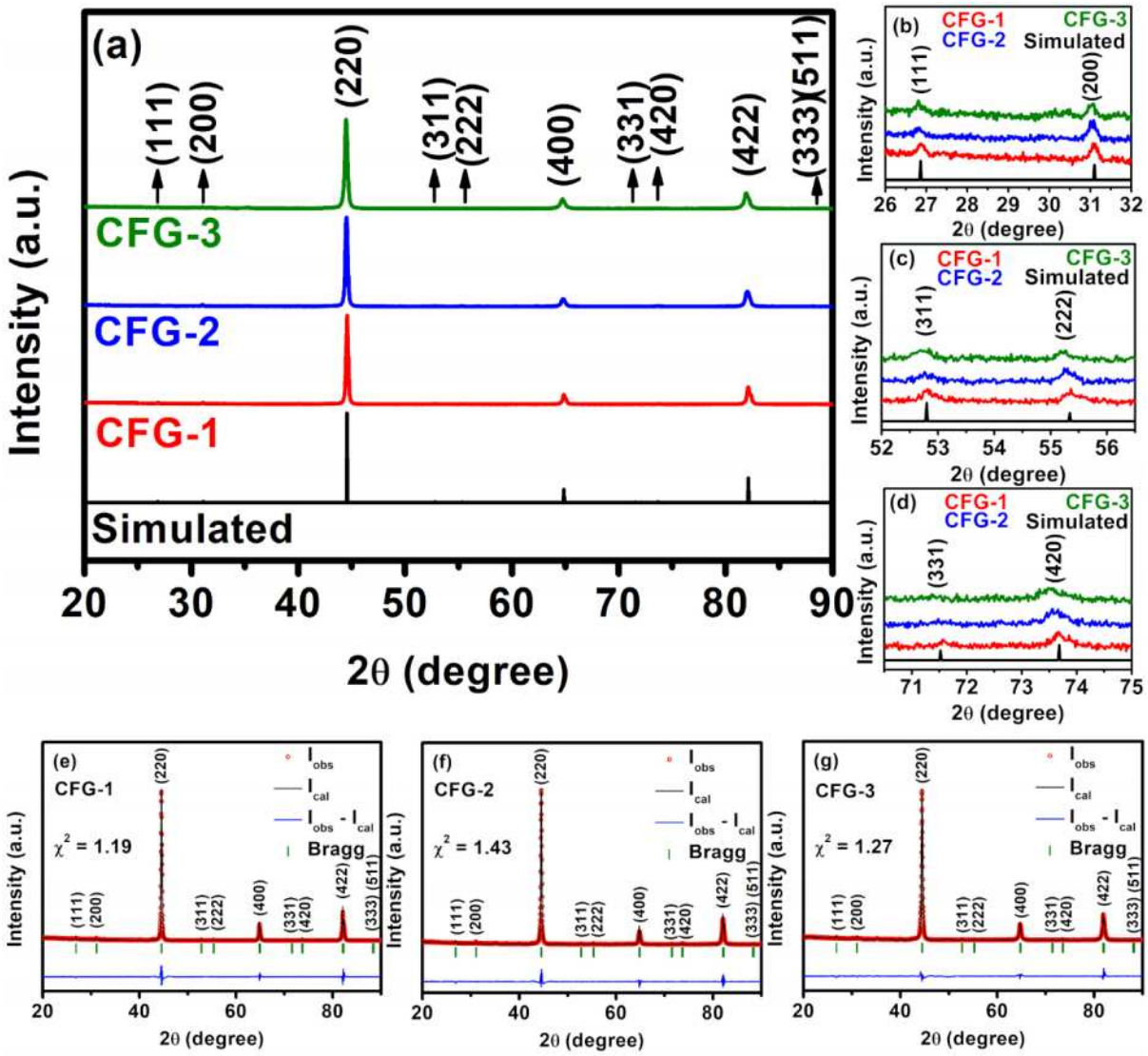

Figure 3.01. (a) Experimental and simulated XRD patterns of CFG-1, CFG-2 and CFG-3. (b, c, d) Enlarged view of select regions and (e, f, g) Rietveld refined XRD patterns of all samples.

As seen from the literature, many researchers could not locate these super-lattice reflections in their XRD data on bulk Co_2FeGa [144,145] and Co_2FeGa thin films [147,149]. This becomes a more arduous task in the case of nanoparticles with peak broadening due to reduced D_v. Basit *et al.* [58] could not observe super-lattice reflections (111) and (200) in Co_2FeGa nanoparticles in powder XRD patterns and had to resort to selective excitation energy induced anomalous XRD measurements to identify them. Wang *et al.* [80] utilized the same technique to obtain super-lattice reflections and but however found Fe and Co impurities in all

the synthesized non-stoichiometric Co_2FeGa nanoparticles. Wang *et al.* [79] employed X-ray absorption fine structure spectroscopy to examine the structure of non-stoichiometric Co_2FeGa nanoparticles in the absence of super-lattice reflections in the powder XRD patterns. Gellesch *et al.* [152,153] did not publish the XRD pattern of their Co_2FeGa nanoparticles for us to make a comparison. Xu *et al.* [81] could not distinguish (111) and (200) reflections in any of their non-stoichiometric Co_2FeGa nanoparticles. Nehla *et al.* [82] had to rely on Raman measurements to corelate with $L2_1$ ordering in the co-precipitated Co_2FeGa nanoparticles in the absence of (111) and (200) reflections in the XRD patterns. However, in the present case, not only weak (111) and (200) super-lattice reflections are visible in the powder XRD patterns, but the whole plethora of weak reflections such as (311), (222) and (420) (see Table 3.02) could be delineated in the experimental powder XRD pattern without any special arrangement or instrumentation. The enlarged view of the relevant regions of the XRD patterns in Figure 3.01(a) are shown in Figure 3.01(b, c and d) manifesting the presence of the characteristic reflections with weak intensities.

Table 3.01. Structural and morphological data and elemental composition of Co_2FeGa nanoparticles prepared under different heat treatment conditions.

Sample ID	Heat treatment conditions		a (Å)	χ^2	Structural order (%)		Measured composition Co:Fe:Ga (at.%)	D_v (nm)	d (nm)
	Temp. (°C)	Time (h)			S_{B2}	S_{L2_1}			
CFG-1	800	5	5.748	1.19	96	84	49.2:25.9:24.9	57 ± 1	66 ± 1
CFG-2	900	1	5.751	1.43	96	79	49.1:25.9:25.0	47 ± 1	64 ± 1
CFG-3	850	1	5.760	1.27	96	90	49.0:25.2:25.8	39 ± 1	62 ± 1

The low values of χ^2 exemplify the Rietveld refinement based on $L2_1$ unit cell as depicted in Figure 3.01(e, f and g) validates the presence of high $L2_1$ ordering in the synthesized Heusler alloy nanoparticles. The degree of *B2* and $L2_1$ ordering defined as S_{B2} and S_{L2_1} [13], respectively, have been estimated in the three synthesized nanoparticles using the equations 1.01 and 1.02 and listed in Table 3.01. High values of S_{B2} (= 0.96) and S_{L2_1} (= 0.84, 0.79 and

0.90) indicate the presence of very small amount (≈ 0.04) of *B2* disorder along with small deviations (≈ 0.16, 0.21 and 0.10) from $L2_1$ ordering. These confirm the formation of Co_2FeGa nanoparticles with high degree of $L2_1$ ordering.

Table 3.02. Interplanar spacing d_{hkl} and normalized intensities of experimental and simulated XRD patterns for $L2_1$ type full Heusler alloy structure of CFG-1, CFG-2 and CFG-3 samples.

Reflection planes (*hkl*)	d_{hkl} (Å)	Normalized intensity of reflections			
		simulated	CFG-1	CFG-2	CFG-3
(111)	3.32	1.10	0.8	0.7	0.9
(200)	2.87	0.87	0.8	0.8	0.8
(220)	2.03	100.00	100.0	100.0	100.0
(311)	1.73	0.70	0.6	0.5	0.5
(222)	1.66	0.33	0.6	0.7	0.5
(400)	1.44	14.54	11.1	8.5	10.8
(331)	1.32	0.33	0.4	-	-
(420)	1.29	0.52	0.7	0.7	0.6
(422)	1.17	27.40	19.2	16.7	17.2
(333)	1.11	0.07	-	-	-
(511)	1.11	0.21	-	-	-

FETEM studies provided further confirmation of the fully ordered $L2_1$ type stable Heusler alloy structure in CFG-1, CFG-2 and CFG-3 nanoparticles. Figure 3.02(a) shows a typical SAED pattern indicating the presence of reflections from the planes (111), (200), (220), (400), (420) and (422) from CFG-1. Figure 3.02(b, c) shows the lattice fringes corresponding to the super-lattice planes (111) and (200) captured by HRTEM and their iFFT images. Presence of both the super-lattice reflections in SAED pattern and the HRTEM images validate the $L2_1$ ordered structure in the nanoparticles.

Reported experimental and predicted theoretical values of the lattice constant *a* of Co_2FeGa nanoparticles lie in range from 5.70 Å to 5.7615 Å [23,37,117,119,124,125,128,134,138,139,142,143,58,145,147–149,80–82,106,114–116]. *a* values extracted from Rietveld analysis and listed in Table 3.01 are all well within this range. The Schërrer's equation (equation 2.18) was used to calculate the D_v of the nanoparticles as

listed in Table 3.01. It can be seen that D_v of the nanoparticles is dependent on the heat treatment condition. In samples CFG-2 and CFG-3, where the heat treatment time was the same (*i.e.*, 1 h), D_v increased upon increasing the heat treatment temperature. On the other hand, the heat treatment temperature used for samples CFG-2 and CFG-3 was higher than that of sample CFG-1. However, the higher heat treatment time (5 times higher) used for sample CFG-1 is responsible for the higher D_v of sample CFG-1 as compared to CFG-2 and CFG-3.

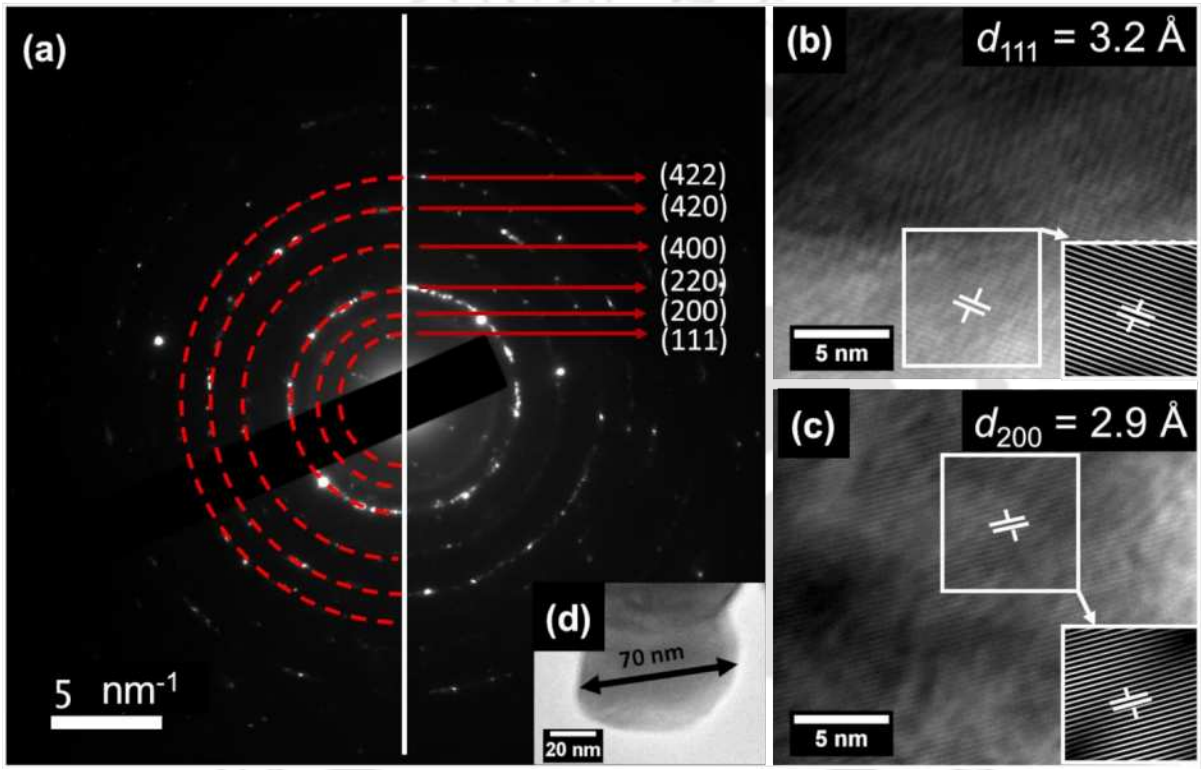

Figure 3.02. (a) SAED pattern and (b and c) HRTEM images of (111) and (200) planes of CFG-1. (d) HRTEM image of CFG-1 nanoparticle. Insets in (b & c) represent the iFFT images of the respective lattice fringes.

3.3 Elemental composition and morphology

The EDS data listed in Table 3.01 confirms that the overall composition of the nanoparticles is close to the desired stoichiometric value of 50 at. % Co, 25 at. % Fe and 25 at. % Ga. It may be noted that the overall composition of the three sets of nanoparticles is nearly the same which

indicates that it is possible to vary D_v of the nanoparticles without disturbing the chemical stoichiometry by this procedure.

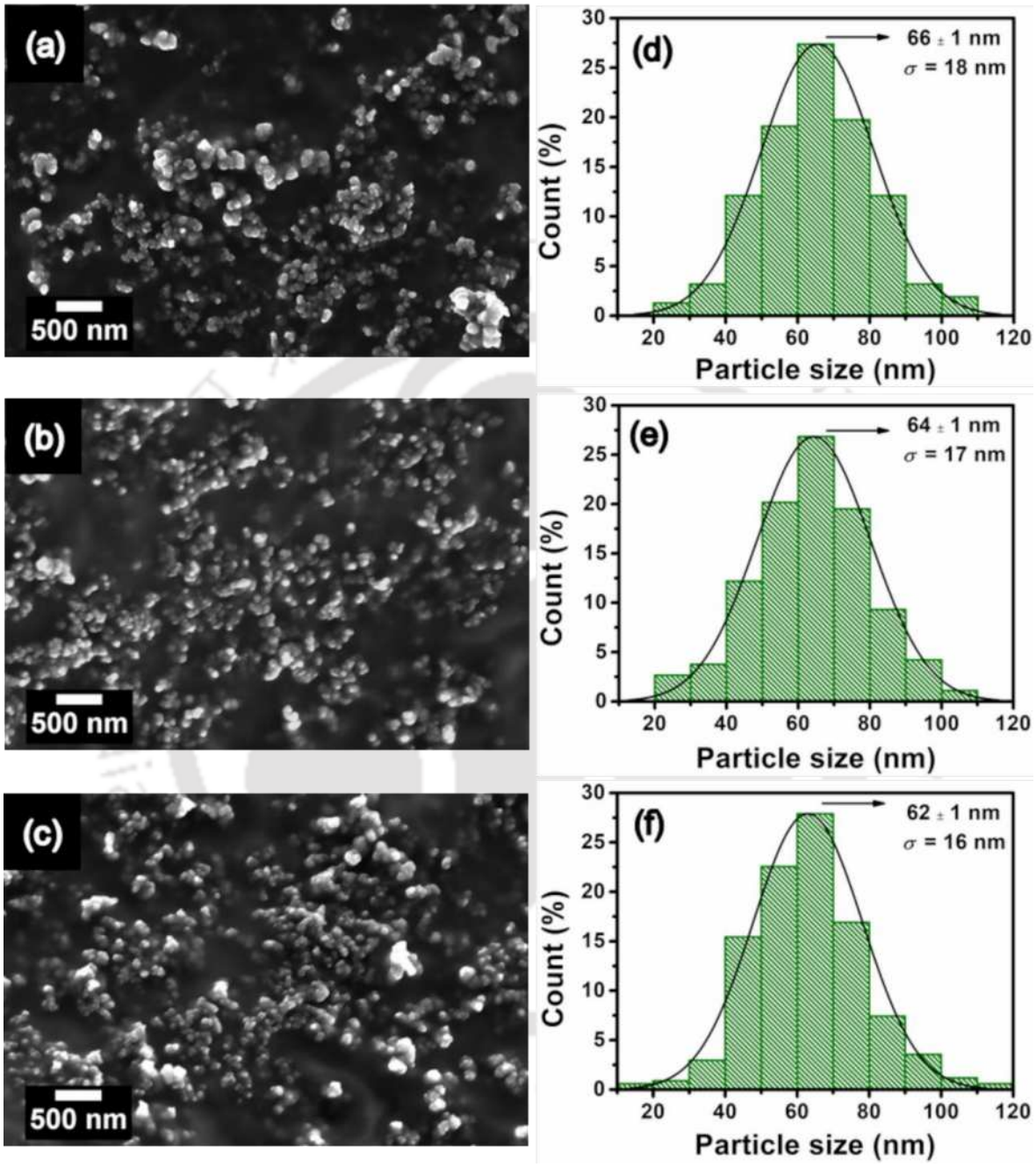

Figure 3.03. FESEM images of (a) CFG-1, (b) CFG-2 and (c) CFG-3 nanoparticles. (d-f) Particle size distribution of nanoparticles in micrographs shown on the left side.

The micrographs displaying the morphology of the nanoparticles and their size distributions are shown in Figure 3.03(a, b, c) and Figure 3.03(d, e, f) respectively. FESEM

images show some agglomeration of particles, which is expected in highly magnetic nanoparticles [44]. The histograms show that *d* ranges from 10 to 120 nm with the average value of *d* listed in Table 3.01. The value of σ was found to decrease with a decrease in *d* (see Figure 3.03). The slightly higher σ in the particle size distribution is expected since no template was used during the synthesis. In the previous reports on Co_2FeGa nanoparticles, Wang *et al.* obtained σ as low as 5.3 nm [80] and 9.3 nm [84]. However, some template-assisted methods have also resulted in higher σ such as 47.3 nm in the case of Co_2FeGa nanoparticles [58].

3.4 DOS calculations

Since Co-based Heusler alloys are generally expected to be half metallic, the half metallic characteristics of Co_2FeGa Heusler alloy was explored, especially since the earlier reports on this alloy are not consistent. On one side, some reports [114,115,117,124] declared that Co_2FeGa is not half metallic, whereas, a few reports claimed that the compound has high *P* of 98 % [125], 96.89 % [135] and 90 % [138], which is a signature of half metallicity. Gao *et al.* [130] claimed pressure induced tunability of half metallicity in this alloy. Deka *et al.* [145] declared bulk Co_2FeGa to be an half metal by an indirect method, *i.e.*, by showing its Rhodes-Wohlfarth ratio is less than unity. In order to resolve this disparity among earlier reports, *ab initio* calculations were performed using Rietveld refined lattice constant values. Figure 3.04 shows the TDOS along with the PDOS for the three constituent elements for Co_2FeGa alloy. In the DOS plots, the valence band of Co_2FeGa has contributions from both the minority and majority spins, whereas the conduction band has major contributions only from minority spins. In the plot shown in Figure 3.04(a), a pseudo gap can be found near E_F. Previous reports on Co_2FeGa [113,114,128,130,131,138,115–117,119,120,123,125,127] also showed such a pseudo gap in the minority DOS near E_F. Özdogan *et al.* [120] pointed out the possibility to tune this pseudo gap near E_F by introducing the Hubbard parameter (U) which accounts for Coulomb interactions in such systems with strong electron correlations, which was not

considered in earlier studies. Kandpal *et al.* [106] introduced U for the first time in the DOS calculations of Co_2FeGa alloys and found that the introduction of U did not destroy or construct half metallicity, but merely expanded, reduced or shifted the existing gap. Kandpal *et al.* [106], following the suggestion of Coey *et al.* [155], classified some Co based Heusler alloys in which the electron spins in one spin direction are localized while those on the other spin direction are of itinerant type, as Type III half metals [106,155]. Thus, in Type III half metals, the bandgap appears in the minority states but at a shifted energy value from E_F [122]. Appearance of a bandgap at a slightly shifted position from E_F imposes a small DOS in the minority spin band, resulting in a decrement in the spin polarization. Therefore, Type III half metals will generally exhibit lower spin polarization [106]. Balke *et al.* [122] categorized Co_2FeGa as Type III half metal through DOS calculations. Kumar *et al.* [123] also obtained similar DOS as Kandpal *et al.* [106] and validated type III half metallicity in Co_2FeGa. In order to understand this novel type of half metallicity in Co_2FeGa, we performed *ab initio* calculations by introducing U values ranging from 0 to 2 eV in increments of 0.5 eV. It was observed that on increasing U from 0.0 to 0.5 eV, this pseudo gap started to diminish and for U ≥ 1.0 eV, the pseudo gap became a physical gap. The presence of E_F at the edge of this gap justified its classification as a Type III half metal as suggested by Balke *et al.* [122].

Table 3.03. Atomic magnetic moments and properties of the electronic states of Co_2FeGa Heusler alloys for different Hubbard parameter (U) values.

U (eV)	M_t (μ_B)	M_{Co} (μ_B)	M_{Fe} (μ_B)	M_{Ga} (μ_B)	$D\uparrow$ (at E_F)	$D\downarrow$ (at E_F)	P % (at E_F)	Gap type near E_F
0.0	5.041	1.176	2.792	- 0.103	3.65	-0.78	65	Pseudo gap
0.5	5.107	1.183	2.860	- 0.120	3.49	-1.22	48	Pseudo gap
1.0	5.187	1.198	2.927	- 0.136	3.36	-1.77	31	Bandgap
1.5	5.280	1.219	2.994	- 0.151	3.23	-3.21	0	Bandgap
2.0	5.307	1.247	2.991	- 0.178	3.02	-10.16	54	Bandgap

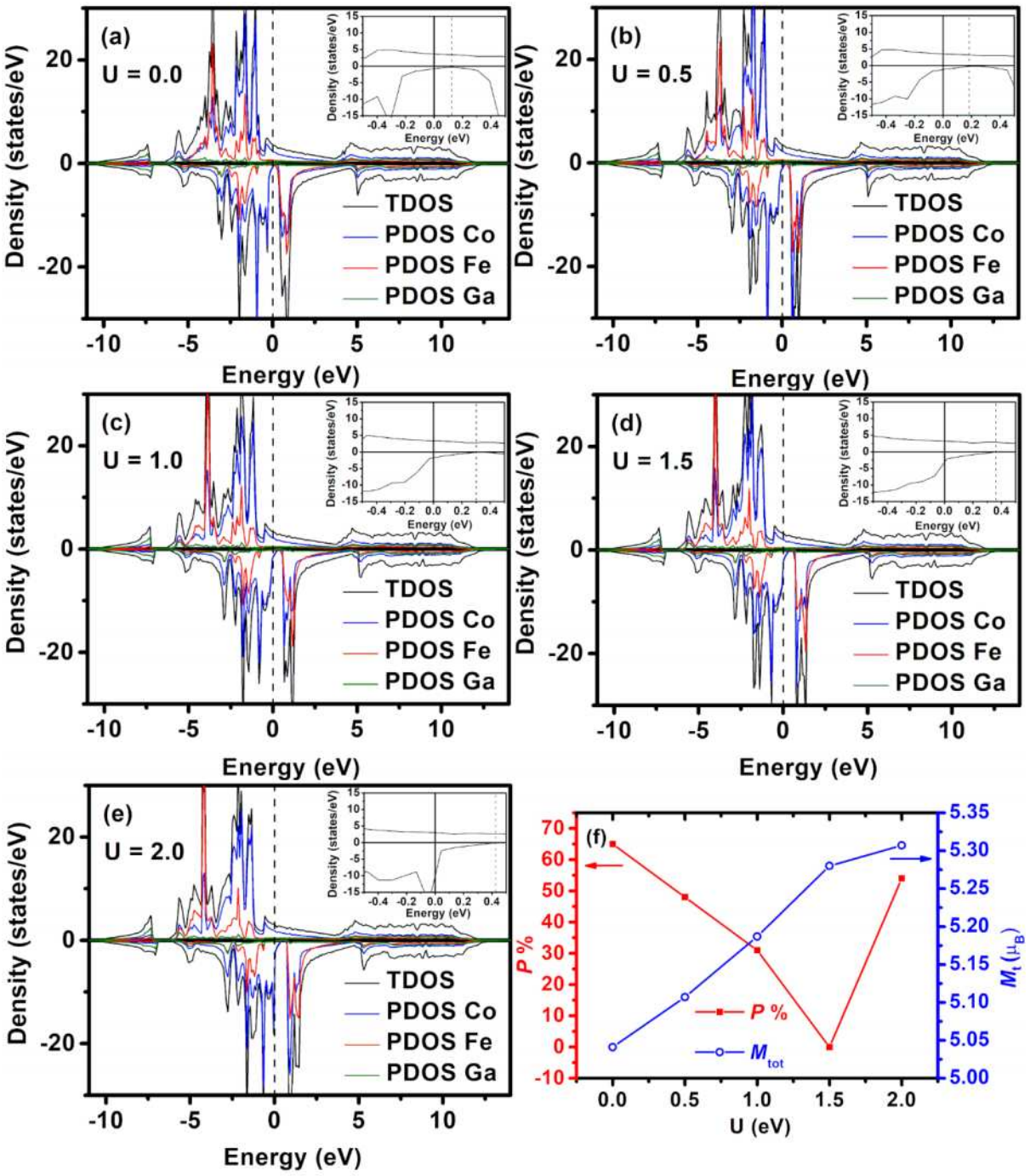

Figure 3.04. TDOS and PDOS of Co, Fe and Ga calculated using (a) U = 0 eV, (b) U = 0.5 eV, (c) U = 1.0 eV, (d) U = 1.5 eV and (e) U = 2.0 eV. (f) Variation of P and M_t with U.

P of 65 % was obtained for Co_2FeGa from these calculations. On introducing U, $D\uparrow$ started to decrease, whereas $D\downarrow$ started to increase. This resulted in a decrement in P for U values up to 1.5 eV, after which P increased. Thus, P is strongly influenced by the Coulombic interactions in this compound. Various P values for Co_2FeGa ranging from 20 % to 98 % have

been reported based on *ab initio* calculations and point contact Andreev reflection (PCAR) studies. Tsunekawa *et al.* [131] approximated *P* to be ~20 % using coherent-potential approximation by Korringa-Kohn-Rostoker method, Umetsu *et al.* [116] found 37 % of *P* using atomic sphere approximation by the linear muffin-tin orbital method, Sargolzaei *et al.* [118] obtained 41-43 % *P* using local spin density approximation in full potential local orbital minimum basis band structure method, Kobayashi *et al.* [141] estimated about 50 % of *P* by linear interpolation from previous reports. Gao *et al.* [130] evaluated *P* ranging 24.84 - 56.41 % using CASTEP code in DFT at different pressure values, Zhang *et al.* [115] and Varaprasad *et al.* [117] achieved 59 % of *P* using PCAR measurements. Kumar *et al.* [123], Ram *et al.* [129], Hussain *et al.* [138], Oumsalem *et al.* [135] obtained *P* values of 51.1 %, 72.44 %, 90 %, 96.89 %, respectively, using GGA by full potential linearized augmented plane wave method having different *k* point sets and other parameters, Ahmadian *et al.* [125] found *P* = 98 % using GGA in augmented plane wave plus local orbital method. It is also relevant to mention that Galdun *et al.* [156] observed that *P* estimated using PCAR technique in Co_2FeSn nanowires was higher than that of bulk Co_2FeSn. This prompted the authors to claim that it is possible to obtain high *P* when the bulk or 3-dimensional alloy is reduced to 1-dimensional nanowire form. Hussain *et al.* [138] also observed a variation in *P* on the surface of Co_2FeGa alloy. Therefore, there is a strong possibility for the synthesized 0-dimensional Co_2FeGa nanoparticles to have higher *P* than the one estimated for the bulk alloy using *ab initio* calculations.

3.5 Magnetic properties

The calculated values of the M_t and element-specific magnetic moment for Co_2FeGa with U = 0 eV is M_t = 5.04 μ_B/f.u. with corresponding magnetic moment of Co, Fe and Ga being M_{Co} = 1.176 μ_B/f.u., M_{Fe} = 2.792 μ_B/f.u. and M_{Ga} = -0.104 μ_B/f.u. These are close to reported values of M_t = 5.00 to 5.07 μ_B/f.u., M_{Co} = 1.142 to 1.210 μ_B/f.u., M_{Fe} = 2.660 to 2.910 μ_B/f.u. and M_{Ga}

= -0.0267 to -0.095 μ_B/f.u. [106,113,126,129,132,134,135,114–116,118–120,123,124]. On introducing U, the Coulomb interaction plays a significant role since each Fe and Ga atom is surrounded by eight Co atoms in their neighbourhood. It can be noticed that the magnitudes of both M_{Co} and M_t increase with an increase in U as listed in Table 3.03. On the other hand, the magnitude of M_{Fe} increases till U = 1.5 eV and then starts to decrease. The calculated results for all the U values and the previous reports show that moment of Co atom is smaller than that of Fe atom. Also, the magnetic moment of the Co atom in the two different Wyckoff positions is the same due to the identical environments of both the Co atoms, *i.e.*, surrounded by 4 Fe and 4 Ga atoms [157]. A weak and anti-parallel magnetic moment is induced in Ga due to the presence of strongly magnetic Co and Fe atoms as neighbours [157]. Therefore, any increment in the magnitude of M_{Co} and M_{Fe} on increasing U results in a weak increment in the magnitude of M_{Ga} as well. Such magnetic behaviour was observed in the case of Sn in Co_2FeSn alloys by Pathak *et al.* [158].

Figure 3.05(a and b) show *M-H* loops recorded for the three sets of Co_2FeGa nanoparticles at temperatures 5 K and 300 K, respectively. For both the temperatures, all the nanoparticles show soft magnetic behaviour in line with the previous reports on Co_2FeGa single crystal [146], thin film [147–150], nanowires [81] and nanoparticles [82]. The obtained values of M_s for Co_2FeGa nanoparticles are listed in Table 3.04. Previously reported theoretical values range from 3.25-5.10 μ_B/f.u. [106,113,126–130,132–135,114–116,118–120,123,124] and the experimental value for bulk Co_2FeGa range from 4.72-5.19 μ_B/f.u. [37,106,145,146,112,114–116,133,139,140,143]. Reported M_s for low dimensional Co_2FeGa ranges from 2.68-4.49 μ_B/f.u. [147–149] for thin films, 3.8 μ_B/f.u. [45] for nanowires and 0.6-6.3 μ_B/f.u. [58,82,152] for nanoparticles. Though it is not easy to compare the present values with the wide range of data in the literature, it is apparent that the present M_s values are in the higher range of the reported values. The obtained M_s values show good agreement with the expected S-P value of

M_t for half metallic Co_2FeGa alloy [12]. In the case of Co_2FeGa, Z_t = 29, which results M_t (= Z_t – 24) of 5 μ_B/f.u. The M_s values are influenced by the heat treatment conditions as also observed by Duan *et al*. [78], Yang *et al.* [76,77], Alikhanzadeh-Arani *et al.* [73] and Huynh *et al.* [70] for Co_2FeAl nanoparticles, who attributed this behaviour to increased crystallinity as a result of reduction in defects at elevated temperatures or for longer heating time. A decrease in M_s and H_c values with a decrease in D_v can be observed from the data shown in Figures 3.05 and 3.06. Alikhanzadeh-Arani *et al.* [73] and Pezeshki-Nejad *et al.* [71] showed that a decrease in D_v resulted in a decrease in M_s for Co_2FeAl nanoparticles, which is consistent with our findings. The core-shell model [40] for the nanoparticles can be used to explain the decrement in M_s with a decrease in D_v. The thickness t of the magnetically dead shell of on their surface, was determined using equation 1.13 by substituting $M_s(b)$ = 5.041 μ_B/f.u. (as estimated by *ab initio* calculations), D_v of the nanoparticles in the place of d and M_s of nanoparticles of size D_v in the place of $M_s(d)$. The calculated values of t were found to increase with a decrease in D_v as listed in Table 3.04, which indicates that the origin of reduction in M_s at lower D_v is the appearance of a magnetically dead layer on the surface. This shows that the variation of M_s with D_v can be explained by the core-shell model. The near zero values of H_c and M_r and the variation of H_c with D_v substantiates that the nanoparticles are in the single (magnetic) domain regime [41]. The reason for this decrease in H_c with D_v in single domain regime has already been explained in chapter 1 using Stoner-Wohlfarth approach [40]. Additionally, the near zero H_c and M_r values of the nanoparticles listed in Table 3.04 indicate that the single domain nanoparticles are superparamagnetic in nature [41]. Further, it was also found that the M_s decreases slightly but systematically at higher temperatures as listed in Table 3.04. Previous reports on Co_2FeGa nanoparticles [80,152] as well as on other Heusler alloy nanoparticles [59,67,69,83,85] show a similar variation in M_s with temperature, indicating that the produced nanoparticles obey Bloch's equation for temperature dependent M_s [70].

Interestingly, at elevated temperatures, the decrease in M_s is very small (*i.e.*, <1%) (see Table 3.04), making these nanoparticles ideal for room temperature device applications. The high value of T_C of this Co_2FeGa alloy is also a result of this nearly temperature-independent M_s, which is indicative of strong ferromagnetic interaction in these nanoparticles [152]. These nanoparticles are also suitable for applications such as magnetic field-driven sensors and ultrahigh density magnetic recording due to their high M_s and low H_c [152].

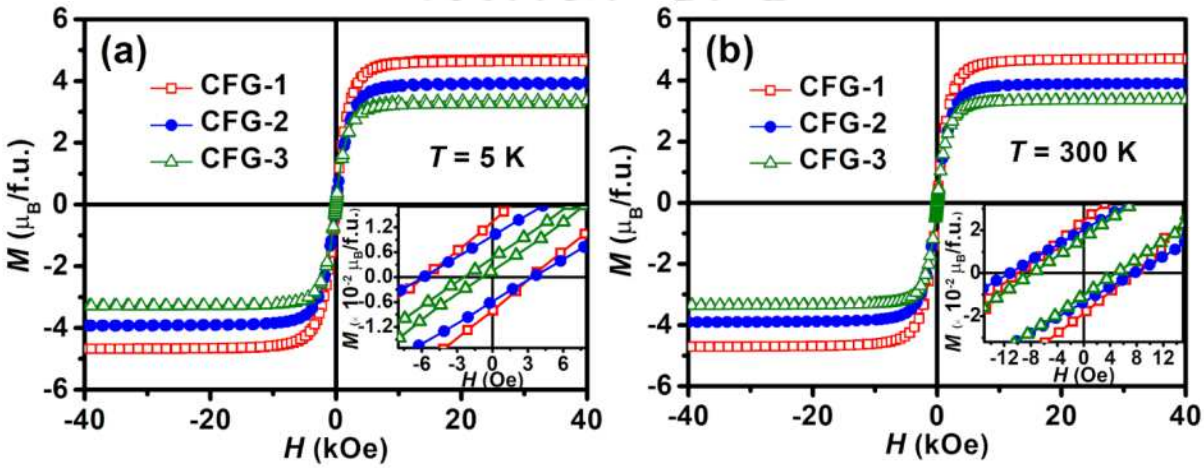

Figure 3.05. *M-H* loops recorded at temperature (a) 5 K and (b) 300 K for Co_2FeGa nanoparticles. The insets in figures provide an expanded view of the data near the origin.

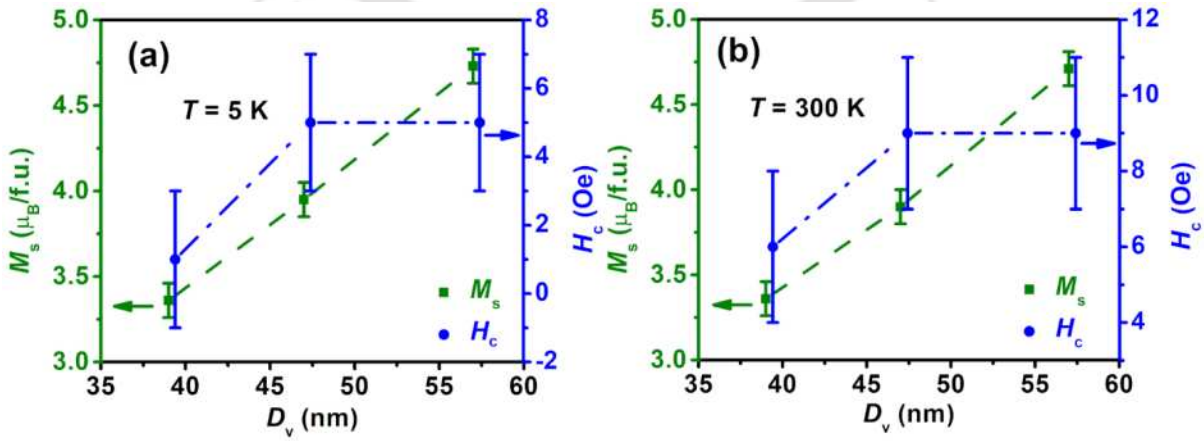

Figure 3.06. Variation of M_s and H_c with D_v at (a) 5 K and (b) 300 K.

Table 3.04. Magnetic properties of the three Co_2FeGa Heusler alloy nanoparticles.

Sample ID	M_s (μ_B/f.u.)			H_c (Oe) measured at		M_r (μ_B/f.u.) measured at		$K_{eff} \times 10^6$ (erg/cc)		t (nm)		T_C (K)
	S-P value	Measured at 5 K	Measured at 300 K	5 K	300 K	5 K	300 K	5 K	300 K	5 K	300 K	
CFG-1	4.99	4.73±0.08	4.71±0.08	5±2	9±2	0.01	0.02	4.87	4.79	0.58	0.62	1137±2
CFG-2	4.96	3.95±0.07	3.90±0.07	5±2	9±2	0.01	0.02	4.03	3.84	1.70	1.77	1137±2
CFG-3	4.80	3.36±0.08	3.36±0.08	1±2	6±2	0.00	0.01	3.17	2.93	2.17	2.17	1131±2

K_{eff} estimated using the LAS method [145] are listed in Table 3.04. The table shows that K_{eff} of all the Co_2FeGa nanoparticles are comparable with the reported K_{eff} values for Co_2FeGa in bulk (= 6.54×10^5 J/m^3) [145], thin film (= 5.3×10^3 J/m^3) [147], nanowires (= 1.02×10^6 J/m^3) [81] and nanoparticles (= $2.99 - 9.0 \times 10^5$ J/m^3) [81,82] forms. Such high values of K_{eff} of the nanoparticles can be attributed to (a) breaking of surface bonds due to high surface area /volume ratio [40,45,46], (b) high interparticle interaction due to agglomeration of magnetic nanoparticles [44], (c) dipole-dipole interaction between the single domain nanoparticles [40]. Heusler alloys with high K_{eff} values have already been identified for use in ultra-high density magnetic recording media [159]. Furthermore, K_{eff} is found to decrease with a decrease in D_v. Similar behaviour of K_{eff} has been reported for cobalt nanoparticles [160] and single domain nickel ferrite nanoparticles [40]. A decrement in H_c and K_{eff} is expected at higher temperatures due to thermal energy disrupting the magnetic alignment and making it easier for the domains to change their orientation. Table 3.04 shows that K_{eff} decreases with increase in temperature, whereas the same is not evident in the temperature dependence of H_c. Though it is clear that H_c values are very low in all the samples, it has to be pointed out that the high field (9T) PPMS based VSM is not sensitive enough to measure very low H_c (< 10 Oe). Hence, it is difficult to establish any trend confidently in $H_c(T)$ data.

The linear variation of ΔE with $\langle V \rangle$ as depicted in Figure 3.07 shows the dominance of K_v over the insignificant K_s, which follows Néel-Brown thermally activated model [42], explained in chapter 1 and indicates that in our case $K_{eff} \approx K_v$ [42]. It should be emphasised that

this linear behaviour is associated with the typical H_c behaviour of single domain nanoparticles [42].

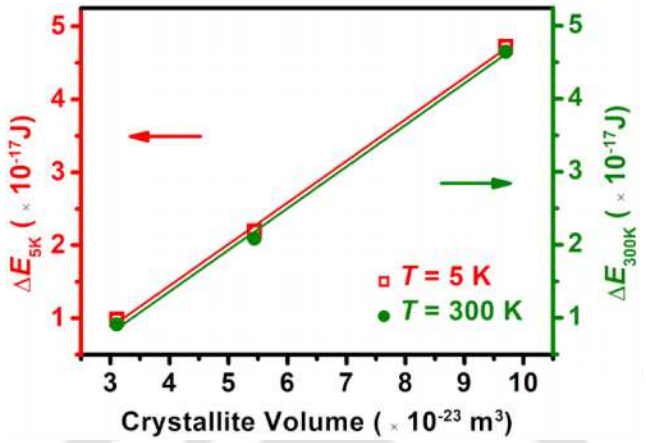

Figure 3.07. Variation of ΔE with crystallite volume for Co_2FeGa nanoparticles at 5 K and 300 K. The solid lines represent linear fits to the respective experimental data.

The *M-T* curves recorded under an applied field of 100 Oe for Co_2FeGa nanoparticles are shown in Figure 3.08(a) with the normalized magnetization value M/M_{1050} along y-axis. Here, M represents the magnetization at temperature T and M_{1050} is the magnetization at 1050 K. The *M-T* curves reveal high values of T_C for the synthesized Co_2FeGa nanoparticles. The literature provides T_C values ranging from 1056 to 1100 K [23,116,117,121,136,139,140,145] for the bulk, 844 to1117 K [147–149] for thin films and 850 to 1317 K [133,137] as theoretical estimates for bulk Co_2FeGa alloy. The T_C values obtained for the synthesized Co_2FeGa nanoparticles are higher than those of bulk and thin films of Co_2FeGa which can be due to the stronger magnetic ordering resulting from enhanced structure ordering and crystallinity in the synthesised Co_2FeGa nanoparticles. Figure 3.08(b) depicts an increase in T_C with D_v which is a common behaviour observed in other Heusler alloy nanoparticles too [161]. It should be mentioned that Mazo-Zuluaga *et al.* [52] ascribed the decrease in T_C with decrease in size to its symmetry loss, whereas Chhabra *et al.* [53] employed a bond and energy based theoretical

model to explain the size dependent magnetic characteristics of the magnetic nanoparticles which is already explained in chapter 1.

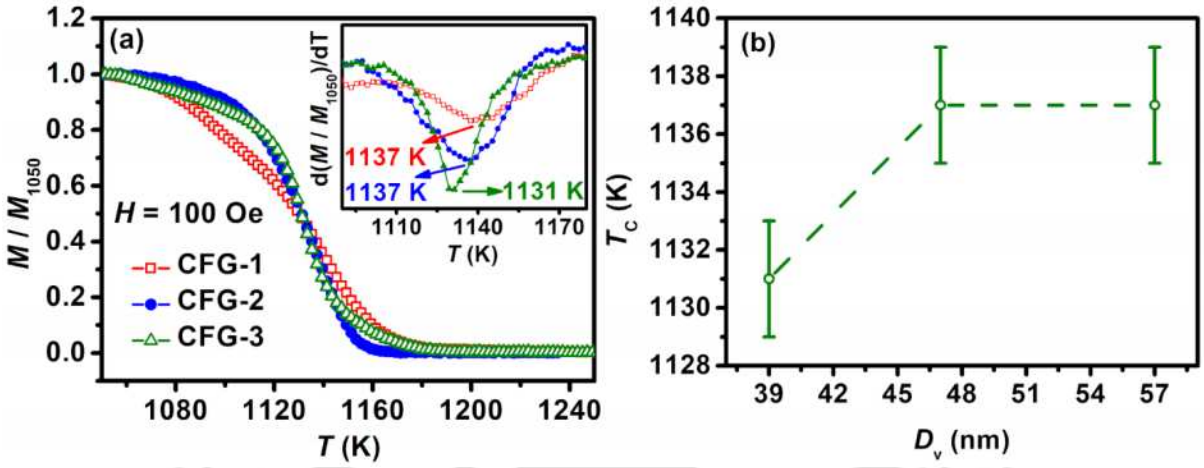

Figure 3.08. (a) *M-T* curves recorded at 100 Oe field with the inset representing the temperature derivative of magnetization and (b) D_v dependent T_C of Co_2FeGa nanoparticles.

The *Q* factor [42,43] calculated for all the three Co_2FeGa nanoparticles using equation 1.22 is > 0.9. Hence, the synthesized nanoparticles are categorized as high anisotropic materials.

Temperature dependent M_s for the largest size sample CFG-1 was recorded in the lower temperature regime as proposed in a previous report [49]. The values of slope *B* from Figure 3.09 and values of *A* and *D* calculated using equations 1.24-1.26 were found to be 1.54×10^{-5}, 4.58×10^{-7} erg/cm, 4.55×10^{-29} erg/cm^2, respectively. The calculated value of *D* is comparable to reported values for Co_2FeGa Heusler alloy which range from $1.81–8.39 \times 10^{-29}$ erg/cm^2 [50,115,148], which validates our calculations. The value of D_{cr} [47,162] calculated using equation 1.23 was found to be 100 nm for Co_2FeGa alloy. The comparison of D_v (see Table 3.01) with the calculated values of D_{cr} clearly shows the obtained D_v are lower than the single domain to multidomain critical size which confirms the formation of single domain Co_2FeGa nanoparticles.

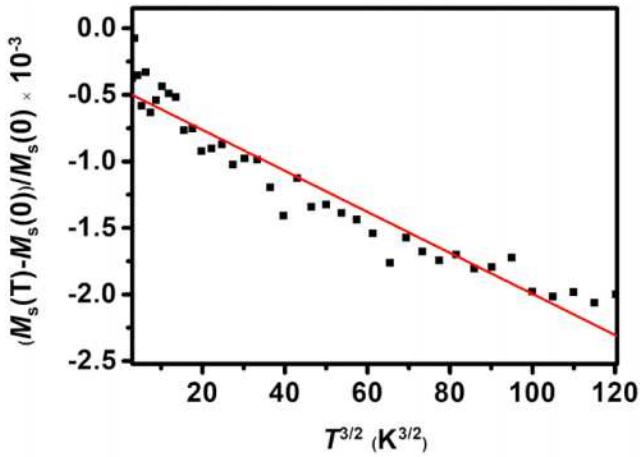

Figure 3.09. $(M_s(T)-M_s(0)) / M_s(0)$ *versus* $T^{3/2}$ plot at 2 T field for CFG-1 nanoparticles.

3.6 Summary and Highlights

The experimental investigations on crystallite size dependent properties of Co_2FeGa nanoparticles supported by theoretical calculations provide the following insights:

- An impurity-free and simple template-free method was used to synthesize single phase Co_2FeGa Heusler alloy nanoparticles with three different D_v. The control on D_v was achieved by merely altering heat treatment conditions during the preparation.
- Structural and compositional analyses established stable and highly order $L2_1$ type full Heusler alloy structure in Co_2FeGa nanoparticles with D_v of 57 nm, 47 nm and 39 nm and near stoichiometric composition.
- DOS calculations revealed the role of electron interactions and the occurrence of Type III half metallicity in this alloy.
- All these nanoparticles exhibit soft ferromagnetic nature with high M_s, low H_c (<10 Oe) and high T_C (>1100 K). The variation of M_s, K_{eff}, H_c and T_C as a function of D_v has been interpreted using standard theoretical models.
- Formation of single domain nanoparticles has been confirmed by estimating D_{cr} of this alloy and from the variation of H_c with D_v. Superparamagnetic nature of these nanoparticles has been ascertained from their near zero H_c and M_r values. The nearly constant (and high)

M_s from 5 K to T_C of these soft ferromagnetic nanoparticles can be exploited for high temperature device applications.

- These superparamagnetic Co_2FeGa nanoparticles are also well suited for use as magnetic field-driven sensors and ultra-high density magnetic recording media due to their high M_s, high K_{eff}, high T_C and low H_c.
- Apart from demonstrating a simple methodology for the synthesis of superparamagnetic Co_2FeGa nanoparticles in a variety of sizes, this study also highlights their potential applications in nanomagnetic devices due to their exceptional magnetic properties.

Chapter 4

Crystallite size dependent properties of Fe_2CoGa nanoparticles

After the assessment of crystallite size dependent properties of a Co rich Heusler alloy (Co_2FeGa) nanoparticles in chapter 3, it was natural to explore the crystallite size dependent properties of an Fe rich compound. Therefore, the focus of this work was on crystallite size dependent properties of Fe_2CoGa nanoparticles. Among all Heusler compounds, Fe_2CoGa occupies a special place due to its high M_s [37,119,132,134,163–166] and high T_C [23,121,164,165]. Surprisingly, Fe_2CoGa is a less explored material both in theoretical and experimental fronts. The published reports on Fe_2CoGa alloys are mostly of theoretical/computational [119,132,134,163–166] nature and the few experimental studies on the bulk form [23,37,167] provide a limited amount of information on its crystal structure and magnetic nature. There is only one report by Wang *et al.* [59] on the synthesis of Fe_2CoGa nanoparticles using silica assisted chemical method. However, their samples contained Fe precipitates as well as the silica template impurities. Thus, the preparation of impurity free Fe_2CoGa nanoparticles with controlled crystallite size remains a challenge to researchers. In this chapter, synthesis of single domain and phase pure Fe_2CoGa nanoparticles using a template-free chemical method and their size dependent structural and magnetic properties are presented. In addition, bulk Fe_2CoGa alloy has been prepared and characterized. *Ab initio* calculations have also been performed on Fe_2CoGa.

4.1 Sample preparation

The methodology already described in Figure 2.01 was used in the preparation of Fe_2CoGa nanoparticles designated as $S5_{800}$, $S3_{800}$, and $S5_{750}$. 1.2548 g of $Fe(NO_3)_3.9H_2O$, 0.3827 g of $CoCl_2.6H_2O$ and 1.2088 g of $Ga(NO_3)_3.8H_2O$ were taken as the metal precursors for to prepare Fe_2CoGa nanoparticles with the required stoichiometry. The as-synthesized powders were then heat treated at different conditions as listed in Table 4.01 to obtain as $S5_{800}$, $S3_{800}$, and $S5_{750}$ nanoparticles with different D_v. Bulk Fe_2CoGa alloy was also prepared by the arc melting method as described in chapter 2 for comparison.

4.2 Structural analysis

The XRD patterns of heat treated bulk Fe_2CoGa and Fe_2CoGa nanocrystalline powders are shown in Figure 4.01. The presence of strong reflections from the Heusler alloy planes (220), (400) and (422) can be observed in the figure. The absence of any impurity reflections in the XRD pattern confirms the formation of single phase Fe_2CoGa Heusler alloy in both nanoparticle and bulk forms. To ascertain the type of Heusler alloy structure formed, XRD patterns were simulated using CaRIne Crystallography 3.1 software using both ordered full Heusler alloy phase $L2_1$ and inverse Heusler alloy phase X type unit cells with the same elemental composition. Table 4.02 shows the relative intensities of the reflections of the experimental and simulated XRD patterns for both $L2_1$ and X type structures along with the d_{hkl} values calculated for each of the planes. Superlattice reflections (111) and (200) corresponding to $L2_1$ and X type unit cells are not discernible even in the simulated XRD patterns due to their very low intensities as compared to the other reflections. A careful look at Figure 4.01 shows that all the three strong XRD reflections in the experimental and simulated patterns exhibit the same relative intensity ratios. The very weak superlattice reflections in Fe_2CoGa can be attributed to the similar scattering factors for the elements belonging to the same horizontal row in the periodic table [154]. However, this observation does not help in clearly assigning

$L2_1$ or *X* type structure to the synthesized bulk and low dimensional Fe_2CoGa alloys due to the close similarity of both the simulated structures with the experimental one.

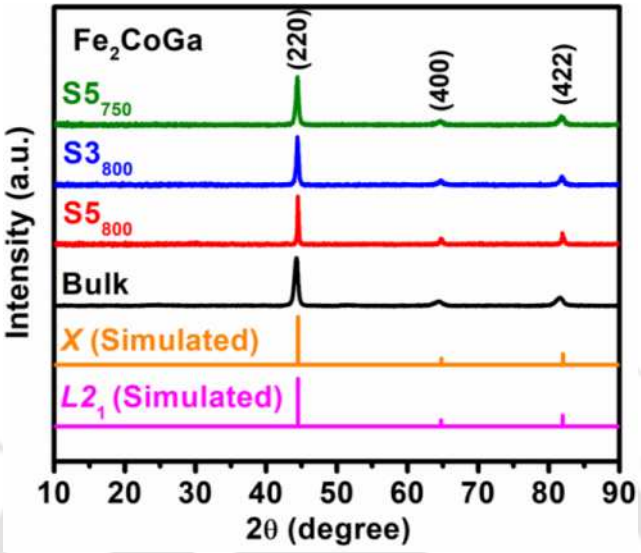

Figure 4.01. Experimental and simulated XRD patterns of synthesized Fe_2CoGa alloys.

Yin *et al.* [167] too faced such a challenge but they preferred to assign the *X* type inverse Heusler alloy structure for bulk Fe_2CoGa on the basis of the earlier report by Liu *et al.* [168]. Liu *et al.* established that an X_2YZ alloy in which the atomic number of Y is higher than the atomic number of X generally exhibits *X* type inverse Heusler alloy structure. Jaggi *et al.* [23] experimentally observed the inverse Heusler alloy structure in this alloy based on the site preferential and local environmental studies of the constituent atoms. Matsushita *et al.* [134] also suggested that Fe_2CoGa stabilizes in inverse Heusler alloy structure on the basis of their theoretical studies. Wang *et al.*[59] suggested that it is possible to identify various phases of this Heusler alloy nanoparticles by comparing the relative intensities of the (111)/(200) and (311)/(222) reflections in the experimental data. But in the case of Fe_2CoGa, the absence of (111) and (200) reflections due to their extremely low intensities creates uncertainty in determining the most appropriate crystal structure of the alloy formed.

Table 4.01. Structural data and elemental composition of bulk and nanocrystalline Fe_2CoGa.

Sample ID	Heat treatment condition		χ^2		a (Å)	D_v (nm)	Composition Fe:Co:Ga (at.%)	d (nm)
	Temp. (°C)	Time (h)	$L2_1$	X				
$S5_{800}$	800	5	2.72	2.64	5.755	56 ± 2	50:25:25	63 ± 2
$S3_{800}$	800	3	1.74	1.65	5.764	26 ± 1	49:26:25	58 ± 1
$S5_{750}$	750	5	1.79	1.76	5.766	21 ± 1	49:26:25	49 ± 1
Bulk	1000	24*	2.08	1.99	5.778	-	51:25:24	-

*Bulk sample was quenched in ice water after 24 hours of homogenization at 1000 °C.

Table 4.02. Normalized intensities of the XRD reflections in experimental and simulated patterns of Fe_2CoGa alloy.

Crystallographic plane (*hkl*)	d_{hkl} (Å)	Normalized intensity of reflections in					
		simulated XRD pattern for unit cell		experimental XRD pattern			
		$L2_1$	X	$S5_{800}$	$S3_{800}$	$S5_{750}$	Bulk
(111)	3.32	0.51	0.87	-	-	-	-
(200)	2.88	0.66	0.27	-	-	-	-
(220)	2.03	100	100	100	100	100	100
(311)	1.73	0.29	0.48	-	-	-	-
(222)	1.66	0.20	0.09	-	-	-	-
(400)	1.44	13.29	13.28	12	10	8	9
(331)	1.32	0.12	0.20	-	-	-	-
(420)	1.29	0.25	0.11	-	-	-	-
(422)	1.17	22.76	22.76	23	18	18	17
(333)	1.11	0.02	0.04	-	-	-	-
(511)	1.11	0.07	0.11	-	-	-	-

Rietveld refinement of the XRD patterns was performed for $L2_1$ type full Heusler alloy structure (space group 225 [$Fm\bar{3}m$]) and X type inverse Heusler alloy structure (space group 216 [$F\bar{4}3m$]) as shown in Figure 4.02. A slightly lower χ^2 value was obtained using space group 216 [$F\bar{4}3m$] as compared to space group 225 [$Fm\bar{3}m$] for all the samples (see Table 4.01). Though a smaller χ^2 indicates that the X type structure is the more probable structure for this alloy, it is not a conclusive proof for the same. The elemental composition analysis indicates that in this X_2YZ (Fe_2CoGa) alloy, Y(Co) has one atomic number higher than X(Fe). This small difference in atomic number Z might be the reason for the small difference in χ^2 between the X

type from $L2_1$ type structures in this alloy. In order to conclusively determine the stable structure, estimation of the total energy for both $L2_1$ and *X* type structures was carried out using *ab initio* calculations. Figure 4.03 shows that the energy *versus* volume graph for the *X* type structure is lower than that of the $L2_1$, confirming that the stable structure of this alloy is the inverse Heusler (or *X*) type structure. Previous total energy calculations performed on this compound by Gilleben *et al.* [163] and Dannenberg *et al.* [164,165] yielded similar conclusion.

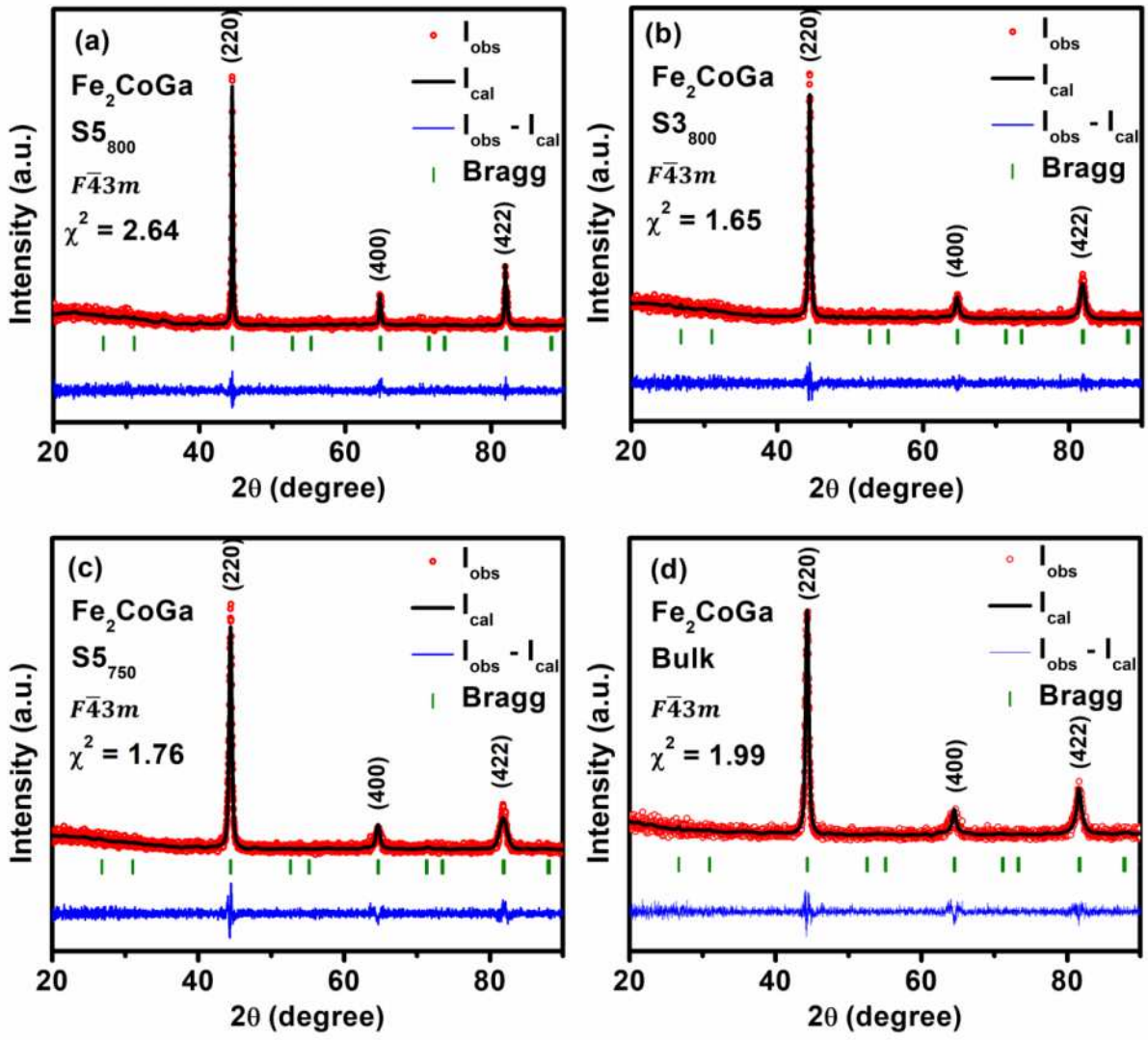

Figure 4.02. Rietveld refined XRD patterns of (a) $S5_{800}$, (b) $S3_{800}$, (c) $S5_{750}$ and (d) bulk Fe_2CoGa obtained using *X* type inverse Heusler alloy unit cell.

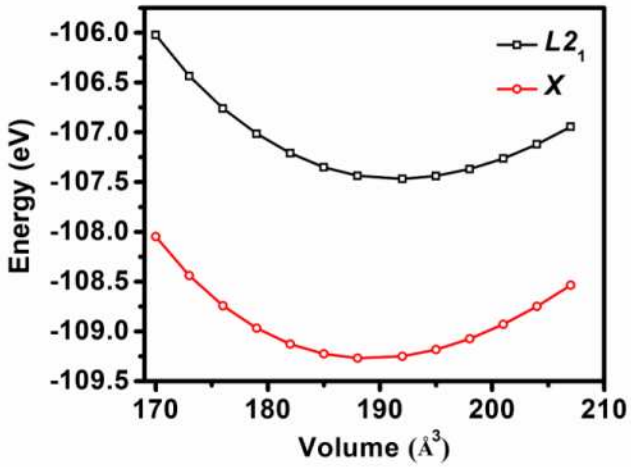

Figure 4.03. Energy *versus* volume plots of Fe_2CoGa obtained using $L2_1$ and *X* type unit cells.

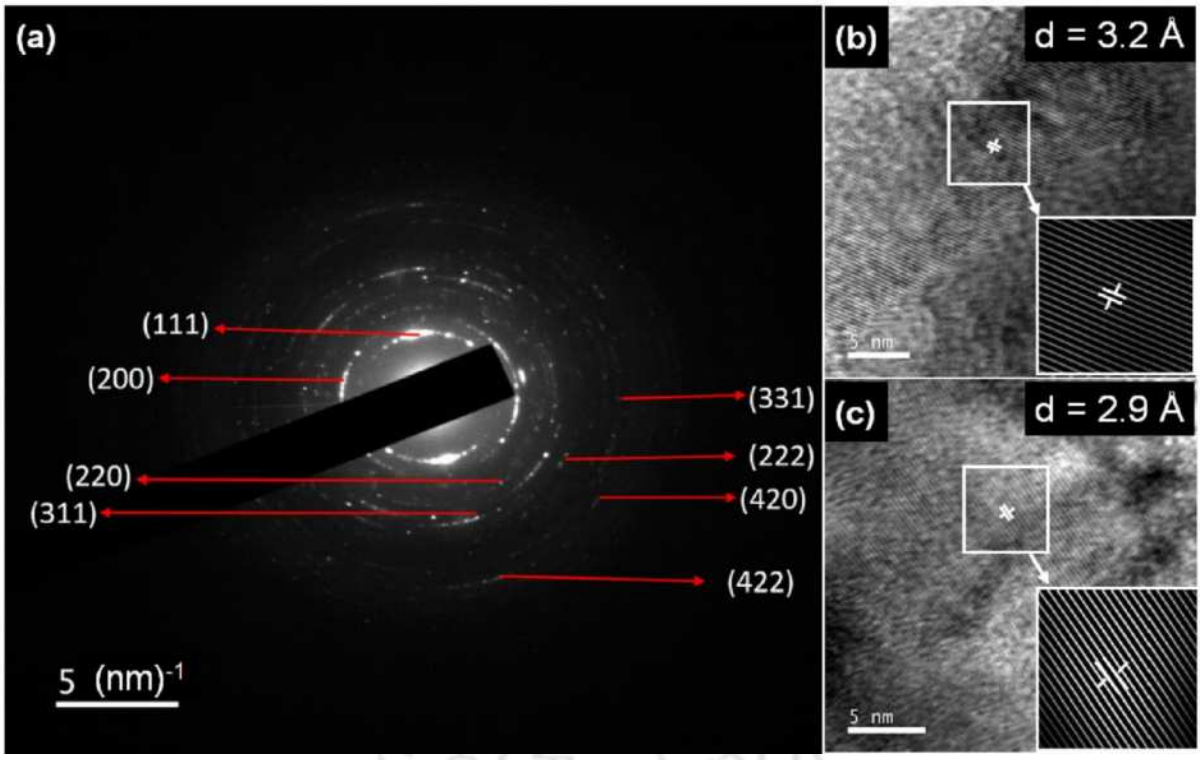

Figure 4.04. (a) SAED pattern and HRTEM images of (b) (111) and (c) (200) planes of $S5_{800}$. Insets in (b) and (c) show the iFFT images of the lattice fringes of the respective planes.

Interestingly, FETEM studies on the nanoparticles have yielded more conclusive experimental results. The SAED pattern of $S5_{800}$ shown in Figure 4.04(a) apart from revealing all the reflections observed in the XRD pattern also reveals additional weak reflections from (111), (200), (311), (222), (331) and (420) planes, that were beyond the sensitivity of powder

XRD technique. The presence of superlattice reflections (111) and (200) in the SAED image confirms the presence of the fully ordered (*X* type) crystal structure in the synthesized nanoparticles. The HRTEM image and its iFFT clearly show the lattice fringes corresponding to (111) and (200) planes as seen in Figure 4.04(b and c). These images further confirm the successful formation of single phase (*X* type) Fe_2CoGa nanoparticles. As already mentioned, the only other experimental report on Fe_2CoGa nanoparticles by Wang *et al.* [59], contained Fe precipitates and fumed silica residues. In contrast, our template-free method has yielded single phase Fe_2CoGa with stable *X* type structure without any observable impurity phase.

The lattice constant (*a*) of all the samples (see Table 4.02) obtained from Rietveld refinement is very close to previously reported values (which range from 5.727 Å to 5.812 Å [37,134,163–165,167].) Table 4.01 shows D_v of all the three nanoparticles estimated using the Schërrer's equation (equation 2.18). It can be seen that D_v decreases with a decrease in heat treatment temperature or time with hardly any change in the overall composition of the three samples. This shows that by merely changing the heat treatment temperature or time, it is possible to tune the crystallite size of these alloys without altering their composition.

4.3 Elemental composition and morphology

Overall composition (Fe:Co:Ga) of all the samples as estimated from the EDS data was found to be close to the stoichiometric composition of 50:25:25 (see Table 4.01). Elemental distribution maps recorded during the EDS analysis (not shown here) indicate good homogeneity in the distribution of the three elements within the nanoparticles. In FESEM images of the nanoparticles, some amount of agglomeration of crystallites was found which is expected in the case of highly magnetic nanoparticles [44]. Figure 4.05(a-c) show the micrographs of the three nanoparticle (0-d) samples. Figure 4.05(d-f) indicate the distribution of nanoparticles with particles sizes ranging from 20-120 nm with average *d* of 63 ± 2 nm, 58 ± 1 nm and 49 ± 1 nm for $S5_{800}$, $S3_{800}$ and $S5_{750}$, respectively. The σ values were 18 nm, 15 nm

and 13 nm for the samples $S5_{800}$, $S3_{800}$ and $S5_{750}$, respectively. As pointed out in the last chapter, σ values of these nanoparticles synthesized by the template-less method is slightly higher than those achieved in some template assisted methods. However, in view of the high phase purity and structural ordering in these samples, the slightly high σ values are acceptable.

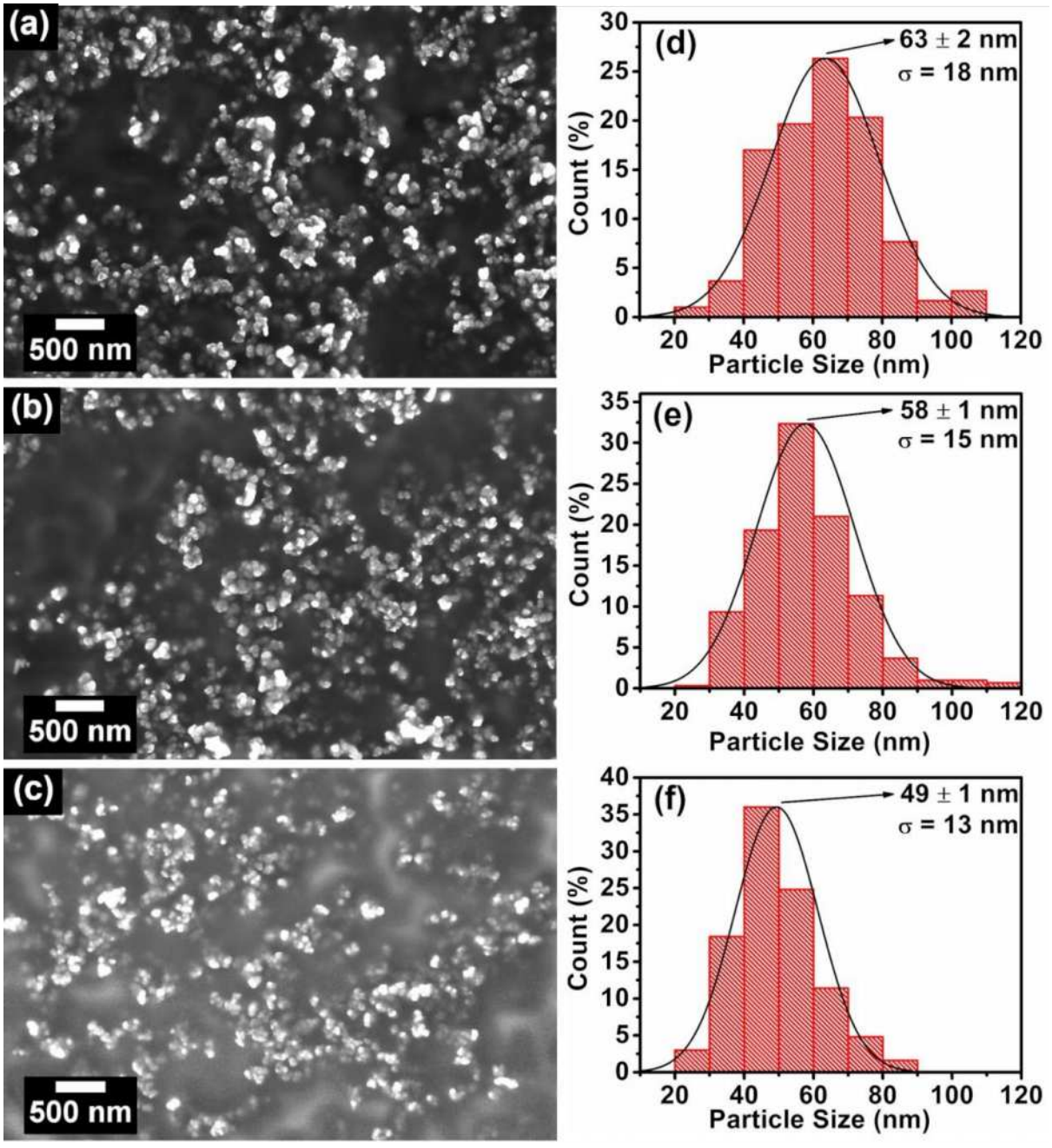

Figure 4.05. FESEM micrographs of (a) $S5_{800}$, (b) $S3_{800}$, and (c) $S5_{750}$ samples. (d-f) Particle size distribution of the nanoparticles whose corresponding image is shown in the left side.

4.4 DOS calculations

Ab initio calculations based on plane wave basis set and PAW methodology performed by Dannenberg *et al.* [165] showed that the total DOS of Fe_2CoGa with $L2_1$ and *X* type structures near the E_F did not show an energy gap in the minority band. However, *ab initio* calculations of Seema and Kumar [166] indicated an energy gap in the majority band of the DOS of Fe_2CoGa with $L2_1$ structure near E_F. In order to resolve this disparity in the published results, *ab initio* calculations were performed on Fe_2CoGa with both the structures as per protocol described in chapter 2. Figure 4.06 shows both the total DOS as well as atom-resolved partial DOS corresponding to the three elements for the $L2_1$ and *X* type structures near E_F. Our calculations agree with those of Dennenberg *et al.* [165] for both the $L2_1$ and *X* type of structures, thus clarifying that Fe_2CoGa with either $L2_1$ or *X* type structure is not completely half metallic. Additionally, our experimental findings also indicates the stable type of structure for Fe_2CoGa. The higher stability of the *X* type structure over the $L2_1$ type structure can also be visualized from the extremely lower DOS near E_F for the *X* type structure which makes it electronically more stable than the $L2_1$ type structure. We can also infer that in both the cases, Ga has very insignificant contribution to the conduction band states. For the stable *X* type structure, both Fe and Co have comparable contributions to the total DOS of the system in the vicinity of E_F.

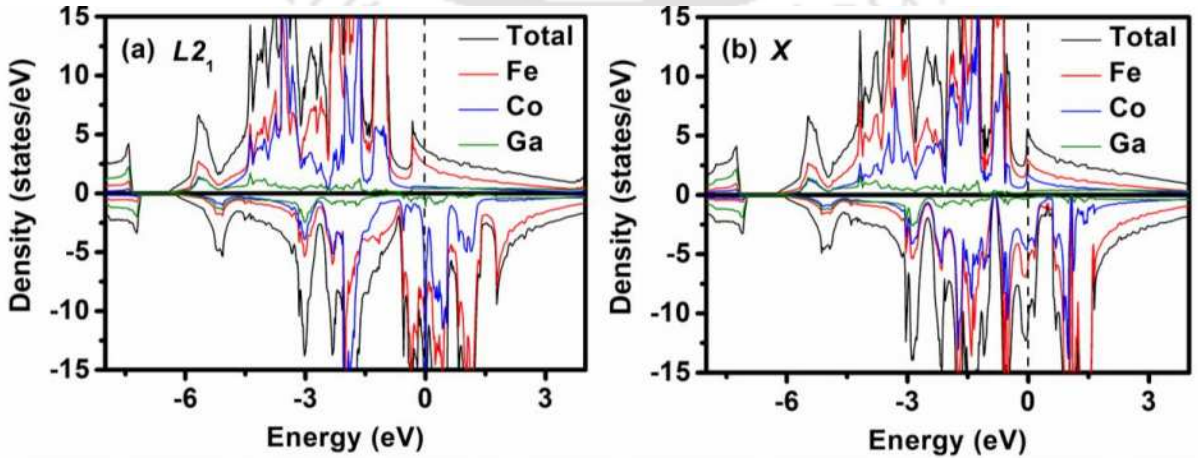

Figure 4.06. DOS of Fe_2CoGa near E_F calculated using (a) $L2_1$ type and (b) *X* type unit cells.

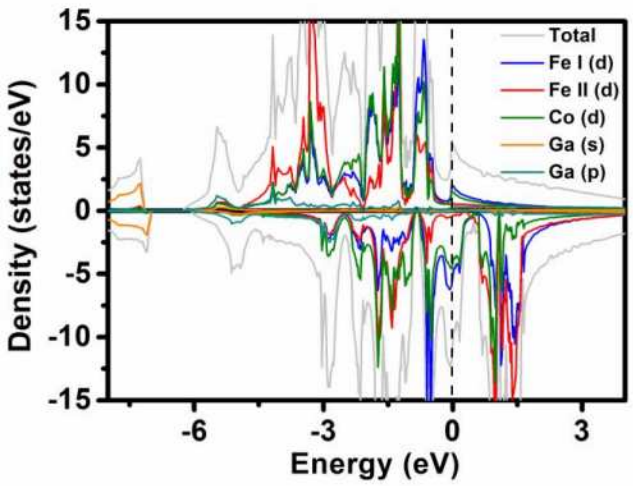

Figure 4.07. Orbital resolved DOS for *X* type Fe_2CoGa. Fe I represents the Fe atom at its original position in $L2_1$ structure and Fe II represents the Fe atom occupying the Co position.

The interchange of position between one of the Fe atoms and the Co atom in the *X* type structure largely modifies the number of states (peaks) around E_F, particularly in the spin down band. The pseudo gap like depression present in the DOS of $L2_1$ structure below E_F becomes prominent in the *X* type structure (at around 0.8 eV) and a new pseudo gap appears just above E_F (at around 0.5 eV). This pseudo gap above E_F also indicates the electronic stability of the compound. The effect of Co occupying one of the conventional Fe positions in the *X* type structure can further be understood from Figure 4.07. Strong *d-d* hybridization amongst the *d* orbitals of Co and Fe I sitting at its original site is primarily responsible for the generation of pseudo gaps. This is so because Fe I and Co experience the same crystal field of tetrahedral symmetry [165].

4.5 Magnetic properties

M_t calculated for the $L2_1$ type structure is 6.01 μ_B/f.u. and the one for the *X* type structure is 5.30 μ_B/f.u. The difference in M_t of the two structures arises from the interchange of positions amongst half of the Fe atoms with Co in the *X* type structure. The magnetic moment of Fe occupying Co sites increases in value while those of Co atoms decrease, resulting in a net

decrease in the overall M_t as one goes from $L2_1$ to *X* type structure. *M-H* curves obtained for the three nanoparticles at 5 K and 300 K are shown in Figure 4.08(a and b), respectively. The *M-H* loops of the three Fe_2CoGa nanoparticles and the bulk counterpart (shown in Figure 4.08) give clear evidence of their soft magnetic nature, in agreement with the previous report on this Heusler alloy nanoparticle [59]. However, no field dependent magnetization data is available for bulk Fe_2CoGa in the literature for comparison with the present data. The measured M_s of Fe_2CoGa nanoparticles and the bulk alloy (see Table 4.03) are closer to the theoretical total magnetic moment of the *X* type inverse Heusler alloy structure than $L2_1$ type full Heusler alloy structure, which further supports the formation of inverse Heusler alloy structure in this compound. The M_s values obtained in this study can be compared with the previously reported experimental value of 5.09 μ_B/f.u. at 4.2 K for the bulk sample [37], simulated values ranging from 5.11 – 6.14 μ_B/f.u. [119,132,134,163–166] and experimental value of 3.89 μ_B/f.u. at 5 K for 20 nm particles [59]. S-P rule [12] yields an M_t of $Z_t - 24$ (= 28 – 24) = 4.0 μ_B/f.u. which is far lower than the experimental M_s values for this alloy. This difference in the value of the magnetic moment is expected since Fe_2CoGa is not half metallic (a presumption on which the S-P ruled is based on) as observed from the DOS near E_F depicted in Figure 4.06. M_s of Fe_2CoGa nanoparticles is found to decrease with a decrease in heat treatment temperature or time as also observed in the case of Co_2FeGa nanoparticles. The increment in the M_s of Heusler alloy nanoparticles at higher temperature or time is due to enhancement in crystallinity at higher heat treatment temperature or time as already explained in chapter 3. Improved crystallinity at higher heat treatment conditions is also responsible for their larger D_v. D_v dependent magnetic measurements on the nanoparticles reveal that the M_s, H_c and M_r decrease with a decrease in the D_v as depicted in Figures 4.08 and 4.09. The decrement in M_s with decrement in D_v can be interpreted using the core-shell model [40] for nanoparticles. The thickness *t* of magnetically dead shell on its surface [40] has been calculated by using M_s of the

nanoparticles of size D_v in the place of $M_s(d)$ and the bulk M_s value in the place of $M_s(b)$ in equation 1.13. The thickness t was found to increase from 0 nm to 0.56 nm and then to 0.71 nm at 5 K as D_v decreased from 56 nm to 26 nm and then to 21 nm for samples $S5_{800}$, $S3_{800}$ and $S5_{750}$, respectively. Similarly, t increases from 0 nm to 0.64 nm and then to 0.78 nm at 300 K for the three samples. The increment in t with decreasing D_v represents the ability of the core-shell model to explain M_s-D_v behaviour. The observed variation of H_c with D_v indicates that all the nanoparticles are in single domain region [41] and can be explained using the Stoner-Wohlfarth approach [40]. For the smallest size nanoparticle ($S5_{750}$), H_c and M_r are extremely low ($H_c \leq 6$ Oe; $M_r \leq 0.01$ μ_B/f.u.) indicating the possibility of superparamagnetism [41]. It was also observed that M_s and H_c of all the samples decrease at higher temperatures (see Table 4.03). Similar variation of M_s with increase in temperature was found in other Heusler alloy nanoparticles [59,67,69,80,83,85,152] including Co_2FeGa nanoparticles described in previous chapter. This reveals that $M_s(T)$ data of the synthesized nanoparticles follow the Bloch's law [70]. Interestingly, the decrement in M_s at higher temperatures is extremely small (see Table 4.03), which makes these nanoparticles suitable for room temperature device applications. Also, this small decrement (less than 1%) is responsible for the relatively high T_C of this alloy [152]. Further, a decrement in H_c at room temperature is also expected for single domain nanoparticles [67,69,83,85,152], as predicted by the Kneller's law [169]. This observation further supports our claim that the synthesized Fe_2CoGa nanoparticles are in single domain regime. Though the M_s values of both Fe_2CoGa (reported in current chapter) and Co_2FeGa (reported in previous chapter) are high, higher M_s of Fe_2CoGa nanoparticles (5.40 μ_B/f.u. at 5 K for D_v = 56 nm) as compared to that of similar size Co_2FeGa nanoparticles (4.73 μ_B/f.u. at 5 K for D_v = 57 nm) makes Fe_2CoGa nanoparticles more attractive for applications requiring high M_s, such as magnetic field driven sensors, *etc.*

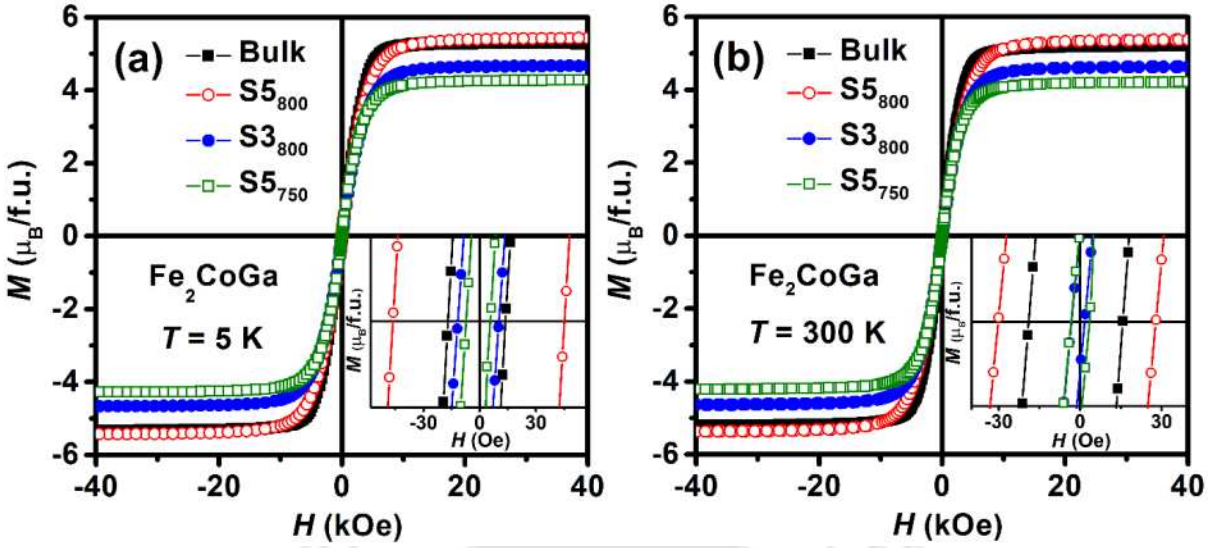

Figure 4.08. *M-H* curves recorded at (a) 5 K and (b) 300 K for Fe_2CoGa samples. Inset shows the magnified view of the curves near the origin.

Table 4.03. Magnetic properties of bulk and nanoparticles of Fe_2CoGa.

Sample ID	M_s (μ_B/f.u.)		H_c (Oe)		M_r (μ_B/f.u.)		K_{eff} ($\times 10^6$ erg/cc)		T_C (K)
	5 K	300 K	5 K	300 K	5 K	300 K	5 K	300 K	
$S5_{800}$	5.4 ± 0.1	5.4 ± 0.1	46 ± 2	29 ± 2	0.07	0.04	8.62	8.49	1204 ± 2
$S3_{800}$	4.7 ± 0.1	4.6 ± 0.1	11 ± 2	3 ± 2	0.02	0.00	6.71	6.39	1198 ± 2
$S5_{750}$	4.3 ± 0.1	4.2 ± 0.1	6 ± 2	3 ± 2	0.01	0.00	5.82	5.68	1196 ± 2
Bulk	5.4 ± 0.1	5.3 ± 0.1	16 ± 2	17 ± 2	0.03	0.03	5.52	5.48	1210 ± 2

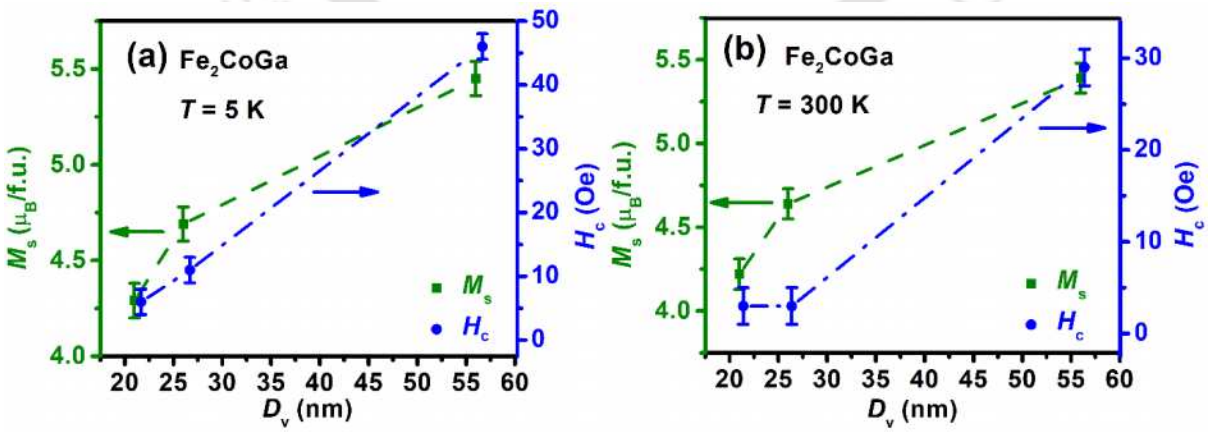

Figure 4.09. Variation of M_s and H_c of Fe_2CoGa nanoparticles with average crystallite size at (a) 5 K and (b) 300 K.

K_{eff} estimated for all the samples using LAS [25] is listed in Table 4.03. It is evident from the table that K_{eff} of all the nanoparticles are higher than that of the bulk alloy. Higher K_{eff} in nanoparticles as compared to their bulk counterpart has been attributed to (i) agglomeration of nanoparticles which can increase interparticle interaction [44], (ii) high surface to volume ratio resulting in breaking of the exchange bonds at the surface [40,45,46], (iii) dipolar interactions between the nanoparticles in single domain regime [40], *etc*. Further, it can be seen that K_{eff} decreased with a decrease in the size of the nanoparticles as also noticed in the case of Co_2FeGa nanoparticles. Similarly, lower K_{eff} at higher temperatures has also been observed in Fe_2CoGa nanoparticles and bulk Fe_2CoGa. K_{eff} values of Fe_2CoGa nanoparticles (5.68-8.62 $\times$ 10^6 erg/cc) reported in this chapter are higher than that of Co_2FeGa nanoparticles (2.93-4.87 $\times$ 10^6 erg/cc) reported in previous chapter. Q estimated using equation 1.22 yielded values ≥ 0.8 for all the Fe_2CoGa nanoparticles, thereby identify them as high anisotropic materials. Hence, Fe_2CoGa nanoparticles are better suited for applications demanding high anisotropy including high density magnetic recording.

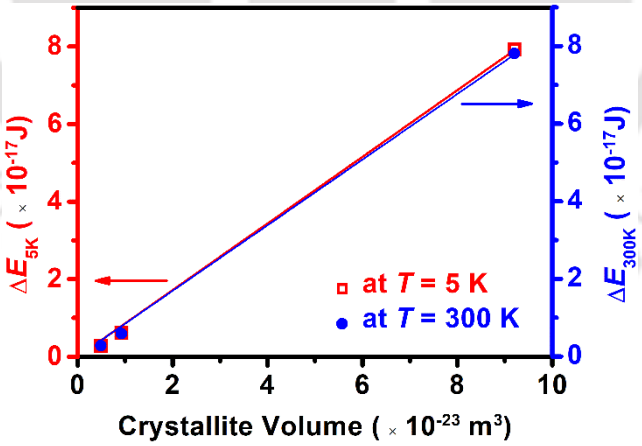

Figure 4.10 Variation of ΔE as a function of crystallite volume of the nanoparticles at 5 K and 300 K. Solid lines are linear fits to the data.

ΔE shows a linear variation with $<V>$ as depicted by the linear fit to the data (see Figure 4.10), which follows the Néel-Brown thermal activated model [42]. Such a linear variation of

the ΔE *versus* $\langle V \rangle$ data is a manifestation of volume or bulk anisotropy with negligible surface anisotropy in these nanoparticles [42]. This indicates that $K_v \approx K_{eff}$. Such linear relationship results in the typical H_c *vs* D_v behaviour of nanoparticles in the single domain regime [42].

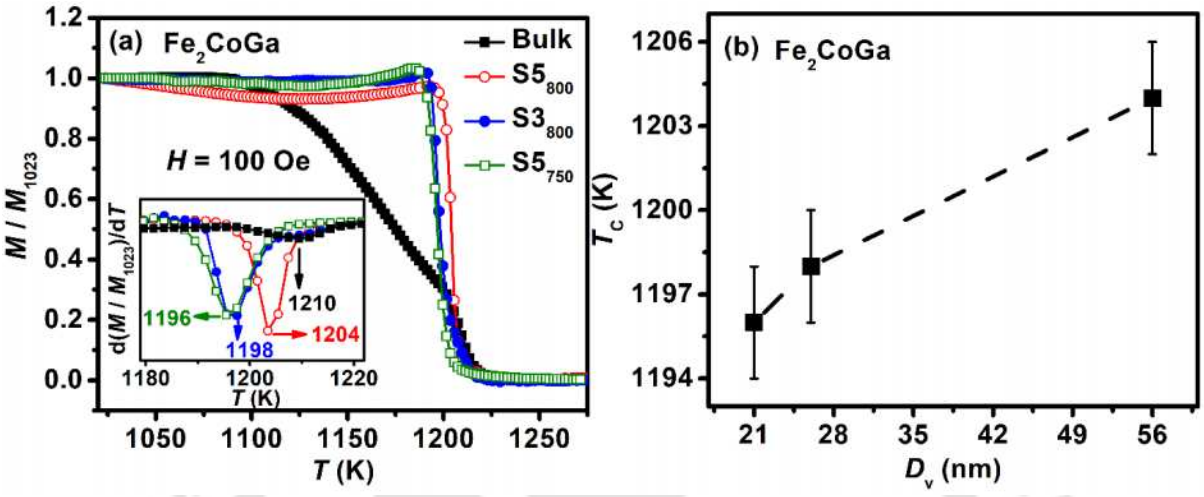

Figure 4.11. (a) *M-T* curves with inset illustrating the derivative of magnetization with temperature and (b) crystallite size dependent Curie temperature of Fe_2CoGa nanoparticles.

M-T curves of bulk and nanocrystalline Fe_2CoGa recorded under an applied field of 100 Oe are shown in Figure 4.11(a). The normalized magnetization with respect to magnetization at temperature 1023 K (M/M_{1023}) is plotted in the y-axis of the figure. Here, M is the magnetization at temperature T and M_{1023} is the magnetization at 1023 K. It can be seen that the ferromagnetic to paramagnetic phase transition is sharper for the nanoparticles as compared to the bulk Fe_2CoGa, which could be due to the single domain nature of the nanoparticles. The *M-T* curves show high T_C for all the Fe_2CoGa samples (see Table 4.03). The literature provides theoretical values of 982 K [121], 1053 K [165] and 1645 K [164] computed by various researchers for this alloy. T_C values obtained in this study are higher than the previously reported experimental value of 1165 K for bulk Fe_2CoGa [23]. Increase in T_C by ~35 K observed in the present studies could be due to the improved long range magnetic ordering in the alloys on account of improved crystallinity and structural order in the

synthesized nanoparticles. Figure 4.11(b) shows an increasing trend in T_C with D_v which is the general behaviour observed in other Heusler alloy nanoparticles as well [161]. Further, T_C of the Fe_2CoGa nanoparticles (1196-1204 K) obtained are higher than those of Co_2FeGa nanoparticles (1131-1137 K) reported in chapter 3, which make Fe_2CoGa nanoparticles more preferred for high temperature device applications.

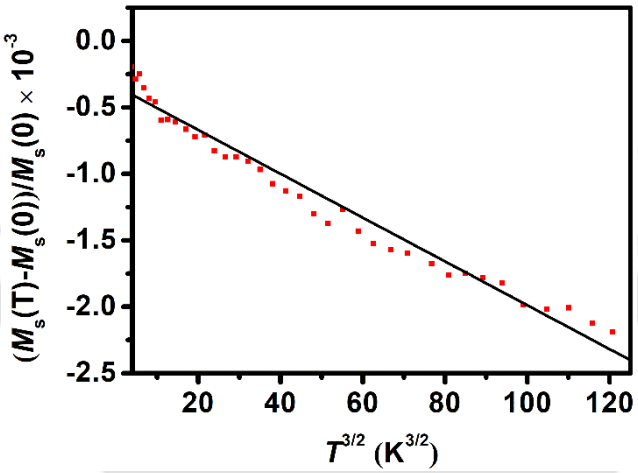

Figure 4.12. $(M_s(T)-M_s(0))/M_s(0)$ *versus* $T^{3/2}$ plot for bulk Fe_2CoGa sample.

Variation in M_s of bulk Fe_2CoGa as a function of temperature was recorded in the low temperature regime. The slope B of the curve depicted in Figure 4.12 and values of A and D estimated using equations 1.24-1.26 are 1.64×10^{-5}, 5.39×10^{-7} erg/cm, 2.89×10^{-29} erg/cm^2, respectively. The estimated value of D_{cr} [47,162] for Fe_2CoGa nanoparticles using equation 1.23 is 93 nm. The authors could not find D_{cr} value of any Heusler alloy particles in the literature for comparison. A comparison with Table 4.01 shows that all the Fe_2CoGa nanoparticles synthesized in this work have size smaller than D_{cr} and hence are single domain nanoparticles.

4.6 Summary and Highlights

The detailed experimental and theoretical investigations on bulk and nanoparticles of Fe_2CoGa has revealed several interesting results. Some of the highlights are given below:

- Single phase Fe_2CoGa Heusler alloy nanoparticles with three D_v of 56 nm, 26 nm, and 21 nm have been synthesized using an impurity free and facile template-less chemical route.
- XRD, SAED and HRTEM image analyses were used to ascertain the *X* type inverse Heusler alloy structure of the Fe_2CoGa nanoparticles.
- The preference of *X* type structure over $L2_1$ type structure as the stable structure of Fe_2CoGa has also been confirmed by first principles based energy calculations.
- The EDS data confirmed the stoichiometric alloy composition of both bulk and nanoparticles of Fe_2CoGa compound.
- Control of M_s, H_c, K_{eff} and T_C of the alloys has been achieved by controlling D_v by merely varying the heat treatment conditions during preparation.
- Fe_2CoGa nanoparticles show soft ferromagnetic behavior with higher M_s (4.2-5.4 μ_B/f.u.), K_{eff} (5.68-8.62 $\times$ 10^6 erg/cc) and T_C (1196-1204 K) as compared to the Co_2FeGa nanoparticles reported in chapter 3.
- Nature of H_c *versus* D_v plots and the estimated value of D_{cr} for Fe_2CoGa nanoparticles confirm that all the nanoparticles are in single domain regime. Near zero values of H_c and M_r for the smallest size ($S5_{750}$) nanoparticles indicate the likelihood of superparamagnetism in these single domain nanoparticles.
- Nearly constant M_s from 5 K to 300 K makes these nanoparticles suitable for room temperature device applications. The superior M_s, K_{eff} and T_C values makes Fe_2CoGa nanoparticles a natural choice for applications in magnetic field driven sensors and ultrahigh density magnetic recording.
- Apart from establishing a facile way to synthesize single domain Fe_2CoGa over a wide range of sizes, this work also brings out their potential applications.

Chapter 5

Crystallite size dependent properties of Fe_2CoAl nanoparticles

The crystallite size dependent properties of Fe_2CoGa nanoparticles served as a motivation to explore the changes in the properties when the Z element (Ga) is replaced with another isovalent Z element (Al). Interestingly, Fe_2CoAl is also known for its remarkable magnetic properties and energy storage capabilities [170]. Bulk Fe_2CoAl alloy was first prepared by Grover *et al.* [35] in 1980 by substituting Co in Fe_3Al alloy. Subsequent to their discovery of high T_C and M_s, its structural, magnetic, electronic, thermoelectric, thermodynamic, mechanical, elastic, spectroscopic and half-metallic properties were explored in the bulk form using both theoretical [132,134,178–180,163,171–177] and experimental [63,167,171,172,181–183] techniques. Some attempts have also been made to synthesize this alloy in thin film [170,184,185] and nanofiber [186] forms. However, there are only two reports, one by Jain *et al.* [63] and the other by Ahmad *et al.* [187] on the preparation and characterization of Fe_2CoAl in 0-d or nanoparticle form. Both these reports discuss their findings on single sized Fe_2CoAl nanoparticles with *A2* type fully disordered Heusler alloy structure. Thus, there are no experimental studies available in the literature demonstrating the energetically stable *X* type structured Fe_2CoAl nanocrystalline alloy to the best of our knowledge. The promising bulk properties of Fe_2CoAl, its limited exploration in the nanocrystalline regime and the challenges faced in obtaining it in its stable structure in the nanometer scale act as further motivations to study this nanocrystalline compound. This chapter

describes the successful synthesis of single domain Fe_2CoAl nanoparticles with three different crystallite sizes using the template-less chemical approach. Apart from achieving highly ordered *X* type Heusler alloy structure in the synthesized Fe_2CoAl nanoparticles, this study also provides an understanding of crystallite size dependent properties of single magnetic domain nanoparticles. Theoretical studies including *ab initio* calculations have also been performed to validate the experimental findings.

5.1 Sample preparation

Three sets of Fe_2CoAl nanoparticles, designated as FCA-1, FCA-2 and FCA-3 were synthesized using a template-less chemical method explained in chapter 2. Weighed quantities of precursors corresponding to the compound's stoichiometry, *viz.*, 1.4555 g of $Fe(NO_3)_3.9H_2O$, 0.4825 g of $CoCl_2.6H_2O$ and 0.4833 g of $Al(NO_3)_3.9H_2O$ were utilized as precursors. The flow chart depicted in Figure 2.01 represents the process followed to synthesize these nanoparticles. The heat treatment conditions used for processing the three samples FCA-1, FCA-2 and FCA-3 are listed in Table 5.01.

5.2 Structural analysis

The XRD patterns of the synthesized Fe_2CoAl Heusler alloy nanoparticles shown in Figure 5.01(a), indicates the presence of (220), (400) and (422) reflections which represent the three highly intense reflections (see Table 5.02) of the Heusler alloy crystal structure. The absence of any unaccounted reflection indicates the single phase structure of the synthesized nanoparticles. A comparison of experimental XRD patterns with CaRIne generated pattern using $L2_1$ and *X* type unit cells shows a close similarity between the strong reflections. However, the weak superlattice reflections (111) and (200) present in the simulated pattern are not observed in the experimental XRD pattern. A comparison with available literature on bulk and low dimensional (thin films, nanowires and nanoparticles) Fe_2CoAl also yields similar results. Jain *et al.* [63] assigned *A2* type disordered structure to the arc melted bulk Fe_2CoAl in

the absence of (111) and (200) reflections in their XRD pattern. Yin *et al.* [167] and Lin *et al.* [172] assigned *B2* type disordered structure in their bulk Fe_2CoAl in the absence of (111) reflection. Though Grover *et al.* [35] and Popiel *et al.* [182] claimed that their bulk Fe_2CoAl samples possess $L2_1$ type structure, no XRD data is provided in their papers for validation. Li *et al.* [186] assigned *B2* and *A2* type disordered structures to electrospun Fe_2CoAl nanowires by analyzing their XRD patterns. In the case of nanoparticles, the only available reports by Jain *et al.* [63] and Ahmad *et al.* [187] accepted *A2* type disordered structure for their Fe_2CoAl nanoparticles on the basis of reflections in their XRD measurements. Absence of the superlattice reflections in the experimental XRD patterns have raised two queries: (i) Whether (111) and (200) reflections are actually absent in this alloy or their small intensities are below the detection limits of XRD measurements? (ii) Even if (111) and (200) reflections could be identified, should one assign $L2_1$ or *X* type structure to this alloy, since the simulated XRD patterns of both the structures are similar (see Table 5.02).

Table 5.01. Structural and elemental composition data of synthesized Fe_2CoAl nanoparticles.

Sample ID	Heat treatment condition		χ^2		a (Å)	D_v (nm)	Average composition Fe:Co:Al (at.%)	d (nm)
	Temp. (°C)	Time (h)	$L2_1$	X				
FCA-1	850	1	2.27	2.22	5.727	51 ± 1	49.4:25.7:24.9	58 ± 1
FCA-2	800	5	2.66	2.35	5.723	45 ± 1	49.8:25.0:25.2	55 ± 1
FCA-3	800	1	2.38	2.08	5.723	41 ± 1	49.5:24.6:25.9	48 ± 1

For resolving the first issue, we resorted to electron diffraction technique. FETEM images of FCA-2 are shown in Figure 5.02. Both the SAED pattern and HRTEM micrographs reveal the presence of weak (111) and (200) superlattice reflections along with highly intense reflections from (220), (400) and (422) planes. The SAED pattern depicted in Figure 5.02(a) confirms the presence of other small reflections from (311), (222), (331) and (420) planes which are even weaker than the superlattice reflections. This confirms the formation of ordered

single phase Heusler alloy structure of either $L2_1$ or *X* type in all the synthesized Fe_2CoAl nanoparticles. The lattice fringes corresponding to superlattice reflections (111) and (200) can be clearly seen in Figure 5.02(b and c) which validate the formation of ordered Heusler alloy structure in the synthesized nanoparticles.

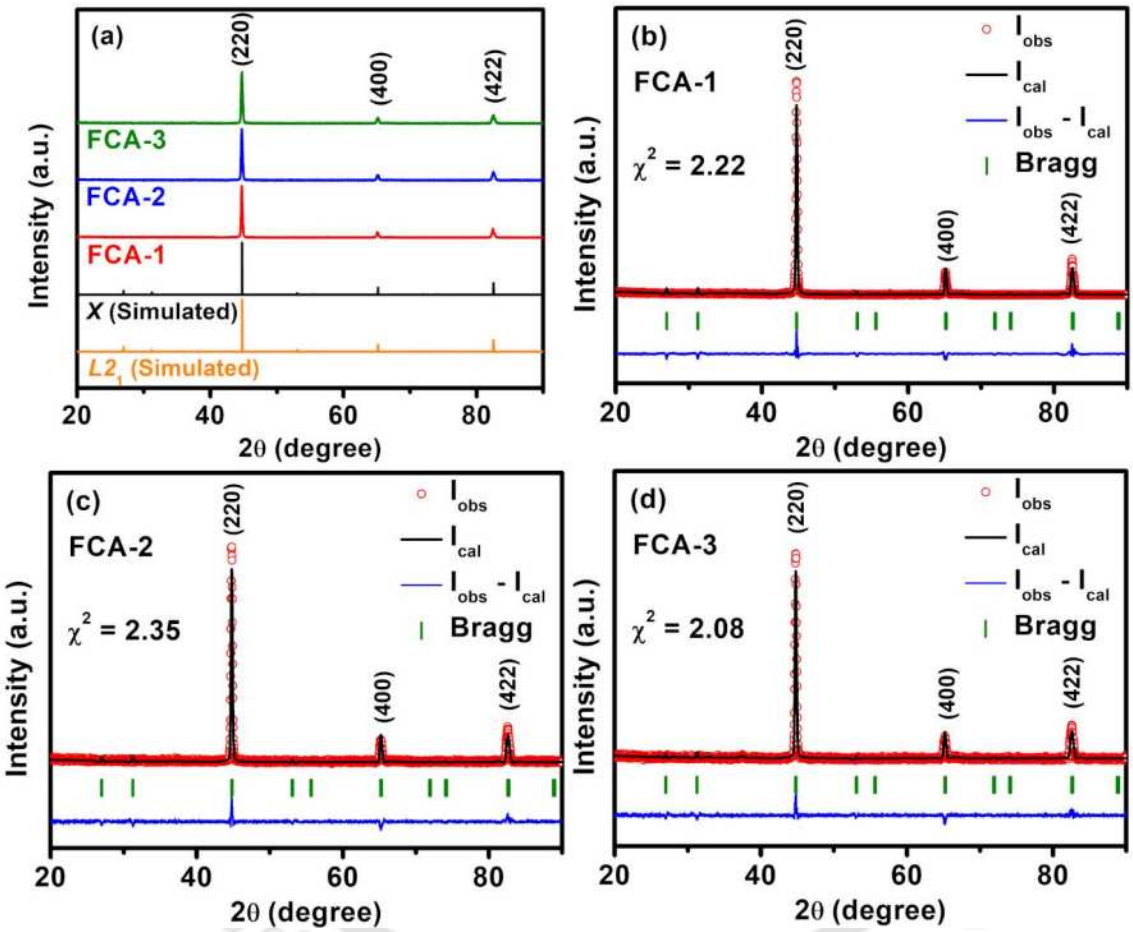

Figure 5.01. (a) Simulated and experimental XRD patterns of Fe_2CoAl nanoparticles. (b, c, d) Rietveld refinement plots of the XRD patterns of the three samples using *X* type unit cell.

After confirming the formation of ordered Heusler alloy structure, it was required to assign the favoured structures between $L2_1$ or *X* type to the nanoparticles. It is generally accepted that a X_2YZ with higher atomic number X atom crystallizes in $L2_1$ type full Heusler alloy structure whereas an alloy having higher atomic number Y prefers the *X* type inverse Heusler alloy structure [167]. Therefore, in the case of Fe_2CoAl, having the higher atomic number of Y(Co) atom than X(Fe) atom, the *X* type structure should be the preferred stable

structure. In order to confirm this, the experimental XRD patterns were refined with $L2_1$ (space group no. 225 [$Fm\bar{3}m$]) and *X* type (space group no. 216 [$F\bar{4}3m$]) unit cells [*c.f.*, Figure 5.01(b, c, d)].

Table 5.02. Crystallographic planes with d_{hkl} and the normalized intensities of the reflections in simulated and experimental XRD patterns of Fe_2CoAl alloy.

Planes (*hkl*)	d_{hkl} (Å)	Normalized intensity of reflections in				
		Simulated XRD pattern for the unit cell type		Experimental XRD pattern of		
		$L2_1$	*X*	FCA-1	FCA-2	FCA-3
(1 1 1)	3.30	8.49	7.19	-	-	-
(2 0 0)	2.86	2.95	4.29	-	-	-
(2 2 0)	2.02	100	100	100	100	100
(3 1 1)	1.72	3.13	2.58	-	-	-
(2 2 2)	1.65	0.56	0.87	-	-	-
(4 0 0)	1.43	13.13	13.13	11	11	12
(3 3 1)	1.31	0.96	0.78	-	-	-
(4 2 0)	1.28	0.53	0.86	-	-	-
(4 2 2)	1.17	22.42	22.42	17	17	18
(3 3 3)	1.10	0.15	0.12	-	-	-
(5 1 1)	1.10	0.46	0.37	-	-	-

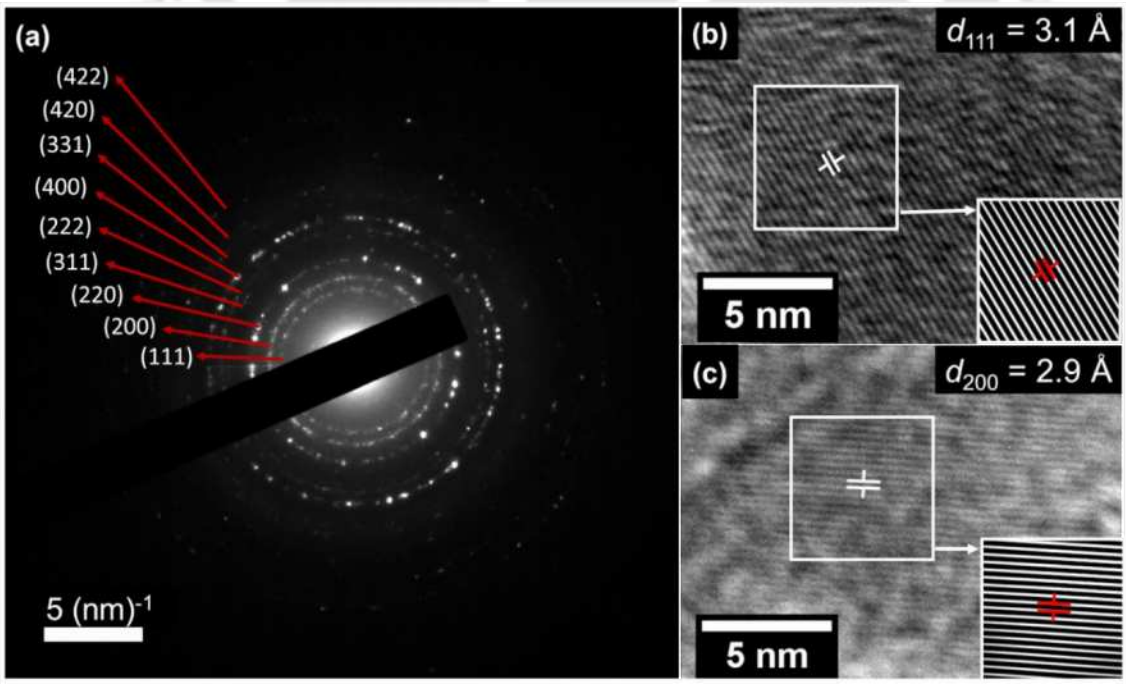

Figure 5.02. (a) SAED pattern (b, c) HRTEM micrographs with their iFFT images showing presence of (111) and (200) superlattice planes.

Rietveld refinement yielded slightly lower χ^2 value for *X* type structure (see Table 5.01), indicating it to be the more probable structure. The small difference in the χ^2 values of the two structures is due to the small (*i.e.*, only one) atomic number difference between X(Fe) and Y(Co) atoms, just as in the case of Fe_2CoGa nanoparticles. So, the total energy of Fe_2CoAl alloy with both $L2_1$ and *X* type structures was computed as a function of lattice parameter *a*. The overall lower energy of the *X* type structure (*cf.* Figure 5.03) clarifies the higher stability of *X* type structure for Fe_2CoAl Heusler alloy over $L2_1$ type structure. Previous reports by Gilleβen *et al.* [163], Matsushita *et al.* [134], Faleev *et al.* [132], and Ahmad *et al.* [175] also validate our energy calculations and the conclusion. Thus, in contrast to previous experimental reports on Fe_2CoAl [63,167,172,186,187], the stable and ordered *X* type structure can be established here.

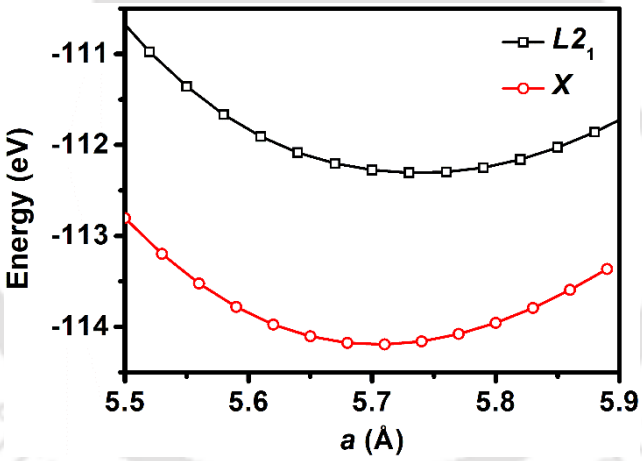

Figure 5.03. Energy as the function of *a* for Fe_2CoAl alloy for the structures $L2_1$ and *X*.

The lattice constant (*a*) values obtained from Rietveld refinement of the XRD patterns of the nanoparticles (see Table 5.01) was found to be within the range of previously published theoretical and experimental values of 5.697 Å to 5.766 Å [35,63,179,181,182,134,163,167,172–175,177]. The Schërrer's equation (equation 2.18) was used to estimate D_v of the prepared Fe_2CoAl nanoparticles listed in Table 5.01. D_v exhibited a

dependence on the heat treatment temperature and time as expected and as also observed in Co_2FeGa (chapters 3) and Fe_2CoGa (chapter 4) nanoparticles.

5.3 Elemental composition and morphology

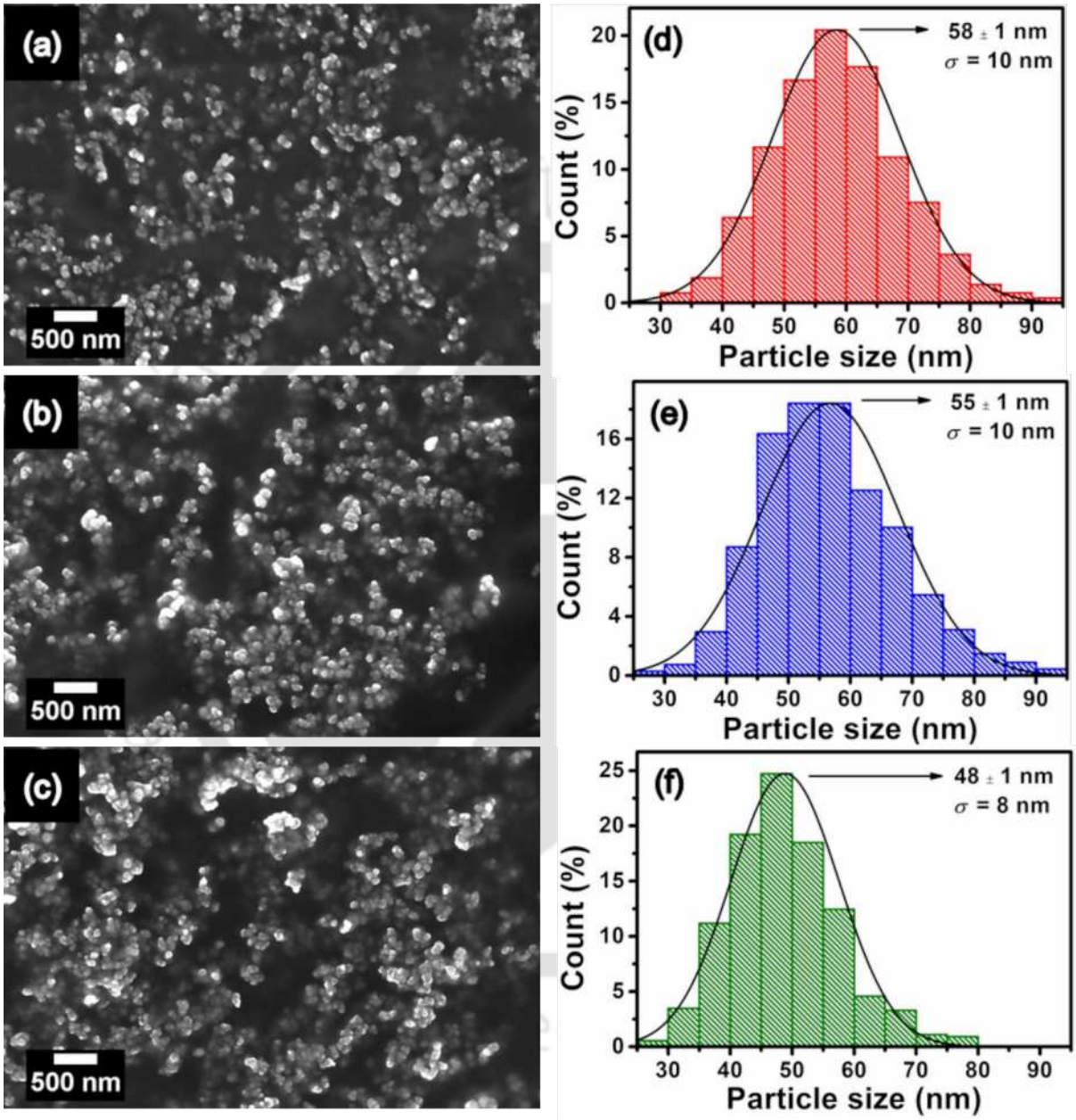

Figure 5.04. FESEM images of (a) FCA-1, (b) FCA-2 and (c) FCA-3 and (d-f) particle size histograms (shown on right side) generated from the micrographs shown on the left side.

The overall composition of the three Fe_2CoAl nanoparticles obtained from EDS measurements, (*c.f.*,Table 5.01), are very close to the stoichiometric composition of

$Fe_{50}Co_{25}Al_{25}$. Of the two earlier reports on these Fe_2CoAl nanoparticles, one [63] does not mention the composition and the other [187] reported off-stoichiometric $Fe_{54.5}Co_{27.5}Al_{18.0}$ composition as $Fe_{50}Co_{25}Al_{25}$. Figure 5.04(a, b and c) and Figure 5.04(d, e and f) show the morphology of the Fe_2CoAl nanoparticles and their histograms displaying their particle size distributions, respectively. The synthesized nanoparticles are found to possess a near-spherical shape with particle sizes clearly conforming to the nanometer scale. Near-spherical Fe_2CoAl nanoparticles have also been synthesized by Ahmad *et al.* [187]. The particle sizes (d) of the three Fe_2CoAl nanoparticles are distributed from 25 to 95 nm are listed in Table 5.01. As compared to D_v (41 - 51 nm), the d (ranging between 48 nm and 58 nm) is slightly bigger in all the cases, which indicates some amount of agglomeration of the crystallites. As already pointed out in chapter 3 and 4, such agglomeration is quite common in magnetic nanoparticles with high magnetic moments and difficult to prevent especially when no templates are used to separate them. The σ values varied from 10 nm → 10 nm → 8 nm as the particle size decreased from 58 nm → 55 nm → 48 nm, respectively. As already discussed in chapter 3 and 4, these σ values are slightly higher than those obtained for template-assisted methods. If one considers the impurities left behind by templates and their detrimental effect on the alloy properties, these σ values are acceptable.

5.4 DOS calculations

Coelho *et al.* [171] calculated TDOS of Fe_2CoAl alloy for the first time and found non-half metallic behaviour of the alloy, whereas, Lin *et al.* [172] showed it to be a half metal in their TDOS calculations on $CoFe_{1+x}Ti_{1-x}Al$ alloys. Siakeng *et al.* [174] computed the DOS of Fe_2CoAl alloy with and without incorporating Hubbard parameter U and declared it to be a non-half metal in both cases. Ahmad *et al.* [175,176] on one side, claimed the material to be non-half metal, and on the other hand, declared it to have a high spin polarization of 78 % [176]. Rai *et al.* [177] found a pseudo bandgap just above E_F in the spin-down channel of

Fe_2CoAl alloy by incorporating U in their calculations and showed that this gap could be tuned towards E_F by applying external pressure. The discrepancies in the previous results inspired us to investigate the DOS of Fe_2CoAl alloy.

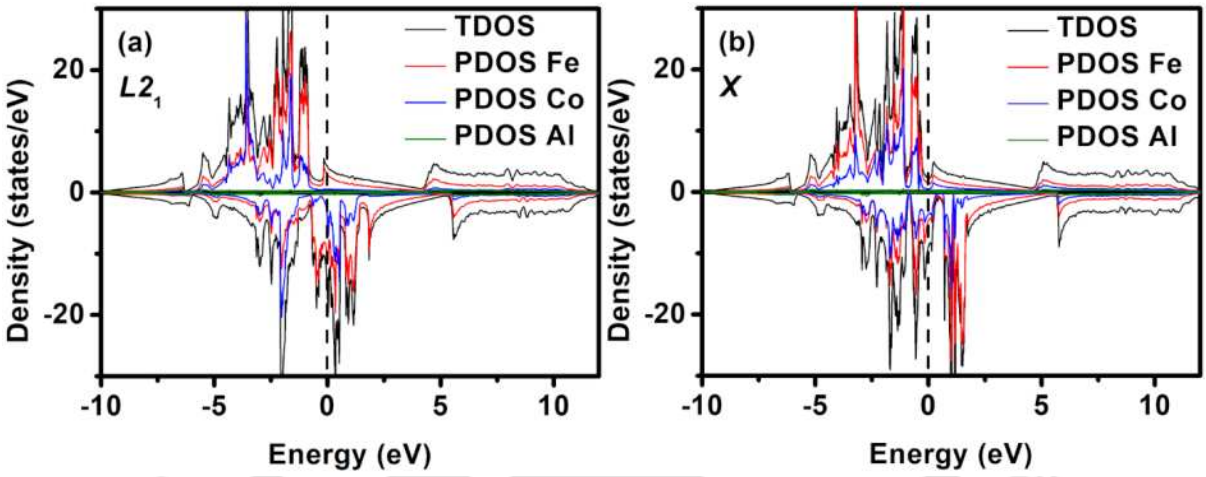

Figure 5.05. TDOS of Fe_2CoAl alloy along with PDOS of elements Fe, Co and Al with (a) $L2_1$ type, and (b) *X* type structures.

Figure 5.05 shows the TDOS as well as element-resolved PDOS for Fe, Co and Al for both $L2_1$ and *X* type structures around E_F. The results show close similarity to the previous DOS calculated by Coelho *et al.* [171] and Ahmad *et al.* [175,176] and clarifies that Fe_2CoAl is not completely half metallic with either $L2_1$ or *X* type structure. The valence band of Fe_2CoAl contains contributions from both the majority and minority spins in the DOS plots, but the conduction band has large contributions just from the minority spins. Additionally, the higher stability of the *X* type structure over $L2_1$ type structure can be inferred from the DOS plots. Here, the fewer states at E_F in the *X* type structure as compared to the $L2_1$ type structure is an indication of the higher stability of the *X* type structure. The PDOS also clarifies that for both the structures, Fe and Co play a significant role, whereas Al plays an insignificant role. The exchange of positions between one of the Fe atoms with the Co atom in the *X* type structure significantly alters the peaks around E_F, especially in the spin down states. Also, a bandgap appears in spin down channel of the *X* type DOS below E_F near about -0.83 eV along with a

pseudo gap at around 0.46 eV above E_F. The value of spin polarization calculated was 59 % for both the structures. Here, it is important to mention that all the above calculated DOS are based on procedures applicable to bulk Fe_2CoAl. As pointed out in the earlier chapters, a previous study on Co_2FeSn nanowires by Galdun *et al.* [156] indicates a possibility to increase the value of spin polarization in the low dimensional forms of the alloy. Further, Hussain *et al.* [138] also found a contrast in spin polarization values at the surface of Co_2FeGa. These results suggest that it may be possible for the present Fe_2CoAl nanoparticles to have higher spin polarization than the one predicted by the DOS calculations given above.

5.5 Magnetic properties

The calculated M_t are 5.898 μ_B/f.u. (for $L2_1$ type structure) and 5.145 μ_B/f.u. (for *X* type structure) for Fe_2CoAl. The difference in M_t of the two structures results from the exchange of atomic positions between half of the Fe atoms and Co atoms in *X* type structure. It can also be observed from the DOS plots that some of the spin-up peaks in the PDOS of Co atoms with $L2_1$ type structure get replaced by peaks from PDOS of Fe atom in the *X* type structure. As we move from $L2_1$ to *X* type structure, the magnetic moment of the Fe atom occupying the Co site increases from 2.087 μ_B/f.u. to 2.542 μ_B/f.u., whereas the magnetic moments of the Fe atom at its original site and the Co atom decrease from 2.087 μ_B/f.u. to 1.610 μ_B/f.u. and 1.764 μ_B/f.u. to 1.041 μ_B/f.u., respectively, which collectively results into an overall decrease in M_t. The *M-H* curves at 5 K and 300 K show soft magnetic behaviour of all the three Fe_2CoAl nanoparticles, as depicted in Figure 5.06(a and b). This behaviour is in line with the previous reports on bulk Fe_2CoAl [63,171] and Fe_2CoAl nanoparticles [63]. The experimental M_s values listed in Table 5.03 of the synthesized nanoparticles are comparable to the previously reported theoretical values ranging from 3.981 to 5.33 μ_B/f.u. [132,134,163,172–175,177], experimental M_s values for bulk Fe_2CoAl range from 4.4 to 5 [35,63,172,181,182], thin film ~5.3 μ_B/f.u. [183], nanowires range from 4.5 to 5.1 μ_B/f.u. [186] and nanoparticles range from 4.5 to 5.17 μ_B/f.u.

[63,187]. Furthermore, the experimental M_s of the three Fe_2CoAl nanoparticles (see Table 5.03) are closer to the theoretical M_t of the *X* type structure than $L2_1$ type structure. M_t value for Fe_2CoAl obtained through S-P rule [12] *viz.*, M_t of $Z_t - 24$ (= 28 – 24) = 4 μ_B/f.u., which is lower compared to the obtained experimental M_s and theoretical M_t values. But, here it should be mentioned that the obtained M_s and M_t values do not follow S-P rule due to their non-half metallic character already confirmed through the DOS calculations. M_s of Fe_2CoAl nanoparticles is lower if the heat treatment temperature or time is reduced. As it is already explained in chapter 3, the increment in M_s of these alloy nanoparticles with increase processing temperatures or time is due to their enhanced crystallinity and defect minimization at elevated temperature or time. D_v dependent magnetic measurements show that M_s, M_r and H_c decrease when the D_v decreases, as shown in Figures 5.06 and 5.07, as also observed in case of Co_2FeGa and Fe_2CoGa nanoparticles. The decrement in M_s with D_v can be explained through the core-shell model [40] for the nanoparticles, elaborated in the introduction chapter. Magnetically dead layer *t* on the surface of the synthesized nanoparticles was calculated using $M_s(b)$ as the theoretical value of M_t, $M_s(d)$ from Table 5.03 and D_v as *d* from Table 5.01. It is clear from Table 5.03 that the value of *t* increases with a decrease in D_v, which shows that formation of a magnetically dead shell on the surface of nanoparticles as the cause for the observed decrease in M_s with decrease in D_v. The decrement of H_c with D_v indicates that the synthesized nanoparticles are in single domain regime [41], similar to previously synthesized Co_2FeGa and Fe_2CoGa nanoparticles. H_c of the three nanoparticles particles measured at 5 K was substituted in equation 1.15 and the resulting plot is shown in Figure 5.08, yielding g = 182 and h = 35846. These values were used to estimate the value of superparamagnetic critical size D_{sp} (= 33 nm) for Fe_2CoAl. The H_c at D_{cr} (whose estimation is described later in this chapter) turned out to be 134 Oe. The Stoner-Wohlfarth approach [40] can explain this decrease in H_c with decreasing D_v in a single domain regime. Also, M_s and H_c values measured at higher

temperatures are lower than the ones at lower temperatures for all the nanoparticles (see Table 5.03). Ahmad *et al*. [187] observed similar trend of M_s and H_c with increasing temperature in Fe_2CoAl nanoparticles. Other Heusler alloy nanoparticles [59,67,69,80,83,85,152], together with the previous studies on Co_2FeGa and Fe_2CoGa nanoparticles also show a similar decrement of M_s with increasing temperature, which demonstrates that the synthesized Fe_2CoAl nanoparticles also obey Bloch's law for $M_s(T)$ [70]. This minimal decrement of M_s (less than 1%) at higher temperatures is also related to their high T_C [152]. The small decrease in M_s at higher temperatures makes these nanoparticles appropriate for device applications at ambient and higher temperatures. Kneller's rule [169] predicts a decrease in H_c at high temperatures for single domain nanoparticles [67,69,83,85,152]. This finding lends credence to our assumption that the synthesized Fe_2CoAl nanoparticles belong to single domain regime, similar to Co_2FeGa and Fe_2CoGa nanoparticles. When we compare the M_s of the three Heusler alloy nanoparticles investigated in this thesis work so far, the value of 4.93 μ_B/f.u. recorded at 5 K for 51 nm size Fe_2CoAl nanoparticles is higher than that of Co_2FeGa nanoparticles (4.73 μ_B/f.u. at 5 K for D_v = 57 nm), but smaller than that of Fe_2CoGa nanoparticles (5.40 μ_B/f.u. at 5 K for D_v = 56 nm).

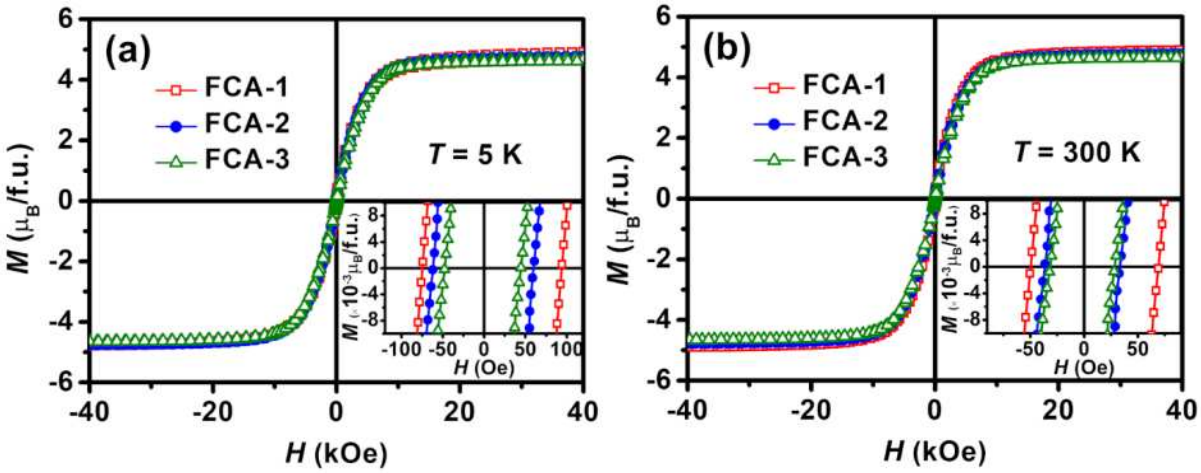

Figure 5.06. *M-H* loops recorded at (a) 5 K, and (b) 300 K for Fe_2CoAl nanoparticles.

Table 5.03. Magnetic properties of Fe_2CoAl nanoparticles.

Sample ID	M_s (μ_B/f.u.)		H_c (Oe)		M_r (μ_B/f.u.)		$K_{eff} \times 10^6$ (erg/cc)		t (nm)		T_C (K)
	5 K	300 K	5 K	300 K	5 K	300 K	5 K	300 K	5 K	300 K	
FCA-1	4.93 ± 0.10	4.89 ± 0.10	84 ± 2	60 ± 2	0.13	0.10	10.24	9.39	0.36	0.42	1225 ± 2
FCA-2	4.79 ± 0.06	4.78 ± 0.06	61 ± 2	35 ± 2	0.08	0.05	8.93	8.72	0.52	0.53	1221 ± 2
FCA-3	4.70 ± 0.06	4.67 ± 0.06	46 ± 2	30 ± 2	0.05	0.04	8.22	8.06	0.59	0.63	1225 ± 2

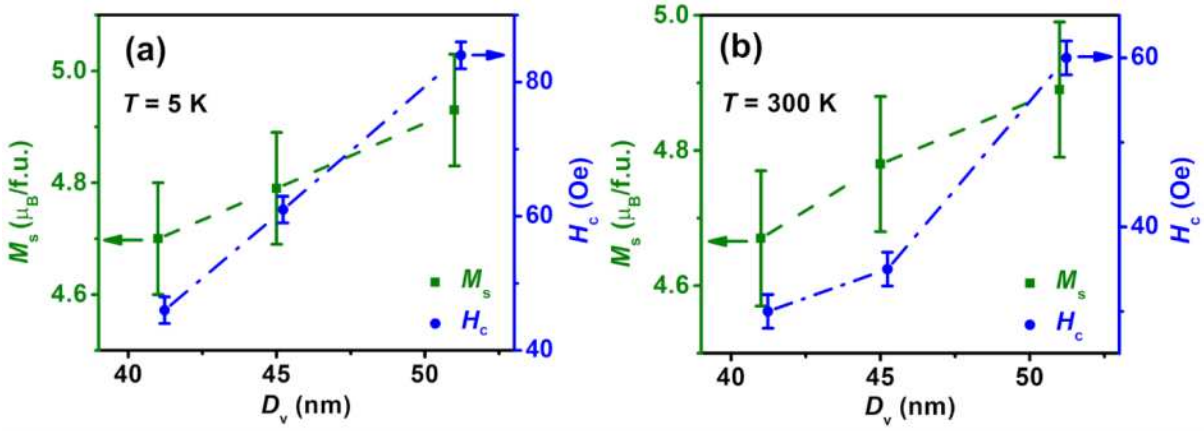

Figure 5.07. M_s and H_c of Fe_2CoAl nanoparticles as a function of D_v at (a) 5 K, and (b) 300 K.

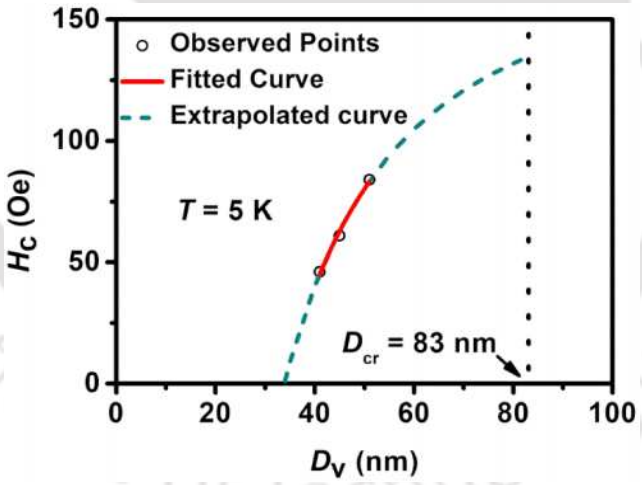

Figure 5.08. Variation of H_c at 5 K with D_v of Fe_2CoAl nanoparticles in single domain regime.

According to LAS [145], the calculated values of K_{eff} listed in Table 5.03 show higher values compared to previously reported values for Fe_2CoAl nanowires (= 4×10^3 J/m^3) [184]. Since K_{eff} values for Fe_2CoAl nanoparticles are not available in the literature, a comparison is made with other Fe and Co based Heusler alloy nanoparticles with high K_{eff} [81,82,188]. The

reason for such a high K_{eff} values can be credited to (i) high *S/V* ratio which can give rise to broken exchange bonds at their surfaces [40,45,46], (ii) high agglomeration of magnetic nanoparticles which can enhance interparticle interactions [44], (iii) inter dipole interactions among the single domain magnetic nanoparticles [40], *etc.*, as mentioned in chapters 3 and 4. Table 5.03 also reveals a decrement in K_{eff} with D_v, as observed in case of Co_2FeGa and Fe_2CoGa nanoparticles. Reduction in K_{eff} at elevated temperatures has also been noticed in these nanoparticles. Interestingly, the observed K_{eff} values for Fe_2CoAl nanoparticles (8.06-10.24 × 10^6 erg/cc) are higher than that of Co_2FeGa (2.93-4.87 × 10^6 erg/cc) and Fe_2CoGa (5.68-8.62× 10^6 erg/cc) nanoparticles reported in chapters 3 and 4. This makes Fe_2CoAl nanoparticles more suitable for high anisotropic applications such as high-density magnetic recording.

According to the Néel Brown thermal activated model [42], described in the introduction section, the linear variation of Δ*E versus* <*V*> curve shown in Figure 5.09 indicates the dominant effect of K_v with a minimal effect of K_s, which implies that $K_{eff} \approx K_v$ [42]. Additionally, the H_c behaviour for single domain nanoparticles is also associated with this linear behaviour of Δ*E versus* <*V*> curve [42].

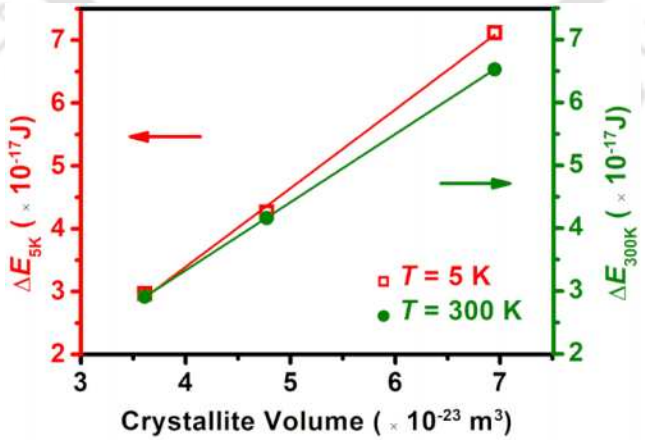

Figure 5.09. Δ*E versus* crystallite volume plots for Fe_2CoAl nanoparticles at two temperatures with the straight lines representing the linear fits to the experimental data.

The *M-T* curves for Fe_2CoAl nanoparticles measured at an applied magnetic field of 100 Oe are depicted in Figure 5.10, where the y-axis shows normalized magnetization M/M_{900}. Here, M and M_{900} represent magnetizations at temperatures T and 900 K, respectively. The curves indicate high values of T_C for all the synthesized Fe_2CoAl nanoparticles (see Table 5.03). The literature provides values of T_C above 1000 K for bulk Fe_2CoAl [35,63], above 873 K for nanowires [186], and a range of 743 K to 1190 K from theoretical estimates [174,177] for Fe_2CoAl alloy. Ahmad *et al.* [187] observed T_C value of 830 K and Jain *et al.* [63] found the T_C value above 1073 K for Fe_2CoAl nanoparticles. Improved structural ordering and crystallinity of the synthesized Fe_2CoAl nanoparticles are the reasons for the higher T_C for our nanoparticles compared to the previous reports. T_C does not show appreciable change with D_v, probably due to the small range of D_v obtained in the current study. Comparing T_C of Co_2FeGa (1131-1137 K) and Fe_2CoGa (1196-1204 K) nanoparticles studied in chapters 3 and 4, respectively, Fe_2CoAl nanoparticles show higher T_C (1221-1225 K), which makes it more appropriate for high temperature applications.

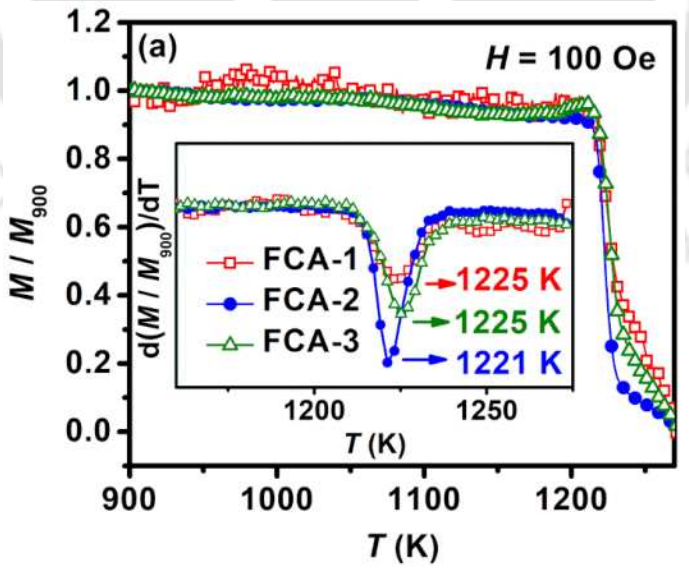

Figure 5.10. *M-T* curves of Fe_2CoAl nanoparticles with the derivative of magnetization shown in the inset.

Q values estimated using equation 1.22 for all the synthesized Fe_2CoAl nanoparticles are >1.5, branding as high anisotropic material [43]. Temperature dependent M_s in low temperature regime [49] of FCA-1 was used to evaluate the D_{cr} value for the Fe_2CoAl alloy using equation 1.23. The obtained value of slope *B* from Figure 5.11 is 8.985×10^{-5} and the calculated values of *A* and *D* are 1.84×10^{-7} erg/cm and 0.83×10^{-29} erg/cm^2, respectively. Using the values of *A* and *D*, D_{cr} for Fe_2CoAl alloy was evaluated to be 83 nm. The literature does not provide any value of D_{cr}, *A*, or *D* for Fe_2CoAl nanoparticles to make a comparison. Further, higher value of D_{cr} compared to D_v of the synthesized nanoparticles (see Table 5.01) shows the production of single domain Fe_2CoAl alloy nanoparticles.

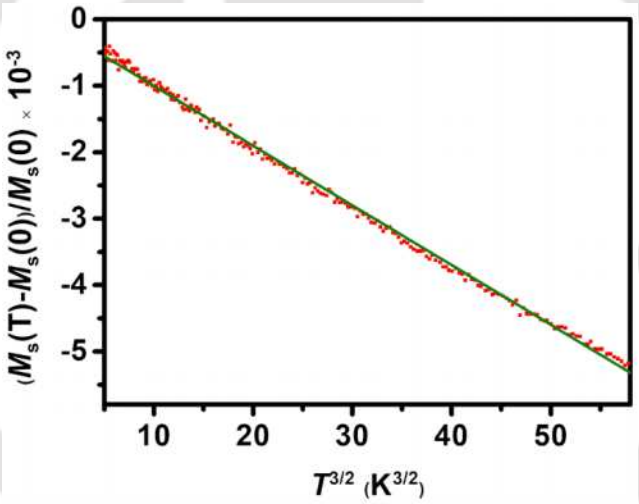

Figure 5.11. $(M_s(T) - M_s(0)) / M_s(0)$ as a function of $T^{3/2}$ at the field 2 T for FCA-1 nanoparticles. The solid line is a linear fit to the data.

5.6 Summary and Highlights

The experimental and theoretical investigations on Fe_2CoAl compound result in following major findings:

- A simple, template-free and cost-effective chemical route has been employed to synthesize single phase Fe_2CoAl nanoparticles with three distinct D_v of 51 nm, 45 nm and 41 nm.
- D_v could be tuned by merely changing the heat treatment conditions during processing.

- *X* type inverse Heusler alloy structure has been established in these near-stoichiometric nanoparticles using XRD, HRTEM and SAED analyses followed by *ab initio* energy computations.
- *Ab initio* calculations establish the preferred crystal structure of this compound and also help in understanding the magnetic and half metallic properties of the alloy.
- Fe_2CoAl nanoparticles exhibit soft ferromagnetic behaviour with high M_s (4.67-4.93 μ_B/f.u.), high K_{eff} (8.06-10.24 $\times$ 10^6 erg/cc), high T_C (1221-1225 K) and low H_c (30-84 Oe).
- The obtained K_{eff} and T_C of Fe_2CoAl nanoparticles are the highest among the three compounds studied, *viz*., Co_2FeGa, Fe_2CoGa and Fe_2CoAl. Hence, Fe_2CoAl appears to be the appropriate choice for applications demanding high anisotropy and high Curie temperature.
- Variations of M_s, K_{eff}, H_c and T_C with D_v have been analysed using well-established models to understand their general behaviour.
- D_{cr} (= 83 nm) estimated for Fe_2CoAl places all the synthesized nanoparticles in the single domain regime. The superparamagnetic critical size D_{sp} (= 33 nm) and H_c (= 134 Oe) at D_{cr} have been estimated for these Fe_2CoAl nanoparticles.
- Promising applications of these nanoparticles in ultra-high-density magnetic recording and magnetic field sensors have been identified from their high M_s, T_C and K_{eff} values and low H_c.

Chapter 6

Composition dependent properties of

$Fe_{2-x}Co_{1+x}Ga$ ($0 \leq x \leq 1$) nanoparticles

Though Fe_2CoGa and Co_2FeGa compounds are well-studied, the intermediate Fe rich and Co rich off-stoichiometric compositions have not been systematically studied. There are some theoretical [189] and experimental [190] reports which reveal that intermediate compositions of bulk $Fe_{2-x}Co_xMnAl$ [189] and $Co_{1+x}Fe_{2-x}Si$ [190] Heusler alloys exhibit better properties than the stoichiometric end compositions. There are some composition-dependent studies which have attempted to explore the properties of intermediate ternary alloy compositions in bulk Heusler alloys and films. For examples, $Co_{2+x}Fe_{1-x}Si$ (x = -1.00, -0.25, 0.00, 0.25) [191], $Co_{2-x}Fe_{1+x}Si$ (x = 0.00, 0.05, 0.10, 0.25, 0.50, 0.75, 1.00) [192], $Co_{3-x}Fe_xSi$ (x = 1.00, 1.25, 1.50, 1.75, 2.00, 2.25, 2.50, 2.75, 3.00) [193], $Fe_{3-x}Co_xSi$ (x = 0.00, 0.25, 0.50, 0.75, 0.90, 1.00) [194], $Co_{1+x}Fe_{2-x}Si$ (x = 0.0, 0.2, 0.4, 0.5, 0.6, 1.0) [190], and $Co_{3-x}Fe_xAl$ (x = 1.0, 1.2, 1.4, 1.5, 1.6, 1.8, 2.0) [195] alloys in bulk or thin film forms have been investigated using theoretical or experimental tools. When it comes to nanoparticles, the existing reports are mostly focused on the synthesis and characterization of a single Heusler alloy composition [58,59,67], or evaluation of synthesis route dependent properties [61,68,77,78,69–76] or particle size dependent properties [79–83]. There are very few composition-dependent studies on off-stoichiometric Co and Fe based nanoparticles such as Co:Fe:Ga with 57:24:19, 53:29:18, 49:32:19, and 42:37:21 [84], $Fe_{53.3-0.6x}Co_{46.7-0.4x}Sn_x$ ($2 \leq x \leq 26$) [65], Co-Ni-Ga (as 47:24:29, 50:18:32) [85], $Co_{2(1+x)}Fe_{1-x}Al_{1-x}$ (x = 0.0, 0.1, 0.2, 0.3, 0.4, 0.5) [86], and $Co_2(Cr_{1-x}Fe_x)Al$ (x =

0.0, 0.2, 0.4, 0.6, 0.8, 1.0) [87]. The available report on Co-Fe-Ga nanoparticles [84] reveal random elemental compositions and presence of impurities, which highlight the difficulty in achieving high quality Heusler alloy nanoparticles. It is also apparent that no systematic composition-dependent studies are available on $Fe_{2-x}Co_{1+x}Ga$ (x = 0.00 - 1.00) alloys in the literature in any physical form ranging from bulk to nanoparticles. This acted as motivation to synthesize highly ordered single domain $Fe_{2-x}Co_{1+x}Ga$ nanoparticles with x = 0.00, 0.25, 0.50, 0.75, and 1.00 using the template-less chemical route and evaluate their magnetic properties. The present study also provides the theoretical basis to interpret the experimental findings.

6.1 Sample preparation

$Fe_{2-x}Co_{1+x}Ga$ (x = 0.00, 0.25, 0.50,0.75, 1.00) nanoparticles have been synthesized using the facile template-less chemical route depicted in Figure 2.01. The amounts of precursors and the heat treatment conditions utilized are listed in Table 6.01.

Table 6.01. Details of precursors and heat treatment conditions used for synthesizing $Fe_{2-x}Co_{1+x}Ga$ nanoparticles.

x	Nominal Sample Composition	Precursor amounts in g			Heat treatment conditions	
		$Fe(NO_3)_3.9H_2O$	$CoCl_2.6H_2O$	$Ga(NO_3)_3.8H_2O$	Temperature (°C)	Time (h)
0.00	Fe_2CoGa	1.2347	0.3701	1.3908	800	4
0.25	$Fe_{1.75}Co_{1.25}Ga$	0.9806	0.3974	1.7201	800	5
0.50	$Fe_{1.5}Co_{1.5}Ga$	0.799	0.4695	1.8206	800	5
0.75	$Fe_{1.25}Co_{1.75}Ga$	0.6442	0.5232	2.0592	800	5
1.00	$FeCo_2Ga$	0.5785	0.6256	1.679	900	1

6.2 Structural analysis

The XRD patterns of the synthesized $Fe_{2-x}Co_{1+x}Ga$ (x = 0.00, 0.25, 0.50, 0.75, 1.00) nanoparticles shown in Figure 6.01(a-d) indicate the presence of reflections from (111), (200), (220), (311), (222), (400), (420), and (422) planes of the stable Heusler alloy structure. The

absence of any unindexed reflection in the XRD patterns confirms the formation of single phase Heusler alloy structure in the synthesized nanoparticles.

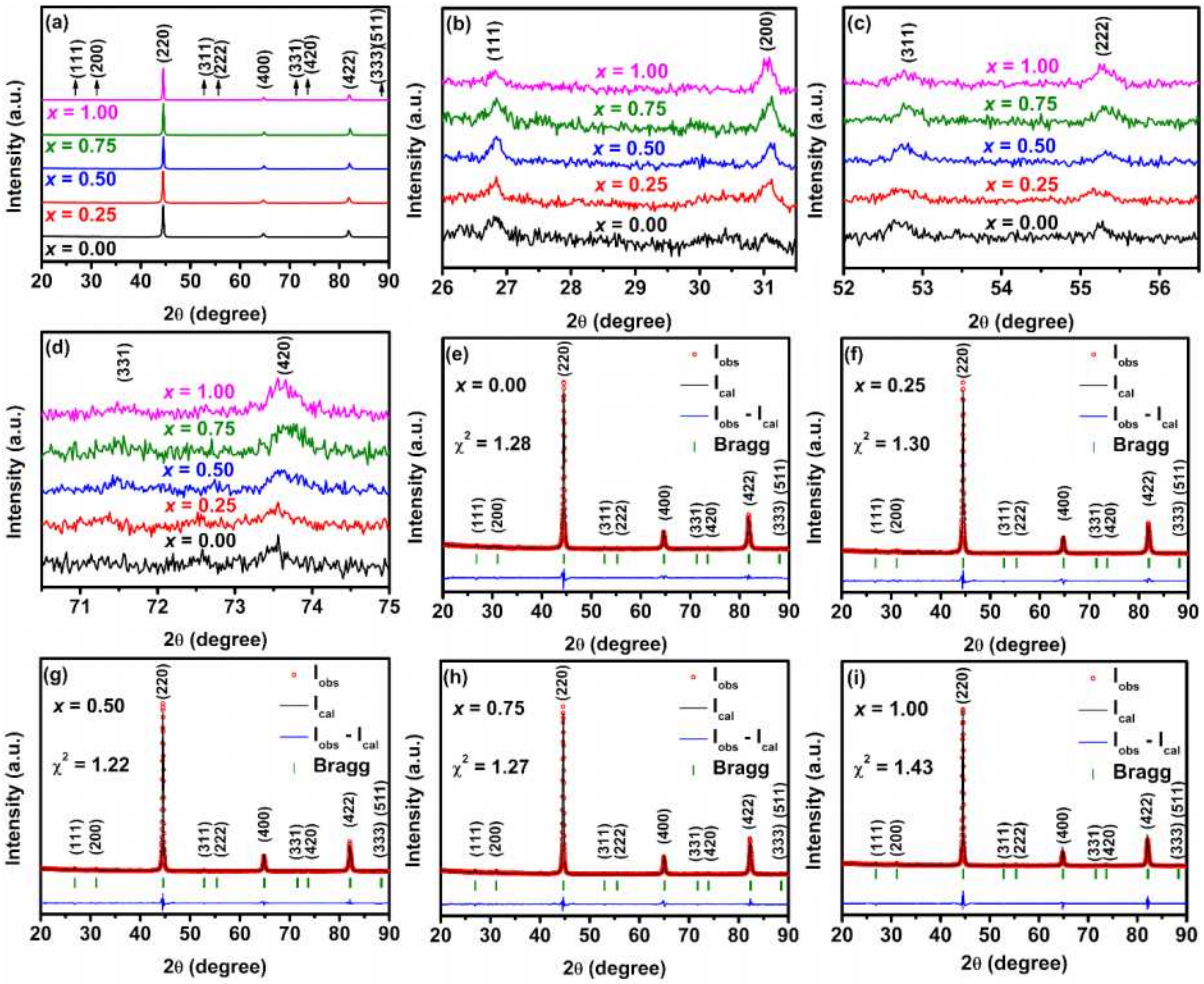

Figure 6.01. (a) XRD patterns of $Fe_{2-x}Co_{1+x}Ga$ nanoparticles, (b, c, d) magnified views of selected parts of (a). (e - i) Rietveld refined XRD patterns of $Fe_{2-x}Co_{1+x}Ga$ nanoparticles.

As cited in chapter 1, in the X_2YZ Heusler alloy, if the atomic number of X atom is higher than the atomic number of Y atom, its crystal structure is known as $L2_1$ type full Heusler alloy structure (space group 225 [$Fm\bar{3}m$]). On the other hand, if the atomic number of Y atom is higher than that of X atom, then the structure is referred to as *X* type inverse Heusler alloy structure (space group 216 [$F\bar{4}3m$]) [12]. By this definition, Co_2FeGa possesses $L2_1$ type full Heusler alloy structure, whereas Fe_2CoGa possesses *X* type inverse Heusler alloy structure as already demonstrated in earlier chapters (chapter 3 and 4). Here, the difference between the

two structures is only in the relative positions of constituent atoms. In Co_2FeGa with $L2_1$ type structure, the higher atomic number X atom (Co atoms) will occupy the Wyckoff positions (¼ ¼ ¼) and (¾ ¾ ¾), the lower atomic number Y (Fe atom) will occupy the Wyckoff position (½ ½ ½) and the Z atom (Ga atom) will occupy the Wyckoff position (0 0 0) [134]. In contrast, in Fe_2CoGa with *X* type structure, the lower atomic number X atom (Fe atoms) will occupy Wyckoff positions (½ ½ ½) and (¾ ¾ ¾), the higher atomic number Y atom (Co atom) will occupy the Wyckoff position (¼ ¼ ¼) and Z atom (Ga atom) will occupy the Wyckoff position (0 0 0) [134]. Now, the question arises about the preferred structure of the intermediate compositions. On the basis of Wyckoff positions of different atoms in the stable configuration of Heusler alloys, the distance between two nearest higher atomic number atoms (Co in our case) in $L2_1$ type alloys must be $a/2$ and the distance between two nearest lower atomic number atoms (Fe in our case) in *X* type alloys must be $\sqrt{3}a/4$. Let us now consider the intermediate composition $Fe_{1.5}Co_{1.5}Ga$ containing equal amounts of Fe and Co atoms. Its most stable structure is expected to be the one having a distance of $a/2$ between the two nearest Co atoms (higher atomic number) following $L2_1$ type structure and a distance of $\sqrt{3}a/4$ between the two nearest Fe atoms (lower atomic number) following *X* type structure. In order to confirm this, the unit cell of $Fe_{1.5}Co_{1.5}Ga$ alloy was designed in all the six possible combinations designated as C1 to C6 (*c.f.* Figure 6.02). This assignment is based on their atomic positions listed in Table 6.02 by keeping the Ga position fixed at the origin (0 0 0). All these six combinations are not unique. They can be further categorized into three unique groups, namely, G1 (including combinations C1 and C2), G2 (including combinations C3 and C4) and G3 (including combinations C5 and C6). Both the combinations in each group have equivalent structures. In both the combinations of group G1 (*i.e.* C1 and C2), the distance between the two nearest Co atoms is $a/2$ and the distance between the two nearest Fe atoms is $\sqrt{3}a/4$, which indicates it to be the stable configuration. On the other hand, in both the combinations of group G2 (*i.e.* C3 and

C4), the distance between the two nearest Co atoms is $\sqrt{3}a/4$ and the distance between the two nearest Fe atoms is $a/2$ which are opposite to the stable configuration. The combinations C5 and C6 in group G3 lie between the two mentioned cases. Here, the distance between the two nearest Co and two nearest Fe atoms is $\sqrt{3}a/4$ in both cases. Thus, these two combinations will be of medium stability. In order to confirm this hypothesis, ground-state energy calculations were performed on the three combinations, *viz.*, C1 of group G1, C3 of group G2 and C5 of group G3. Figure 6.03 illustrates the energy *E versus* volume *V* plots for $Fe_{1.5}Co_{1.5}Ga$ for the three mentioned combinations. It reveals that the combination C1 has the minimum energy, combination C3 has the maximum energy and combination C5 has energy value in between that of C1 and C3 as predicted above. The analysis clarifies that the combination C1 corresponds to the most stable configuration. Now, addressing the assignment of $L2_1$ or *X* type structure to $Fe_{1.5}Co_{1.5}Ga$, it was evident that being exactly in the middle, either substitution of 0.5Fe in $L2_1$ type Co_2FeGa (moving from right to left in Table 6.03) or substitution of 0.5Co in *X* type Fe_2CoGa (moving from left to right in Table 6.03) would result in the same structure. Therefore, we can conclude that both $L2_1$ and *X* type structures are equivalent for the alloy $Fe_{1.5}Co_{1.5}Ga$. The alloy $Fe_{1.75}Co_{1.25}Ga$ being Fe rich will correspond to *X* type structure and the alloy $Fe_{1.25}Co_{1.75}Ga$ being Co rich will correspond to $L2_1$ type structure.

Table 6.02. All possible combinations of Wyckoff positions for $Fe_{1.5}Co_{1.5}Ga$.

Site	Position	Elements and their occupancies in each combination					
		Group G1		Group G2		Group G3	
		C1	C2	C3	C4	C5	C6
4d	¾ ¾ ¾	0.5Fe	Co	0.5Fe	Fe	Fe	Co
		0.5Co		0.5Co			
4b	½ ½ ½	Fe	Fe	Co	Co	0.5Fe	0.5Fe
						0.5Co	0.5Co
4c	¼ ¼ ¼	Co	0.5Fe	Fe	0.5Fe	Co	Fe
			0.5Co		0.5Co		
4a	0 0 0	Ga	Ga	Ga	Ga	Ga	Ga

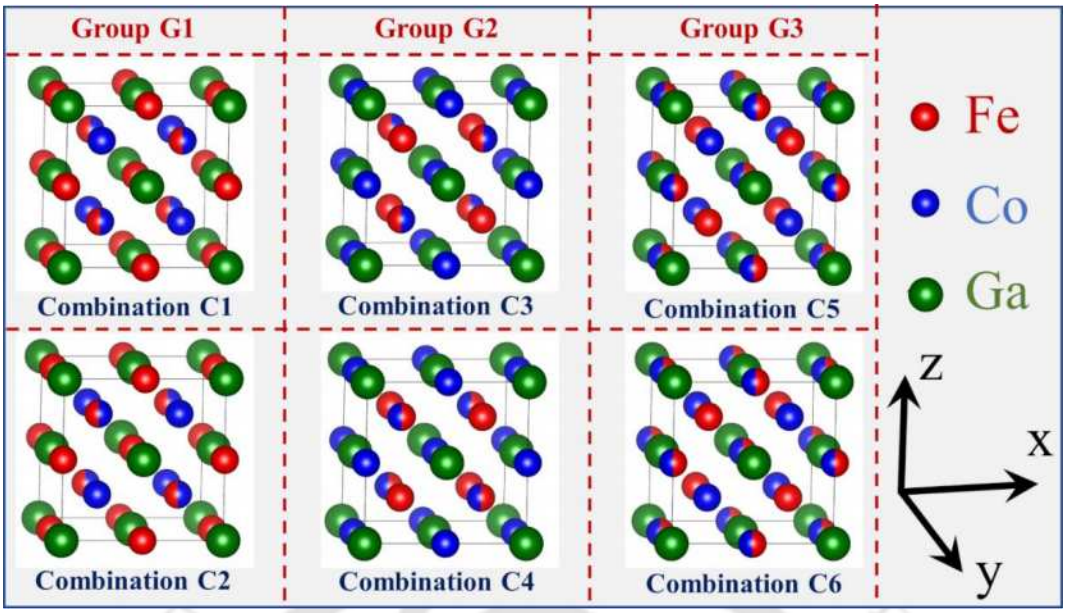

Figure 6.02. Schematic diagram representing all possible combinations of unit cells for $Fe_{1.5}Co_{1.5}Ga$ alloy by keeping Ga position fixed at the origin (000).

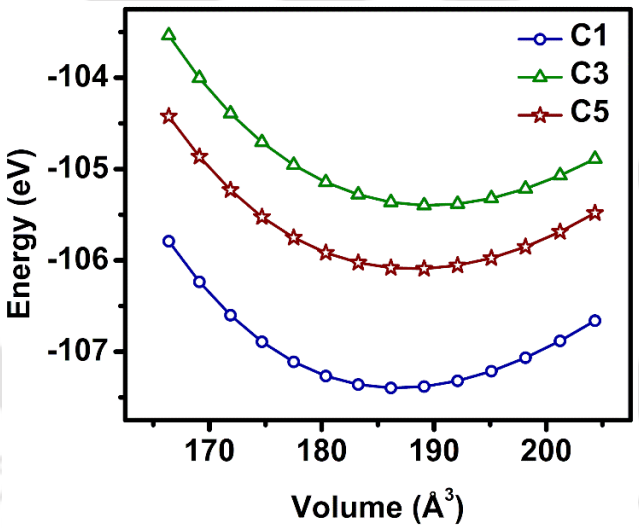

Figure 6.03. Variation of energy as a function of volume for $Fe_{1.5}Co_{1.5}Ga$ alloy.

Table 6.03. Wyckoff atomic positions of $Fe_{2-x}Co_{1+x}Ga$ alloys.

Wyckoff position (Site)	Atoms along with their occupancies at different Wyckoff positions for				
	x = 0.00 (Fe_2CoGa)	x = 0.25 ($Fe_{1.75}Co_{1.25}Ga$)	x = 0.50 ($Fe_{1.5}Co_{1.5}Ga$)	x = 0.75 ($Fe_{1.25}Co_{1.75}Ga$)	x = 1.00 ($FeCo_2Ga$)
¾ ¾ ¾ (4d)	1Fe	0.75Fe	0.5Fe	0.25Fe	1Co
		0.25Co	0.5Co	0.75Co	
½ ½ ½ (4b)	1Fe	1Fe	1Fe	1Fe	1Fe
¼ ¼ ¼ (4c)	1Co	1Co	1Co	1Co	1Co
0 0 0 (4a)	1Ga	1Ga	1Ga	1Ga	1Ga

On the basis of the above discussion, the Wyckoff positions for $Fe_{2-x}Co_{1+x}Ga$ (x = 0.00, 0.25, 0.50, 0.75, 1.00) alloys in their stable configuration are listed in Table 6.03. These atomic positions were used in the Rietveld refinement of the experimental XRD patterns of the nanoparticles using the FullProf Suite software (*c.f.* Figure 6.01(e-i)). The low χ^2 values listed in Table 6.04 indicate the good fits obtained to the experimental XRD patterns. The Rietveld refined data were used to generate the simulated XRD patterns using the Vesta software. The normalized intensities of reflections in the simulated and experimental XRD patterns are listed in Table 6.05. The elements Fe, Co and Ga in the alloys produce very weak superlattice reflections (111) and (200) due to their nearly identical X-ray scattering factors [154]. As a result, the intensities of the superlattice reflections (111) and (200) are ~1 % of the most intense (220) reflection (listed in Table 6.05), making it difficult to identify them above the noise level in powder XRD patterns. This could be the reason why many earlier researchers were unable to detect these superlattice reflections in their XRD patterns even in bulk/thin film forms of stoichiometric Co_2FeGa [142,145,147,149] and Fe_2CoGa [167] alloys. As mentioned earlier, detection of these superlattice peaks becomes even more arduous in off-stoichiometric alloy nanoparticles. So, several researchers had to rely on other specialized techniques such as selective energy-based anomalous/modified XRD measurements, extended X-ray absorption fine structure spectroscopy, X-ray absorption near edge structure measurements and Raman spectroscopy to establish crystalline order in Co_2FeGa and Fe_2CoGa nanoparticles synthesized by them [58,59,79–82,84]. As mentioned earlier, such syntheses performed using templates revealed Fe and/or Co impurity phases in their XRD patterns [59,80,84]. However, in our case, the XRD patterns of all the synthesized $Fe_{2-x}Co_{1+x}Ga$ nanoparticles clearly reveal the presence of not only the intrinsically weak (111) and (200) reflections but even weaker reflections like (311), (222) and (420) in the XRD patterns without the need for any special instrumentation or arrangement. Figure 6.01(b-d) represents the enlarged view of different regions in the XRD

pattern shown in Figure 6.01(a) to highlight the presence of these intrinsically weak reflections. Thus, the high crystalline order in the synthesized $Fe_{2-x}Co_{1+x}Ga$ nanoparticles is evident. The degree of *B2* and $L2_1$ (or *X*) ordering [13], which are termed as S_{B2} and S_{L2_1}(or S_X), respectively, in the synthesized $Fe_{2-x}Co_{1+x}Ga$ nanoparticles have been estimated using the intensity ratios of (111) and (200) to (220) reflection in equations 1.01 and 1.02. The estimated values of S_{B2} and S_{L2_1}(or S_X) for the synthesized nanoparticles listed in Table 6.04 are close to the ideal value of unity for fully ordered $L2_1$ (or *X*) type structures. In all these nanoparticles, the fraction of *B2* disorder is ≤ 9 % and the deviation from full $L2_1$ (or *X*) type ordered structure is ≤ 21 %, which further validate the high degree of $L2_1$ (or *X*) ordering achieved in the synthesized nanoparticles.

Table 6.04. Structural data and overall elemental composition of $Fe_{2-x}Co_{1+x}Ga$ nanoparticles.

x	*a* (Å)	χ^2	Degree of structural order		D_v (nm)	*d* (nm)	Nominal Composition	Measured Composition	Measured Composition (in f.u.)
			S_{B2}	S_{L2_1}/ S_X			Fe:Co:Ga (at. %)		
0.00	5.764	1.28	0.91	0.82	42±1	56±1	50.00:25.00:25.00	49.3:25.9:24.8	$Fe_{1.97}Co_{1.04}Ga_{0.99}$
0.25	5.758	1.30	0.96	0.88	42±1	56±1	43.75:31.25:25.00	44.2:31.8:24.0	$Fe_{1.77}Co_{1.27}Ga_{0.96}$
0.50	5.750	1.22	0.96	0.93	49±1	64±1	37.50:37.50:25.00	37.5:37.8:24.7	$Fe_{1.50}Co_{1.51}Ga_{0.99}$
0.75	5.738	1.27	0.96	0.93	48±1	63±1	31.25:43.75:25.00	31.2:44.2:24.6	$Fe_{1.25}Co_{1.77}Ga_{0.98}$
1.00	5.751	1.43	0.96	0.79	47±1	64±1	25.00:50.00:25.00	25.9:49.1:25.0	$Fe_{1.04}Co_{1.96}Ga_{1.00}$

FETEM studies provided additional support to the high ordering of the synthesized nanoparticles. Figure 6.04(a) represents the SAED pattern consisting of concentric ring patterns for the planes (111), (200), (220), (311), (222), (400), (331), (420) and (422) from $Fe_{1.5}Co_{1.5}Ga$ nanoparticles. Figure 6.04(b and c) show HRETM micrographs and their iFFT images representing the presence of superlattice planes (111) and (200) in $Fe_{1.5}Co_{1.5}Ga$ nanoparticles. Thus, the presence of superlattice reflections in both the SAED pattern and HRTEM micrographs authenticates the formation of fully ordered $L2_1$/*X* type structures in the synthesized nanoparticles. The FETEM image of $Fe_{1.5}Co_{1.5}Ga$ nanoparticles shown in Figure 4(d) reveals that the particle size is ~ 66 nm.

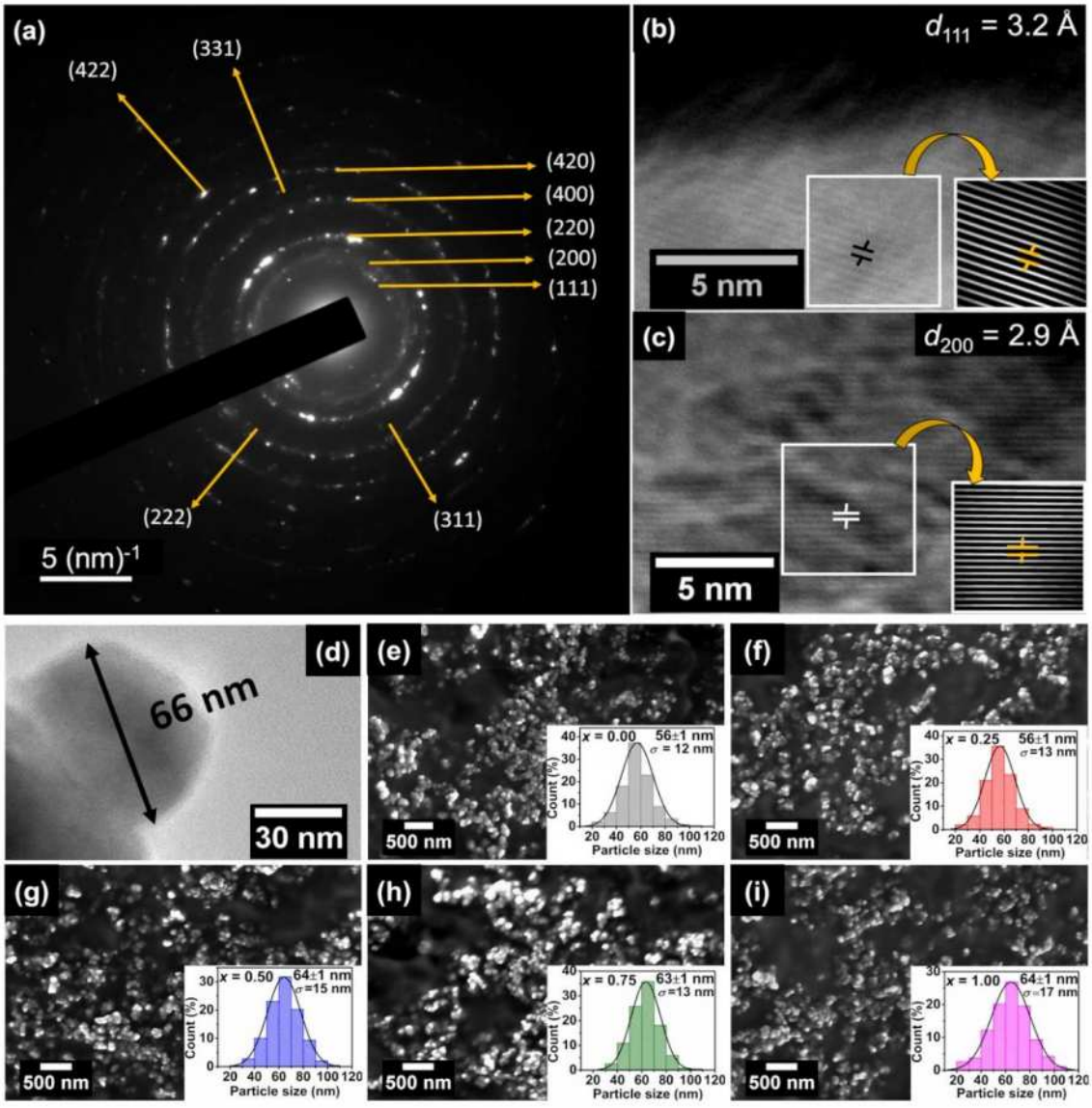

Figure 6.04. (a) SAED pattern, (b, c) HRTEM images with their iFFT images as insets, and (d) FETEM image of a $Fe_{1.5}Co_{1.5}Ga$ nanoparticle. (e-i) FESEM images of alloys with (e) x = 0.00, (f) x = 0.25, (g) x = 0.50, (h) x = 0.75, and (i) x = 1.00, with particle size distributions as insets.

The lattice constant (a) values obtained from the Rietveld refinement and D_v estimated using Schërrer's equation (equation 2.18) of the synthesized alloy nanoparticles are listed in Table 6.04. a of stoichiometric end compounds lie within the reported range of 5.727-5.812 Å for Fe_2CoGa [37,134,163–165,167] and 5.70 –5.7615 Å for Co_2FeGa [23,37,117,119,124,125,128,134,138,139,142,143,58,145,147–149,80–82,106,114–116]. The lattice constant does not show any trend with x as also observed in $Co_{2-x}Fe_{1+x}Si$ [192], Co_{3-}

$_xFe_xSi$ [193], $Fe_{3-x}Co_xSi$ [194], $Co_{1+x}Fe_{2-x}Si$ [190] and $Co_{3-x}Fe_xAl$ [195] alloys due to the small difference in the radii of Fe and Co. Since D_v influences the properties of the nanoparticles, heat treatment conditions were chosen carefully to obtain D_v in a close range of 42 - 49 nm.

Table 6.05. Structural information obtained from simulated (Sim.) and experimentally recorded (Exp.) XRD patterns of $Fe_{2-x}Co_{1+x}Ga$ nanoparticles.

Plane (*hkl*)	d_{hkl} (Å)	Normalized intensity of reflections in various samples									
		x = 0.00		x = 0.25		x = 0.50		x = 0.75		x = 1.00	
		Sim.	Exp.	Sim.	Exp.	Sim.	Exp.	Sim.	Exp.	Sim.	Exp.
(111)	3.32	1.1	0.8	1.1	0.9	1.1	1	1.1	1	1.1	0.7
(200)	2.88	0.72	0.6	0.76	0.7	0.87	0.8	0.87	0.8	0.87	0.8
(220)	2.03	100	100	100	100	100	100	100	100	100	100
(311)	1.73	0.71	0.6	0.7	0.4	0.7	0.6	0.71	0.6	0.7	0.5
(222)	1.66	0.26	0.6	0.28	0.4	0.33	0.4	0.33	0.6	0.33	0.7
(400)	1.44	14.64	10.2	14.61	9.1	14.55	9.1	14.53	10.4	14.54	8.5
(331)	1.32	0.33	-	0.33	0.3	0.33	0.3	0.33	-	0.33	-
(420)	1.29	0.4	0.6	0.43	0.5	0.52	0.4	0.52	0.5	0.52	0.7
(422)	1.17	27.7	20.4	27.62	17.6	27.4	17.6	27.39	21.1	27.4	16.7
(333)	1.11	0.07	-	0.07	-	0.07	-	0.07	-	0.07	-
(511)	1.11	0.22	-	0.21	-	0.21	-	0.21	-	0.21	-

6.3 Elemental composition and morphology

EDS analysis shows that the overall compositions of the nanoparticles are very close to the nominal compositions as listed in Table 6.04. Fig. 6.04(e-i) represent the morphology and the particle size histograms of the synthesized nanoparticles. All the synthesized nanoparticles exhibit nearly spherical shape, which is consistent with the morphology of other Heusler alloy nanoparticles prepared using similar methodology [187]. Table 6.04 shows the particle size (d) values of the synthesized nanoparticles. The value of d ranges from 56 to 64 nm with σ ranging from 12 to 17 nm (see Figure 6.04(e-i)). The d values of 8.5 to 35 nm have been reported for Fe_2CoGa and Co_2FeGa nanoparticles synthesized using template assisted methods [58,59,79–82,152]. Here, it is also relevant to point out that d > 77 nm have also been reported for Co_2FeGa nanoparticles prepared by template assisted methods [79,80]. Thus, our methodology provides impurity free Heusler alloy nanoparticles with acceptable d values. In comparison to

D_v, d is somewhat larger in all cases, indicating some amount of crystallite agglomeration. As we approach the nanometer regime, the surface energy of the particles increases due to the increase in the surface to volume (S/V) ratio. To minimize the surface energy, the nanocrystallites tend to agglomerate and form bigger particles. Moreover, if the particles are magnetic with high magnetic moment, then the strong magnetic interaction can further enhance this agglomeration. As a result, the d can be bigger than the D_v. This type of agglomeration is common in magnetic nanoparticles [44], and also observed in Co_2FeGa, Fe_2CoGa and Fe_2CoAl nanoparticles discussed in previous chapters. As mentioned in the earlier chapters 3, 4 and 5, obtained σ values though slightly higher than that of nanoparticles synthesized using templates, are within acceptable range.

6.4 DOS calculations

Fe_2CoGa is known to be a non-half metal whereas Co_2FeGa has been established as a Type III half metal in chapters 3 and 4 of this thesis. Some earlier studies have pointed out that intermediate off-stoichiometric compounds exhibit better half metallic properties and P as compared to the stoichiometric end compositions [189]. Therefore, *ab initio* studies were carried out on $Fe_{1.75}Co_{1.25}Ga$, $Fe_{1.5}Co_{1.5}Ga$ and $Fe_{1.25}Co_{1.75}Ga$ alloys as per the procedure explained in chapter 2 using the stable configuration (see Table 6.03) and experimental a values. The TDOS plots of all the intermediate alloys (*c.f.* left panel of Figure 6.05) show that the valance band comprises of both the minority and majority spins, whereas, the conduction band has a huge contribution mainly from the minority spins. The PDOS plots of the intermediate compounds (*c.f.* right panel of Figure 6.05) illustrate that the Fe and Co states are the primary contributors to the DOS with minor contributions from Ga states. A careful look at the TDOS of $Fe_{2-x}Co_{1+x}Ga$ (including Fe_2CoGa (see Figure 4.06) and Co_2FeGa (see Figure 3.04)) shown in the left panel of Figure 6.05 would reveal a pseudo bandgap like depression in the minority DOS near E_F. As mentioned in case of Co_2FeGa in chapter 3, incorporation of

Hubbard parameter (U) converts this pseudo bandgap to an actual bandgap, resulting in Type III half metallicity. Such behavior can also be obtained in the intermediate compounds, especially in $Fe_{1.25}Co_{1.75}Ga$ with $x = 0.75$ being closest to Co_2FeGa due to the pseudo bandgap situated at the least distance from E_F as compared to the rest of the intermediate compositions as listed in Table 6.06.

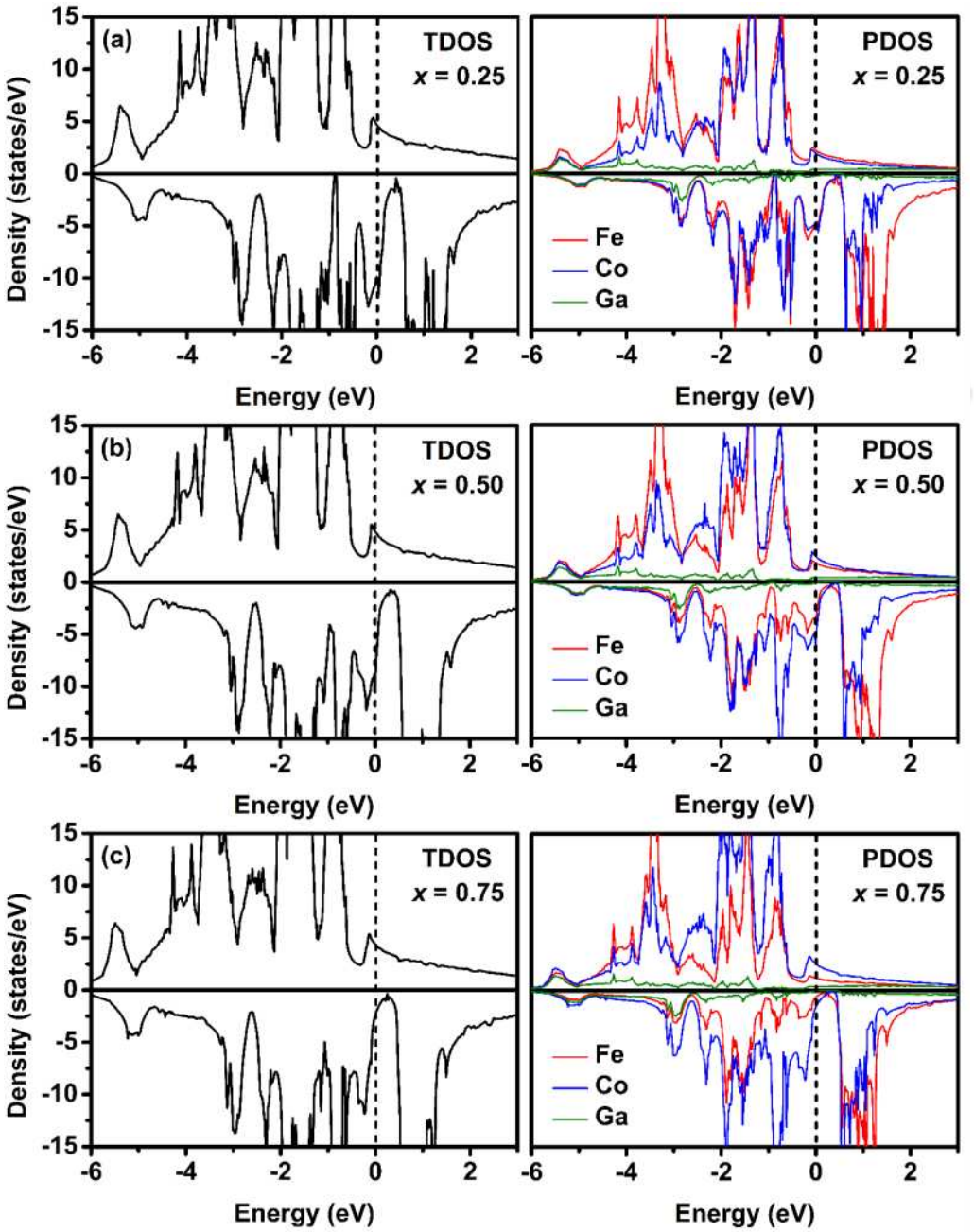

Figure 6.05. TDOS (left panel) and PDOS (right panel) near E_F of $Fe_{2-x}Co_{1+x}Ga$ alloys with (a) $x = 0.25$, (b) $x = 0.50$, and (c) $x = 0.75$.

Interestingly, it was found that this pseudo bandgap approaches close to E_F as the Co concentration is increased as depicted in Table 6.06. The pseudo bandgap which is at the distance of 0.42 eV in Fe_2CoGa is only at 0.13 eV in Co_2FeGa. The *P* values listed in Table 6.06 do not reveal any specific trend with change in Fe or Co content which is consistent with the previous study on $Co_{2+x}Fe_{1-x}Si$ by Herper *et al.* [191]. Here, one has to bear in mind that these *ab initio* calculations corresponds to the bulk crystal in its fully ordered state at 0 K, whereas the present samples are 0-d crystals and the experimental data were obtained at finite temperatures. Despite these limitations, these calculations provide valuable insights on the electronic and magnetic properties of these alloys which can serve as the ideal (theoretical limit) values for the sake of comparison with the experimental data. It may be recalled that Galdun *et al.* [156] observed higher *P* in Co_2FeSn nanowires as compared to the bulk counterpart. This creates a strong expectation for higher *P* in the synthesized $Fe_{2-x}Co_{1+x}Ga$ nanoparticles as compared to the bulk *P* estimated in our calculations and listed in Table 6.06.

Table 6.06. Electronic parameters of $Fe_{2-x}Co_{1+x}Ga$ alloys obtained from *ab initio* calculations.

x	$D_\uparrow$ at E_F (states/eV)	$D_\downarrow$ at E_F (states/eV)	*P* % (at E_F)	Separation of pseudo gap from E_F (eV)	DOS at pseudo bandgap (states/eV)
0.00	5.08	-10.41	34	0.42	-1.26
0.25	4.71	-9.96	36	0.41	-0.45
0.50	4.83	-10.55	37	0.33	-0.70
0.75	4.35	-2.36	30	0.25	-0.35
1.00	3.65	-0.78	65	0.13	-0.28

6.5 Magnetic properties

The calculated M_t of $Fe_{2-x}Co_{1+x}Ga$ alloys are listed in Table 6.07. M_t of stoichiometric end compounds lie within the M_t ranges of 5.11 to 6.14 μ_B/f.u. [119,132,134,163–166] for Fe_2CoGa and 5.00 to 5.07 μ_B/f.u. [106,113,126,129,132,134,135,114–116,118–120,123,124] for Co_2FeGa alloys. However, no reports on the intermediate compounds $Fe_{2-x}Co_{1+x}Ga$ (x = 0.25, 0.50, 0.75) are available for comparison in the literature. M_t values estimated using S-P rule

[24] are also listed in Table 6.07. The *M-H* curves of $Fe_{2-x}Co_{1+x}Ga$ nanoparticles at temperatures 5 K and 300 K are displayed in Figures 6.06(a and b), respectively. The soft magnetic behavior of the synthesized nanoparticles concurs with the previous reports on Fe_2CoGa [59] and Co_2FeGa [58,80] nanoparticles. The M_s values obtained for Fe_2CoGa and Co_2FeGa nanoparticles listed in Table 6.07 are comparable to the reported experimental M_s values of Fe_2CoGa (3.89 μ_B/f.u.) [59] and Co_2FeGa (4.5 - 4.9 μ_B/f.u.) [58,152] nanoparticles. M_s values of all the synthesized nanoparticles are within the limits of theoretically estimated M_t values of the respective alloy composition as listed in Table 6.07.

Table 6.07. Magnetic properties of $Fe_{2-x}Co_{1+x}Ga$ nanoparticles.

x	M_t (μ_B/f.u.)		M_s (μ_B/f.u.)		H_c (Oe)		M_r (μ_B/f.u.)		$K_{eff} \times 10^6$ (erg/cc)		t (nm)		D_{cr} (nm)	T_C (K)
	(S-P value)	Theo.	5 K	300 K	5 K	300 K	5 K	300 K	5 K	300 K	5 K	300 K		
0.00	4.076	5.30	5.15	5.08	12	7	0.03	0.02	7.44	6.32	0.20	0.29	93	1203
0.25	4.472	5.23	4.62	4.62	8	1	0.02	0.00	4.71	4.65	0.82	0.82	68	1199
0.50	4.572	4.99	4.86	4.81	7	2	0.02	0.00	6.16	6.09	0.21	0.30	69	1187
0.75	4.848	4.92	4.61	4.59	5	0	0.02	0.00	4.73	4.65	0.50	0.54	100	1153
1.00	4.964	5.04	3.95	3.90	4	9	0.01	0.02	4.03	3.84	1.70	1.77	100	1137

The small decrement in M_s of synthesized nanoparticles in respect to theoretically estimated M_t can be explained using the core-shell model [40]. The dead layer thickness t values corresponding to $Fe_{2-x}Co_{1+x}Ga$ nanoparticles have been estimated from equation 1.13 using experimental M_s values in the place of $M_s(d)$ and theoretically estimated M_t values in the place of M_s(b). It is clear from Table 6.07 that M_s of samples with higher t deviate more from their M_t. However, the resulting M_s or M_t values do not exhibit any particular pattern as a function of composition as also observed in prior studies on $Co_{2+x}Fe_{1-x}Si$ [191], $Co_{2-x}Fe_{1+x}Si$ [192], $Co_{3-x}Fe_xSi$ [193], $Fe_{3-x}Co_xSi$ [194], $Co_{1+x}Fe_{2-x}Si$ [190] and $Co_{3-x}Fe_xAl$ [195] alloys. Room temperature M_s values were found to be slightly lower than the M_s at 5 K. This decrement of M_s at higher temperatures follows the Bloch's law [70] for temperature dependent M_s as observed in many Heusler alloy nanoparticles [59,67,69,80,83,85,152] including those studied

in chapters 3, 4 and 5. Surprisingly, this decrease in M_s at elevated temperature is extremely small (*i.e.*, < 2 %) which indicates that these nanoparticles are suitable for device applications at high temperatures. This nearly constant M_s at high temperature ranges is the reason for the strong ferromagnetic interaction and high T_C of $Fe_{2-x}Co_{1+x}Ga$ nanoparticles [152].

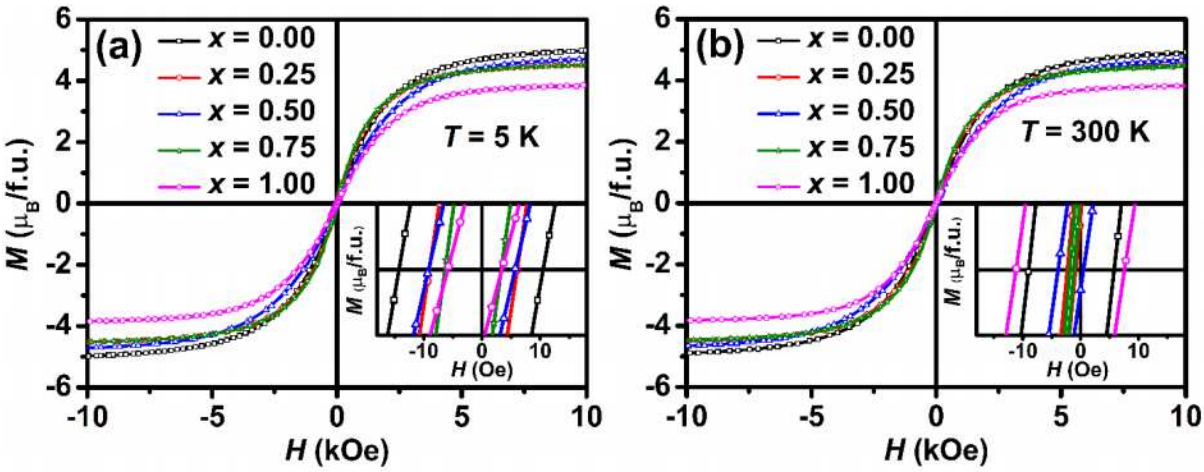

Figure 6.06. *M-H* loops recorded for $Fe_{2-x}Co_{1+x}Ga$ nanoparticles at temperatures (a) 5 K, and (b) 300 K. Insets provide an enlarged view of the data near the origin.

The LAS [145] was used to calculate the K_{eff} of the synthesized $Fe_{2-x}Co_{1+x}Ga$ nanoparticles which reveal high values of K_{eff} as listed in Table 6.07. Such high K_{eff} values in the range of $2.99 - 10.2 \times 10^6$ erg/cc have also been observed in Co_2FeGa nanoparticles [81,82]. At high temperatures, the thermal energy breaks the magnetic alignment and makes it easier for the domains to change their orientations. This can decrease the H_c and K_{eff} at higher temperatures. Such a decrease in H_c at higher temperatures can be explained through Kneller's law [169] and has been observed in single-domain nanoparticles [67,69,83,85,152] and in the single domain nanoparticles studied in chapters 3, 4 and 5. A decrease in K_{eff} at higher temperatures has also been observed in other magnetic nanoparticles [46,196–198] including those covered in previous chapters. Table 6.07 indicates that both H_c (except for $x = 1.00$) and K_{eff} of the synthesized nanoparticles decrease with increasing temperature in support of the above arguments. Further, the H_c values are very low (≤ 12 Oe) in all samples. Considering the

limited sensitivity of the high field (9 T) PPMS-based VSM system, precise measurement of such low coercivities (≤ 12 Oe) is not possible to demonstrate the expected trend as mentioned above. H_c values (≤ 12 Oe) of the synthesized nanoparticles are significantly lower than the reported H_c values of 110 Oe [59] for Fe_2CoGa and 40 – 585 Oe [58,80–82,152] observed in Co_2FeGa nanoparticles synthesized using template assisted methods. It is reported that the presence of the silica matrix hinders the movement of the magnetic domain walls and hence increases the H_c of the nanoparticles grown using silica templates [88]. Since lower H_c results in lower magnetic energy losses, template-less synthesis route is advantageous.

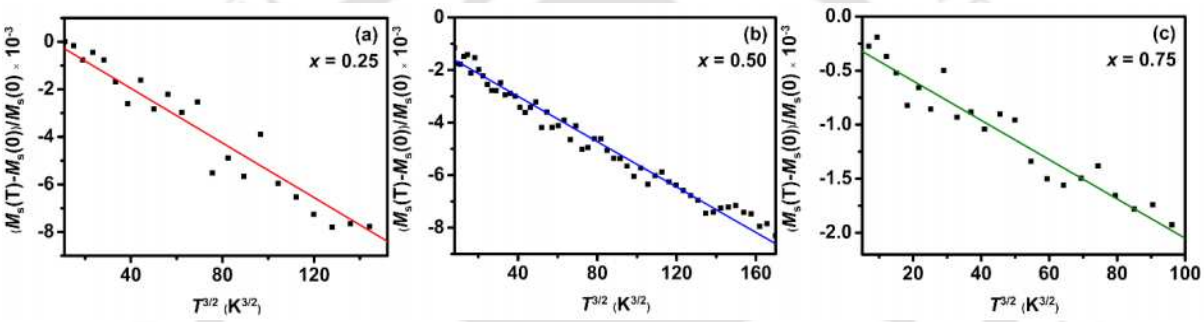

Figure 6.07. (($M_s(T)$ - $M_s(0)$) / $M_s(0)$) *versus* $T^{3/2}$ curves recorded at 2 T for $Fe_{2-x}Co_{1+x}Ga$ nanoparticles with (a) x = 0.25, (b) x = 0.50 and (c) x = 0.75. The solid lines are linear fits to the experimental data.

The evaluated Q values using equation 1.22 of all the prepared $Fe_{2-x}Co_{1+x}Ga$ nanoparticles were found to be > 0.9 which designates the synthesized nanoparticles as high anisotropic materials [42,43]. The identification of synthesized nanoparticles in single or multidomain regimes can be done using the estimation of this D_{cr} value for the synthesized $Fe_{2-x}Co_{1+x}Ga$ nanoparticles as per the procedure [47] mentioned in the introduction chapter. The slope B for intermediate composition nanoparticles with x = 0.25, x = 0.50 and x = 0.75 were estimated to be 5.74×10^{-5}, 4.32×10^{-5} and 1.82×10^{-5}, respectively, from Figures 6.07(a-c) in low temperature regime [49]. They were used to evaluate $A = 1.95 \times 10^{-7}$ erg/cm and $D = 1.81 \times 10^{-29}$ erg/cm^2 for the composition with x = 0.25, $A = 1.90 \times 10^{-7}$ erg/cm and $D = 3.35 \times 10^{-29}$

erg/cm^2 for the composition with x = 0.50, and A = 4.31 × 10^{-7} erg/cm and D = 3.69 × 10^{-29} erg/cm^2 for the composition with x = 0.75 using equations 1.24 – 1.26. Finally, the obtained A and D were used in equation 1.23 to calculate the D_{cr} values which are listed in Table 6.07. The D_{cr} values for end compositions Co_2FeGa and Fe_2CoGa have already been estimated in earlier chapters 3 and 4. Comparing the calculated D_{cr} values listed in Table 6.07 with the D_v of the respective sample listed in Table 6.04, it is clear that all the synthesized nanoparticles are in single domain regime. Additionally, the near zero H_c (≤ 12 Oe) and near zero magnetic remanence M_r (≤ 0.03 μ_B/f.u.) of the synthesized nanoparticles as listed in Table 6.07 indicate that these nanoparticles are likely to superparamagnetic in nature.

Figure 6.08(a) shows the *M-T* curves of the nanoparticles recorded at an applied field of 100 Oe. The y-axis of the graph shows normalized magnetization M/M_{1050}, where M and M_{1050} are magnetic moments measured at temperatures T and 1050 K, respectively. The *M-T* curves manifest high T_C values of all the synthesized $Fe_{2-x}Co_{1+x}Ga$ nanoparticles as listed in Table 6.07. The observed T_C values of stoichiometric Fe_2CoGa (1203 K) and Co_2FeGa (1137 K) nanoparticles are higher than the experimental T_C values of 1165 K for Fe_2CoGa [23] and 844 – 1117 K [23,116,149,117,121,136,139,140,145,147,148] of Co_2FeGa compounds reported earlier. Thus, the highly ordered $Fe_{2-x}Co_{1+x}Ga$ alloy nanoparticles exhibit the highest experimental T_C reported so far in any form (bulk/nanowires/nanoparticles) of the mentioned Heusler alloys. This enhancement in T_C is clearly due to the enhanced crystallinity of these nanoparticles. T_C values were found to decrease with an increase in Co content as depicted in Figure 6.08(b). A similar dependence of T_C was also found in $Co_{2-x}Fe_xCrAl$ alloys [199]. The reason for this decrease in T_C with increasing Co content lies in the structural differences between Fe-rich and Co-rich compounds. In Fe_2CoGa (for x = 0) with *X* type unit cell, Ga atom is situated at (0 0 0), Co atom is situated at (¼ ¼ ¼) and both Fe atoms are situated at (½ ½ ½) and (¾ ¾ ¾). Therefore, the magnetic interactions are dominated by both Fe-Fe and Fe-Co

interactions at their nearest neighbourhood. On the other hand, in Co_2FeGa (for $x = 1$) with $L2_1$ type unit cell, Ga atom is situated at (0 0 0), Fe atom is situated at (½ ½ ½) and both the Co atoms are situated at (¼ ¼ ¼) and (¾ ¾ ¾). Therefore, the magnetic interactions are mainly dominated by Fe-Co interactions at the nearest neighbour sites. Thus, in *X* type ordered Fe rich compounds, the stronger Fe-Fe interactions dominate over weak Fe-Co interactions. As the Co content is increased, the *X* type structure gradually transforms to $L2_1$ type structure. In this process, the strong Fe-Fe interactions decrease and the weak Fe-Co interaction increase. This in turn decreases the overall strength of the magnetic interaction in the alloys. Hence, the T_C decreases with an increase in Co content.

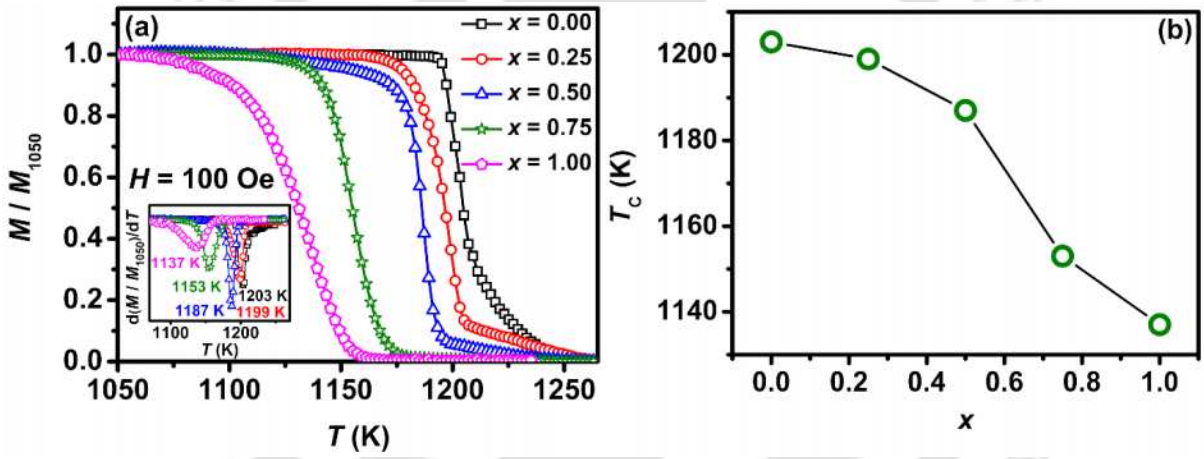

Figure 6.08. (a) *M-T* curves of $Fe_{2-x}Co_{1+x}Ga$ nanoparticles with the inset depicting the derivative of magnetization with respect to temperature and (b) plot of T_C as a function of *x*.

6.6 Summary and highlights

The first ever comprehensive composition dependent study has been carried out on chemically synthesized $Fe_{2-x}Co_{1+x}Ga$ ($0 \leq x \leq 1$) nanoparticles using both experimental and theoretical tools which opens up possibility of developing new nanomaterials for nanomagnetic applications. The highlights of this study are summarized below:

- Highly ordered single domain $Fe_{2-x}Co_{1+x}Ga$ nanoparticles with x = 0.00, 0.25, 0.50, 0.75, and 1.00 have been successfully synthesized using a simple template less chemical route.

Adoption of a template-free preparation route ensured impurity-free and phase-pure Heusler alloy nanoparticles.

- Depending on the composition, these nanoparticles exhibit highly ordered $L2_1$ or *X* type Heusler alloy structure. The stability of the crystal structures has been confirmed using energy calculations. The formation of highly ordered $L2_1$ and *X* type structures have been confirmed by the presence of superlattice reflections in the XRD and SAED patterns of the synthesized nanoparticles.
- These magnetic nanoparticles exhibit high M_s (3.90 – 5.15 μ_B/f.u.), high T_C (1137-1203 K), high K_{eff} (3.84-7.44 × 10^6 erg/cc), very low H_c (≤ 12 Oe) and very low M_r (≤ 0.03 μ_B/f.u.).
- The calculated D_{cr} show that the nanoparticles are in single domain regime. Negligible H_c and M_r indicate a strong probability of superparamagnetism in the synthesized nanoparticles.
- Systematic DOS calculations performed on $Fe_{2-x}Co_{1+x}Ga$ alloys indicate a means to find improved half metallicity in off-stoichiometric compositions of Heusler alloys.
- A strong dependence of T_C is observed with Co/Fe composition and the T_C values increase with increase in Fe content in $Fe_{2-x}Co_{1+x}Ga$ alloy nanoparticles.
- Negligible decrement of M_s at higher temperatures demonstrates the stability of the ferromagnetic phase over a large temperature range.
- T_C values well above room temperatures demonstrates the suitability of the materials to high temperature device applications.
- All these results indicate $Fe_{2-x}Co_{1+x}Ga$ nanoparticles to be promising candidates for high density magnetic media and nanomagnetic sensor applications.

Chapter 7

Investigations on $Fe_2CoGa_{0.5}Al_{0.5}$ nanoparticles

Though ternary Fe_2CoGa and Fe_2CoAl compounds are well-studied alloys in bulk (3-d) as well as low (2-, 1- and 0-) dimensional forms, the intermediate quaternary composition of $Fe_2CoGa_{0.5}Al_{0.5}$ has not been explored till now either in bulk or lower dimensional forms. The interest in quaternary Heusler alloys such as $Fe_2CoGa_{0.5}Al_{0.5}$ stems from the fact that these intermediate compositions carry the benefits of the two end ternary compositions and hence have better potential for applications. While it is relatively easy to prepare bulk quaternary Heusler alloys by arc melting, it is extremely difficult to prepare quaternary Heusler alloy nanoparticles with desired stoichiometry. Thus, one can find only a few reports on bulk quaternary Heusler alloys containing *s-p* elements Ga and Al, say, $Cu_{50}Mn_{25}Ga_xAl_{25-x}$ ($0 \leq x \leq 10$) [200], $Ru_2VGa_xAl_{1-x}$ ($0 \leq x \leq 1$) [201], $NiMnGa_{2-x}Al_x$ ($0 \leq x \leq 2$) [202], $Fe_2MnGa_{1-x}Al_x$ ($0 \leq x \leq 1$) [203], and $Fe_{50}Mn_{25}Ga_xAl_{25-x}$ ($0 \leq x \leq 10$) [204] *etc.* alloys in the literature, with none pertaining to investigations on nanoparticles. This provided the impetus to synthesize quaternary $Fe_2CoGa_{0.5}Al_{0.5}$ nanoparticles using template-less chemical approach and explore their structural and magnetic properties.

7.1 Sample preparation

$Fe_2CoGa_{0.5}Al_{0.5}$ nanoparticles have been synthesized using a chemical method without utilizing any templates following the procedure shown in Figure 2.01. Estimated amounts of precursors, *i.e.*, 1.3373 g of $Fe(NO_3)_3.9H_2O$, 0.4001 g of $CoCl_2.6H_2O$, 0.6904 g of $Ga(NO_3)_3.8H_2O$ and

0.2331 g of $Al(NO_3)_3.9H_2O$ were utilized as precursors. The dried powders were heat-treated at optimized conditions (800 ℃ for 5 h) in appropriate environment as explained in chapter 2.

7.2 Structural analysis

The Rietveld refined XRD patterns of the synthesized $Fe_2CoGa_{0.5}Al_{0.5}$ nanoparticles using *X*-type inverse Heusler alloy unit cell (space group 216 [$F\bar{4}3m$]) is displayed in Figure 7.01(a). Presence of the three prominent reflections of the Heusler alloy crystal planes, namely, (220), (400), and (422), validates the formation of single-phase Heusler alloy structure. The higher atomic number of Y(Co) atom than that of X(Fe) atom in formula $X_2YZ_{0.5}Z^*_{0.5}$ ($Fe_2CoGa_{0.5}Al_{0.5}$) predicts the formation of *X*-type inverse Heusler alloy structure rather than $L2_1$-type full HA structure [12]. Moreover, the stability of *X*-type structure has already been confirmed in Fe_2CoGa (chapter 4) and Fe_2CoAl (chapter 5). However, the XRD patterns of $Fe_2CoGa_{0.5}Al_{0.5}$ Heusler alloy simulated for $L2_1$ and *X*-type unit cells as depicted in Table 7.01, are nearly indistinguishable. Rietveld refinements of the experimental XRD data based on $L2_1$ and *X*-type unit cells also could not resolve the issue due to similar values of χ^2. So, total energy calculations were performed as a function of cell volume for $Fe_2CoGa_{0.5}Al_{0.5}$ considering both $L2_1$ and *X*-type structures as performed in case of Fe_2CoGa (chapter 4) and Fe_2CoAl (chapter 5. Figure 7.01(b) shows that the energy curve corresponding to the *X*-type structure has lower energy which signifies that $Fe_2CoGa_{0.5}Al_{0.5}$ is stabler with *X*-type inverse Heusler alloy structure. To understand the absence of superlattice reflections (111) and (200) in its experimental XRD pattern, let us look at the intensities of these reflections in the simulated patterns. Table 7.01 clarified that intensities of (111) and (200) reflections are < 1 % of that of (220) which make them non-detectable in the experimental XRD pattern above the noise level, as also observed in the cases of Fe_2CoGa and Fe_2CoAl synthesized by us (chapters 4 and 5) as well as by other authors [63,167,172]. This task becomes more arduous in a quaternary alloy with more probability of intermixing, apart from smearing effect due to surface defects and

finer crystallites [59,63]. In order to resolve this, FETEM studies were performed on $Fe_2CoGa_{0.5}Al_{0.5}$ nanoparticles. The presence of weak (111) and (200) superlattice reflections in the SAED patterns and HRTEM micrographs, as depicted in Figure 7.01(c-e), conclusively establishes the formation of fully ordered *X*-type structure in $Fe_2CoGa_{0.5}Al_{0.5}$ nanoparticles. The values of *a* obtained from the Rietveld refinement and D_v estimated using Schërrer's equation (equation 2.18) for the $Fe_2CoGa_{0.5}Al_{0.5}$ nanoparticles are 5.745 Å and 42±1 nm, respectively. Comparison of *a* obtained for $Fe_2CoGa_{0.5}Al_{0.5}$ nanoparticles with *a* of similar sized Fe_2CoGa (5.764 Å with D_v of 42 nm as mentioned in chapter 6) and Fe_2CoAl (5.723 Å with D_v of 41 nm as mentioned in chapter 5) nanoparticles, show a decreasing trend in *a* with increasing Al content. Similar trend was also observed in bulk $Ru_2VGa_xAl_{1-x}$ ($0 \leq x \leq 1$) [201], $NiMnGa_2$-$NiMnAl_2$ [202], and $Fe_{50}Mn_{25}Ga_xAl_{25-x}$ ($0 \leq x \leq 10$) [204] Heusler alloys. Mishra *et al.* [204] correctly attributed this behavior to the difference in the atomic radii of Ga and Al. Interestingly, the linear increment in *a* with Ga content follows the relation,

$$a_{Fe_2CoGa_{0.5}Al_{0.5}} \approx (a_{Fe_2CoGa} + a_{Fe_2CoAl})/2 \quad \text{------} \quad 7.01$$

in line with the Vegard's law [205].

Table 7.01. Simulated (Sim.) and experimental (Expt.) XRD data of $Fe_2CoGa_{0.5}Al_{0.5}$ nanoparticles.

Crystallographic plane (*hkl*)	d_{hkl} (Å)	Normalized intensity of the reflection in		
		Sim. XRD pattern for unit cell of		XRD pattern (Expt.)
		$L2_1$	*X*	
(111)	3.32	0.67	0.66	-
(200)	2.88	0.32	0.35	-
(220)	2.03	100.00	100.00	100
(311)	1.73	0.32	0.29	-
(222)	1.66	0.07	0.09	-
(400)	1.44	14.60	14.60	10.3
(331)	1.32	0.15	0.13	-
(420)	1.29	0.10	0.14	-
(422)	1.17	27.67	27.67	16.7
(333)	1.11	0.04	0.03	-
(511)	1.11	0.11	0.09	-

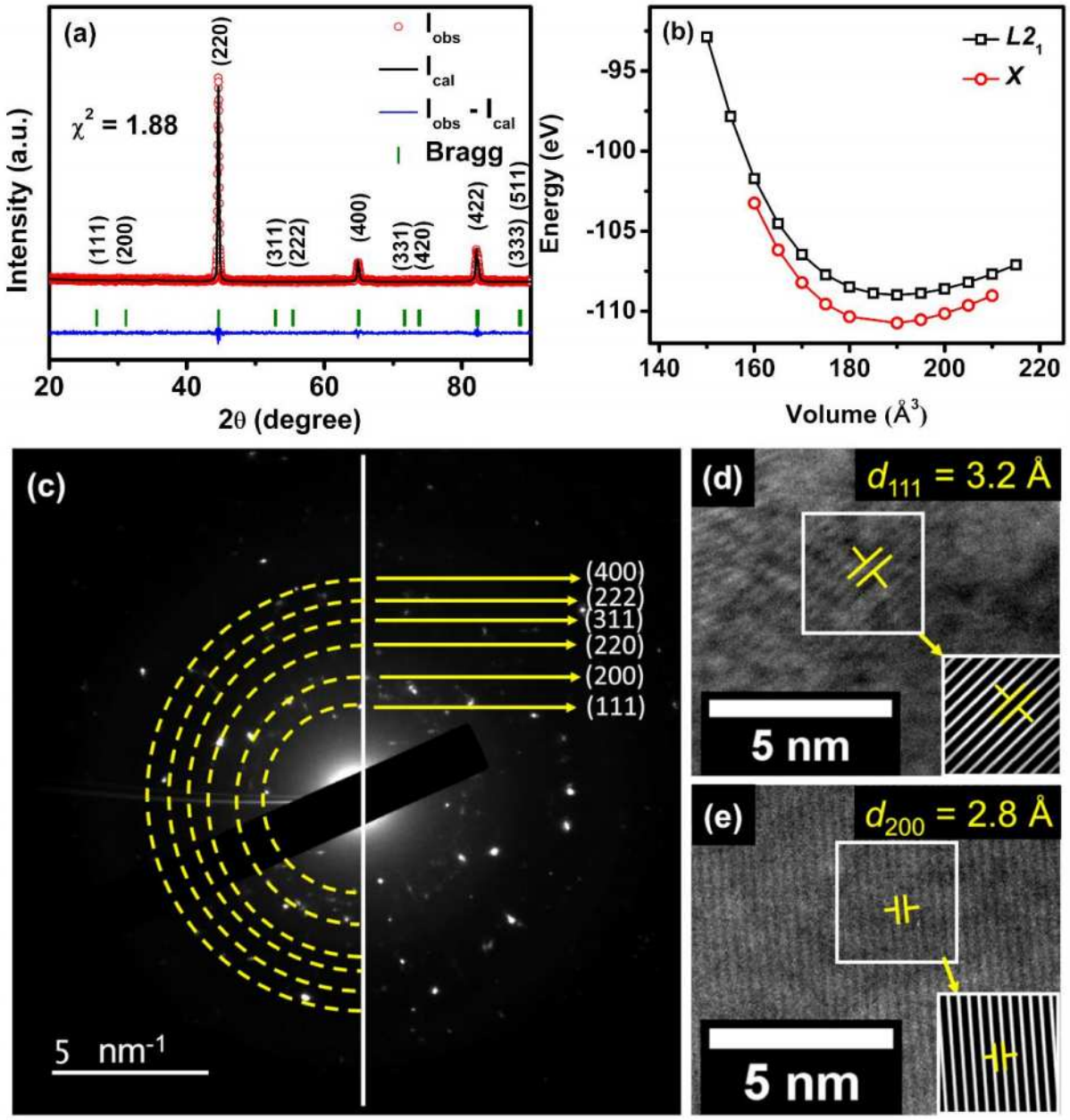

Figure 7.01. (a) Rietveld refined XRD pattern, (b) energy *versus* volume plot, and (c) SAED pattern and (d, e) HRTEM micrographs of $Fe_2CoGa_{0.5}Al_{0.5}$ nanoparticles. Insets in (d, e) show iFFT images of the respective HRTEM micrographs.

7.3 Elemental composition and morphology

EDS measurements reveal an overall composition of $Fe_{49.8}Co_{25.2}Ga_{13.1}Al_{11.9}$, which is close to the nominal composition of $Fe_{50}Co_{25}Ga_{12.5}Al_{12.5}$. The homogeneity of the nanoparticles has been confirmed by elemental mapping (not shown here) using EDS. The particle morphology of the synthesized nanoparticles is depicted in Figure 7.02. The morphology resembles those

of previously reported chemically synthesized Heusler alloy nanoparticles by other authors [187] and synthesized nanoparticles reported in chapters 3, 4 and 5. From the fitting to the histograms shown in the inset of Figure 7.02, d = 52±1 nm with σ = 12 nm was estimated. The slightly bigger d compared to D_v indicates some amount of unavoidable crystallite agglomeration as observed in case of Co_2FeGa, Fe_2CoGa and Fe_2CoAl nanoparticles discussed in chapters 3, 4 and 5, particularly when no templates are used to physically separate the crystallites. A slightly higher σ is observed in current nanoparticles compared to that obtained by template-assisted methods. Though the customary utilization of templates [58,59,67,79–82,84], provides slightly narrow size distribution of nanoparticles, the σ obtained in the present case is acceptable range when one considers the detrimental impact of using templates.

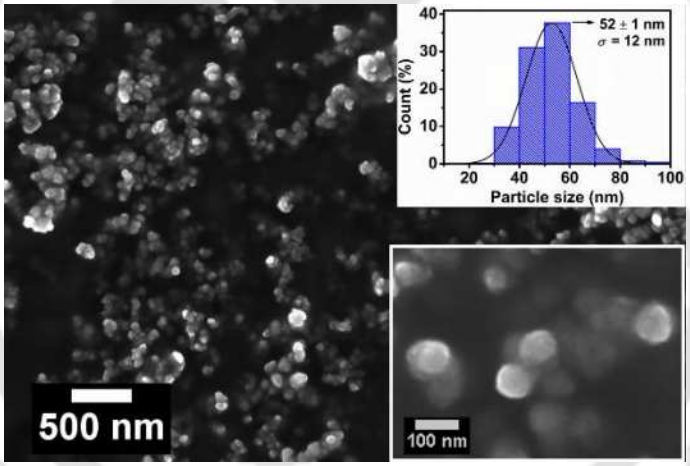

Figure 7.02. FESEM micrograph of $Fe_2CoGa_{0.5}Al_{0.5}$ nanoparticles with their particle size distribution and a magnified image of the particles as insets.

7.4 DOS calculations

Both the end compositions Fe_2CoGa and Fe_2CoAl are known to be non-half-metallic as shown in our previous studies (mentioned in chapters 4 and 5). However, some earlier studies have demonstrated superior half-metallic characteristics and P in intermediate quaternary compositions such as $Co_2FeGa_xGe_{1-x}$ as compared to the ternary end compositions [117].

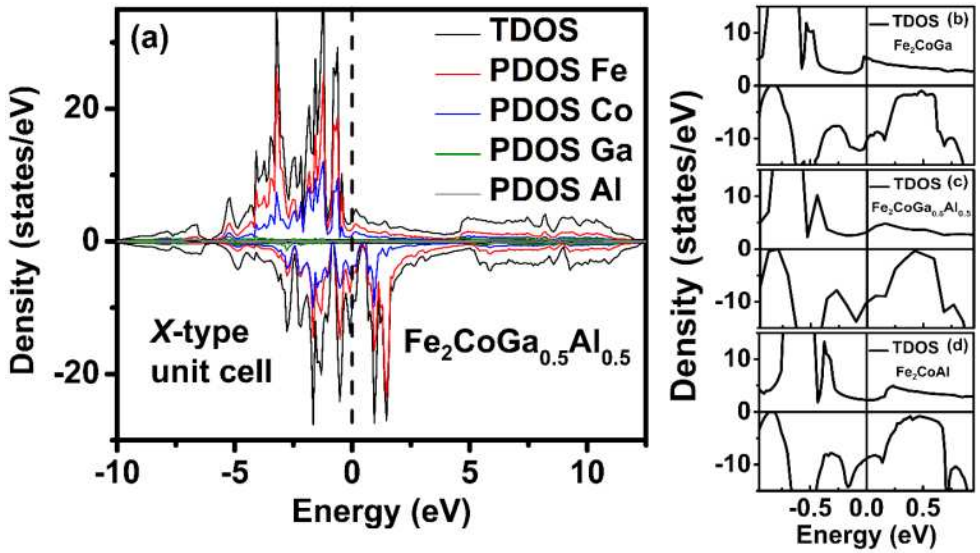

Figure 7.03. (a) PDOS for the elements Fe, Co, Ga, and Al and TDOS of (b) Fe_2CoGa, (c) $Fe_2CoGa_{0.5}Al_{0.5}$, and (d) Fe_2CoAl.

Therefore, *ab initio* calculations were performed on $Fe_2CoGa_{0.5}Al_{0.5}$ as per procedure outlined in chapter 2 using the experimentally determined lattice constant *a*. The TDOS and element resolved PDOS plots of $Fe_2CoGa_{0.5}Al_{0.5}$ alloy shown in Figure 7.03(a) reveal the valance band containing both majority and minority spins, whereas conduction band is primarily dominated by minority spins. It is apparent that $Fe_2CoGa_{0.5}Al_{0.5}$ is also not half-metallic just as the stoichiometric end compounds. An expanded view of the TDOS about E_F is depicted for end compounds Fe_2CoGa (shown in chapter 4), Fe_2CoAl (shown in chapter 5) and the intermediate quaternary compound $Fe_2CoGa_{0.5}Al_{0.5}$, in Figures 7.03(b), 7.03(d) and 7.03(c), respectively. Presence of a physical gap and a pseudo-gap like depression in the minority DOS at -0.8 eV (physical-gap) and +0.5 eV (pseudo-gap) can been seen for all three compositions. In the case of $Fe_2CoGa_{0.5}Al_{0.5}$, both these gaps are slightly closer to E_F (at -0.79 eV and +0.42 eV, respectively) than the end compounds (at -0.82 eV and +0.48 eV for Fe_2CoGa and at -0.83 eV and +0.46 eV for Fe_2CoAl). Moreover, the minority DOS at the pseudo-gap at ~0.5 eV is less dense in $Fe_2CoGa_{0.5}Al_{0.5}$ (-0.33) than the end compounds Fe_2CoGa (-0.96) and Fe_2CoAl (-0.81). These indicate the relatively higher stability of the intermediate composition

$Fe_2CoGa_{0.5}Al_{0.5}$ as compared to the end compounds. *P* of $Fe_2CoGa_{0.5}Al_{0.5}$ is 51 % which is higher than that of Fe_2CoGa (*P* = 34 %) but lower than that of Fe_2CoAl (*P* = 59%). Here, it should be noted that *P* estimated from *ab initio* calculations pertain to the bulk Heusler alloys, which can improve in the case of nanoparticles as demonstrated in the case of 1-d Co_2FeSn nanowires [156].

7.5 Magnetic properties

The theoretically estimated M_t of $Fe_2CoGa_{0.5}Al_{0.5}$ from *ab initio* calculations is 5.26 μ_B/f.u. When M_t of the ternary end compositions Fe_2CoGa (= 5.30 μ_B/f.u. from chapter 4) and Fe_2CoAl (= 5.15 μ_B/f.u. from chapter 5) are compared, M_t of the quaternary compound is in between those of the end compositions. Similar variation in M_t was observed by Chakrabarti *et al.* [202] while investigating $NiMnGa_{2-x}Al_x$ alloys. The *M-H* curves of the $Fe_2CoGa_{0.5}Al_{0.5}$ nanoparticles shown in Figure 7.04(a), clearly displays the soft ferromagnetic nature of the synthesized nanoparticles similar to the previously reported ternary Fe_2CoGa [59] and Fe_2CoAl [63] nanoparticles by other authors as well as in earlier chapters of this thesis. The measured M_s of the $Fe_2CoGa_{0.5}Al_{0.5}$ nanoparticles are 5.18±0.04 μ_B/f.u. at 5 K and 5.17±0.04 μ_B/f.u. at 300 K. Comparison of these with M_s of similar size Fe_2CoGa (= 5.15 μ_B/f.u. at 5 K; 5.08 μ_B/f.u. at 300 K from chapter 6) and Fe_2CoAl (4.70 μ_B/f.u. at 5 K; 4.67 μ_B/f.u. at 300 K from chapter 4) nanoparticles, show no discernible pattern as a function of composition. The deviation observed in experimental M_s as compared to the theoretically obtained M_t of the three nanoparticles might be due to the slight variation in elemental compositions or dead layer thickness at the surface of the nanoparticles. Prior studies on bulk $Fe_2MnGa_{1-x}Al_x$ [203] and $Fe_{50}Mn_{25}Ga_xAl_{25-x}$ [204] alloys also report such variations in M_s with Ga/Al content. The minor decrease in the experimental M_s as compared to the theoretical M_t can be interpreted using the core-shell model [40]. The dead layer thickness *t* corresponding to the synthesized $Fe_2CoGa_{0.5}Al_{0.5}$ nanoparticles (determined using equation 1.13) is 0.11 nm at 5 K (and 0.12 nm

at 300 K), explains the small deviation in experimental M_s from the estimated M_t. M_t evaluated using the S-P rule, *i.e.*, $M_t = Z_t - 24 = 28 - 24$ is 4.0 μ_B/f.u., which shows a deviation from the experimental M_s due to its non-half-metallic character. M_s at room temperature is less than the value at 5 K as observed in Co_2FeGa (chapter 3), Fe_2CoGa (chapter 4) and Fe_2CoAl (chapter 5), which is in agreement with the Bloch's law [70] for temperature dependent M_s. Interestingly, the drop in M_s at high temperatures is very small (*i.e.*, < 1 %), indicating the suitability for high-temperature device applications. The high T_C of the $Fe_2CoGa_{0.5}Al_{0.5}$ nanoparticles is also a consequence of this [152]. The H_c and M_r values of the $Fe_2CoGa_{0.5}Al_{0.5}$ nanoparticles are 89±2 Oe and 0.16±0.04 μ_B/f.u. at 5 K and 60±2 Oe and 0.12±0.04 μ_B/f.u. at 300 K, respectively.

The K_{eff} estimated from LAS is high (= 8.29×10^6 erg/cc at 5 K and 7.89×10^6 erg/cc at 300 K) and is in similar range as observed in previous chapters for stoichiometric Co_2FeGa, Fe_2CoGa and Fe_2CoAl nanoparticles. The K_{eff} of $Fe_2CoGa_{0.5}Al_{0.5}$ nanoparticles are higher than that of Fe_2CoGa nanoparticles (K_{eff} = 6.32-7.44 $\times 10^6$ erg/cc with D_v = 42 nm) but lower than that of Fe_2CoAl nanoparticles (K_{eff} = 8.06-8.22 $\times 10^6$ erg/cc with D_v = 41 nm) of similar size. Both H_c and K_{eff} were found to decrease when measured at higher temperatures. Similar behaviour of H_c [67,69,83,85,152] and K_{eff} [46,196–198] was noted in other magnetic nanoparticles and the previously synthesized stoichiometric Co_2FeGa, Fe_2CoGa and Fe_2CoAl nanoparticles due to the breaking of magnetic alignment by the thermal energy, making it easier for the magnetic domains to reorient along the field direction. The decrement in H_c follows the Kneller's law [169] of temperature dependent H_c variation for single-domain nanoparticles.

Q = 1.28 at 5 K (and 1.23 at 300 K) estimated using equation 1.22 for the synthesized $Fe_2CoGa_{0.5}Al_{0.5}$ nanoparticles categorizes it as a high anisotropic material. For high anisotropic materials, the D_{cr} [47], can be evaluated using Bloch's $T^{3/2}$ law for temperature dependent M_s measurements [48,50,51] at low temperatures [49]. Following the procedure laid down in

chapter 1, D_{cr} for $Fe_2CoGa_{0.5}Al_{0.5}$ nanoparticles was estimated to be 87 nm (*i.e.* $D_{cr} > D_v$), indicating them to be single-domain nanoparticles. The obtained D_{cr} is close to that estimated for the ternary end compositions Fe_2CoGa (93 nm) and Fe_2CoAl (83 nm) in earlier chapters.

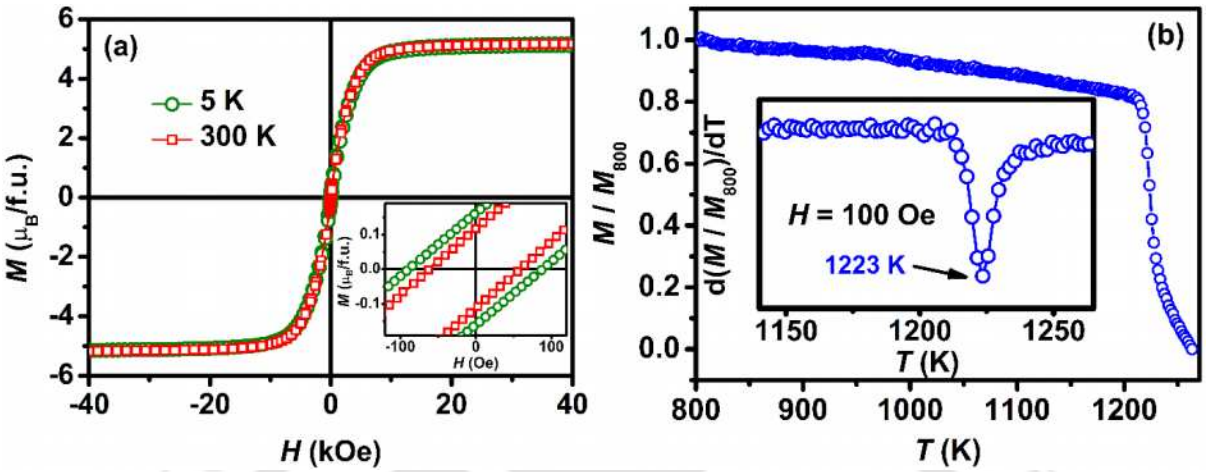

Figure 7.04. (a) *M-H* loops, and (d) *M-T* curves of $Fe_2CoGa_{0.5}Al_{0.5}$ nanoparticles. Inset in (a) gives an enlarged view of the data close to origin and inset in (b) depicts the derivative curve used to determine T_C.

The *M-T* curve recorded for the $Fe_2CoGa_{0.5}Al_{0.5}$ nanoparticles is shown in Figure 7.04(b). Here, the *y* axis represents the normalized magnetization M/M_{800}, where M and M_{800} represent the magnetizations at temperatures T and 800 K, respectively. The curves indicate a high T_C of 1223±2 K for the synthesized $Fe_2CoGa_{0.5}Al_{0.5}$ nanoparticles. Comparison of the obtained T_C with that of similar size Fe_2CoGa (1203 K) and Fe_2CoAl (1225 K) nanoparticles shows an increment in T_C on increasing Al content as also observed in bulk $Fe_{50}Mn_{25}Al_{25-x}Ga_x$ alloys [204].

7.6 Summary and highlights

The investigations on $Fe_2CoGa_{0.5}Al_{0.5}$ Heusler alloy nanoparticle reveal novel properties of the system, which are summarized below:

- This study provides the first account of synthesizing highly ordered quaternary $Fe_2CoGa_{0.5}Al_{0.5}$ Heusler alloy nanoparticle using template-less chemical technique.

- These nanoparticles crystallize in the stable *X* type inverse Heusler alloy structure as confirmed by XRD, SAED, HRTEM measurements and *ab initio* calculations with an average D_v of 42 nm.
- *Ab initio* calculations and standard models have been used to analyze and interpret the experimental findings.
- The synthesized single domain nanoparticles with high M_s (5.18 μ_B/f.u. at 5 K), high K_{eff} (8.29×10^6 erg/cc at 5 K), high T_C (1223 K), high ρ (7.71 g/cc), low M_r (< 0.2 μ_B/f.u.) and low H_c (< 90 Oe), declare their suitability for fabricating various nanomagnetic devices including perpendicular magnetic recording media in high density magnetic recording, magnetic field sensors, SARC-CoV-2 detection, *etc.*
- This pioneering work on the synthesis of quaternary Heusler alloy nanoparticles paves way to develop new Heusler alloy nanoparticles with desired properties.

Chapter 8

Summary and scope for future work

This chapter presents the significant findings and conclusions drawn on the structural, morphological, compositional and magnetic properties of the synthesized Co and Fe based Heusler alloy nanoparticles. A summary of the principal findings of the investigations and potential avenues for future research are provided below.

8.1 Summary of the current study

A series of impurity free, single phase, soft ferromagnetic, single domain Fe and Co based Heusler alloy nanoparticles, *viz.*, Co_2FeGa, Fe_2CoGa, Fe_2CoAl, $Fe_{2-x}Co_{1+x}Ga$ ($0 \leq x \leq 1$), and $Fe_2CoGa_{0.5}Al_{0.5}$, have been synthesized using a facile template-less chemical method. The establishment of highly ordered and stable $L2_1$ or *X* type Heusler alloy structures depending upon their compositions has been done by X-ray and electron diffraction pattern analyses together with *ab initio* energy calculations. EDS analysis confirms the near-stoichiometric compositions of all the nanoparticles close to the desired nominal compositions. The validation of single domain behavior of the nanoparticles has been achieved through the evaluation of D_{cr} values (and demonstrating that $D_{cr} > D_v$ for all the nanoparticles) and H_c dependence on D_v. Initially, D_v of Co_2FeGa, Fe_2CoGa, and Fe_2CoAl nanoparticles were tuned by altering the heat treatment temperatures and/or time, to explore their crystallite size dependent properties. For this, Co_2FeGa nanoparticles with D_v of 57 nm, 47 nm, and 39 nm having $L2_1$ type full Heusler alloy structure, Fe_2CoGa nanoparticles with D_v of 56 nm, 26 nm, and 21 nm having *X* type inverse Heusler alloy structure, Fe_2CoAl nanoparticles possessing D_v of 51 nm, 45 nm, and 41

nm having *X* type inverse Heusler alloy structure were synthesized. Well-established theoretical models have been utilized to interpret the variations of M_s, H_c, T_C and K_{eff} with D_v.

After evaluating the D_v dependent properties of Co_2FeGa and Fe_2CoGa nanoparticles, a systematic composition dependent investigation was carried out on $Fe_{2-x}Co_{1+x}Ga$ ($0 \leq x \leq 1$) nanoparticles with D_v (42-49 nm) having stable $L2_1$ or *X* type Heusler alloy structures depending upon their composition. The stable atomic configuration of the intermediate compositions has been ascertained by *ab initio* energy computations. Finally, the first-ever synthesis and investigations on quaternary Heusler alloy nanoparticles $Fe_2CoGa_{0.5}Al_{0.5}$ with D_v of 42 nm having *X* type inverse Heusler alloy structure was carried out. Apart from the experimental studies, *ab initio* calculations were performed to establish the stable crystal structure and to obtain the DOS plots to infer the half-metallic properties of these Heusler alloy compounds.

The synthesized nanoparticles exhibit several promising properties which are summarized in Table 8.01. Though all the aforementioned compounds show remarkable properties, Table 8.01 indicates unique advantages and hence different targeted applications for each 0-d compound. Co_2FeGa nanoparticles being the softest ferromagnetic material (lowest H_c and M_r) among all the synthesized compounds, exhibit the least magnetic energy loss. This negligibly small H_c and M_r also indicate the possibility of the emergence of superparamagnetism in these nanoparticles. The appearance of Type III half metallicity in this compound is another novelty in this compound. Thus, Co_2FeGa nanoparticles with Type III half-metallicity and the highest spin polarization among all the studied compounds are best suited for spintronic applications. Fe_2CoGa nanoparticles having the highest M_s among all synthesized nanoparticles are suitable for applications demanding high M_s such as magnetic sensors. Fe_2CoAl nanoparticles with the highest achievable K_{eff} are appropriate for applications

such as high density magnetic recording media which require high anisotropy. Additionally, the highest T_C registered by Fe_2CoAl nanoparticles makes them suitable for very high temperature device applications. The synthesized $Fe_{2-x}Co_{1+x}Ga$ nanoparticles can also be considered to possess superparamagnetic nature due to their near zero H_c and M_r values. The systematic composition dependent study of $Fe_{2-x}Co_{1+x}Ga$ nanoparticles along with the study on quaternary $Fe_2CoGa_{0.5}Al_{0.5}$ Heusler alloy nanoparticles showcases a pathway for developing new Heusler alloy nanoparticles with superior properties.

Table 8.01. Comparison of salient magnetic properties of the synthesized nanoparticles.

Compound	M_s (μ_B/f.u.)	H_c (Oe)	M_r (μ_B/f.u.)	K_{eff} ($\times 10^6$ erg/cc)	T_C (K)	D_{cr} (nm)	P (%)
Co_2FeGa	3.36-4.73	**1-9**	**0.00-0.02**	2.93-4.87	1131-1137	100	**65**
Fe_2CoGa	**4.20-5.40**	3-46	0.00-0.07	5.68-8.62	1196-1204	93	34
Fe_2CoAl	4.67-4.93	30-84	0.04-0.13	**8.06-10.24**	**1221-1225**	83	59
$Fe_{2-x}Co_{1+x}Ga$	3.90-5.15	**0-12**	**0.00-0.03**	3.84-7.44	1137-1203	68-100	30-65
$Fe_2CoGa_{0.5}Al_{0.5}$	5.17-5.18	60-89	0.12-0.16	7.89-8.29	1223	87	51

8.2 Scope for future work

Being at a nascent stage (less than 20 decades old), the initial studies on Heusler alloy nanoparticles were only focused on their impurity-free production and (structural and magnetic) property estimates. As already pointed out in the introduction chapter, various magnetic particles having high M_s, high ρ, high K_{eff}, and low H_c have been identified for their utilization as magnetic field driven sensors, perpendicular magnetic recording media in highly dense magnetic recording, *etc*. Therefore, the present study highlights various phenomenal, superior, and enhanced features of the synthesized Heusler alloy nanoparticles including high M_s, high ρ, high K_{eff}, high T_C and extreme low H_c compared to the aforementioned benchmarks (mentioned in chapter 1), which opens a way to apply them for various device applications. The stable M_s up to T_C and high T_C of the synthesized nanoparticles provide an opportunity to apply them in high temperature device applications. Therefore, the practical application of

these nanoparticles in various fields is the next step which could not be explored in this thesis work.

Further investigations on the other optical, thermal, and mechanical properties of these materials, which have not been explored till now, can further open the door to numerous newer applications of these nanoparticles. The off-stoichiometric composition dependent study on $Fe_{2-x}Co_{1+x}Ga$ ($0 \leq x \leq 1$) nanoparticles and the first-ever study on the preparation of quaternary $Fe_2CoGa_{0.5}Al_{0.5}$ nanoparticles highlight a pathway to explore the uncharted territories in materials science to synthesize and investigate new magnetic nanoparticles with remarkable properties.

References

[1] K.H.J. Buschow, F.R. de Boer, Physics of Magnetism and Magnetic Materials, Kluwer Academic Publishers, New York, 2004.

[2] S. Pradhan, P.R. Chaudhuri, Experimental demonstration of all-optical weak magnetic field detection using beam-deflection of single-mode fiber coated with cobalt-doped nickel ferrite nanoparticles, Appl. Opt. 54 (2015) 6269–6276.

[3] M.R. Karim, S. Naryan Panda, A. Barman, I. Sarkar, Strain and crystallite size controlled ordering of Heusler nanoparticles having high heating rate for magneto-thermal application, Nanotechnology. 33 (2022) 235701.

[4] U.R. Dahiya, G.D. Gupt, R.S. Dhaka, D. Kalyanasundaram, Functionalized Co_2FeAl Nanoparticles for Detection of SARS CoV-2 Based on Reverse Transcriptase Loop-Mediated Isothermal Amplification, ACS Appl. Nano Mater. 4 (2021) 5871–5882.

[5] T. Kojima, Y. Nakaya, H. Ham, S. Kameoka, S. Furukawa, Synthesis of Co_2FeGe Heusler alloy nanoparticles and catalysis for selective hydrogenation of propyne, RSC Adv. 11 (2021) 18074–18079.

[6] D. Kappe, L. Bondzio, J. Swager, A. Becker, B. Büker, I. Ennen, C. Schröder, A. Hütten, Reviewing Magnetic Particle Preparation: Exploring the Viability in Biosensing, Sensors. 20 (2020) 4596.

[7] C.Y. Fong, J.E. Pask, L.H. Yang, Half-metallic materials and their properties, Imperial College Press, London, 2013.

[8] F. Heusler, No Title, Verh Dtsch. Phys. Gellschaft. 5 (1903) 219.

[9] O. Heusler, Kristallstruktur und Ferromagnetismus der Mangan-Aluminium-

Kupferlegierungen, Ann. Phys. 411 (1934) 155–201.

[10] A.J. Bradley, J.W. Rodgers, The crystal structure of the Heusler alloys, Proc. R. Soc. London. 144 (1934) 340–359.

[11] Z. Bai, L. Shen, G. Han, Y.P. Feng, Data storage: Review of Heusler compounds, Spin. 2 (2012) 1230006.

[12] C. Felser, A. Hirohata, Heusler Alloys : Properties, Growth, Applications, Springer Series in Materials Science 222, London, 2016.

[13] Y. Takamura, R. Nakane, S. Sugahara, Analysis of $L2_1$ -ordering in full-Heusler Co_2FeSi alloy thin films formed by rapid thermal annealing, J. Appl. Phys. 105 (2009) 07B109.

[14] R.O. Suzuki, T. Kyono, Thermoelectric properties of Fe_2TiAl Heusler alloys, J. Alloys Compd. 377 (2004) 38–42.

[15] J.H. Wernick, G.W. Hull, T.H. Geballe, J.E. Bernardini, J. V. Waszczak, Superconductivity in ternary Heusler intermetallic compounds, Mater. Lett. 2 (1983) 90–92.

[16] S. Chadov, X. Qi, J. Kübler, G.H. Fecher, C. Felser, S.C. Zhang, Tunable multifunctional topological insulators in ternary Heusler compounds, Nat. Mater. 9 (2010) 541–545.

[17] J. Deniszczyk, On the origin of the heavy-fermion-like behavior of the Heusler-type $Fe_{3-x}V_xM$ (M = Al, Ga) alloys, Acta Phys. Pol. B. 32 (2001) 529–533.

[18] R. Tickle, R.D. James, T. Shield, M. Wuttig, V. V. Kokorin, Ferromagnetic shape memory in the NiMnGa system, IEEE Trans. Magn. 35 (1999) 4301–4310.

[19] W.Q. He, H.B. Huang, Z.H. Liu, X.Q. Ma, First-principles investigation of magnetic

properties and metamagnetic transition of NiCoMnZ(Z = In, Sn, Sb) Heusler alloys, Intermetallics. 90 (2017) 140–146.

[20] M. Jourdan, J. Minár, J. Braun, A. Kronenberg, S. Chadov, B. Balke, A. Gloskovskii, M. Kolbe, H.J. Elmers, G. Schönhense, H. Ebert, C. Felser, M. Kläui, Direct observation of half-metallicity in the Heusler compound Co_2MnSi, Nat. Commun. 5 (2014) 3974.

[21] S. Wurmehl, G.H. Fecher, H.C. Kandpal, V. Ksenofontov, C. Felser, H.J. Lin, J. Morais, Geometric, electronic, and magnetic structure of Co_2FeSi: Curie temperature and magnetic moment measurements and calculations, Phys. Rev. B - Condens. Matter Mater. Phys. 72 (2005) 184434.

[22] Y. He, G.H. Fecher, C. Fu, Y. Pan, K. Manna, J. Kroder, A. Jha, X. Wang, Z. Hu, S. Agrestini, J. Herrero-Martín, M. Valvidares, Y. Skourski, W. Schnelle, P. Stamenov, H. Borrmann, L.H. Tjeng, R. Schaefer, S.S.P. Parkin, J.M.D. Coey, C. Felser, A New Highly Anisotropic Rh-Based Heusler Compound for Magnetic Recording, Adv. Mater. 32 (2020) 2004331.

[23] N.K. Jaggi, K.R.P.M. Rao, A.K. Grover, L.C. Gupta, R. Vijayaraghavan, L.D. Kohi, Mossbauer and NMR Study of Site Preference and Local Environment Effects in Co_2FeGa & Fe_2CoGa, Hyperfine Interact. 4 (1978) 402–406.

[24] I. Galanakis, P.H. Dederichs, Half-Metallic Alloys: Fundamentals and Applications, Springer-Verlag, Netherlands, 2006.

[25] B. Deka, R. Modak, P. Paul, A. Srinivasan, Effect of atomic disorder on magnetization and half-metallic character of Cr_2CoGa alloy, J. Magn. Magn. Mater. 418 (2016) 107–111.

[26] R.A. de Groot, F.M. Muller, P.G. van Engen, K.H.J. Buschow, New Class of Materials:

Half Metallic Ferromagnets, Phys. Rev. Lett. 50 (1983) 2024–2027.

[27] I. Galanakis, P.H. Dederichs, N. Papanikolaou, Slater-Pauling behavior and origin of the half-metallicity of the full-Heusler alloys, Phys. Rev. B - Condens. Matter Mater. Phys. 66 (2002) 174429.

[28] S. Skaftouros, K. Özdoğan, E. Şaşioğlu, I. Galanakis, Generalized Slater-Pauling rule for the inverse Heusler compounds, Phys. Rev. B - Condens. Matter Mater. Phys. 87 (2013) 024420.

[29] C.E. Jackson, L.S.J. Johnson, D.A. Williams, H.U. Laasch, D.W. Edwards, A.G. Harvey, A viewpoint on material and design considerations for oesophageal stents with extended lifetime, J. Mater. Sci. 57 (2022) 3–26.

[30] I. Galanakis, E. Şaşioğlu, High T_C half-metallic fully-compensated ferrimagnetic Heusler compounds, Appl. Phys. Lett. 99 (2011) 052509.

[31] M. Meinert, M.P. Geisler, Phase stability of chromium based compensated ferrimagnets with inverse Heusler structure, J. Magn. Magn. Mater. 341 (2013) 72–74.

[32] H. Luo, Z. Zhu, G. Liu, S. Xu, G. Wu, H. Liu, J. Qu, Y. Li, Prediction of half-metallic properties for the Heusler alloys Mn_2CrZ (Z=Al, Ga, Si, Ge, Sb): A first-principles study, J. Magn. Magn. Mater. 320 (2008) 421–428.

[33] N. Xing, Y. Gong, W. Zhang, J. Dong, H. Li, First-principle prediction of half-metallic properties for the Heusler alloys V_2YSb (Y = Cr, Mn, Fe, Co), Comput. Mater. Sci. 45 (2009) 489–493.

[34] H.A. Zhou, T. Xu, H. Bai, W. Jiang, Efficient spintronics with fully compensated ferrimagnets, J. Phys. Soc. Japan. 90 (2021) 081006.

[35] A.K. Grover, R.G. Pillay, V. Nagarajan, P.N. Tandon, Site preference and local

environment effects in ferromagnetic ternary alloys, J. Magn. Magn. Mater. 15–18 (1980) 699–700.

[36] K.H.J. Buschow, P.G. van Engen, Magnetic and Magneto-optical Properties of Heusler Alloys based on Aluminium and Gallium, J. Magn. Magn. Mater. 25 (1981) 90–96.

[37] K.H.J. Buschow, P.G. Van Engen, R. Jongebreur, Magneto-optical properties of Metallic Ferromagnetic Materials, J. Magn. Magn. Mater. 38 (1983) 1–22.

[38] G.L. Whittle, P.E. Clark, R. Cywinski, An Investigation of the Magnetic Order in Pseudo Binary Co(Ga, Fe), J. Magn. Magn. Mater. 30 (1983) 319–330.

[39] K. Yoshimura, A. Miyazaki, R. Vijayaraghavan, Y. Nakamura, Hyperfine Field of the Co_2YZ Heusler Alloy (Y = V, Cr, Mn and Fe; Z = Al, Ga), J. Magn. Magn. Mater. 53 (1985) 189–198.

[40] S.K. Paswan, S. Kumari, M. Kar, A. Singh, H. Pathak, J.P. Borah, L. Kumar, Optimization of structure-property relationships in nickel ferrite nanoparticles annealed at different temperature, J. Phys. Chem. Solids. 151 (2021) 109928 1–26.

[41] B.D. Cullity, C.D. Graham, Introduction to Magnetic Materials, 2nd ed., A John Wiley & Sons, Inc., Publication, 2009.

[42] Y. Prado, S. Mazerat, E. Rivière, G. Rogez, A. Gloter, O. Stéphan, L. Catala, T. Mallah, Magnetization reversal in $CsNi^{II}Cr^{III}(CN)_6$ coordination nanoparticles: Unravelling surface anisotropy and dipolar interaction effects, Adv. Funct. Mater. 24 (2014) 5402–5411.

[43] W.F. Brown, The Fundamental Theorem of Fine Ferromagnetic-Particle Theory, J. Appl. Phys. 39 (1968) 993.

[44] F. Arteaga-Cardona, N.G. Martha-Aguilar, J.O. Estevez, U. Pal, M.Á. Méndez-Rojas,

U. Salazar-Kuri, Variations in magnetic properties caused by size dispersion and particle aggregation on $CoFe_2O_4$, SN Appl. Sci. 1 (2019) 412 1–12.

[45] Y. Xu, M. Liu, X. Huang, Z. Dai, H. Qiu, G. Yu, L. Pan, Magnetic and structural characterizations of Heusler Ni_2FeGa nanoparticles, Mater. Res. Express. 3 (2016) 115012.

[46] B.J. Sarkar, A. Bandyopadhyay, Studies of magnetic behavior of chemically synthesized interacting superparamagnetic copper ferrite nanoparticles, J. Mater. Sci. Mater. Electron. 32 (2021) 1491–1505.

[47] A.P. Guimaraes, Nanoscience and Technology: Principles of Nanomagnetism, Springer Dordrecht Heidelberg, London, 2009.

[48] C.A.F. Vaz, J.A.C. Bland, G. Lauhoff, Magnetism in ultrathin film structures, Reports Prog. Phys. 71 (2008) 056501.

[49] P.C. Riedi, Temperature Dependence of the Hyperfine Field and Hyperfine Coupling Constant of Iron, Phys. Rev. B. 8 (1973) 5243–5246.

[50] R.Y. Umetsu, A. Okubo, A. Fujita, T. Kanomata, K. Ishida, R. Kainuma, Spin Wave-Stiffness Constants of Half-Metallic Ferromagnets Co_2YZ (Y = Cr, Mn and Fe, Z = Ga, Al and Si) Heusler Alloys, IEEE Trans. Magn. 47 (2011) 2451–2454.

[51] R.Y. Umetsu, T. Kanomata, Spin Stiffness Constant of Half-Metallic Ferrimagnet in Mn-Based Heusler Alloys, Phys. Procedia. 75 (2015) 890–897.

[52] J. Mazo-Zuluaga, J. Restrepo, J. Mejía-López, Effect of surface anisotropy on the magnetic properties of magnetite nanoparticles: A Heisenberg-Monte Carlo study, J. Appl. Phys. 103 (2008) 113906.

[53] H. Chhabra, M. Kumar, Development of size and shape dependent model for magnetic

properties from bulk to nanoscale, Indian J. Phys. 95 (2021) 267–274.

[54] Y.D. Wang, Y. Ren, Z.H. Nie, D.M. Liu, L. Zuo, H. Choo, H. Li, P.K. Liaw, J.Q. Yan, R.J. McQueeney, J.W. Richardson, A. Huq, Structural transition of ferromagnetic Ni_2MnGa nanoparticles, J. Appl. Phys. 101 (2007) 063530.

[55] X. Dai, G. Liu, Y. Li, J. Qu, J. Li, J. Chen, G. Wu, Structure and magnetic properties of highly ordered Co_2NiGa alloys, J. Appl. Phys. 101 (2007) 09N503.

[56] A.T. Zayak, P. Entel, J.R. Chelikowsky, Minority-spin polarization and surface magnetic enhancement in Heusler clusters, Phys. Rev. B. 77 (2008) 212401.

[57] A.T. Zayak, S.P. Beckman, M.L. Tiago, P. Entel, J.R. Chelikowsky, Switchable Ni-Mn-Ga Heusler nanocrystals, J. Appl. Phys. 104 (2008) 074307.

[58] L. Basit, C. Wang, C.A. Jenkins, B. Balke, V. Ksenofontov, G.H. Fecher, C. Felser, E. Mugnaioli, U. Kolb, S.A. Nepijko, G. Schönhense, M. Klimenkov, Heusler compounds as ternary intermetallic nanoparticles: Co_2FeGa, J. Phys. D. Appl. Phys. 42 (2009) 084018.

[59] C. Wang, F. Casper, T. Gasi, V. Ksenofontov, B. Balke, G.H. Fecher, C. Felser, Y.K. Hwu, J.J. Lee, Structural and magnetic properties of Fe_2CoGa Heusler nanoparticles, J. Phys. D. Appl. Phys. 45 (2012) 295001.

[60] J.H. Du, Y.L. Zuo, Z. Wang, J.H. Ma, L. Xi, Properties of Co_2FeAl Heusler Alloy Nano-particles Synthesized by Coprecipitation and Thermal Deoxidization Method, J. Mater. Sci. Technol. 29 (2013) 245–248.

[61] T. Li, J. Duan, C. Yang, X. Kou, Synthesis, microstructure and magnetic properties of Heusler Co_2FeSn nanoparticles, Micro Nano Lett. 8 (2013) 143–146.

[62] H.G. Zhang, C.Z. Zhang, W. Zhu, E.K. Liu, W.H. Wang, H.W. Zhang, J.L. Cheng, H.Z.

Luo, G.H. Wu, Significant disorder-induced enhancement of the magnetization of Fe_2CrGa by ball milling, J. Appl. Phys. 114 (2013) 013903.

[63] V. Jain, J. Nehra, V.D. Sudheesh, N. Lakshmi, K. Venugopalan, Comparative study of the structural and magnetic properties of bulk and nano-sized Fe_2CoAl, AIP Conf. Proc. 1536 (2013) 935–936.

[64] T. Fichtner, C. Wang, A.A. Levin, G. Kreiner, C.S. Mejia, S. Fabbrici, F. Albertini, C. Felser, Effects of annealing on the martensitic transformation of Ni-based ferromagnetic shape memory heusler alloys and nanoparticles, Metals (Basel). 5 (2015) 484–503.

[65] B. Malaman, G. Le Caër, B.F.O. Costa, *B*2 long-range order in mechanically alloyed $Fe_{53.3-0.6x}Co_{46.7-0.4x}Sn_x$ ($2 \leq x \leq 26$) annealed at moderate temperatures, J. Mater. Sci. 51 (2016) 5775.

[66] A. Ahmad, S.K. Srivastava, A.K. Das, First-principles calculations and experimental studies on Co_2FeGe Heusler alloy nanoparticles for spintronics applications, J. Alloys Compd. 878 (2021) 160341.

[67] C. Wang, A.A. Levin, L. Nasi, S. Fabbrici, J. Qian, C.E.V. Barbosa, S. Ouardi, J. Karel, F. Albertini, H. Borrmann, G.H. Fecher, C. Felser, Chemical Synthesis and Characterization of γ-Co_2NiGa Nanoparticles with a Very High Curie Temperature, Chem. Mater. 27 (2015) 6994–7002.

[68] M. Hakimi, P. Kameli, H. Salamati, Y. Mazaheri, Evolution of microstructural and mechanical properties of nanocrystalline Co_2FeAl Heusler alloy prepared by mechanical alloying, Powder Metall. 56 (2013) 111–116.

[69] P. Li, X. Kou, Diffusion-assisted Synthesis of Co_2FeSn Heusler Nanoparticles and Their Magnetic Properties, Chem. Lett. 44 (2015) 1706–1708.

[70] L.T. Huynh, S.N. Bonvicini, A.C. Pinon, S. Trudel, Nanocrystalline alloys: Synthesis and characterization of non-stoichiometric Co_2FeAl nanocrystals, Can. J. Chem. 94 (2016) 367–372.

[71] Z. Pezeshki-Nejad, A. Ramazani, S. Alikhanzadeh-Arani, M. Almasi-Kashi, M. Salavati-Niasari, Influence of the surfactant and annealing rate on the morphology, magnetic and structural characteristics of Co_2FeAl nanoparticles, J. Magn. Magn. Mater. 412 (2016) 243–249.

[72] Z. Pezeshki-Nejad, M. Almasi-Kashi, S. Alikhanzadeh-Arani, A. Ramazani, M. Salavati-Niasari, Magnetic and Structural Characterizations of Co-based Heusler Nanoparticles Fabricated via Simple Co-precipitation Method, J. Clust. Sci. 27 (2016) 1031–1039.

[73] S. Alikhanzadeh-Arani, M. Almasi-Kashi, A. Ramazani, M. Salavati-Niasari, Z. Pezeshki-Nejad, Size effects on the magnetic characteristics of a nanostructured Heusler alloy, J. Mater. Sci. 51 (2016) 1354–1362.

[74] S. Alikhanzadeh-Arani, M. Almasi-Kashi, Z. Pezeshki-Nejad, A. Ramazani, M. Salavati-Niasari, Detection of Single-Domain Co_2FeAl Nanoparticles Using First-Order Reversal Curve Method, Metall. Mater. Trans. A. 47A (2016) 5234–5241.

[75] M. Almasi-Kashi, A. Ramazani, S. Alikhanzadeh-Arani, Z. Pezeshki-Nejad, A. Hassan Montazer, Synthesis, characterization and magnetic properties of hollow Co_2FeAl nanoparticles: The effects of heating rate, New J. Chem. 40 (2016) 5061–5070.

[76] F. Yang, D. Liu, W. Li, P. Xiong, Y. Jia, X. Chen, C. Yang, Morphology, microstructure and magnetic properties of Co_2FeAl alloy nanostructures prepared at low temperature, J. Alloys Compd. 735 (2018) 1206–1210.

[77] F. Yang, D. Liu, P. Xiong, Y. Jia, W. Li, X. Chen, The preparation, oxidation resistance and magnetic properties of Co_2FeAl@C core-shell nanoparticles, J. Alloys Compd. 785 (2019) 553–556.

[78] W. Duan, L. Yang, Y. Li, J. Guo, M. Song, The influence of solvents on the microstructure and magnetic properties of Co_2FeAl Heusler alloy nanoparticles, Mater. Chem. Phys. 256 (2020) 123724.

[79] C.H. Wang, Y.Z. Guo, F. Casper, B. Balke, G.H. Fecher, C. Felser, Y. Hwu, Size correlated long and short range order of ternary Co_2FeGa Heusler nanoparticles, Appl. Phys. Lett. 97 (2010) 103106.

[80] C. Wang, L. Basit, Y. Khalavka, Y. Guo, F. Casper, T. Gasi, V. Ksenofontov, B. Balke, G.H. Fecher, C. Sönnichsen, Y.K. Hwu, J.J. Lee, C. Felser, Probing the Size Effect of Co_2FeGa-SiO_2@C Nanocomposite Particles Prepared by a Chemical Approach, Chem. Mater. 22 (2010) 6575–6582.

[81] Y. Xu, D. Yang, Z. Luo, F. Wu, C. Chen, M. Liu, L. Yi, H.G. Piao, G. Yu, Fabrication and magnetic properties of structure-tunable Co_2FeGa-SiO_2 Heusler nanocompounds, AIP Adv. 8 (2018) 055107.

[82] P. Nehla, C. Ulrich, Rajendra Singh Dhaka, Investigation of the structural, electronic, transport and magnetic properties of Co_2FeGa Heusler alloy nanoparticles, J. Alloys Compd. 776 (2019) 379–386.

[83] A. Ahmad, S. Mitra, S.K. Srivastava, A.K. Das, Size-dependent structural and magnetic properties of disordered Co_2FeAl Heusler alloy nanoparticles, J. Magn. Magn. Mater. 474 (2019) 599–604.

[84] C. Wang, F. Casper, Y. Guo, T. Gasi, V. Ksenofontov, B. Balke, G.H. Fecher, C. Felser,

Y.K. Hwu, J.J. Lee, Resolving the phase structure of nonstoichiometric Co_2FeGa Heusler nanoparticles, J. Appl. Phys. 112 (2012) 124314.

[85] C. Wang, A.A. Levin, S. Fabbrici, L. Nasi, J. Karel, J. Qian, C.E. Viol Barbosa, S. Ouardi, F. Albertini, W. Schnelle, H. Borrmann, G.H. Fecher, C. Felser, Tunable structural and magnetic properties of chemically synthesized dual-phase Co_2NiGa nanoparticles, J. Mater. Chem. C. 4 (2016) 7241–7252.

[86] F.J. Yang, J.J. Min, Z.W. Kang, S.Y. Tu, H.B. Chen, D.G. Liu, W.J. Li, X.Q. Chen, C.P. Yang, The influence of pH value and composition on the microstructure, magnetic properties of Co-Fe-Al Heusler nanoparticles, Chem. Phys. Lett. 670 (2017) 1–4.

[87] Y. Srivastava, S.K. Vajpai, S. Srivastava, Structure and magnetic properties of $Co_2(Cr_{1-x}Fe_x)Al$, $(0 \leq x \leq 1)$ Heusler alloys prepared by mechanical alloying, J. Magn. Magn. Mater. 433 (2017) 141–147.

[88] T. Dippong, E. Andrea Levei, O. Cadar, I. Grigore Deac, M. Lazar, G. Borodi, I. Petean, Effect of amorphous SiO_2 matrix on structural and magnetic properties of $Cu_{0.6}Co_{0.4}Fe_2O_4/SiO_2$ nanocomposites, J. Alloys Compd. 849 (2020) 156695.

[89] T. Dippong, E.A. Levei, C. Leostean, O. Cadar, Impact of annealing temperature and ferrite content embedded in SiO_2 matrix on the structure, morphology and magnetic characteristics of $(Co_{0.4}Mn_{0.6}Fe_2O_4)_\delta(SiO_2)_{100-\delta}$ nanocomposites, J. Alloys Compd. 868 (2021) 159203.

[90] T. Dippong, I.G. Deac, O. Cadar, E.A. Levei, Effect of silica embedding on the structure, morphology and magnetic behavior of $(Zn_{0.6}Mn_{0.4}Fe_2O_4)_\delta/(SiO_2)_{(100-\delta)}$ nanoparticles, Nanomaterials. 11 (2021) 2232.

[91] B.D. Cullity, S.R. Stock, Elements of X-ray diffraction, Third, Addision-Wesley

Publishing Company Inc., Massachusetts, 1956.

[92] J. Rodriguez-Carvajal, FULLPROF: a program for Rietveld refinement and pattern matching analysis, Abstr. Satell. Meet. Powder Diffr. XV Congr. IUCr, Toulouse, Fr. 127 (1990) 1.

[93] S. Sarma, Preparation and Characterization of Co-Ni-Ga Ferromagnetic Shape Memory Alloys, Indian Institute of Technology Guwahati, 2008.

[94] P. Scherrer, Zsigmondy's Kolloidchemie, Nachrichten Der Gottinger Gesellschaft. 98 (1918) 394.

[95] T. Pradeep, Nano: The Essentials, Tata McGraw-Hill Publishing Company Limited, New Delhi, 2007.

[96] P. Hohenberg, W. Kohn, Inhomogeneous Electron Gas, Phys. Rev. 136 (1964) B 864-871.

[97] W. Kohn, L.J. Sham, Self-Consistent Equations Including Exchange and Correlation Effects, Phys. Rev. 140 (1965) A 1133-1138.

[98] M. Born, W. Heisenberg, Zur quantentheorie der molekeln, Orig. Sci. Pap. Wissenschaftliche Orig. 4 (1985) 216--246.

[99] J.P. Perdew, K. Burke, M. Ernzerhof, Generalized Gradient Approximation Made Simple, Phys. Rev. Lett. 77 (1996) 3865–3868.

[100] G. Kresse, J. Hafner, *Ab initio* molecular dynamics for liquid metals, Phys. Rev. B. 47 (1993) 558–561.

[101] G. Kresse, J. Hafner, *Ab initio* molecular-dynamics simulation of the liquid-metal-amorphous- semiconductor transition in germanium, Phys. Rev. B. 49 (1994) 14251–

14269.

[102] P.E. Blöchl, Projector augmented-wave method, Phys. Rev. B. 50 (1994) 17953–17979.

[103] G. Kresse, D. Joubert, From ultrasoft pseudopotentials to the projector augmented-wave method, Phys. Rev. B. 59 (1999) 1758–1775.

[104] https://www.vasp.at/wiki/index.php/The_VASP_Manual, (n.d.).

[105] C. Tsirogiannis, I. Galanakis, Effect of the double-counting functional on the electronic and magnetic properties of half-metallic magnets using the GGA+U method, J. Magn. Magn. Mater. 393 (2015) 297–304.

[106] H.C. Kandpal, G.H. Fecher, C. Felser, Calculated electronic and magnetic properties of the half-metallic, transition metal based Heusler compounds, J. Phys. D. Appl. Phys. 40 (2007) 1507–1523.

[107] S. Nia, S. Khenchoul, I.K. Lefkaier, B. Lagoun, DFT-based investigation of the structural, magnetic, electronic, half-metallicity and elastic properties in the all-*d* heusler compounds: the case of Co_2VZn and CoVZn, Eur. Phys. J. B. 94 (2021) 118.

[108] X.G. Xu, D.L. Zhang, W. Wang, Y. Wu, Y.K. Wang, Y. Jiang, Surface effects on the magnetic properties of Co_2FeAl(0 0 1): An *ab initio* study, J. Magn. Magn. Mater. 322 (2010) 3351–3354.

[109] X. Xu, Y. Wang, D. Zhang, Y. Jiang, Electronic structures and the spin polarization of Heusler alloy Co_2FeAl surface, J. Phys. Conf. Ser. 263 (2011) 012016.

[110] L. Yu, G. Gao, L. Zhu, L. Deng, Z. Yang, K. Yao, First principles study of magnetoelectric coupling in $Co_2FeAl/BaTiO_3$ tunnel junctions, Phys. Chem. Chem. Phys. 17 (2015) 14986–14993.

[111] S. Dudarev, G. Botton, S.Y. Savrasov, C.J. Humphreys, A.P. Sutton, Electron-energy-loss spectra and the structural stability of nickel oxide: An LSDA+U study, Phys. Rev. B. 57 (1998) 1505–1509.

[112] M. Kawakami, M. Nagahama, S. ichi Satohira, Hyperfine Fields at ^{51}V in Heusler Alloys $Co_2T_{1-x}V_xGa$ (T=Ti, Cr, Mn, Fe) and Estimation of Magnetic Moments of the Constituent Atoms, J. Phys. Soc. Japan. 59 (1990) 4466–4471.

[113] S. Ishida, S. Sugimura, S. Fujii, S. Asano, The influence of the T atom in Co_2TZ on the hyperfine fields (T=Ti,V,Cr,Mn,Fe; Z=Ga,Al), J. Phys. Condens. Matter. 3 (1991) 5793–5803.

[114] A. Deb, M. Itou, Y. Sakurai, N. Hiraoka, N. Sakai, Magnetic Compton scattering study of the Co_2FeGa Heusler alloy: Experiment and theory, Phys. Rev. B. 63 (2001) 064409.

[115] M. Zhang, E. Brück, F.R. De Boer, Z. Li, G. Wu, The magnetic and transport properties of the Co_2FeGa Heusler alloy, J. Phys. D. Appl. Phys. 37 (2004) 2049–2053.

[116] R.Y. Umetsu, K. Kobayashi, A. Fujita, K. Oikawa, R. Kainuma, K. Ishida, N. Endo, K. Fukamichi, A. Sakuma, Half-metallic properties of $Co_2(Cr_{1-x}Fe_x)Ga$ Heusler alloys, Phys. Rev. B. 72 (2005) 214412.

[117] B.S.D.C.S. Varaprasad, A. Srinivasan, Y.K. Takahashi, M. Hayashi, A. Rajanikanth, K. Hono, Spin polarization and Gilbert damping of $Co_2Fe(Ga_xGe_{1-x})$ Heusler alloys, Acta Mater. 60 (2012) 6257–6265.

[118] M. Sargolzaei, M. Richter, K. Koepernik, I. Opahle, H. Eschrig, I. Chaplygin, Spin and orbital magnetism in full Heusler alloys: A density functional theory study of Co_2YZ (Y=Mn,Fe; Z=Al,Si,Ga,Ge), Phys. Rev. B. 74 (2006) 224410.

[119] S.E. Kulkova, S. V. Eremeev, T. Kakeshita, S.S. Kulkov, G.E. Rudenski, The Electronic

Structure and Magnetic Properties of Full- and Half-Heusler Alloys, Mater. Trans. 47 (2006) 599–606.

[120] K. Özdoğan, B. Aktaş, I. Galanakis, E. Şaşioğlu, Influence of mixing the low-valent transition metal atoms (Y, Y* = Cr, Mn, Fe) on the properties of the quaternary $Co_2[Y_{1-x}Y^*_x]Z$ (Z=Al, Ga, Si, Ge, or Sn) Heusler compounds, J. Appl. Phys. 101 (2007) 073910.

[121] R. Ducher, R. Kainuma, I. Ohnuma, K. Ishida, Phase equilibria and stability of *B*2 and $L2_1$ ordered phases in the Co-Fe-Ga Heusler alloy system, J. Alloys Compd. 437 (2007) 93–101.

[122] B. Balke, S. Wurmehl, G.H. Fecher, C. Felser, J. Kübler, Rational design of new materials for spintronics: Co_2FeZ (Z=Al, Ga, Si, Ge), Sci. Technol. Adv. Mater. 9 (2008) 014102.

[123] M. Kumar, T. Nautiyal, S. Auluck, Full potential results on the magneto-optical properties of the Heusler compounds Co_2FeX (X = Al, Ga, Si and Ge), J. Phys. Condens. Matter. 21 (2009) 196003.

[124] S. Ram, M.R. Chauhan, K. Agarwal, V. Kanchana, *Ab initio* study of Heusler alloys Co_2XY (X = Cr, Mn, Fe; Y = Al, Ga) under high pressure, Philos. Mag. Lett. 91 (2011) 545–553.

[125] F. Ahmadian, A. Boochani, Half-metallic properties of the $Co_2Ti_{1-x}Fe_xGa$ Heusler alloys and $Co_2Ti_{0.5}Fe_{0.5}Ga$ (0 0 1) surface, Phys. B. 406 (2011) 2865–2870.

[126] X.B. Liu, Z. Altounian, Volume dependence of the exchange interaction and Curie temperature in Co_2MGa (M = Ti and Fe): A first-principles study, J. Appl. Phys. 109 (2011) 07B108.

[127] D.A. Kukusta, V.N. Antonov, A.N. Yaresko, X-ray magnetic circular dichroism in Co_2FeGa: First-principles calculations, Low Temp. Phys. 37 (2011) 684–689.

[128] Y. Feng, B. Wu, H.K. Yuan, H. Chen, Electronic structure and magnetic properties of Ga-doped Heusler alloy Co_2FeSi, Appl. Mech. Mater. 130–134 (2012) 1430–1434.

[129] S. Ram, V. Kanchana, Fermi surface studies of Co-based Heusler alloys: *Ab-initio* study, AIP Conf. Proc. 1512 (2013) 1102–1103.

[130] Q.X. Gao, Pressure-induced tunable magnetism and half-metallic stability in Co_2FeGa Heusler alloy, Appl. Mech. Mater. 477–478 (2014) 1303–1306.

[131] M. Tsunekawa, Y. Hattori, A. Sekiyama, H. Fujiwara, S. Suga, T. Muro, T. Kanomata, S. Imada, Soft X-ray photoemission study of $Co_2(Cr_{1-x}Fe_x)Ga$ Heusler compounds, Jpn. J. Appl. Phys. 54 (2015) 082401.

[132] S. V. Faleev, Y. Ferrante, J. Jeong, M. G. Samant, B. Jones, Origin of the Tetragonal Ground State of Heusler Compounds, Phys. Rev. Appl. 7 (2017) 034022.

[133] J.N. Gonçalves, N.M. Fortunato, J.S. Amaral, V.S. Amaral, Volume dependence of magnetic properties in $Co_2Cr_{1-x}Y_xGa$ (Y=Ti-Ni) Heusler alloys: A first-principles study, J. Magn. Magn. Mater. 428 (2017) 362–367.

[134] Y.I. Matsushita, G. Madjarova, J.K. Dewhurst, S. Shallcross, C. Felser, S. Sharma, E.K.U. Gross, Large magnetocrystalline anisotropy in tetragonally distorted Heuslers: A systematic study, J. Phys. D. Appl. Phys. 50 (2017) 095002.

[135] A. Oumsalem, Y. Bourezig, Z. Nabi, B. Bouabdallah, *Ab initio* study of the structural, electronic, and magnetic properties of Co_2FeGa and Co_2FeSi and their future contribution to the building of quantum devices, Turkish J. Electr. Eng. Comput. Sci. 26 (2018) 1249–1260.

[136] V. V. Marchenkov, V.Y. Irkhin, Y.A. Perevozchikova, Peculiarities of Electronic Transport and Magnetic State in Half-Metallic Ferromagnetic and Spin Gapless Semiconducting Heusler Alloys, Phys. Met. Metallogr. 120 (2019) 1325–1332.

[137] C.O. Amorim, J.N. Gonçalves, V.S. Amaral, J.S. Amaral, In-Silico Thermodynamic Description of Heusler Compounds Applied to Magnetocalorics by Monte Carlo Simulations Starting from Ab-Initio, Eur. J. Inorg. Chem. 2020 (2020) 1271–1277.

[138] M.K. Hussain, Half-metallicity of bulk and (001) surface in the Co_2FeGa Heusler compound: A theoretical study, Surf. Rev. Lett. 27 (2020) 1950130.

[139] P.J. Brown, K.U. Neumann, P.J. Webster, K.R.A. Ziebeck, The Magnetization Distributions in Some Heusler alloys Proposed as Half-Metallic Ferromagnets, J. Phys. Condens. Matter. 12 (2000) 1827–1835.

[140] K. Kobayashi, R.Y. Umetsu, A. Fujita, K. Oikawa, R. Kainuma, K. Fukamichi, K. Ishida, Magnetic properties and phase stability of half-metal-type $Co_2Cr_{1-x}Fe_xGa$ alloys, J. Alloys Compd. 399 (2005) 60–63.

[141] K. Kobayashi, R. Kainuma, K. Ishida, Phase separation and stability of $L2_1$-type phase in $Co_2(Cr_{1-x}Fe_x)(Ga_{1-y}Al_y)$ alloys, Mater. Trans. 47 (2006) 20–24.

[142] B. Balke, S. Wurmehl, G.H. Fecher, C. Felser, M.C.M. Alves, F. Bernardi, J. Morais, Structural characterization of the Co_2FeZ (Z=Al, Si, Ga, and Ge) Heusler compounds by x-ray diffraction and extended x-ray absorption fine structure spectroscopy, Appl. Phys. Lett. 90 (2007) 172501.

[143] R.Y. Umetsu, K. Kobayashi, R. Kainuma, Y. Yamaguchi, K. Ohoyama, A. Sakuma, K. Ishida, Powder neutron diffraction studies for the $L2_1$ phase of Co_2YGa (Y = Ti, V, Cr, Mn and Fe) Heusler alloys, J. Alloys Compd. 499 (2010).

[144] R.Y. Umetsu, A. Okubo, R. Kainuma, Magnetic and chemical order-disorder transformations in $Co_2Fe(Ga_{1-x}Si_x)$ and $Co_2Fe(Al_{1-y}Si_y)$ Heusler alloys, J. Appl. Phys. 111 (2012) 073909.

[145] B. Deka, D. Chakraborty, A. Srinivasan, Magnetic properties of $Co_2Fe(Ga_{1-x}Si_x)$ alloys, Phys. B. 448 (2014) 173–176.

[146] P. Chen, G.H. Wu, X.X. Zhang, Magnetic, transport and thermal properties of single crystal Co_2FeGa, J. Alloys Compd. 454 (2008) 52–56.

[147] M. Ramudu, M.M. Raja, J.A. Chelvane, S. V. Kamat, Structure, magnetic properties and electrical resistivity of $Co_2FeSi_{1-x}Ga_x$ Heusler alloy thin films, J. Magn. Magn. Mater. 418 (2016) 42–47.

[148] N. Patra, C.L. Prajapat, R. De, K.D. Rao, P.D. Babu, A.K. Sinha, S. John, H.C. Barshilia, S.N. Jha, D. Bhattacharyya, Correlation of structural ordering with magnetic properties of pulsed laser deposited Co_2FeGa Heusler alloy thin films, J. Alloys Compd. 748 (2018) 653–670.

[149] M. Ramudu, M.M. Raja, H. Basumatary, S. V. Kamat, Role of film thickness on magnetic properties of sputter deposited Co_2FeGa alloy thin films, Mater. Res. Express. 6 (2019) 086404.

[150] H. Wei, X. Kou, Controllable Structure and Magnetic Properties of Co_2FeGa Films Prepared by Electrodeposition, J. Electrochem. Soc. 167 (2020) 102506.

[151] P. Simon, D. Wolf, C. Wang, A.A. Levin, A. Lubk, S. Sturm, H. Lichte, G.H. Fecher, C. Felser, Synthesis and Three-Dimensional Magnetic Field Mapping of Co_2FeGa Heusler Nanowires at 5 nm Resolution, Nano Lett. 16 (2016) 114–120.

[152] M. Gellesch, M. Dimitrakopoulou, M. Scholz, C.G.F. Blum, M. Schulze, J. Van Den

Brink, S. Hampel, S. Wurmehl, B. Büchner, Facile Nanotube-Assisted Synthesis of Ternary Intermetallic Nanocrystals of the Ferromagnetic Heusler Phase Co_2FeGa, Cryst. Growth Des. 13 (2013) 2707–2710.

[153] M. Gellesch, F. Hammerath, V. Süß, M. Haft, S. Hampel, S. Wurmehl, B. Büchner, Compositional analysis of multi-element magnetic nanoparticles with a combined NMR and TEM approach, J. Nanoparticle Res. 19 (2017) 307.

[154] T. Graf, F. Casper, J. Winterlik, B. Balke, G.H. Fecher, C. Felser, Crystal Structure of New Heusler Compounds, Zeitschrift Fur Anorg. Und Allg. Chemie. 635 (2009) 976–981.

[155] J.M.D. Coey, M. Venkatesan, M.A. Bari, Half-Metallic Ferromagnets, Springer-Verlag, Berlin Heidelberg, 2002.

[156] L. Galdun, P. Szabo, V. Vega, E.D. Barriga-Castro, R. Mendoza-Reséndez, C. Luna, J. Kovac, O. Milkovic, R. Varga, V.M. Prida, High Spin Polarization in Co_2FeSn Heusler Nanowires for Spintronics, ACS Appl. Nano Mater. 3 (2020) 7438–7445.

[157] S. Nepal, R. Dhakal, I. Galanakis, Ab initio study of the half-metallic full-Heusler compounds Co_2ZAl [Z = Sc, Ti, V, Cr, Mn, Fe]; the role of electronic correlations, Mater. Today Commun. 25 (2020) 101498.

[158] P. Pathak, G.S. Bisht, A. Srinivasan, Enhanced Magnetic Properties of Electrodeposited Co_2FeSn Film with High Structural Order, J. Electrochem. Soc. 169 (2022) 092508.

[159] Y. He, G.H. Fecher, C. Fu, Y. Pan, K. Manna, J. Kroder, A. Jha, X. Wang, Z. Hu, S. Agrestini, J. Herrero-Martín, M. Valvidares, Y. Skourski, W. Schnelle, P. Stamenov, H. Borrmann, L.H. Tjeng, R. Schaefer, S.S.P. Parkin, J.M.D. Coey, C. Felser, A New Highly Anisotropic Rh-Based Heusler Compound for Magnetic Recording, Adv. Mater.

32 (2020) 2004331.

[160] D. Peddis, F. Orrù, A. Ardu, C. Cannas, A. Musinu, G. Piccaluga, Interparticle Interactions and Magnetic Anisotropy in Cobalt Ferrite Nanoparticles: Influence of Molecular Coating, Chem. Mater. 24 (2012) 1062–1071.

[161] C. Wang, A.A. Levin, J. Karel, S. Fabbrici, J. Qian, C.E. ViolBarbosa, S. Ouardi, F. Albertini, W. Schnelle, J. Rohlicek, G.H. Fecher, C. Felser, Size-dependent structural and magnetic properties of chemically synthesized Co-Ni-Ga nanoparticles, Nano Res. 10 (2017) 3421–3433.

[162] C. Kittel, Physical Theory of Ferromagnetic Domains, Rev. Mod. Phys. 21 (1949) 541–583.

[163] M. Gilleben, R. Dronskowski, A combinatorial Study of Inverse Heusler Alloys by First-Principles Computational Methods, J. Comput. Chem. 31 (2010) 612–619.

[164] A. Dannenberg, M.E. Gruner, M. Wutting, P. Entel, Characterization of new ferromagnetic Fe-Co-Zn-Ga alloys by ab initio investigations, ESOMAT. (2009) 04004.

[165] A. Dannenberg, M. Siewert, M.E. Gruner, M. Wuttig, P. Entel, Competing structural ordering tendencies in Heusler-type alloys with high Curie temperatures: $Fe_2CoGa_{1-x}Zn_x$ studied by first-principles calculations, Phys. Rev. B. 82 (2010) 214421.

[166] K. Seema, R. Kumar, An *Ab-initio* Study of Full Heusler Alloy Fe_2CoGa, AIP Conf. Proc. 1536 (2013) 805–806.

[167] M. Yin, P. Nash, S. Chen, Enthalpies of formation of selected Fe_2YZ Heusler compounds, Intermetallics. 57 (2015) 34–40.

[168] G.D. Liu, X.F. Dai, S.Y. Yu, Z.Y. Zhu, J.L. Chen, G.H. Wu, H. Zhu, J.Q. Xiao, Physical and electronic structure and magnetism of Mn_2NiGa: Experiment and density-functional

theory calculations, Phys. Rev. B. 74 (2006) 054435.

[169] E.F. Kneller, F.E. Luborsky, Particle Size Dependence of Coercivity and Remanence of Single-Domain Particles, J. Appl. Phys. 34 (1963) 656–658.

[170] S. Wang, Y. Wang, Y. Song, J. Zhang, X. Jia, J. Yang, D. Shao, Y. Li, J. Liao, H. Song, Synergistic regulating of dynamic trajectory and lithiophilic nucleation by Heusler alloy for dendrite-free Li deposition, Energy Storage Mater. 50 (2022) 505–513.

[171] A.A. Coelho, M. Imaizumi, B. Laks, A.A. Araújo, M.A. Mota, S. Gama, M. Jafelicci, L.C. Varanda, The change in magnetic properties of Fe_3Al compound due to substitution of Fe by Co, J. Magn. Magn. Mater. 272–276 (2004) 769–770.

[172] T.T. Lin, X.F. Dai, J.X. Zhao, L.Y. Wang, X.T. Wang, Y.T. Cui, G.D. Liu, The structural, electronic and magnetic properties for the transition process between nonmagnetic and magnetic states in $CoFe_{1+x}Ti_{1-x}Al$, J. Alloys Compd. 684 (2016) 143–150.

[173] M. Friák, S. Oweisová, J. Pavlu, D. Holec, M. Šob, An *Ab Initio* study of thermodynamic and mechanical stability of Heusler-Based Fe_2AlCo polymorphs, Materials (Basel). 11 (2018) 1543.

[174] L. Siakeng, G.M. Mikhailov, D.P. Rai, Electronic, elastic and X-ray spectroscopic properties of direct and inverse full Heusler compounds Co_2FeAl and Fe_2CoAl, promising materials for spintronic applications: a DFT+U approach, J. Mater. Chem. C. 6 (2018) 10341–10349.

[175] A. Ahmad, S. Mitra, S. Biswas, S.K. Srivastava, A.K. Das, Site preferences of Fe_2CoAl Heusler alloy: A first-principles DFT study, AIP Conf. Proc. 2115 (2019) 030508.

[176] A. Ahmad, A.K. Das, S.K. Srivastava, Competition of $L2_1$ and XA ordering in Fe_2CoAl

Heusler alloy: a first-principles study, Eur. Phys. J. B. 93 (2020) 96.

[177] D.P. Rai, Lalrinkima, Lalhriatzuala, L.A. Fomin, I. V. Malikov, A. Sayede, M.P. Ghimire, R.K. Thapa, L. Zadeng, Pressure dependent half-metallic ferromagnetism in inverse Heusler alloy Fe_2CoAl: A DFT+U calculations, RSC Adv. 10 (2020) 44633–44640.

[178] Lalrinkima, L.A. Fomin, I. V. Malikov, L. Zadeng, D.P. Rai, Perpendicular magnetocrystalline anisotropy energy (MAE) of 111-surface slab of Fe_2CoAl, Mater. Res. Express. 7 (2020) 064003.

[179] H. Joshi, T. V. Vu, N.N. Hieu, R. Khenata, D.P. Rai, Mechanical and thermodynamical properties of Fe_2CoAl a full-Heusler alloy under hydrostatic pressure: A DFT study, Mater. Chem. Phys. 270 (2021) 124792.

[180] M. Friák, J. Pavlů, M. Šob, Impact of disorder on properties of vacancies: A case study of *B*2 and *A*2 polymorphs of non-stoichiometric Fe_2CoAl, Crystals. 11 (2021) 1207.

[181] K. Szymański, M. Biernacka, L. Dobrzyński, K. Perzyńska, K. Rećko, D. Satula, J. Waliszewski, P. Zaleski, Mossbauer and magnetic studies of $Fe_{3-x}Co_xAl$, J. Magn. Magn. Mater. 210 (2000) 150–162.

[182] E.S. Popiel, W. Zarek, M. Tuszyński, Mössbauer study of the Heusler-type Fe_2MAl compounds for M = V, Cr, Fe, Co, Ni, Nukleonika. 49 (2004) S49–S52.

[183] T. Saito, D. Nishio-Hamane, Magnetic and thermoelectric properties of melt-spun ribbons of Fe_2XAl (X = Co, Ni) Heusler compounds, J. Appl. Phys. 124 (2018) 075105.

[184] I. V. Malikov, L.A. Fomin, V.A. Berezin, A. V. Chernykh, D.P. Rai, G.M. Mikhailov, Study of the Fe_2CoAl Heusler alloy films growth on the R-plane sapphire substrate by scanning probe microscopy, Ferroelectrics. 541 (2019) 79–92.

[185] I. V. Vorotyntsev, A.E. Rassadin, L.A. Fomin, I. V. Malikov, Model of Growth of Heusler-Alloy Epitaxial Films, J. Surf. Investig. 15 (2021) 389–395.

[186] Y. Li, X. Kou, N. Hou, Synthesis, microstructure and magnetic properties of Fe_2CoAl nanofibers, Funct. Mater. Lett. 10 (2017) 1750035.

[187] A. Ahmad, S. Mitra, S.K. Srivastava, A.K. Das, Structural, magnetic, and magnetocaloric properties of Fe_2CoAl Heusler nanoalloy, J. Magn. Magn. Mater. 540 (2021) 168449.

[188] M. Srivastava, M.B. Sahariah, A. Srinivasan, Size-dependent properties of single domain Fe_2CoGa nanoparticles prepared by a facile template-less chemical route, J. Mater. Chem. C. 10 (2022) 11946–11958.

[189] V.K. Jain, N. Lakshmi, R. Jain, V. Jain, A.R. Chandra, K. Venugopalan, Electronic structure, magnetic and optical properties of quaternary $Fe_{2-x}Co_xMnAl$ Heusler alloys, J. Mater. Sci. 52 (2017) 6800–6811.

[190] J.E. Fischer, J. Karel, S. Fabbrici, P. Adler, S. Ouardi, G.H. Fecher, F. Albertini, C. Felser, Magnetic properties and Curie temperatures of disordered Heusler compounds: $Co_{1+x}Fe_{2-x}Si$, Phys. Rev. B. 94 (2016) 024418.

[191] H.C. Herper, B. Krumme, D. Ebke, C. Antoniak, C. Weis, A. Warland, A. Htten, H. Wende, P. Entel, $Co_{2+x}Fe_{1-x}Si$/MgO(001) Heusler alloys: Influence of off-stoichiometry and lattice distortion on the magnetic properties in bulk and on MgO(001), J. Appl. Phys. 109 (2011) 07E128.

[192] K. Srinivas, T. Prasanna Kumari, M. Manivel Raja, S. V. Kamat, Effect of Fe substitution for Co on structure, electrical resistivity, and magnetic properties of Heusler type $Co_{2-x}Fe_{1+x}Si$ alloys, J. Appl. Phys. 114 (2013) 033911.

[193] M. Debbichi, B. Hamad, Impact of excess iron on the calculated electronic and magnetic properties of $Co_{3-x}Fe_xSi$ Heusler-compound, J. Appl. Phys. 116 (2014) 103902.

[194] M.M. Raja, S. V. Kamat, Structure, Magnetic, and Electrical Properties of Heusler-Type $Fe_{3-x}Co_xSi$ Ferromagnetic Alloys, Metall. Mater. Trans. A Phys. Metall. Mater. Sci. 46 (2015) 4688–4697.

[195] R. Wang, Q. Gao, R. Liu, Y. Zhao, J. Ning, P. Yan, Y. Sun, J. Wang, Q. Zeng, J. Du, Y. Xu, L. He, Structural and magnetic properties in the Heusler compounds $Co_{3-x}Fe_xAl$ thin films, J. Phys. D. Appl. Phys. 55 (2022) 395002.

[196] R. Topkaya, O. Akman, S. Kazan, B. Aktaş, Z. Durmus, A. Baykal, Surface spin disorder and spin-glass-like behaviour in manganese- substituted cobalt ferrite nanoparticles, J. Nanoparticle Res. 14 (2012) 1156.

[197] S. Yoon, Temperature dependence of magnetic anisotropy constant in cobalt ferrite nanoparticles, J. Magn. Magn. Mater. 324 (2012) 2620–2624.

[198] M. Atif, Synthesis and temperature dependent magnetic properties of nanocrystalline $Ni_{0.5}Zn_{0.5}Fe_2O_4$ ferrites, Mater. Res. Express. 6 (2019) 076104.

[199] J. Nehra, N. Lakshmi, K. Venugopalan, Effect of substitution of Co with Fe on the structural, electronic and magnetic properties of Heusler alloy Co_2CrAl, Phys. B. 459 (2015) 46–51.

[200] D. Singh, R.S. Tiwari, O.N. Srivastava, Structural and magnetic properties of $Cu_{50}Mn_{25}Al_{25-x}Ga_x$ Heusler alloys, J. Magn. Magn. Mater. 328 (2013) 72–79.

[201] B. Ramachandran, Y.H. Lin, Y.K. Kuo, C.N. Kuo, A.A. Gippius, C.S. Lue, Thermoelectric properties of Heusler-type $Ru_2VAl_{1-x}Ga_x$ alloys, Intermetallics. 92 (2018) 36–41.

[202] A. Chakrabarti, J. Bhattacharya, R. Dutt, D. Pandey, Unusual magnetic and electronic properties of Al-substituted Ga_2MnNi: An *ab initio* study, J. Magn. Magn. Mater. 490 (2019) 165521.

[203] C.E.A. Guimarães, A.C. Krohling, C. Larica, W.L. Scopel, E.C. Passamani, Structural phase transition in Al-substituted Fe_2MnGa Heusler alloy, J. Appl. Phys. 125 (2019) 075105.

[204] S.S. Mishra, T.P. Yadav, R.M. Yadav, A.B. Puthirath, L. Deng, M. Adnani, C.W. Chu, R. Vajtai, P.M. Ajayan, K. Biswas, N.K. Mukhopadhyay, O.N. Srivastava, Effect of Ga substitution on structural and magnetic properties of $Fe_{50}Mn_{25}Al_{25-x}Ga_x$ Heusler alloys, J. Alloys Compd. 854 (2021) 156756.

[205] L. Vegard, Die Konstitution der Mischkristalle und die Raumfullung der Atome, Zeitschrift Fur Phys. 5 (1921) 17–26.

Publications/Presentations

List of publications from the thesis work:

1. **Manisha Srivastava**, Munima B. Sahariah, and Ananthakrishnan Srinivasan, Size-dependent properties of single domain Fe_2CoGa nanoparticles prepared by a facile template-less chemical route, *Journal of Materials Chemistry C*, **2022**, 10, 11946, DOI: 10.1039/d2tc02729a.
2. **Manisha Srivastava**, Gajendra S. Bisht, and Ananthakrishnan Srinivasan, Single domain Co_2FeGa nanoparticles with highly crystalline order synthesized by template-less chemical method, *Journal of Alloys and Compounds*, **2023**, 949, 169848, DOI: 10.1016/j.jallcom.2023.169848.
3. **Manisha Srivastava**, Payal Saha, and Ananthakrishnan Srinivasan, Single-domain Fe_2CoAl nanoparticles and their crystallite size dependent properties, *Journal of Physical Chemistry C*, **2023**, 127, 10215 – 10226, DOI: 10.1021/acs.jpcc.3c01539.
4. **Manisha Srivastava**, Payal Saha, and Ananthakrishnan Srinivasan, Highly ordered single domain $Fe_{2-x}Co_{1+x}Ga$ ($0 \leq x \leq 1$) nanoparticles synthesized by a template-less chemical route, *Materials Research Bulletin*, **2024**, 172, 112659, DOI: 10.1016/j.materresbull.2023.112659.
5. **Manisha Srivastava**, Gajendra S. Bisht, and Ananthakrishnan Srinivasan, Single-domain $Fe_2CoGa_{0.5}Al_{0.5}$ Heusler alloy nanoparticles with enhanced properties, *Physical Chemistry Chemical Physics*, **2024**, 26, 2863, DOI: 10.1039/d3cp05382b.

List of publications outside the thesis work:

1. Debraj Mahata, **Manisha Srivastava**, and Ananthakrishnan Srinivasan, Synthesis and characterization of single phase γ-$Co_{46-x}Ni_{22+x}Al_{32}$ (x = 0, 10, 20) Heusler alloy nanoparticles, *IEEE Transactions on Magnetics*, **2023**, 59, 2500605, DOI: 10.1109/TMAG.2023.3281150.
2. Pushpesh Pathak, **Manisha Srivastava**, Gajendra S. Bisht, Ananthakrishnan Srinivasan, Electrodeposited Fe_2CoSn thin film with enhanced structural and magnetic properties, *Journal of the Electrochemical Society*, **2023**, 170, 122504, DOI: 10.1149/1945-7111/ad155b.

Presentations in conferences:

1. **Manisha Srivastava** and Ananthakrishnan Srinivasan, Comparison between the template-assisted and template-less chemical routes to prepare Heusler alloy nanoparticles, *International Conference on Advanced Materials and Mechanical Characterization (ICAMMC 2021)*, 2-4 December 2021, SRM Institute of Science and Technology, virtual (Poster).
2. **Manisha Srivastava** and Ananthakrishnan Srinivasan, Influence of heat treatment conditions on the structural and magnetic properties of chemically synthesized Co_2FeGa nanoparticles, *International Conference on Magnetic Materials and Applications (ICMAGMA-2023)*, 4-6 December 2023, Hyderabad (Oral).

***